2010

Friction and Wear at Elevated Velocities

Adam Lodygowski
Louisiana State University and Agricultural and Mechanical College

FRICTION AND WEAR AT ELEVATED VELOCITIES

A Dissertation

Submitted to the Graduate Faculty of the
Louisiana State University and
Agricultural and Mechanical College
in partial fulfillment of the
requirements for the degree of
Doctor of Philosophy

in

The Department of Civil and Environmental Engineering

by
Adam Lodygowski
B.S. in Civil Engineering., Poznan University of Technology, 2003
M.S. in Civil Engineering, Poznan University of Technology/University of Hannover, 2005
May, 2010

Acknowledgments

This work, standing as it does on the interface of experimental and theoretical/numerical approach required me to stretch beyond my previous training and preparation and would not have been possible without the help and support of the people I now wish to acknowledge.

First, I would like to warmly thank my advisor Boyd Professor George Z. Voyiadjis for his guidance and support, his persistence on excellence and unwillingness to settle along the way. I appreciate his warm approach and always friendly atmosphere. I also wish to show my appreciation towards him for supporting my masters in the field of mathematics that sufficiently expanded my knowledge and horizons. Without him my work would have never been accomplished.

I wish to turn now to my readers, Professors Suresh Moorthy, Ayman Okeil, Ed Overton and Su-Seng Pang whom I would like to thank for their patience in reading this dissertation and their many pertinent comments. I wish to acknowledge the help of Professors Sylvain Philippon, Laurent Faure and Alexis Rusinek, from ENIM, Metz, France, for their scientific and financial help on the experimental approach. My deepest appreciation to Dr Anthony Palazotto from AFIT for fruitful discussions and Wright Peterson Air Force Base for providing the experimental specimens.

I would also like to take this opportunity to acknowledge the Advanced Computational Solid Mechanics Laboratory (CSM Lab) in particular Dr Babur Deliktas and Danial as well as old graduates Amin and Ziad for their encouragement and always free will to help.

In particular way I wish to express my gratefulness to my parents: Anna and Tomasz. Not only for their never ending love, their constant support and belief in me but also for raising me in this particular way and shaping me to become the person I am today. I thank my Dad for his help and time to puzzle me over material mechanics nuances.

Thank you to my friends, particlarly Rafael and Stan, who provided me with their encouragement and help at various occasions.

Further on, I would like to thank my sisters and family for their love and support. This was an extraordinary challenge to pursue two graduate degrees at the same time and thanks to their warm words and constant encouragement it was easier to overcome the everyday difficulties and obstacles.

Finally, I thank Agnieszka. There are no words I could write to express my special feelings for her. She gives special sense and meaning to all my efforts and is my inspiration. Thank you for constant, unwavering support that helped me through the hardest times, for your patience and, above all, for your endless love...

Table of Contents

List of Tables

List of Figures

Abstract

Severe contact stress problems generate high temperature and create thermomechanical gouging and wear due to high velocity sliding between contacting materials. The major consideration is to develop an experimental and theoretical model for the material constitutive behavior in order to better characterize and predict the internal failure surroundings the gouging and wear events and understand the physical behavior of high speed contact environment.

An enhancement of an existing tribometer device developed by Philippon et al. [2004] is made up of a dynamometer ring and a load sensor that allows to apply an apparent normal force on specimens and measure frictional forces, respectively. The setup has been adapted on a hydraulic testing machine and pressure gas gun to carry out Steel 1080 on Steel VascoMax experiments. The recordings of the normal and tangential forces allows the determination of the friction coefficient. The effects of the sliding velocity on the surface roughness and the dry fiction coefficient are investigated. Performed scans (SEM) show the roughness decrease and reveal the occurrence of the wear.

The second part is devoted to the theoretical approach capturing the phenomena of the wear with extension to incorporate gauging problems. The principle of virtual power is used by introducing the contributions from damage and its corresponding gradients. In addition two internal state variables are introduced on the frictional contact interface measuring the tangential slip and the wear. The constitutive model is formulated with state laws based on the free energies and the complimentary laws based on the dissipation potentials. The proposed model is implemented as user defined subroutine VUMAT in ABAQUS Explicite to analyze the structural response of the high speed sliding experiment from the first part. This model provides a potential feature to relate the non-local continuum plasticity and damage of the bulk material to friction and wear at the contact interfaces. This research is invaluable in providing a multiscale material model and numerical procedure that will be used within a hydrocode to better facilitate the design components of the severe contact stress applications.

Chapter 1

Introduction

1.1 Motivation

Contact problems involving friction are of crucial importance in many engineering applications. When bodies come into contact with each other frictional (shear) forces appear on the contact plane that resist sliding. The frictional behavior on the contact surface is often assumed to be independent of the sliding velocity (rate-independent frictional law). However, this assumption is valid only at small velocities and needs to be revised when dealing with the high velocity or even hypervelocity phenomena ($0-100m/sec$). In particular for this kind of engineering applications combining wear, lubrication and rolling with high speed, and a precise description of the frictional behavior on the contact surface is crucial and needs to be addressed.

Achieving higher and higher sliding velocities coerces the evolvement of used theories to predict the wear and its design. Researches are successful in developing the constitutive models and codes for velocities in the range of $200-600m/s$ Voyiadjis et al. [2008]. However, numerical simulations with velocities of $2000m/s$ and more are still under consideration. Addressing hypervelocity impact and associated high energy is of extreme interest in the research community. A specific example of this emphasis is in the US Air Force test facility at Holloman Air Force Base which specializes in the field of hypervelocity impacting testing. The Holloman High Speed Test Track (HHSTT) is currently working to increase the speed of their sliding vehicle (see Figure 1.1) up to Mach 10. However, already tests with speeds in the range of Mach 8.5 cause increased material interaction which leads to "gauging" in the rails or sled's "shoes". This kind of phenomenon results in damaging adjacent materials and may lead to catastrophic failure.

1.1.1 HHSTT Brief Introduction

The HHSTT with its 50,788 foot long sled track (roughly 9.62 miles) is the longest of its kind in the world with the target area at the north end of the track. It is also the world record holder in rocket sled test established 30^{th} of April 2003 at 00:33. The sled attained a velocity of 9,465 feet per second or 6,453 miles per hour (10,384.8km/h

Figure 1.1: Speed vehicle at Holloman AFB High Speed Test Track Palazotto [2007].

= 2.88km/s), delivering a 192-lb. payload into a target[1]. The vehicle runs on rails and carries a test load that impacts the stationary target. The test sled's "shoe" made from the VascoMax 300 high-strength steel is attached to the rail constructed of 1080 Steel.

The HHSTT is a Custom Built Rocket Sleds and has an in-house design and manufacturing process for each and every sled. This facility treats each customer individually to integrate their payload or test item onto the sled that meets the mission requirements. Some stages of the rocket sled can be used multiple times, while others run off of the end of the track usually impacting a target and are unusable. Each rocket sled train consists of different sled segments. Most commonly used test sled train has four stages: two "Pupfish" pusher sleds, one "Super Road Runner (SRR)" pusher, and one SRR forebody sled that carries the test payload. This configuration is presented in Figure 1.2 and is similar to the previously mentioned world record sled configuration from 2003.

Figure 1.2: Four Stage Rocket Sled Train.

[1]Information found at http://www.holloman.af.mil

The sled segments are not mechanically connected or linked together. When the rocket motor for the first stage burns out, that stage will fall behind and either coast to a stop, or stops via various braking (water, rope drag, etc) methods. The Train runs on rails which are made of 1080 steel and are continuously welded and pre-stressed to remain under tension at temps below 125^oF. The track has 3 rails: A, B, and C. A and B rail run for 50,970 feet and are 84 inches apart. This is called the dual rail. The C rail is 20,320 feet long. The B and C rails are 26 inches apart and are called the "narrow gauge" rail which is used for hypersonic testing. Periodically, red oxide and white epoxy coatings are applied at the north (high velocity) end of the track. Preparations and mounting the train on the rails is presented in Figure 1.3.

(a) (b)

Figure 1.3: Figure 1.3(a) shows the preparation of the Rocket Sled for supersonic testing and Figure 1.3(b) presents the precise mounting process of a particular segments on the rails (in both cases rail B and C are presented).

.

The preparation process is elaborated and requires lots of attention. After accomplishing the first stages of mounting and assembling it is necessary to transport each segment to the launching point established according to the desired final velocity. This towing procedure is presented in Figure 1.4.

Figure 1.4: Towing the Super Road Runner Sled to the launch point.

Because each sled is custom designed and built, the slipper sizes varies to meet the design purposes. The slippers are mostly made of VascoMax 300 material, however occasionally steel 4340 or 4130 are used for the slipper or slipper insert material. Each slipper is specifically manufactured. The channels for the rail are cut out with an electrical discharge machine (EDM), welded together with the other parts that make up the slipper beam and fittings to attach to the sled. Each slipper has a specific part number and drawing attached, as well as the detailed process and the manufacturing history. The typical configuration of slipper and rail arrangement is presented in Figure 1.5.

Figure 1.5: The typical shoe/rail configuration before the launch Palazotto [2007].

1.1.2 Physical Phenomena behind the Supersonic Tests

It is very important to understand the basic physics regarding the sliding friction phenomenon. This is one of the oldest problems in physics, introduced by ancient Egyptians rolling the huge granite blocks to the top of the pyramids. Every year billions of dollars are wasted due to disregarding the tribology related issues. It can be easily stated that modern world depends upon the smooth and satisfactory operation of countless tribological systems, very often taken for granted. However, without sliding friction there would not be cello music and the breaking car would never stop. Therefore it is of great importance to keep improving existing techniques estimating friction minimization or maximization effects depending on particular cases. Sliding friction was studied intensively for several hundred years by the brightest scientists such as Leonardo Da Vinci, Coulomb, Newton, Raynolds. Nowadays many research groups all over the world inquire and investigate different aspects of friction (ASM [1997], Persson [1998] and many others) very often presenting them in many scientific journals such as *The International Journal of Wear* devoted only to friction-related problems. This only expresses the great need for improvement in the field of tribology.

It is obvious that the complexity of the presented problem is tremendous and stands on the interface of physics, engineering and materials science. Supersonic velocities are not studied on the regular basis in aspect of steel on steel dry friction sliding. Obtaining extreme sliding velocities will not only result in substantial temperature increase but might also cause material phase transformation, melting or even evaporation. Addressing these problems is not possible in a single approach and must be considered separately. Therefore this research will fully concentrate on experimental and numerical problems with sliding velocity up to $200m/s$ between steel 1080 (rail) and VascoMax 300 (slipper). Experiments with higher velocities followed by the numerical validation might be possible in the close future within further development of the experimental approach described in this work.

1.2 Objectives of Study

The main objective of this dissertation is to understand the physics within the wear phenomenon at wide range of velocities $(0 - 200m/s)$ and evaluate the effect of wear on an experimental sleigh at the Holloman AFB. In order to handle such problem it is necessary to combine a wide range of different engineering related disciplines. This research stands on the interface between traditional Solid Mechanics, Materials Science, Structural Engineering, Mathematics and Physics. Due to the complexity of the problem multi length scale approach is required to characterize high velocity Wear. There are many issues related to micromechanics such as asperities and material roughness which need to be extended to macromechanics. Neglecting them will affect tremendously the final results. Investigation of the smaller length scale and results obtained there are going to be a prelude to the unit cell model at the meso-scale in order to use it in conjunction with continuum mechanics for computational modeling of the high velocity wear. The proposed constitutive model captures the thermo-elasto-viscoplasticity with viscodamage, a yield criterion of the von Mises type and a dynamic viscodamage criterion including strain and strain rate hardening and temperature softening Voyiadjis et al. [2003]. The influence the material roughness (asperities) affecting the friction of sliding is taken into account.

This research, as it stands, is a comprehensive analysis of friction and wear experiments consisting of both innovatory experimental approach as well as newly developed theory supported and confirmed by numerical implementation and simulations. The goal is to conduct the friction experiments with the use of pressure gun followed by estimation of the friction coefficient and numerical implementation of the entire phenomena according to the newly developed theory. Computational non-local algorithms with the capability of spanning a wide range of velocity wear problems including impact, is studied. The two dimensional simulation for establishing the material parameters for the presented theoretical model and the three dimensional for mimicking the experimental approach are conducted with use of the commercial Finite Element software ABAQUS Explicit. The developed theory describing the constitutive relations is implemented in the User Defined Material Subroutine (VUMAT) supported by ABAQUS which uses explicit time integration not necessarily forming the Jacobian matrix ABAQUS [2009].

While ABAQUS performs the standard finite element procedure using standard types of finite element method the implemented VUMAT is responsible for defining the proposed mechanical constitutive behavior of the material under investigation.

Validating the numerical results with experimental data is of crucial importance especially for this new area of research: hypervelocity impact testing. A number of high velocity different contact tests were performed Borvik et al. [2002], Hartley et al. [1985], Montgomery [1976], Rusinek et al. [2007], however, it is extremely difficult and rare to conduct sliding contact tests showing material behavior and interactions on such elevated velocities Philippon et al. [2004]. These tests, thanks to the USA-Polish-French collaboration were performed in the Laboratory of Physics and Mechanics of Materials at the University of Paul Verlaine in Metz (France) with material samples provided by the Holloman Air Force Base in New Mexico, USA. Despite the fact that maximal testing velocity reaches only up to $200m/s$ it allows to capture the main material behavior and validate the numerical results. Therefore, the constitutive relations developed and used in the Finite Element analysis are compared, critically analyzed and evaluated using the available experimental data. All occurring phenomena will be precisely documented and described in details.

1.3 Chapters Content

This work consist of two major parts. First one, included in Chapters 2, 3, 4 is devoted to all experimental approaches necessary to obtain the data regarding the complete spectrum of physical phenomena. This spectrum is further considered in Chapters 5, 6, 7 defining the theoretical material and constitutive model and applying this theory utilizing experimental results and model calibration to the numerical examples mimicking the friction experiments presented in Chapter 4. Hence, this work is a conjunction of the experimental, theoretical and numerical approach. Linking these different disciplines, which always must correspond to each other, makes this research complete.

In Chapter 2 the determination of the material behavior and response to the uniaxial monotonic and cyclic loading is presented. The experimental approach, conducted in LSU's laboratories results in the stress-strain curves which are vital in the evaluation of the further proposed model and numerical simulations. The material parameters for the most popular materials such as steel alloys as well as pure metals are published in a wide variety of journals. However, in case of new or unpopular materials, like steel VascoMax, it is desired to conduct the set of experiments and compare the results with the other, very limited available sources. High strength steels, such as VascoMax, are most often used in defense applications and therefore the results of material testings are readily for academic or public use. This chapter presents the complete analysis of steel 1080 and VascoMax and comparison of the curves to existing source (Yun and Palazotto [2007]).

Chapter 3 deals with the important aspect of roughness changes before and after the experiment described in details in Chapter 4. It was already stated in 1953 by J. F. Archard (Archard [1953]) that "When two nominally mating surfaces are brought

together, they touch at the tips of the higher asperities and the local area of intimate contact is determined by the deformation of the material in these regions under applied load." This first sentence of the paper was the turning point in understanding the contact phenomenon of two material interfaces. In this chapter the detailed description of the roughness measurement approach is described. With the use of modern technology such as Scanning Electro Microscope (SEM) with software, equipped with the statistical analysis it is possible to measure the material roughness of some area generating the 2D and 3D view of the scanned array. This measurement approach is adopted to the particular case of friction experiments, described in Chapter 4, measuring the particular arrays of the material surface before and after the conducted experiment. Following cases are considered for both materials i.e. steel 1080 and VascoMax: roughness measurement of the unpolished specimens in order to check the effectiveness of the scanning procedure, roughness measurements before and after quasi-static experiments conducted for velocities $0m/s - 4m/s$, and finally the roughness measurements before and after the dynamical experimental approach for velocities $10m/s - 60m/s$. The obtained results are gathered together in a tabular and graphical form and are the foundation to determining the wear definition presented in the theoretical approach.

Following Chapter 4 describes the major experimental part conducted during this research. The set-up used represents a significant evolution of an original friction apparatus developed by Philippon et al. [2004] and used by Sutter et al. [2003] for high speed machining investigation. The beginning of this Chapter consists of the brief overview to the existing measurement techniques for both, sliding movement and different measurements applications. The following Section of Chapter 4 describes in details the friction device utilized for this experimental approach. Important issues such as calibration of the both distinctive parts, proper placement of the strain gauges considering sensitivity of the loading surface, cross-sensitivity and the entire data acquisition setup are scrupulously presented. Further on, the trial experimental approaches with the use of regular steel for both quasi-static and dynamic approaches is shown. After validating the device effectiveness and confirming its accuracy the experiments with the desired materials are presented. Once more, results are shown in the tabular and graphical way and considered with the high does of criticism. Chapter ends with the final remarks and conclusions regarding obtained results. This Chapter concludes the first part with the experimental work and turns to the second one containing theoretical model, implementation and numerical simulations.

First Chapter of the second part, Chapter 5, describes the theoretical approach to the dynamic problem considered experimentally in the fist part. The discussion begins with introducing the basic concepts for solving impact problems. The main contribution to this research area are made, among many others, by Perzyna [1963, 1966, 1971], Litonski [1977], Johnson and Cook [1983], Zerilli and Armstrong [1987], Rusinek and Klepaczko [2001], Voyiadjis et al. [2003], Voyiadjis, Deliktas, Lodygowski, Palazotto, Philippon, Rusinek, Faure and Chevrier [2009*b*]. Further on, the basic framework for the numerical implementation is presented based on the development of Voyiadjis et al. [2003]. The concepts of the thermodynamically consistent constitutive equations and plastic dissipation potential and evolution equation are presented along with the elasto-plastic tangent stiffness. Based on these theoretical ideas the numerical

framework is given allowing the implementation of the theory into the fortran code as a user subroutine VUMAT. Description of the discretization and the radial return mapping algorithm is given along with the smoothing of the elasto-plastic transition. This information is a crucial foundation to understand the theoretical modeling presented in the last section of this Chapter: non-local modeling of the heterogeneous media to assess high velocity frictional contact using coupled viscoplasticity damage model. This model is introduced and analyzed in details.

In Chapter 6 the constitutive model presented in the previous Chapter is calibrated. The material constants are obtained in two distinct ways; some of them are acquired from existing sources such as steel tables and other publications and the ones mainly related to hardening laws are obtained by the least square approach and further small practical adjustments, to fit the stress-strain curve in the closest possible way. Obtaining the constants is possible thanks to FE software ABAQUS, conducting uniaxial tension analysis, and the experimental uniaxial tension results from Chapter 2. The calibrated model generates both uniaxial tension as well as uniaxial cyclic loading stress-strain curves which are graphically compared to the experimental data.

The application of presented model with calibrated constants is shown in Chapter 7. The simulated model is mimicking the experimental setup from Chapter 4. All necessary ABAQUS inputs are shown in details. While developed user subroutine deals with the material response and upgrading the stress increment $\Delta\sigma$ the ABAQUS takes this value and thanks to next numerical step provides the strain increment $\Delta\varepsilon$. The obtained results are stated clearly and discussed in details. It is important to note that this project is under constant development with respect to sliding velocity and registering new independent variable that cold be compared with the numerical approach. One of this variable is flash temperature which in a close future should be possible to capture and compare as an individual and independent variable.

Chapter 2

Material Characterization

2.1 Introduction

Determining the material experimentally is vital for use in the evaluation of the proposed model and numerical simulations. The material parameters for most popular materials such as steel alloys as well as pure metals are published in a wide variety of journals. However, in case of new or not very popular materials, like steel VascoMax, it is desired to conduct the set of experiments and compare the results with the other available sources. High strength steels, such as VascoMax, are most often used in defense applications and therefore the results of material testings are readily for academic or public use. Due to wide cooperation on this research between several universities, in particular the Air Force Institute of Technology, it was possible to conduct and obtain the results of quasi-static and dynamic tests for both, VascoMax and Steel 1080.

Experimental results obtained by Kennan [2005] evaluating most of the material parameters for steel 1080 and VascoMax were very valuable information. However, due to limited experimental results available for these two particular materials, it was decided to validate the results presented by Kennan [2005] in the uniaxial quasi-static tensile test.

2.2 Uniaxial Testing of Steel 1080 and VascoMax 300

2.2.1 Experimental Setup - Monotonic Loading

An MTS 810 Hydraulic Materials Testing System was used to apply monotonic uniaxial stresses on the specimens. The strain data were obtained using one inch gage length MTS extensometer (Model No: 634.11EĐ24) and one millimeter gage length Omega general purpose pre-wired 1-axis strain gages. The actual cross-sectional dimensions of the specimens were measured prior to the tests using a digital caliper, and the measured dimensions are presented in Table 2.1.

One specimen from each material type was tested under monotonic increasing tensile loading in order to obtain the mechanical properties (yield strength and ultimate strength) of the materials. The rate of loading of the MTS testing machine was

Table 2.1: Specimen dimensions for VascoMax 300 and Steel 1080

Specimen Type	**Cross Section** $[mm \times mm]$	**Applied Loading**
Steel 1080	0.9906×10.16	Monotonic Increasing
Steel VascoMax 300	1.6256×7.9502	Monotonic Increasing

set to be $0.5mm/min$ for both types of specimens and it was applied until the material failure. Determination of the loading rate values were made based on the ASTM E8, Standard Test Methods for Tension Testing of Metallic Materials. Even though the recommended rate of loading values in ASTM E8 are higher than the ones used in this study, slower loading rates were used in this study because the cross-sections of the specimens are considerably smaller than the standard tension testing specimens addressed in the standards.

The experimental setup for the uniaxial monotonic loading is presented in Figure 2.1. During the tests, only the longitudinal strain values were recorded in the midsection of the specimens using one inch gage length MTS extensometer as presented in Figure 2.1(d).

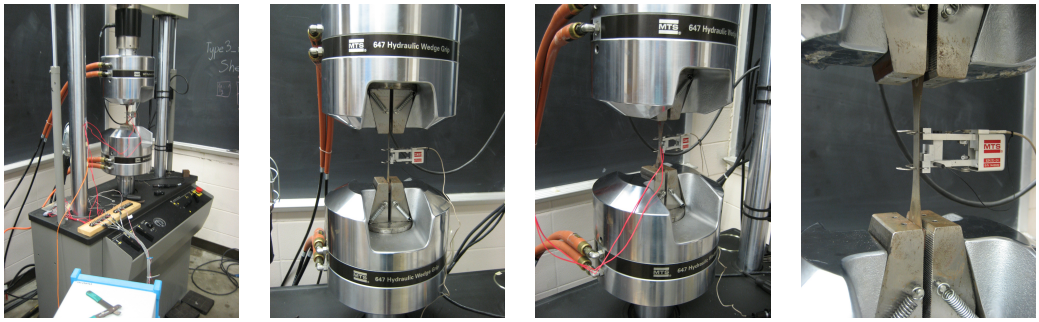

(a) (b) (c) (d)

Figure 2.1: Figure 2.1(a) shows the entire setup of the experimental device. Figure 2.1(b) and 2.1(c) present the different views of the hydraulic elements applying the load to the specimen whereas Figure 2.1(d) presents the measurement of the specimen longitudinal strains with mounted strain gauges and holding clamps.

.

In Figure 2.2, different stages of the tested specimens are presented. Figure 2.2(a) presents the specimen just before the experiment with mounted strain gauges. Figures 2.2(b) and 2.2(c) present the specimens after testing. The necking implying plastic deformation is clearly visible in both cases. Figure 2.2(d) presents the specimen during the actual experiment. Necking, mounted strain gauges as well as the clamps holding the specimen are clearly observed. The strain gauges attached to the specimen are connected to the computer and all information regarding lateral displacement is registered.

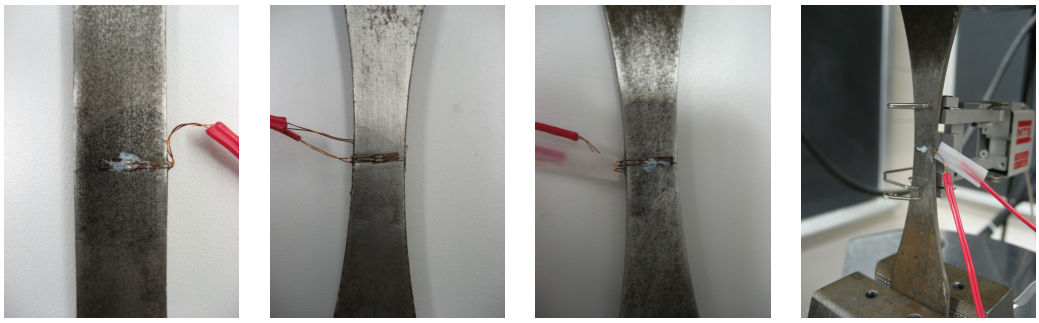

(a) (b) (c) (d)

Figure 2.2: Figure 2.2(a) shows the initial stage of the specimen attached to the hydraulic machine with mounted strain gauges. Figures 2.2(b) and 2.2(c) present the specimens under tensile stress undergoing the necking whereas Figure 2.2(d) presents the necking of the specimen with mounted strain gauges.

2.2.2 Results from Uniaxial Monotonic Loading Tests

During this experimental procedure different types of loading scenarios were taken into account. A set of material specimens were tested with uniaxial monotonic loading. Both, Steel 1080 and VascoMax 300 materials gave good correlation with the results obtained from the literature Kennan [2005]. The obtained curves are presented in Figures 2.3 and 2.4.

It is very important to notice that the plot of the stress strain curve is exactly the same as that tested by Kennan [2005], however, the value of the true stresses presented by here differs from the values of stress obtained in Kennan [2005]. It is mainly due to two different methods of calculating the stresses during the experiment. The first method calculates the stresses with respect to the unchanged cross sectional area of the specimen ($\sigma = \frac{F}{A}$) whereas the second method calculates the true stress accounting for the decrease of the cross section of the tested specimen ($\sigma_{true} = \frac{F}{A_{true}}$). Obviously, with the constant increment of the applied force to the specimen the decrease of the denominator will generate the greater value of stress. This is the reason why the maximum values of stresses are larger in case of the true stress, as presented in Kennan [2005] and smaller in this approach which does not account for the reduction in the cross sectional area.

Another interesting aspect for both steels lies in their ductility. The first type of specimens made of Steel 1080 shows very *typical* steel behavior- elastic regime followed by yielding, then hardening resulting in specimen necking and visibly followed by material failure. Steel VascoMax, however, shows quite different and more unusual material behavior among steel alloys. In this case the elastic regime is followed by yielding and very short, almost non existing hardening, immediately followed by strong softening. This is not only due to the material crystallographic structure but also due to strong temperature dependency. Due to other performed tests with the higher loading rates the failure of this material, although it's much stronger than the previous one, is less ductile than expected. This makes it more difficult to evaluate the material fatigue par-

ticularly in commercial applications, such as the slipper of a speed vehicle at HHSTT.

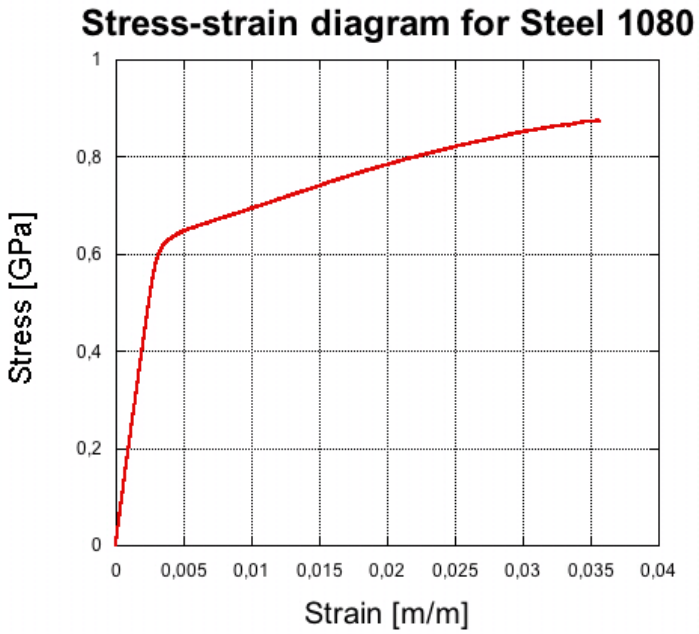

Figure 2.3: The stress strain curve for the quasi static monotonic loading for steel 1080.

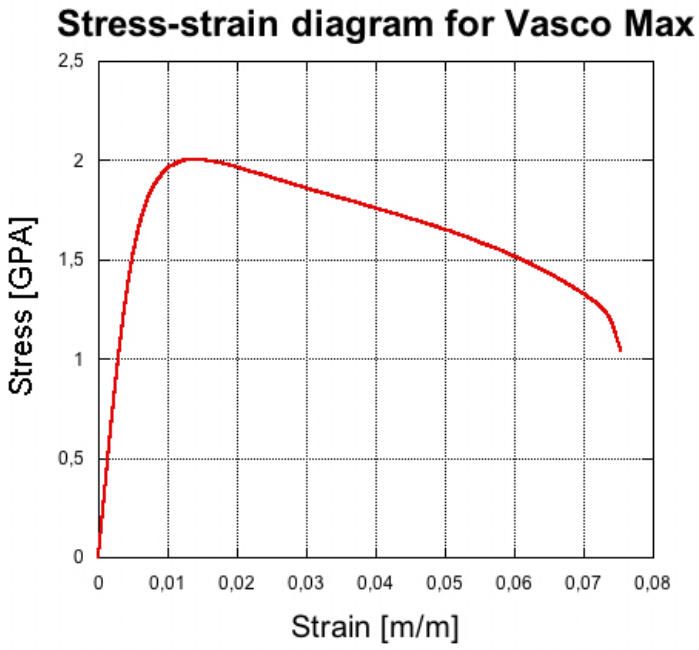

Figure 2.4: The stress strain curve for the quasi static monotone loading for VascoMax 300.

2.3 Cyclic Testing of Steel 1080 and VascoMax 300

2.3.1 Experimental Setup - Cyclic Loading

The experimental setup for the cyclic loading is similar to the previous, monotonic loading, setup and is already presented in Figure 2.1. The cyclic loading experiments are performed in a similar fashion as described in Section 2.2.1. The main difference for this case is that MTS 810 Hydraulic Materials Testing System was used to apply cyclic uniaxial stresses on the specimens. The strain data were obtained using one inch gage length MTS extensometer (Model No: 634.11EĐ24) and one millimeter gage length Omega general purpose pre-wired 1-axis strain gages. The actual cross-sectional dimensions of the specimens were measured prior to the tests using a digital caliper, and the measured dimensions are presented in Table 2.2.

Table 2.2: Specimen dimensions for VascoMax 300 and Steel 1080

Specimen Type	**Cross Section** $[mm \times mm]$	**Applied Loading**
Steel 1080	0.9906×10.16	Cyclic
Steel VascoMax 300	1.6256×7.9756	Cyclic

One specimen from each material type was tested under cyclic tensile and compressive loading in order to obtain the cyclic stress strain curve for both materials, necessary for further numerical validation. The rate of loading of the MTS testing machine was set to be $0.5mm/min$ for both types of specimens. In this second phase of experiments the specimens were loaded up to a stress/strain level and then they were unloaded until the applied force was equal to zero. Several cycles were applied in such a way that the peak strain value of each cycle exceeded the one from the previous cycle. For Steel 1080 it was decided to conduct four full loading cycles and for Steel VascoMax 300, due to its already observed brittleness, only two. For this purpose special test procedures were defined using the MTS controller software. The following values such as time, machine displacement, applied force and strain values were recorded and stored. In order to calculate the applied stresses, the average of the transverse strain obtained from the two strain gages was used. The transverse strain along the thickness of the specimen was assumed to be equal to the transverse strain along the width. Determination of these loading rate values were made based on the ASTM E8, Standard Test Methods for Tension Testing of Metallic Materials. Even though the recommended rate of loading values in ASTM E8 are higher than the ones used in this study, slower loading rates were used in this study because the cross-sections of the specimens are considerably smaller than the standard tension testing specimens addressed in the standards.

2.3.2 Results from Uniaxial Cyclic Loading Tests

During this experimental procedure different kind of loading scenarios were used. A set of material specimens were tested with uniaxial cyclic loading. Both, Steel 1080

and VascoMax 300 materials gave good correlation with the results obtained from the literature Kennan [2005]. The obtained curves are presented in Figures 2.5 and 2.6.

It is very important to note that the overall behavior curves for the cyclic loading follows uniaxial monotonic approach. In both Figures 2.5 and 2.6 monotonic and cyclic loading approaches are compared. It is clearly visible that both curves oscillate around similar values. Once more as it was already stated in the previous section the stresses are calculated with respect to the unchanged cross sectional area of the specimen ($\sigma = \frac{F}{A}$). In case of cyclic loading however, it is not possible to compare the obtained results with any external source. No similar experimental uniaxial cyclic loading results for steel VascoMax 300 and hence the comparison was not possible.

In case of Steel 1080 despite the fact that the loading rate was the same for both, monotonic and cyclic loading (Figure 2.5) the presented curves do not match as well as they match for steel VascoMax 300. This is not a computational or experimental mistake but due to several factors such as slight sliding around the grip during loading and unloading, and slight different material structure for different specimens resulting in different damage and micro void evolution.

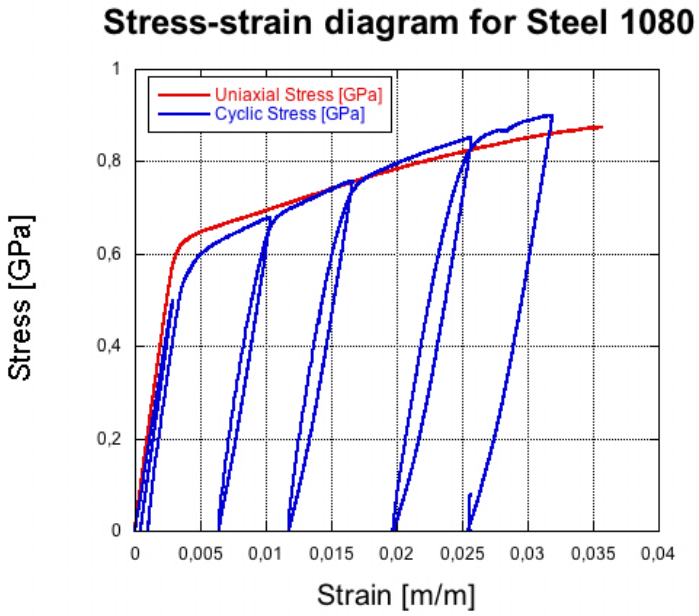

Figure 2.5: The stress strain curve for the quasi static cyclic loading for steel 1080.

2.4 Conclusions

The static uniaxial monotonic and cyclic loading tests for Steel 1080 and VascoMax 300 were conducted with the use of the MTS 810 Hydraulic Materials Testing System. The obtained results give a good correlation with those presented in the literature and confirm the validity of the material constants presented by other sources. It is very important to notice that steel 1080 behaves like a regular steel with the characteristic yielding and common positive hardening, however, steel VascoMax

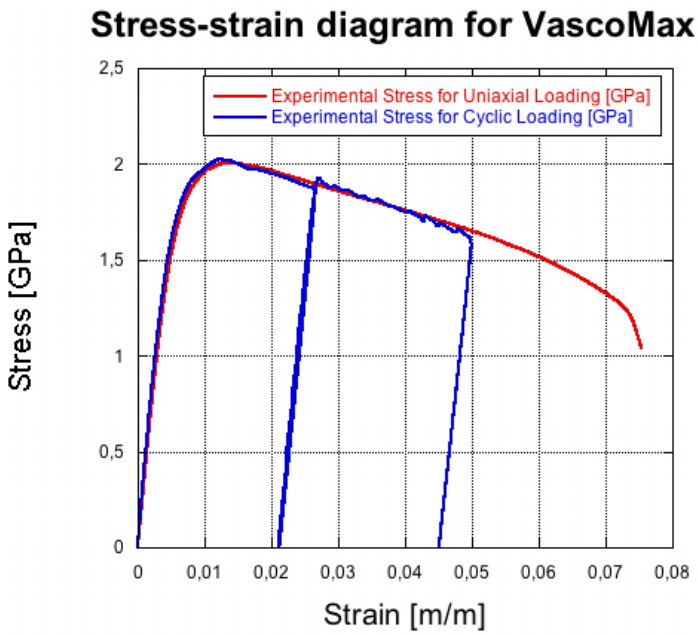

Figure 2.6: The stress strain curve for the quasi static cyclic loading for VascoMax 300.

300 is quite different. The yielding stresses are very close to the maximum obtained stresses and following that point the material immediately experiences softening. This is due to the very high strength of this kind of steel and specific crystallographic structure which enforces high brittleness. Additionally, the fact that the true stress was not calculated in the experiments but rather the nominal stress intensifies this phenomenon. When the true stress is evaluated then it is possible to impose the positive hardening as shown by Kennan [2005]. Apart from this it is also interesting to notice that the cyclic loading experiments show very good correlation with the monotonic tests as shown in Figures 2.5 and 2.6. No experimental data were found for cyclic loading experiments for steel VascoMax 300. Hence, these experiments are of a significant importance in calibrating the constitutive model proposed in this work.

Chapter 3

Roughness Measurements

3.1 Introduction

"When two nominally mating surfaces are brought together, they touch at the tips of the higher asperities and the local area of intimate contact is determined by the deformation of the material in these regions under applied load." This first sentence of the paper by J. F. Archard back in 1953 Archard [1953] was the turning point in understanding the contact phenomenon of two material interfaces. The interpretation of certain phenomena occurring at nominally flat surfaces in stationary or sliding contact is dependent on the assumed distribution of the real area of contact between the surfaces. Moreover, the most realistic model is this one in which increasing the load increases both the number and size of the contact areas (Figure 3.1). In general, mechanical wear should also depend on the generated model. These revolutionary conclusions changed the way of thinking and pointed new problems which need to be addressed.

Even a surface which appears to be flat on a millimeter scale may contain micrometer scale asperities i.e. the surface is rough (Figure 3.1- top). If two surfaces are brought in contact, only asperities really touch each other. Friction is due to the interaction between the asperities of the different surfaces and the resulting energy dissipation is due to the interaction of these asperities. The real area of contact is therefore a few orders of magnitude smaller than the apparent area of contact. This important fact has to be taken into account while modelling a friction process.

Wear of the material is one possible reason of friction. The earliest works on this topic were written by (Archard [1953], Bowden and Tabor [1950] and others) who initiated the problem and distinguished the wear from the typical material behavior being not in contact. These authors suggested that the area of contact between two seemingly flat surfaces strongly depend on applied normal force F_N. Therefore they suggested that mechanical wear should find its representation in the material models. Following development and new ideas were suggested in Michalowski and Mroz [1978]. They implied that sliding rules of rigid or elastic bodies along a contact surface can be derived by using the velocity rules associated with the limit friction condition $f = 0$. Moreover it is suggested that the model of wedge asperities makes it possible to derive the non-associated sliding rules. Using very simple geometrical relationships constitu-

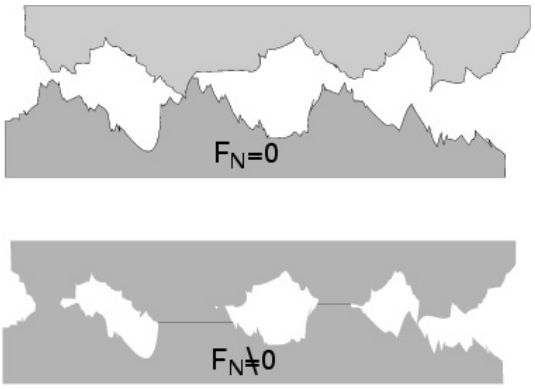

Figure 3.1: Asperities under no load (on the top) and the same surface after a load is applied (left bottom).

tive relations for contact sliding with account for elastic and plastic deformation are proposed and their accuracy is discussed. It is observed that due to non-associated character of local sliding rule, the rigid body motion on the edge asperities does not obey the normality rule in the horizontal plane.

Investigation of the phenomena occurring on the interface between sled track and slipper at Holloman High Speed Test Track requires conducting a series of experiments. In order to understand the physical behavior during hyper velocity friction and wear it is necessary to use the multi-scale approach. First part of this research concentrates on measuring and investigating the surface roughness of steel VascoMax 300 (material used for the slipper) and steel 1080 (material used for the rail). Material parameters for both materials can be found in Table 3.1 as obtained from Yun and Palazotto [2007].

Table 3.1: Material parameters for VascoMax 300 and Steel 1080

Parameter	**Steel 1080**	**VascoMax 300**
Young's Modulus E $[GPa]$	202.8	180.7
Poisson Ratio ν	0.27	0.283
T_{melt} $[K]$	1670	1685
Density ρ $[kg/m^3]$	7800	8000
Thermal Conductivity $[W/m \cdot K]$	18	19.6
Specific Heat C_p $[J/kg \cdot K]$	460	452

The material samples (Figure 3.2(a)), provided by HHSTT, were scanned with **Veeco** Scanning Electro Microscope (SEM) (Figure 3.2(b)). This Optical Profiling System sends the stream of light to the measured surface and by interpreting its reflection creates a 3D surface profile of the sample under investigation. It provides many of the performance attributes including: easy measurement setup, fast data acquisition and comprehensible and extensible data analysis. A data stitching option adds a motorized stage and support software (Viosion32) to scan larger surface areas. The device used for these particular measurements was equipped with IXL 5 lens and the magnification factor was set to be 2.5.

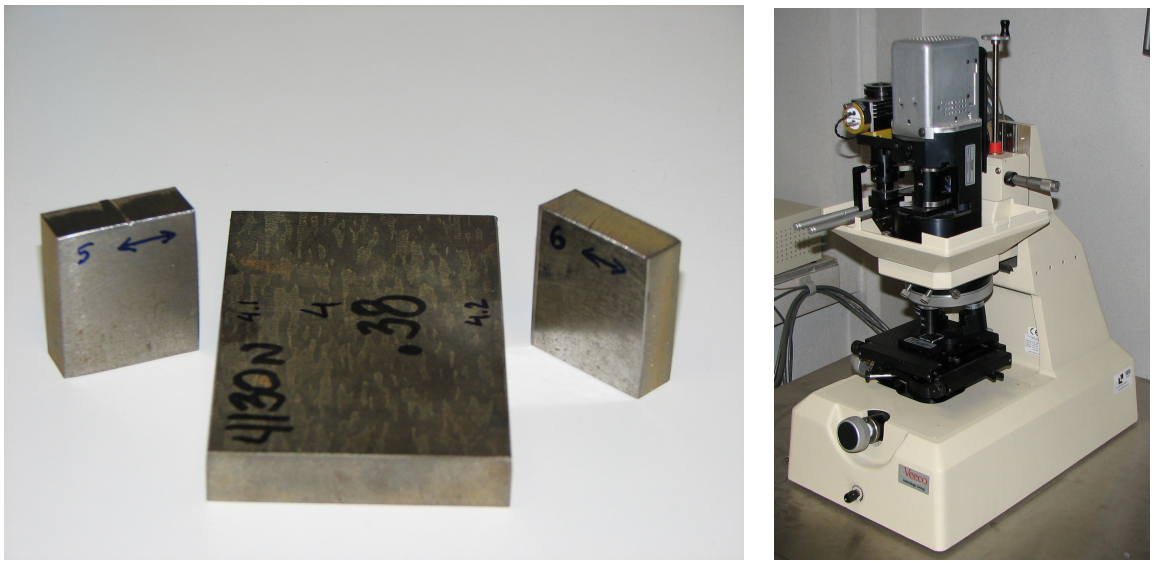

(a) (b)

Figure 3.2: 3.2(a) Material samples: VascoMax 300 in the middle and two steel 1080 samples on the sides. 3.2(b) Scanning Electro Microscope in ENIM, Metz, used to obtain surface roughness.

The emphasis of this part of the research is to establish the average material roughness for VascoMax 300 and Steel 1080 as well as investigating the changes in roughness before and after the tests conducted in ENIM (Ecole Nationale d'Ingénieurs de Metz) in Metz, France (see Chapter 4).

3.2 Measurement Procedure

Determining the area of the surface to be scanned was directly dictated by the experimental setup (Figure 3.3). In order to capture the average roughness of the material it would be sufficient to conduct measurements in any place of the specimen. However, in order to account for the surface change during the experiment the measurements had to be in particular places where contact and wear between specimens occur.

The following measurement strategy is adopted. On each surface remaining in contact during the experiment three scans were performed as presented in Figure 3.4 and 3.5. One scan directly in the middle and two scans on both sides close to the contact surface edge. It is important to notice that smaller specimens attached on the side of the dynamometer ring and representing the rail have only one contact surface while the middle, larger specimen representing the slipper has two contact surfaces. For the entire roughness measurement process each VascoMax 300 and Steel 1080 specimens taking part in the sliding friction experiments (Chapter 4) were investigated and scanned with the use of the previously described SEM. The results and conclusions are presented in the following sections.

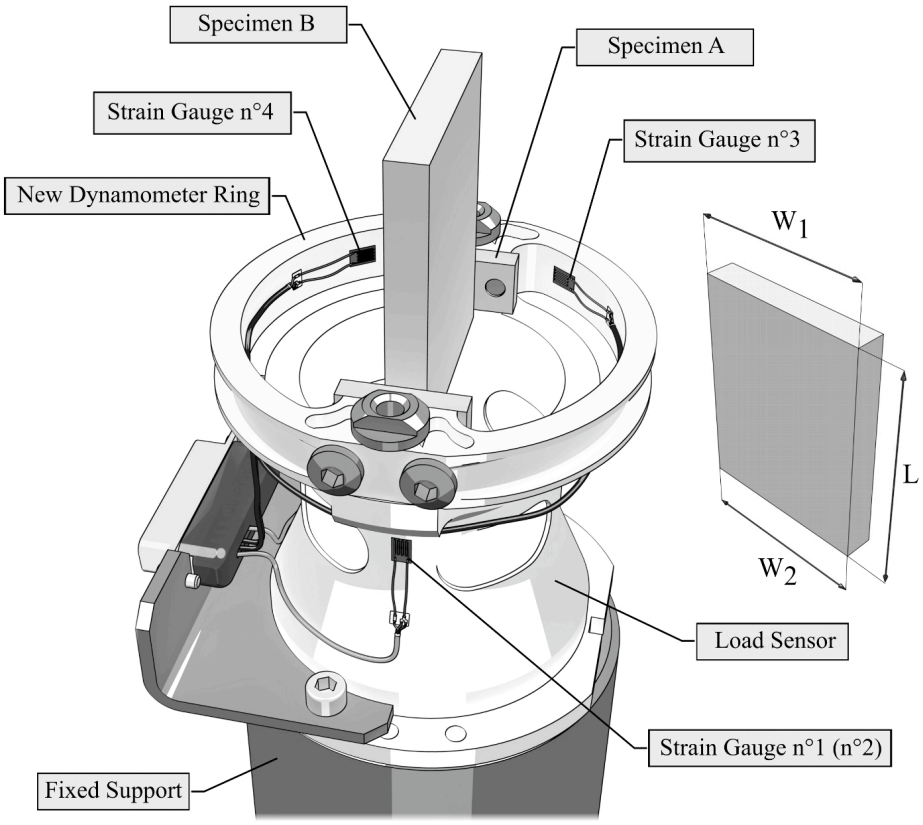

Figure 3.3: Introduction of the experimental setup with the full description given in Chapter 4.

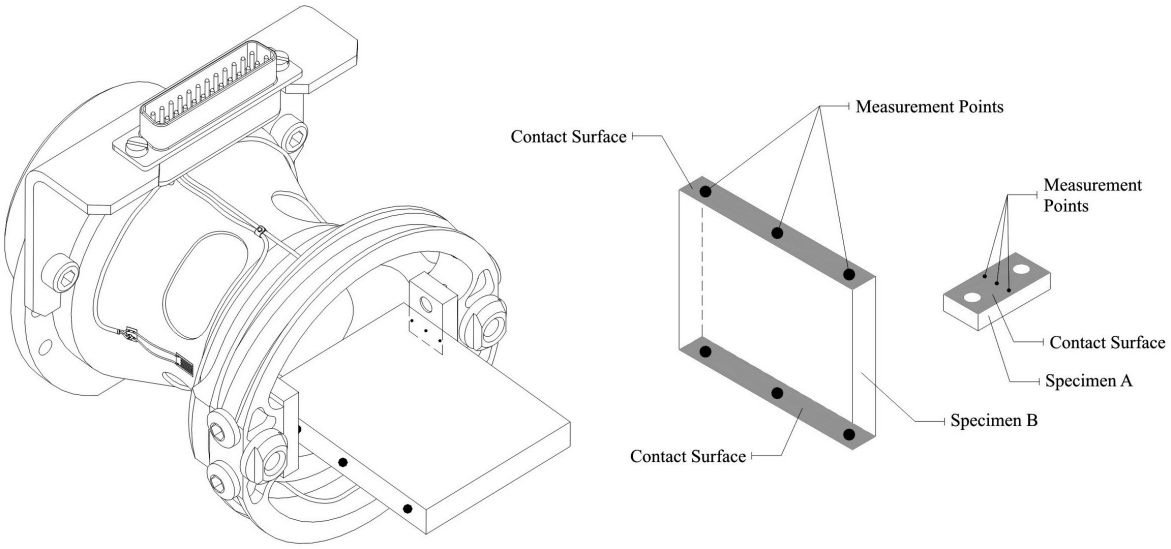

Figure 3.4: Black dots represent the approximate locations where scans were conducted.

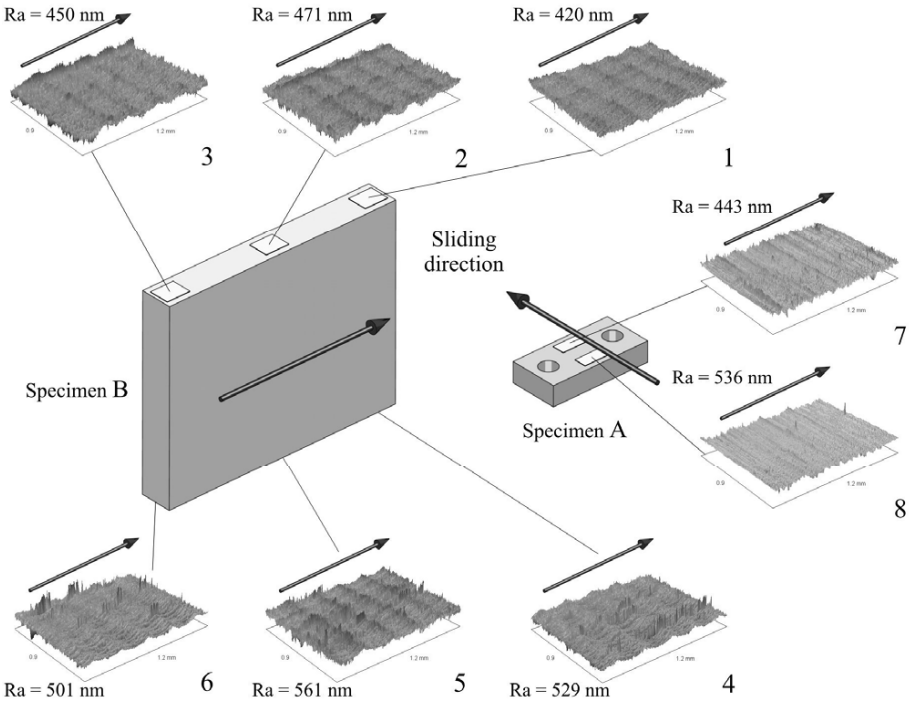

Figure 3.5: Detailed description of the measurements in both specimens in the initial condition before contact is initiated.

3.2.1 Roughness Measurements of Unpolished Specimens

The initial roughness measurements were conducted for the unpolished specimens in their initial condition. That is why the initially obtained roughness is by far greater than the next one obtained based on prepared and polished specimens. The measurements preformed by Veeco Scanning Electro Microscope were sent directly to the PC computer connected to the device. With use of the advanced software provided by Veeco Meteorology Group termed **Vision32** the interpretation and visualization of the obtained results was possible. This software provides 2D and 3D pictures of the scanned surfaces, enables visualization of the surface profile along any line within the scanned area, provides full statistical data regarding the surface roughness and provides full analysis option such as terms removal, data restore, filtering and many others.

The main outcome of the surface statistics is presented by four values. **Ra** is the average roughness calculated over the entire measured array as can be found in Degroot [1980]. It can be expressed as

$$R_a = \frac{1}{n}\sum_{i=1}^{n} |Z_i - \bar{Z}| \tag{3.1}$$

where n is the number of measurements along one scan, Z_i is a current measurement and $\bar{Z}$ is the average from all taken measurements. This value is most important for this research and will be further investigated in detail. The other three values (to be found

in Degroot [1980]) are represented by R_q the root-mean-squared (RMS) roughness

$$R_q = \sqrt{\frac{1}{n}\sum_{i=1}^{n} |Z_i - \bar{Z}|^2} \tag{3.2}$$

R_z is the average of the ten greatest peak to valley separations

$$R_z = \frac{1}{10}[(H_1 + H_2 + ... + H_{10}) \cdot (L_1 + L_2 + ... + L_{10})] \tag{3.3}$$

where $H_1...H_{10}$ are the ten highest peaks in the array and $L_1...L_{10}$ are the ten lowest valleys in the array. The last parameter R_t represents the maximum peak to valley difference. All of the above mentioned quantities are calculated over the entire measured array which for this research was left as a standard value equal to $368\mu m$ by $240\mu m$.

The obtained results for 24 scans performed on VascoMax 300 specimens as well as 36 scans performed on steel 1080 specimens are gathered and presented in Table 3.2. The illustration describing the numbering of the scanned areas is presented in Figure 3.6. It is important to notice that the R_f measurements that stand for the difference between highest pick and lowest valley do not particularly affect the average roughness. In Table 3.2 it is clearly visible that in case of high value of R_f the average roughness R_a does not necessarily have to be high. It is resulting from the fact that single imperfection of the material has got minor impact on the entire surface roughness. The values of R_a for particular specimens show close convergence to one characteristic value both for the VascoMax 300 and steel 1080 specimens.

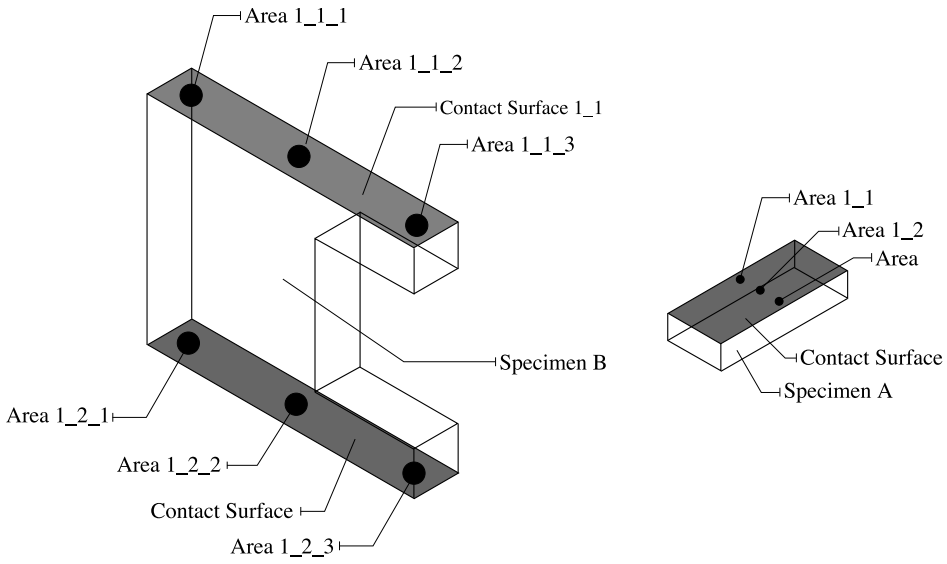

Figure 3.6: Clarification of the measurement areas for a sample specimen.

The average roughness differences between specimens of the same kind are relatively small and oscillate around similar values. This analysis provides extremely valuable information and allows one to estimate the overall roughness for both type

(a) Data for Vasco Max specimens

Area	**Scan**	$R_a[\mu m]$	$R_f[\mu m]$
1_1_1	1	6.59	79.86
1_1_2	2	5.96	99.46
1_1_3	3	5.24	60.42
1_2_1	4	6..20	65.31
1_2_2	5	5.89	62.74
1_2_3	6	6.50	214.94
2_1_1	7	6.96	114.52
2_1_2	8	7.08	147.9
2_1_3	9	5.68	125.43
2_2_1	10	4.89	103.86
2_2_2	11	5.58	199.14
2_2_3	12	5.26	131.66
3_1_1	13	7.75	119.08
3_1_2	14	6.15	115.93
3_1_3	15	7.41	99.42
3_2_1	16	5.89	121.22
3_2_2	17	6.13	123.42
3_2_3	18	5.59	104.22
4_1_1	19	4.87	115.19
4_1_2	20	5.81	148.17
4_1_3	21	5.74	137.95
4_2_1	22	5.62	181.41
4_2_2	23	8.08	136.52
4_2_3	24	5.55	98.53

(b) Data for steel 1080 specimens

Area	**Scan**	$R_a[\mu m]$	$R_f[\mu m]$
1_1	1	1.52	126.38
1_2	2	1.50	79.87
1_3	3	1.34	189.37
2_1	4	2.52	137.60
2_2	5	3.52	103.98
2_3	6	2.02	130.67
3_1	7	2.71	185.88
3_1	8	1.74	197.22
3_3	9	1.42	92.08
4_1	10	0.77	205.01
4_2	11	0.87	163.07
4_3	12	0.68	176.66
5_1	13	3.77	199.89
5_2	14	3.04	192.22
5_3	15	3.54	84.22
6_1	16	1.36	81.70
6_2	17	1.13	73.98
6_3	18	0.80	212.72
7_1	19	2.43	168.32
7_2	20	2.39	71.32
7_3	21	2.59	125.72
8_1	22	4.27	152.38
8_2	23	4.29	154.89
8_3	24	3.50	83.76
9_1	25	4.06	127.08
9_2	26	2.10	71.92
9_3	27	0.89	97.27
10_1	28	2.23	169.68
10_2	29	2.08	198.44
10_3	30	1.96	251.34
11_1	31	3.28	157.37
11_2	32	3.43	203.39
11_3	33	3.48	240.83
12_1	34	5.38	192.31
12_2	35	5.22	247.37

Table 3.2: Values of R_a and R_f for specimens VascoMax 300 (a) and steel 1080 (b)

of materials. The averaging procedure is performed and its output is presented on two graphs; the steel 1080 specimens are presented in Figure 3.7 and the VascoMax

300 specimens in Figure 3.8. The final average roughness accounting for all performed scans of VascoMax 300 and steel 1080 specimens is $6.21\mu m$ and $2.53\mu m$, respectively.

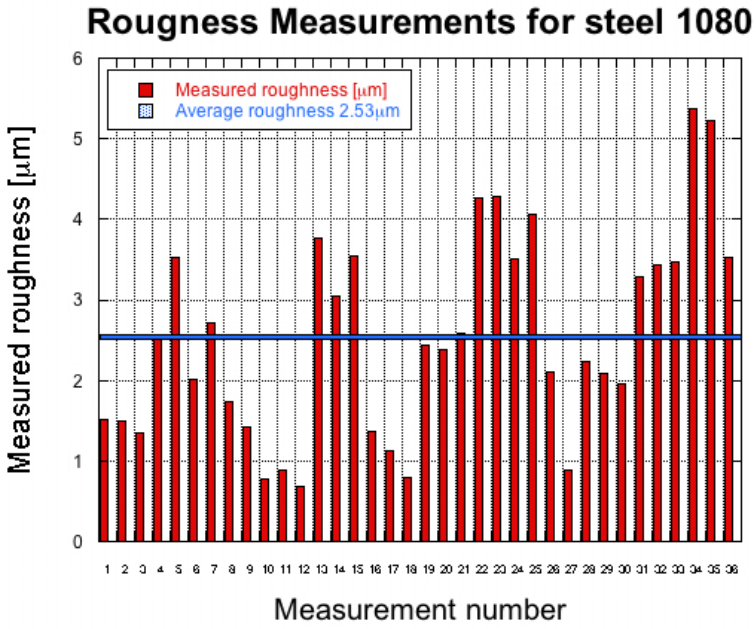

Figure 3.7: Roughness measurements for Steel 1080 specimens and calculated average value.

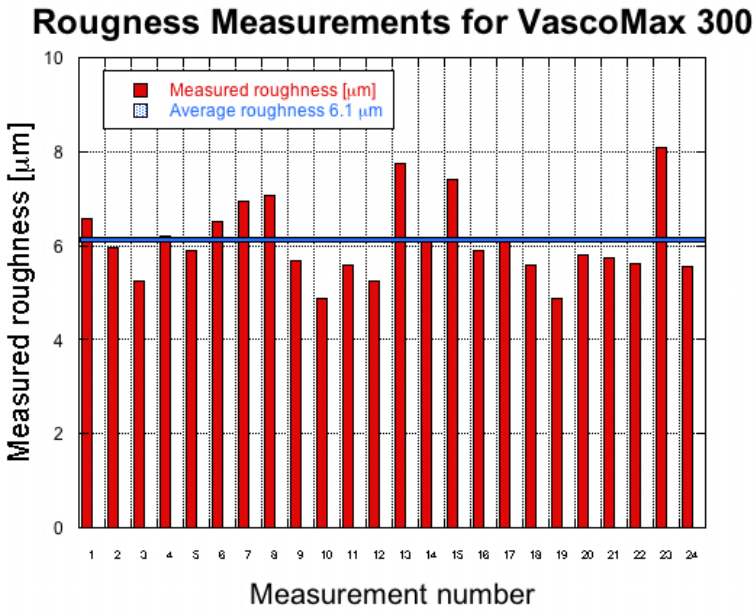

Figure 3.8: Roughness measurements for VascoMax specimens and calculated average value.

As previously mentioned the Vision32 software provides not only statistical data

concerning particular scans but also gives the wide range of graphical and visualization options along the entire scanned surfaces. These techniques and their graphical output, also presented in this work, are very helpful to understand the surface conditions at the micro level. Within only a couple of moments it is possible to generate the 2D as well as 3D views representing the microscopical approach to the scanned surfaces. For illustration purposes the entire graphical output of the two randomly selected specimens, one of each kind, are presented in this work. Figure 3.9 shows 2D graphical views of specimen 5 (steel 1080) and specimen 1 (VascoMax 300), respectively.

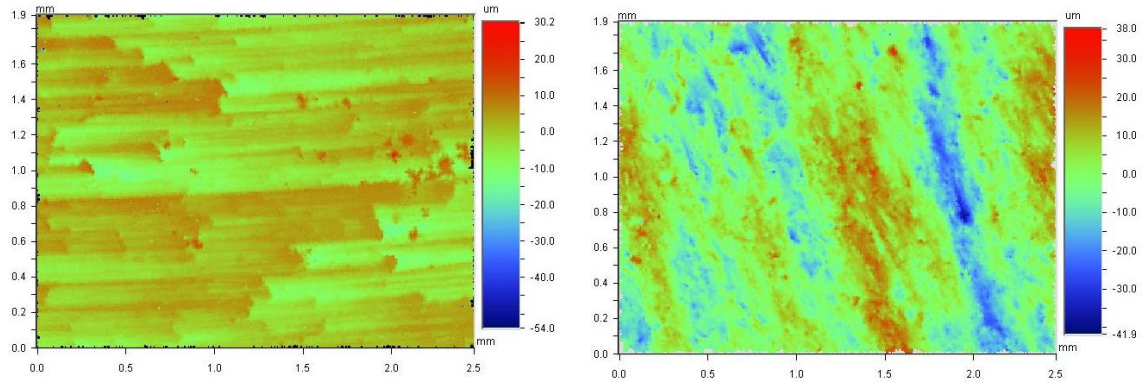

(a) (b)

Figure 3.9: 3.9(a) 2D view of the steel 1080 specimen for area 5_3 and 3.9(b) 2D view of the VascoMax 300 specimen for area 1_1_1.

Figure 3.10 presents the same specimen areas but in 3D. It is clear that the flat view on the continuum scale is quite different with the use of this sophisticated magnifying equipment in 3D.

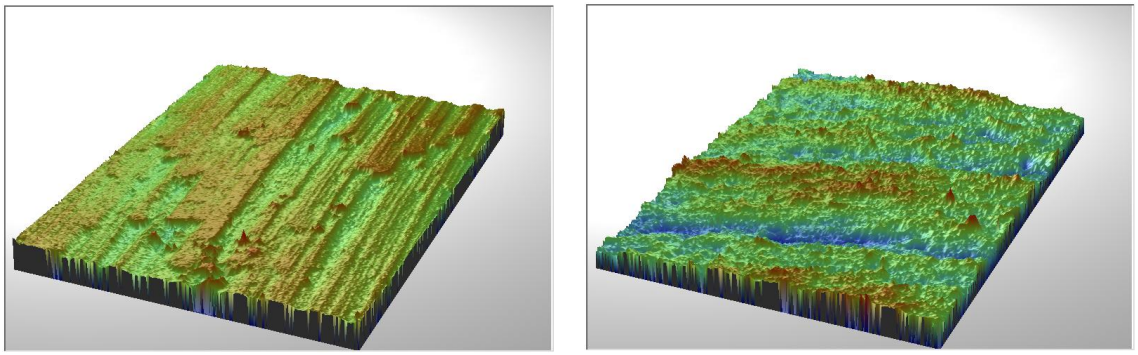

(a) (b)

Figure 3.10: 3.10(a) 3D view of the specimen steel 1080 for area 5_3 () and 3.10(b) 3D view of the VascoMax 300 for area 1_1_1.

Vision32 software is also capable of providing the 2D roughness profiles of measurements along any vertical or horizontal line. Figure 3.11 shows vertical and horizon-

tal lines, blue and red respectively along the 2D profiles. The specimen areas used for presenting this feature are the same with those used previously for area 5_3 in Figure 3.11(a) and area 1_1_1 in Figure 3.11(b). The values of the peaks and valleys in this 2D surface profile closely match those presented by Pierce et al. [2008].

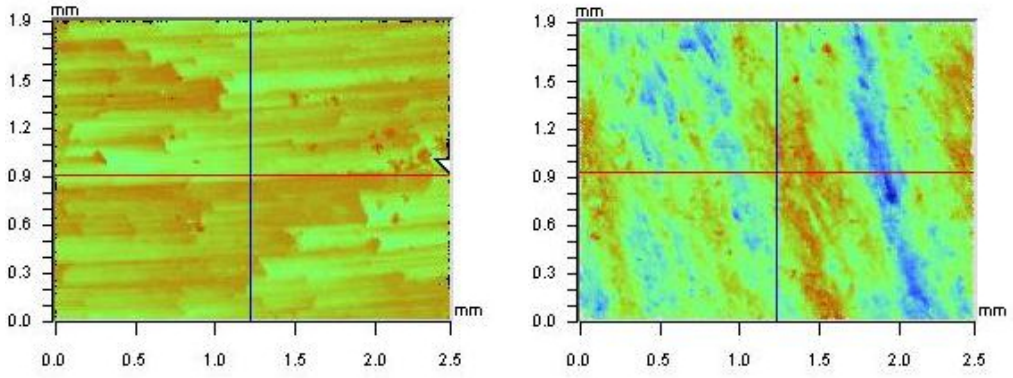

(a) (b)

Figure 3.11: 2D Measurements of Surface Roughness along Horizontal Lines (Red) and Vertical Lines (Blue) for: 3.11(a) Steel 1080 and 3.11(b) for VascoMax 300.

This feature enables one to notice the surface differences existing within one scanned area. It also indicates that describing the material roughness on the continuum scale is possible only through the statistical and averaging techniques. Analyzing the roughness along different horizontal and vertical lines shows that in using micro scale approach the material surface differs significantly within one measurement. Therefore the bridging approach between micro and continuum scale cannot concentrate on particular profiles but rather should capture the wider picture of the investigated surface. Figure 3.12 show both X and Y profiles for Steel 1080 and VascoMax 300.

3.2.2 Conclusions Regarding the Roughness of the Specimens in Unpolished Initial Condition

The description of measuring roughness technique as well as explanation of the capabilities of used software is presented here. The average roughness for Steel 1080 and VascoMax 300 specimens in the unmachined state are $2.53\mu m$ and $6.21\mu m$, respectively. All measurements were conducted by the material samples provided by HHSTT[1] and AFIT[2]. Different kinds of machining and preparing the specimen surface significantly affects the measured roughness. However, the ultimate roughness investigation and comparison of the values obtained before and after the experiment is presented in the following sections. Samples under investigation are prepared using exactly the same machining process which took place in ENIM[3], Metz, and also maintaining the same

[1]Holloman High Speed Test Track
[2]Air Force Institute of Technology in Ohio
[3]Ecole Nationale d'Ingénieurs de Metz i.e. National School of Engineering

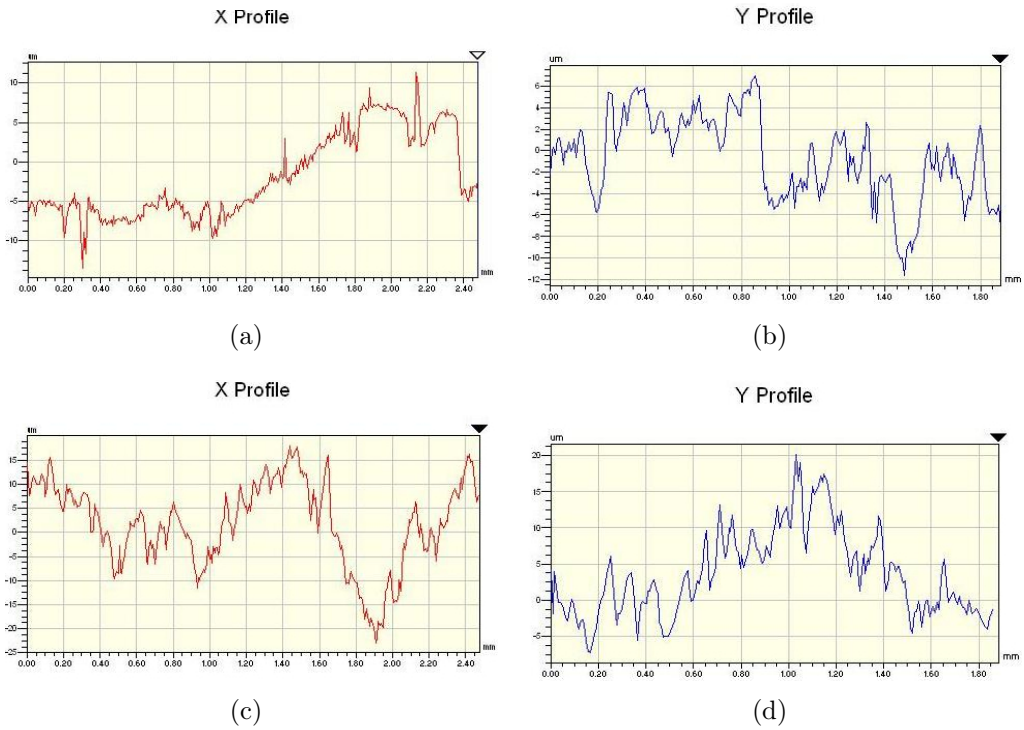

Figure 3.12: Figures 3.12(a) and 3.12(b) present the profiles of steel 1080 along the horizontal and vertical lines, respectively, presented in Figure 3.11(a). Figures 3.12(c) and 3.12(d) present the corresponding profiles of VascoMax specimen along the lines indicated in Figure 3.11(b).

direction of the grinding for each specimen, in order to keep the roughness as identical as possible. The detailed description of the experimental setup as well as the device preparation and calibration is given in the following Chapter 4.

3.2.3 Roughness Measurements of Machined Specimens before and after the Experiments Using the Hydraulic Jack, up to $4m/s$

In order to perform the quasi-static and dynamic experiments the specimens provided by HHSTT had to be machined and adjusted for the newly developed experimental device. The description of the entire procedure of the experiment followed by the detailed description concerning the initial experimental setup are presented in Chapter 4. In this section a total of 9 experimental results are investigated. For each experimental set (one specimen B and two specimens A) the roughness measurements for the quasi-static and dynamic conditions up to $4m/s$ are given.

To obtain the desired dimensions the specimens were cut and machined on the grinder (details explained in the following Chapter 4, Section 4.3.2). The same grinding direction of all surfaces being in contact during the experiment was uniformly applied to all specimens. The final roughness measurements before and after each particular

experiment, taken according to the procedure presented in Section 3.2 are given in the following Tables.

It can be clearly seen that out of 9 experiments only 7 roughness data were

(a) Roughness measurements for Experiment 1

Specimen	$R_a^{before}[nm]$	$R_a^{after}[nm]$
A 1_1	513.33	372.26
A 1_2	654.90	298.24
A 1_3	723.75	348.90
A 2_1	726.75	329.58
A 2_2	726.38	272.70
A 2_3	443.74	366.84
B 1_1_1	766.30	514.20
B 1_1_2	636.55	613.90
B 1_1_3	727.16	689.19
B 1_2_1	676.93	646.34
B 1_2_2	759.83	610.37
B 1_2_3	692.40	548.07

(b) Roughness measurements for Experiment 2

Specimen	$R_a^{before}[nm]$	$R_a^{after}[nm]$
A 1_1	513.33	332.84
A 1_2	654.90	299.15
A 1_3	723.75	372.27
A 2_1	726.75	402.08
A 2_2	726.38	306.20
A 2_3	443.74	370.42
B 1_1_1	766.30	614.50
B 1_1_2	636.55	510.90
B 1_1_3	727.16	605.04
B 1_2_1	676.93	629.24
B 1_2_2	759.83	510.37
B 1_2_3	692.40	538.07

Table 3.3: Values of average roughness R_a before and after Experiments 1 and 2.

(a) Roughness measurements for Experiment 3

Specimen	$R_a^{before}[nm]$	$R_a^{after}[nm]$
A 1_1	269.00	291.43
A 1_2	380.28	348.10
A 1_3	333.97	256.66
A 2_1	457.92	385.00
A 2_2	464.93	440.02
A 2_3	474.20	348.16
B 1_1_1	766.30	685.71
B 1_1_2	667.25	696.56
B 1_1_3	715.59	663.04
B 1_2_1	649.30	557.68
B 1_2_2	775.47	719.89
B 1_2_3	690.70	614.63

(b) Roughness measurements for Experiment 4

Specimen	$R_a^{before}[nm]$	$R_a^{after}[nm]$
A 1_1	549.81	299.16
A 1_2	573.42	338.73
A 1_3	520.84	354.65
A 2_1	396.35	525..60
A 2_2	336.72	546.22
A 2_3	369.35	480.35
B 1_1_1	455.13	422.00
B 1_1_2	447.41	424.45
B 1_1_3	437.90	396.06
B 1_2_1	407.03	387.59
B 1_2_2	482.48	430.04
B 1_2_3	429.12	403.10

Table 3.4: Values of average roughness R_a before and after Experiments 3 and 4.

listed in the table. This is due to the fact that during the experiment number 7 one of the oscilloscopes did not register the experimental progress, and therefore the experimental data are incomplete. This particular attempt will not be taken into account

(a) Roughness measurements for Experiment 5

Specimen	$R_a^{before}[nm]$	$R_a^{after}[nm]$
A 1_1	469.76	281.09
A 1_2	539.70	274.23
A 1_3	489.38	249.95
A 2_1	458.80	356.28
A 2_2	429.50	286.37
A 2_3	389.48	307.64
B 1_1_1	689.78	563.33
B 1_1_2	628.70	627.75
B 1_1_3	648.18	583.87
B 1_2_1	711.26	581.87
B 1_2_2	592.40	591.33
B 1_2_3	529.94	548.95

(b) Roughness measurements for Experiment 6

Specimen	$R_a^{before}[nm]$	$R_a^{after}[nm]$
A 1_1	493.20	509.43
A 1_2	549.60	565.46
A 1_3	599.35	495.22
A 2_1	561.51	579.57
A 2_2	563.05	458.20
A 2_3	526.64	514.35
B 1_1_1	705.00	539.94
B 1_1_2	630.86	530.45
B 1_1_3	625.66	489.80
B 1_2_1	541.74	376.89
B 1_2_2	520.20	366.32
B 1_2_3	598.23	402.00

Table 3.5: Values of average roughness R_a before and after Experiments 5 and 6.

(a) Roughness measurements for Experiment 8

Specimen	$R_a^{before}[nm]$	$R_a^{after}[nm]$
A 1_1	575.81	542.74
A 1_2	528.01	515.38
A 1_3	578.70	491.93
A 2_1	607.27	520.45
A 2_2	440.04	490.04
A 2_3	530.46	470.21
B 1_1_1	436.97	463.09
B 1_1_2	393.04	386.26
B 1_1_3	433.62	363.19
B 1_2_1	444.48	386.48
B 1_2_2	411.09	407.65
B 1_2_3	481.47	419.87

Table 3.6: Values of average roughness R_a before and after Experiments 8.

for further investigation and discussion. On the other hand experiment number 9 is strictly quasi static and was conducted mainly for the sake of completeness of the tests for the entire range of tested velocities rather than for importance of the friction coefficient at such low velocity. Furthermore it does not indicate the plastic deformations at the micro scale for such low velocities. The rest of the results are shown in Tables 3.3, 3.4, 3.5 and 3.6.

3.2.4 Analysis of Roughness Changes During the Friction Experiments on Hydraulic Jack up to $4m/s$

It can be clearly seen that the vast majority of the roughness values presented in Tables 3.3, 3.4, 3.5 and 3.6, decrease substantially after the performed experiments. This change is due to the plastic deformations, creation of the shear bands and finally wearing phenomena on the micro level between the asperities that stay in contact during the duration of the experiment. These results are of a significant importance in understanding the bridging processes between stresses and phenomena occurring on the micro and continuum level. The average roughness calculated based on the set of the measurement results (Tables 3.3, 3.4, 3.5 and 3.6) performed for each set of specimens along with the percentage decrease of this roughness are presented in Table 3.7. The overall percentage decrease in the material roughness is calculated as 20.22%.

Table 3.7: The average roughness based on all the measurements before and after the set for all experiments.

Exp. Number	**Average Roughness Before Experiment** $[nm]$	**Average Roughness After Experiment** $[nm]$	**Roughness Decrease** [%]
1	670.62	467.55	30.28
2	670.79	457.59	31.78
3	553.74	500.57	9.60
4	450.46	417.33	7.35
5	548.07	437.72	20.13
6	576.25	485.64	15.72
8	488.41	454.77	6.88
9	680.73	405.38	40.04

3.2.5 Roughness Measurements of Machined Specimens before and after the Experiments on the Gas Gun, up to $60m/s$

The second set of purely dynamic experiments is performed with the use of modified Hopkinson Bar supported by a Gas Gun. The experimental device composed out of the load sensor and dynamometer ring (Figure 3.3) remains unchanged for this approach and is mounted on the receiving tube as shown in Figure 3.13. The projectile, also visible on Figure 3.3, is launched with the use of a Gas Gun and impacts Specimen B initiating the sliding process. Similarly as for the quasi-static approach the detailed information regarding the dynamical setup is presented in Chapter 4.

In this section a total of 8 experimental results are introduced and analyzed. For each experimental set (one specimen B and two specimens A) the roughness measurements for the dynamic conditions in the range of velocities $10m/s - 70m/s$ are used. Due to the big variation of velocity, unlike the quasi-static approach, and for the sake of

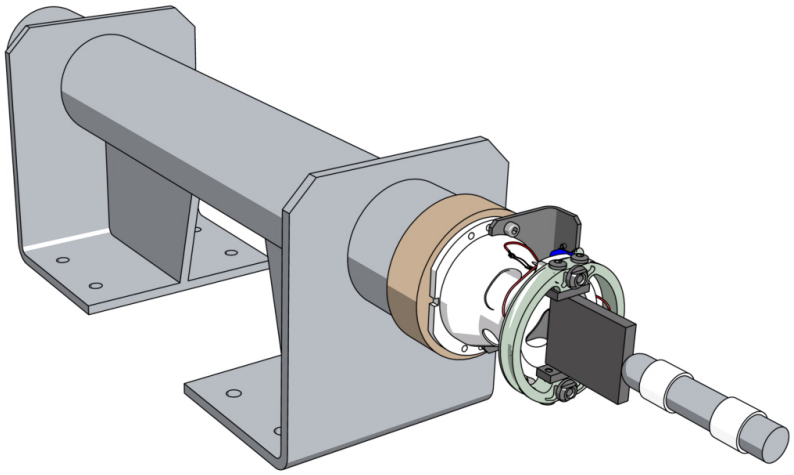

Figure 3.13: Experimental device mounted on the receiving tube for the dynamical approach.

completeness the velocities for each particular experiment are also presented. Obtaining the desired dimensions for the specimens is possible due to machining and using a precise grinder. The same grinding direction of all surfaces being in contact during the experiment was uniformly applied to all specimens in order to obtain the most uniform conditions for all the experimental setups. The final roughness measurements before and after each particular experiment, taken according to the procedure presented in Section 3.2 are given in the following Tables.

3.2.6 Analysis of Roughness Changes During the Friction Experiments on the Gas Gun, up to $60m/s$

The measurements of specimens A and B performed on SEM clearly indicate the substantial decrease of roughness after conducting the dry sliding friction experiments for purely dynamic condition. It can be clearly seen in Tables 3.8, 3.9, 3.10 and 3.11 that the increase of the sliding velocity enforces the higher roughness reduction. Moreover, it confirms the hypothesis that the increase of plastic deformation, shear band creation and finally wearing phenomena between asperities staying in contact during the experiment is invoked by the increase of the sliding velocity.

The current set-up does not physically allow one to simulate the velocities obtained in the experiments conducted using the speed vehicle on HHSTT (in a range of $2000m/s$). However, these lower velocities still cause the roughness decrease and hence the increase of plastic deformation and shear bands. From the physical point of view

(a) Roughness measurements for dynamic Experiment 1

Specimen	$R_a^{before}[nm]$	$R_a^{after}[nm]$
A 1_1	1,580	1,270
A 1_2	1,270	1,280
A 1_3	1,320	1,190
A 2_1	1,240	1,150
A 2_2	1,210	1,200
A 2_3	1,320	1,190
B 1_1_1	868.86	825.10
B 1_1_2	604.29	597.29
B 1_1_3	801.15	619.11
B 1_2_1	1,320	990.01
B 1_2_2	571.00	619.11
B 1_2_3	758.33	595.75

(b) Roughness measurements for dynamic Experiment 2

Specimen	$R_a^{before}[nm]$	$R_a^{after}[nm]$
A 1_1	1,240	1,260
A 1_2	1,400	1,360
A 1_3	1,460	1,030
A 2_1	1,300	1,230
A 2_2	1,290	1,240
A 2_3	1,560	1,150
B 1_1_1	1,300	885.15
B 1_1_2	559.36	530.00
B 1_1_3	606.49	667.90
B 1_2_1	753.62	729.45
B 1_2_2	610.50	596.45
B 1_2_3	820.06	744.18

Table 3.8: Values of average roughness R_a before and after Experiments 1 and 2 on a Gas Gun.

(a) Roughness measurements for dynamic Experiment 3

Specimen	$R_a^{before}[nm]$	$R_a^{after}[nm]$
A 1_1	1,390	1,390
A 1_2	1,480	1,400
A 1_3	1,410	1,410
A 2_1	1,120	1,120
A 2_2	1,310	1,230
A 2_3	1,390	1,330
B 1_1_1	1,210	1,140
B 1_1_2	829.79	773.56
B 1_1_3	555.03	540.90
B 1_2_1	697.14	645.44
B 1_2_2	641.00	590.97
B 1_2_3	589.76	549.51

(b) Roughness measurements for dynamic Experiment 4

Specimen	$R_a^{before}[nm]$	$R_a^{after}[nm]$
A 1_1	1,630	1,600
A 1_2	1,510	1,370
A 1_3	1,320	1,250
A 2_1	1,870	1,670
A 2_2	1,200	1,090
A 2_3	1,370	1,350
B 1_1_1	1,260	701.12
B 1_1_2	548.65	595.68
B 1_1_3	680.92	585.71
B 1_2_1	990.70	702.09
B 1_2_2	601.23	562.12
B 1_2_3	821.10	811.91

Table 3.9: Values of average roughness R_a before and after Experiments 3 and 4 on a Gas Gun.

it clearly indicates the increase of the temperature with the increase of velocity and implies possible phase transformation for the velocities not covered by the laboratory experimental approach. Table 3.12 summarizes the roughness analysis for different velocities and Figure 3.14 presents the relation between different velocities and roughness

(a) Roughness measurements for dynamic Experiment 5

Specimen	$R_a^{before}[nm]$	$R_a^{after}[nm]$
A 1_1	1,620	1,600
A 1_2	1,840	1,550
A 1_3	1,420	1,430
A 2_1	1,770	1,610
A 2_2	1,710	1,550
A 2_3	1,780	1,580
B 1_1_1	1,570	1,490
B 1_1_2	1,110	848.26
B 1_1_3	569.58	597.48
B 1_2_1	690.25	654.13
B 1_2_2	584.79	560.49
B 1_2_3	732.20	664.73

(b) Roughness measurements for dynamic Experiment 6

Specimen	$R_a^{before}[nm]$	$R_a^{after}[nm]$
A 1_1	1,050	984.14
A 1_2	1,210	1,140
A 1_3	1,370	1,200
A 2_1	1,490	1,500
A 2_2	1,720	1,530
A 2_3	1,670	1,320
B 1_1_1	1,160	768.99
B 1_1_2	583.03	544.59
B 1_1_3	702.31	571.89
B 1_2_1	771.30	551.84
B 1_2_2	689.49	662.35
B 1_2_3	1,110	1,020

Table 3.10: Values of average roughness R_a before and after Experiments 5 and 6 on a Gas Gun.

(a) Roughness measurements for dynamic Experiment 7

Specimen	$R_a^{before}[nm]$	$R_a^{after}[nm]$
A 1_1	1,290	1,280
A 1_2	1,560	1,440
A 1_3	1,560	1,360
A 2_1	1,360	1,280
A 2_2	1,180	1,200
A 2_3	1,620	1,340
B 1_1_1	697.45	674.23
B 1_1_2	657.16	626.63
B 1_1_3	788.21	740.99
B 1_2_1	817.91	416.47
B 1_2_2	639.61	397.27
B 1_2_3	1,200	486.82

(b) Roughness measurements for dynamic Experiment 8

Specimen	$R_a^{before}[nm]$	$R_a^{after}[nm]$
A 1_1	1,340	1,140
A 1_2	1,640	1,230
A 1_3	1,630	1,480
A 2_1	1,780	1,670
A 2_2	1,830	1,720
A 2_3	1,860	1,430
B 1_1_1	1,410	317.01
B 1_1_2	644.13	422.66
B 1_1_3	746.51	477.84
B 1_2_1	878.79	748.11
B 1_2_2	605.74	644.29
B 1_2_3	725.43	709.80

Table 3.11: Values of average roughness R_a before and after Experiments 7 and 8 on a Gas Gun.

decrease.

Table 3.12: The average roughness based on all measurements before and after the set of dynamic experiments.

Exp. Number	Initial Velocity	Average Roughness Before Experiment	Average Roughness After Experiment	Roughness Decrease
	$[m/s]$	$[nm]$	$[nm]$	[%]
1	26.49	1071.83	960.42	10.39
2	21.27	1074.83	951.75	11.45
3	25.31	1051.75	1009.75	3.99
4	30.76	1150.00	1023.83	10.97
5	39.60	1282.92	1177.75	8.19
6	47.05	1127.08	982.50	12.83
7	47.05	1114.00	936.58	15.93
8	52.63	1257.33	998.92	20.55

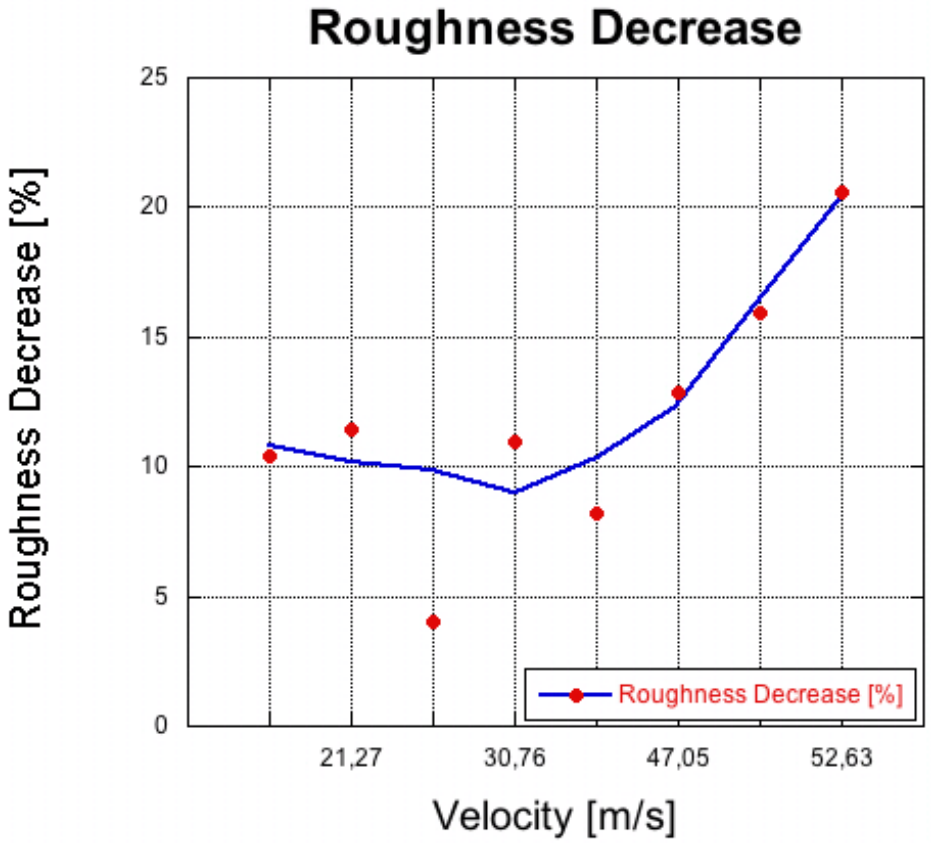

Figure 3.14: Relation between percentage roughness decrease and velocity increase based on roughness measurements before and after the dynamic experiments.

3.3 Roughness Testing Conclusions

The roughness measurements are of a significant importance in particular for application to dislocation on the micro and nano length scale. The appearance of the roughness decrease phenomena during most of the experiments as well as significant percentage decrease in the statistical analysis of all collected roughness data clearly indicate the occurrence of plastic deformation on the micro level. It also implies the development of shear bands followed by the wearing phenomenon not only for the dynamic tests but also for the quasi-static approaches, where standard constitutive models Johnson and Cook [1983] are not sufficient to simulate the problem. These phenomena are taken into account and captured in the self developed material model further implemented as a self defined subroutine VUMAT in the commercial FE software *ABAQUS*.

The average roughness decrease for the quasi static approach is slightly above 20% and the average roughness decrease for higher velocities, presented in Figure 3.14, is varying between 4% and 21% and increases with the increase of the sliding velocity. The overall roughness decrease for the dynamic approach would be greater if it would be possible to conduct these experiments on the hydraulic jack and hence assure the constant sliding velocity during the entire test. This will be shown in subsequent Chapters during the dynamic approach and projectile impact, some amount of kinetic energy is used to overcome the imposed friction forces during the sliding process. Hence, the initial velocity is not equal to the final velocity. Unlike the quasi-static approach, where the hydraulic jack delivers constant force and constant velocity along the entire duration of the experiment, the projectile in the dynamic approach delivers initial kinetic energy which is further decreased by the friction forces and hence results in the velocity decrease.

Chapter 4

Dry Sliding Friction Experiments

4.1 Introduction

The set-up used in this work represents a significant evolution of an original friction apparatus developed by Philippon et al. [2004] and used by Sutter et al. Sutter et al. [2003] for high speed machining investigation. Dry friction coefficient μ for a sliding pair of materials, defined by G. Amontons and later by C.A. Coulomb, is obtained by the ratio between the tangential (or frictional) force F_T due to friction and the apparent normal force F_N applied on the sliding surface S. In the original configuration Philippon et al. [2004], Sutter et al. [2003], the value of F_N, calibrated before the test, is applied by the use of a dynamometer ring and is assumed to be constant during all the friction process. Tangential force F_T is determined with a specific load sensor based on the elastic deformation of a thin tube where a set of two strain gauges are glued. The new configuration, presented in this dissertation, allows controlling or measuring the value of apparent normal force F_N during the friction process. A new dynamometer ring whose stiffness has been increased in comparison to the original version is also equipped by additional two strain gauges; each of them is connected to form a Wheatstone quarter-bridge. Therefore, a possible variation of the apparent normal force F_N can be recorded and observed.

The higher velocities and higher normal pressure which is not possible to obtain by pin-on-disc method can be generated by modified torsional pressure Split-Hopkinson bar (Hartley et al. [1985], Rajagopalan and Prakash [1999]), pressure-shear plate impact (Prakash [1995], Nemat-Nasser and Isaacs [1997], Borvik et al. [2002]) or with a spun steel ball grabbing with other samples (Bowden and Persson [1960]). In particular for investigating friction behavior the torsional Kolsky bar designed to monitor high strain rate behavior (Hartley et al. [1985]) can be modified to capture and measure friction processes (Rajagopalan and Prakash [1999]). The incident and the transmitter of the conventional configuration are replaced by a thin-walled incident tube and by rigid support, respectively. A thin-walled tubular specimen having the same cross section as the incident tube is fixed at the extremity of this one and placed in contact with a rigid support. A static compressive force of predetermined magnitude is applied to the solid bar by a hydraulic actuator. The relative movement at the specimen-rigid support interface is produced by the torsional elastic wave

generated by the Kolsky bar set-up. This kind of set-up is capable of handling the experiments of interfacial normal pressure of $20 - 100MPa$, sliding velocities up to $10m/s$ and a slip distance of approximately $10mm$ allowing the characterization of aluminum and steel dry friction phenomena. Except of this set-up literature describe other modifications and testing (Bowden and Persson [1960], Prakash [1995], Ogawa [1997]and many others) however they are not of a significant importance to this research therefore are not described in details here.

At this point it is very important to notice the influence of roughness, velocity and normal force in metal on metal dry friction experiments. At low velocities ($V < 1m/s$) the friction coefficient μ strongly depends on the roughness (size of the microscopic asperities Stupkiewicz [2007]) of the surfaces in contact (Lim et al. [1989], Palasantzas [2004]). Frictional force is produced during sliding due to work used on deforming or shearing the asperities[1]. These tests where velocity does not exceed $1m/s$ are mainly performed with the use of hydraulic machines. As we increase the velocity $V > 1m/s$ the initial surface condition is quickly replaced by one characteristic for the wear process (Archard [1953]) and the coefficient of friction soon becomes increasingly (Palasantzas [2004]) dependent on the pressure at the surface and the sliding velocity rather than surface state. At very high values of velocity and load a layer of molten metal forms between the sliding surfaces created due to plastic and resulting thermal processes, and reduces μ to very low values.

In the following sections, different tribometer devices and their technical principles, allowing to apply and to measure apparent normal force F_N and tangential force F_T, are described briefly. The range of the sliding velocity V and of the apparent normal pressure p are specified when the experimental data were provided by external sources. For specific applications such as cutting process or interaction in extreme conditions, other interesting concepts for the design of dynamometer are reviewed. These apparatus are generally based on the elastic behavior of a specific part on which strain gauges are mounted. In following section, the evolution of the tribometer set-up is described and adapted on both a hydraulic testing machine for the quasi-static approach and the Gas Gun for the dynamic testing, to determine the dry friction coefficient between a pair of metallic materials. The static calibrations of the main parts of the device are reported and discussed. The experimental results concerning steel-on-steel dry friction are reported as well. These tests are carried out for a range of a sliding velocity V varying from 0.12 to $3.75m/s$ and for two average normal pressures p ($8MPa$ and $80MPa$).

4.2 Overview of Force Measurement Techniques

The literature introduces plenty of devices investigating the friction laws. Already back in the 15^{th} century Leonardo da Vinci (1452-1519) was the first one to propose

[1]Several concepts of dealing with multi-length scales (Voyiadjis and Abu Al-Rub [2005]) asperities problem, their interactions and friction forces they are producing during dry friction test are described later

the experimental set-up for measuring friction. His theories were used in many applications until 1871 when Coulomb with a similar device made a distinction between static friction and force required to maintain it (preliminaries to dynamic friction). The very first attempts of dynamic experiments did not exceeded $4m/s$ however already in the middle of 19^{th} century this range was brought up to $25m/s$ with the first attempts of introducing the dependance between friction coefficient and sliding velocity (Bochet and others).

Sliding friction is a very complicated process where many important aspects require special attention. Normal forces pressing against two rubbing surfaces are investigated and in particular the sliding velocity (Johnson [1995], Philippon et al. [2004] and others), material properties including material roughness due to asperities visible only the micro level (Stupkiewicz and Mroz [2003], Stupkiewicz [2007]), size of material surface being in contact, lubricated or dry contact (Bowden and Tabor [1950]) and thermal effects (among others Bowden and Hughes [1939], Zsidai et al. [2004]). Friction tests between a pair of sliding specimens against each other depends not only on intrinsic characteristic of the interface previously mentioned and the condition considered but also on the dynamic properties of the device used during the testing such as mass, inertia, stiffness and damping (Rajagopalan and Prakash [1999], Martins et al. [1990]). These different set-ups are briefly described in the following sections.

In the following sections different tribometer devices and their technical principles, allowing to apply and to measure apparent normal force F_N and tangential force F_T, are described briefly. The range of the sliding velocity V and of the apparent normal pressure p are specified when experimental data were provided by external sources. For specific applications such as cutting process or interaction in extreme conditions, other interesting concepts for the design of dynamometer are reviewed. These apparatus are generally based on the elastic behavior of a specific part on which strain gauges are mounted.

4.2.1 Friction Force Measurement for Sliding Movement

The development of experimental techniques is of major importance in order to understand the friction phenomena as it increase the machines efficiency and consequently decrease the energy consumption. Some engineering applications are heavily affected by dry friction such as metal forming, machining processes or braking systems. Thus many tribometer devices have been designed to measure sliding friction coefficient μ under dynamic conditions. However, their performance is very different in terms of the range of normal pressure p, sliding velocity V and also in terms of the process time duration. An overview of a few interesting setups used under different experimental conditions is shown in Figure 4.1. The most commonly used and certainly the easiest to design is the pin-on-disk apparatus, which generates friction by contact between a pin tip and a rotating disk Philippon et al. [2003]. Generally, the range of normal pressure p and of the sliding velocity V is limited to $30MPa$ and $60m/s$, respectively. The difficulty or the quasi-impossibility to apply a loading and a sliding movement instantaneously leads to merging the friction coefficient μ and the wear rate measurements. In this case, the sliding distance is about ten meters and can reach

several hundred meters for specific investigations. Note that both the pin diameter and the disk diameter, more precisely the sliding path diameter of the disk, play an important part in the velocity variation on the contact surface. For apparent normal pressures p varying from 20 to $100MPa$ and from 500 to $3000MPa$, the modified Kolsky bar Espinosa et al. [2000*a*,*b*], Rajagopalan and Prakash [1999] and the impact plate experiment Clifton and Klopp [1985], Prakash [1995] have been used respectively. Unfortunately, sliding velocities V cannot exceed around a few tens of meters per second and the time duration of friction process was relatively short lived, in the order of a few milliseconds or a few microseconds. Thus the tribometer device made up of a spun ball grabbing with three other specimens Bowden and Freitag [1958] allows to reach the highest sliding velocity V close to $800m/s$ but apparent normal pressure p is relatively small ($p = 0.015MPa$). Note in this last case that the sliding surface changes from a point at the beginning of contact to a spherical mark at the end of the test. This device enables one to measure friction and temperature on the surface. However, due to its inability to obtain higher pressure it is inadequate for this research.

The tribometer device developed by Philippon et al. [2004], presented succinctly in the introduction and detailed in Section 4.3, gives frictional conditions have a wide range for both the apparent normal pressure p as well as for the sliding velocity V. The linear sliding movement imposes the same velocity for any contact surface point for a length of about tens millimeters. The quasi-instantaneous loading avoids to merge wear rate and dry friction coefficient measurements during the process. No current technical approach exists to control the apparent normal force F_N due to the dynamometer ring action; the authors Philippon et al. [2004], Sutter et al. [2004] assumed it constant during the friction experiment. The new evolution concerning the dynamometer ring described in this work allows one to measure and to control the apparent normal force F_N accurately.

4.2.2 Force Measurement for Other Applications

Other applications, naturally, need force measurements as well. Although there are numerous dynamometers available in the market, they do not always meet specific requirements such as the force range, the sensitivity, the size and the loading frequency. Therefore, the scientific literature gives interesting technical solutions regarding generally the machining process and more precisely High Speed Machining. For these applications, the loading under high frequency is short-lived. The dynamometers dedicated to these dynamic conditions are mostly based on the principle of elastic behavior of the main component where strain gauges are glued. When subjected to loading, these sensor types produce an output signal proportional to the deformation. The use of only one (or two) deformable part(s) avoids inputting gaps and friction phenomena in the different joint parts and thus a non-linear response of the developed sensor Couetard [2000]. Figure 4.2 illustrates this concept for applications regarding the orthogonal and oblique cutting processes or interaction in extreme conditions. The range of measured cutting force F_C and imposed interaction velocity V_C is reported when data is provided.

The combined type tool dynamometer adapted on an ultra-precision lathe is like

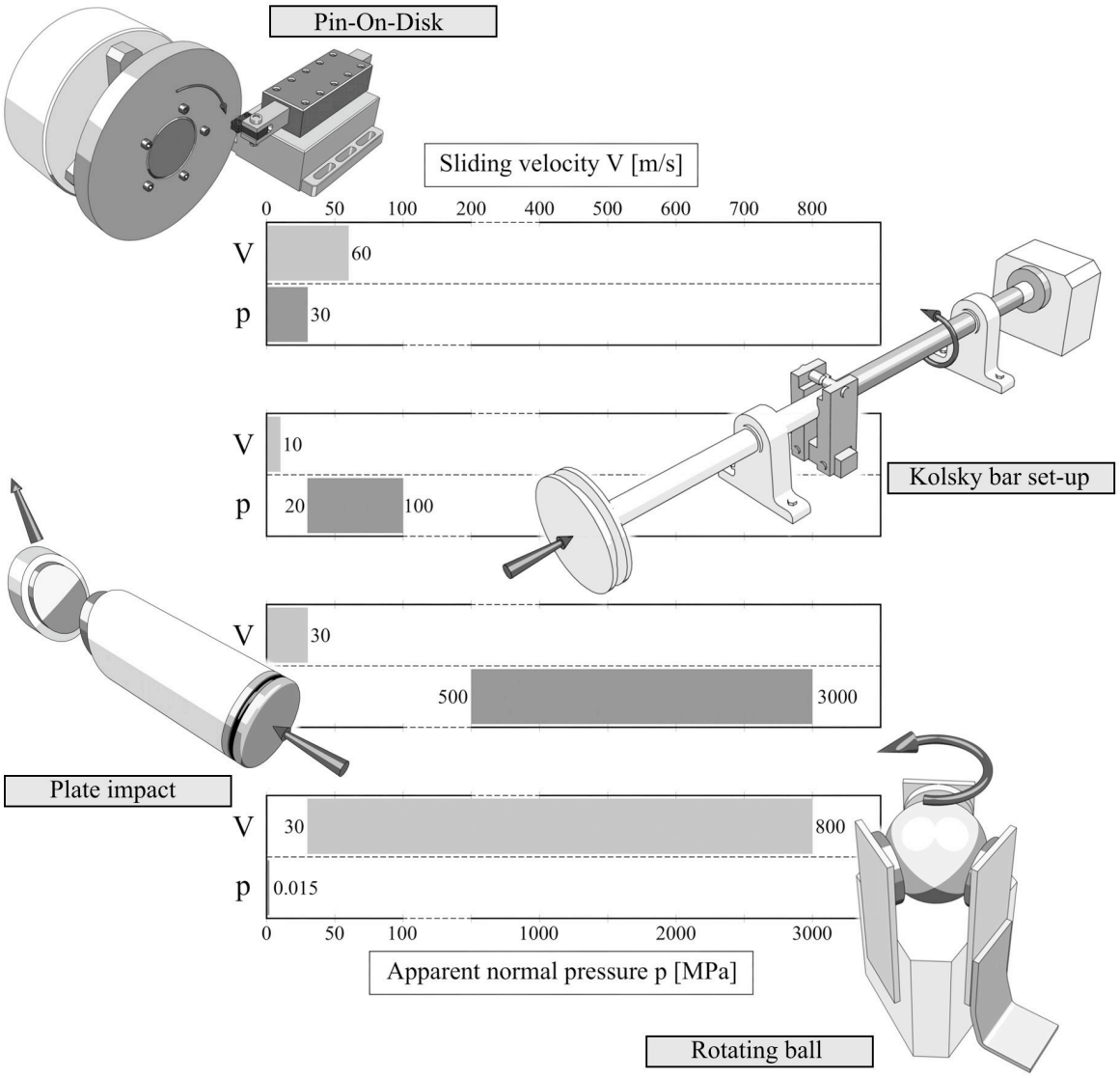

Figure 4.1: Different tribometer devices and their associated performances (sliding velocity V and apparent normal pressure p range).

a beam with slots and holes working in bending Kim and Kim [1997]. This structure gives good sensitivity, especially for small forces but its low stiffness is unfavorable for dynamic conditions. The mean (or the static) value of the cutting force F_C is measured by means of strain gauges and the dynamic component by a piezo-film type accelerometer associated to a low pass filter and a high pass filter respectively. The total cutting force is calculated by processing of both values.

The dynamometer using four elastic octagonal rings held between two rigid plates is initially designed for the force measurement in milling applications Korkut [2003] but can be also used for other machining operations such as turning and milling Yaldiz and Unsacar [2006*a*,*b*]. The output signals delivered by 16 strain gauges mounted on the rings allowed, after calibration, the measurement of three static force components dur-

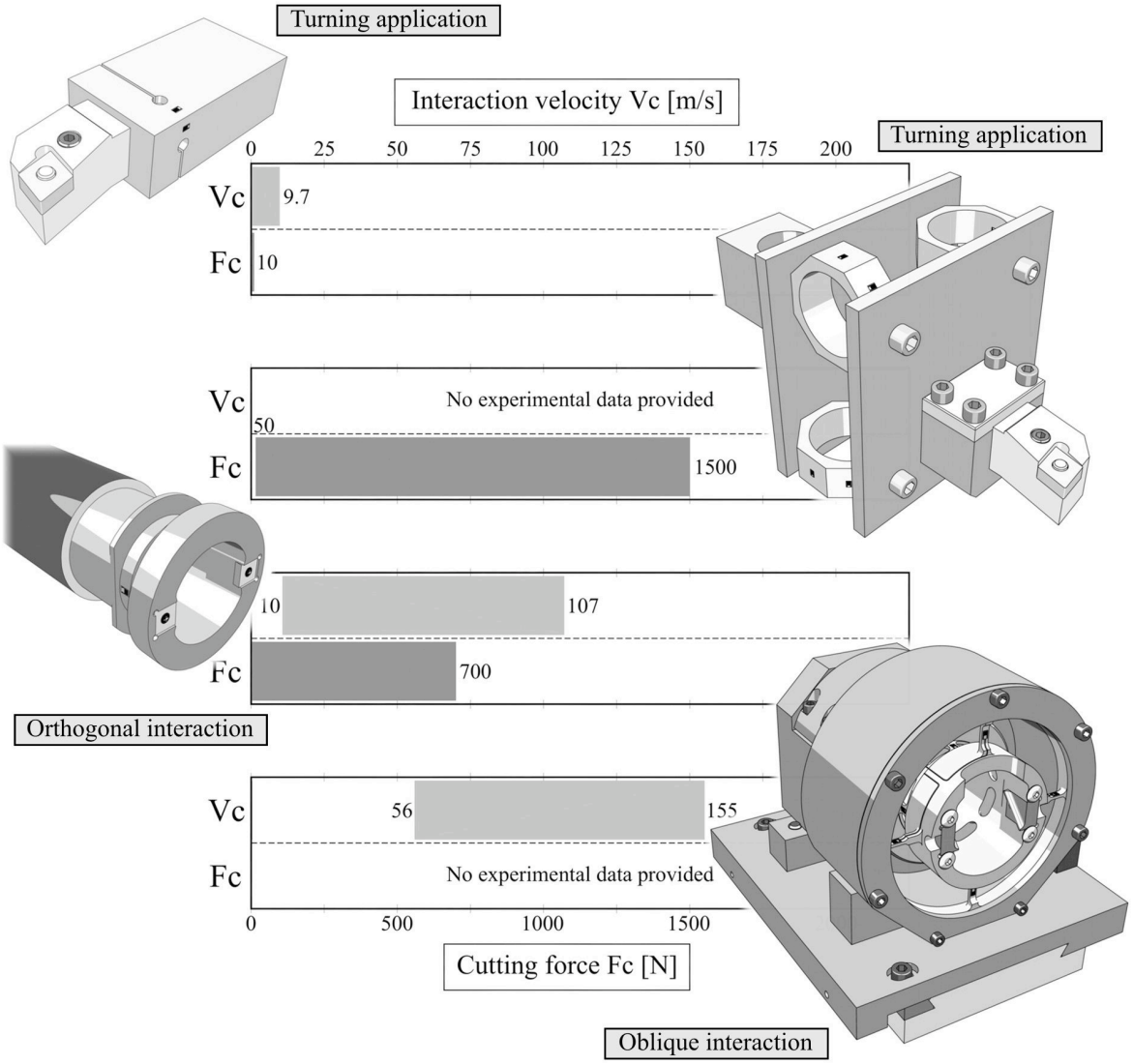

Figure 4.2: Dynamometers based on the elastic deformation of a specific part and their associated performances (interaction velocity V_C and cutting force F_C range).

ing the metal cutting process. The use of 20 strain gauges provides the torque value for the milling operations Yaldiz et al. [2006]. In addition, a piezo-electric accelerometer completed the data acquisition set up and evaluated dynamic force components Yaldiz and Unsacar [2006*a*,*b*], Yaldiz et al. [2006]. This dynamometer was subjected to different tests to characterize its static and dynamic responses.

Finally, in extreme conditions where the contact velocity can reach few hundred meters per second under high loading, other original load sensors adapted on gas gun have been developed Sutter et al. [2006], Zineb et al. [2008]. These devices were designed to investigate interaction phenomena occurring between the blade tip and the compressor casing of the aircraft engines. These load sensors were based on a similar idea, i.e. on the elastic behavior of a specific part where strain gauges are glued and connected to form the Wheatstone bridge. These load sensors which geometries are

more or less complex Zineb et al. [2008], can measure from one to three applied force components after the use of correction functions. These correction functions have to be built in taking into account the dynamic behavior of the load sensor in order to clean up the strain gauges recordings or piezoelectric dynamometer recordings Castro et al. [2006], Tounsi and Otho [2000*a*,*b*]. The goal is to deduce accurately the cutting forces applied on the tools. In this study, the determination of frictional force F_T and of the apparent normal force F_N is based only on the static calibration of two main parts; i.e. the dynamometer ring and the load sensor.

4.3 Device Development

In the following section the modifications to the pioneer device, presented by Philippon et al. [2004], capturing the frictional forces and hence friction coefficient are presented. At this point it is important to notice that the evolution of this device is a continuous process (Voyiadjis, Deliktas, Lodygowski, Palazotto, Philippon, Rusinek, Faure and Chevrier [2009*a*], Voyiadjis, Lodygowski and Deliktas [2009], Faure et al. [2009*c*], Faure et al. [2009*a*]). Hence it should be pointed out that inspite that the experimental setup used in this research is the most current one, however, it is highly possible that within a few weeks or months the device maybe enhanced and capable of handing wider range of velocities. The most current available friction device is presented in Figure 4.3.

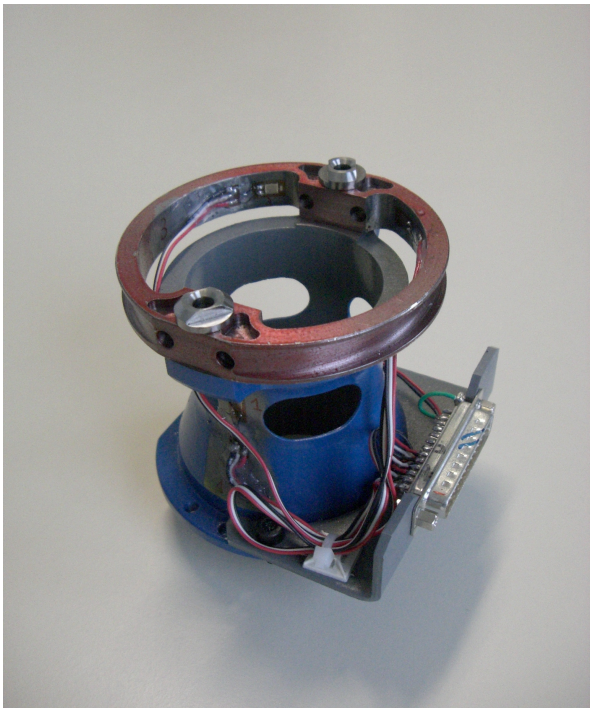

Figure 4.3: New friction device used in experiments presented in this work

.

4.3.1 Presentation

The experimental device, presented in Figure 4.3 and further in Figure 4.4 has been designed to investigate dry friction between materials A and B which are mainly made up of two distinct parts. A dynamometer ring allows applying a known apparent normal force F_N on the contact surfaces between specimens A and B, and a thin tube, on which a set of two strain gauges is glued, that measures the tangential force due to friction. The ring is mounted on the thin tube (load sensor) and rigidly fixed by two screws. Specimen B is placed between two specimens A fixed symmetrically in the inner surfaces of the dynamometer ring. The value of the apparent normal force F_N exerted by this ring is calibrated by the thickness of A (W_A) and the width of B (W_B, see Figure 4.5).

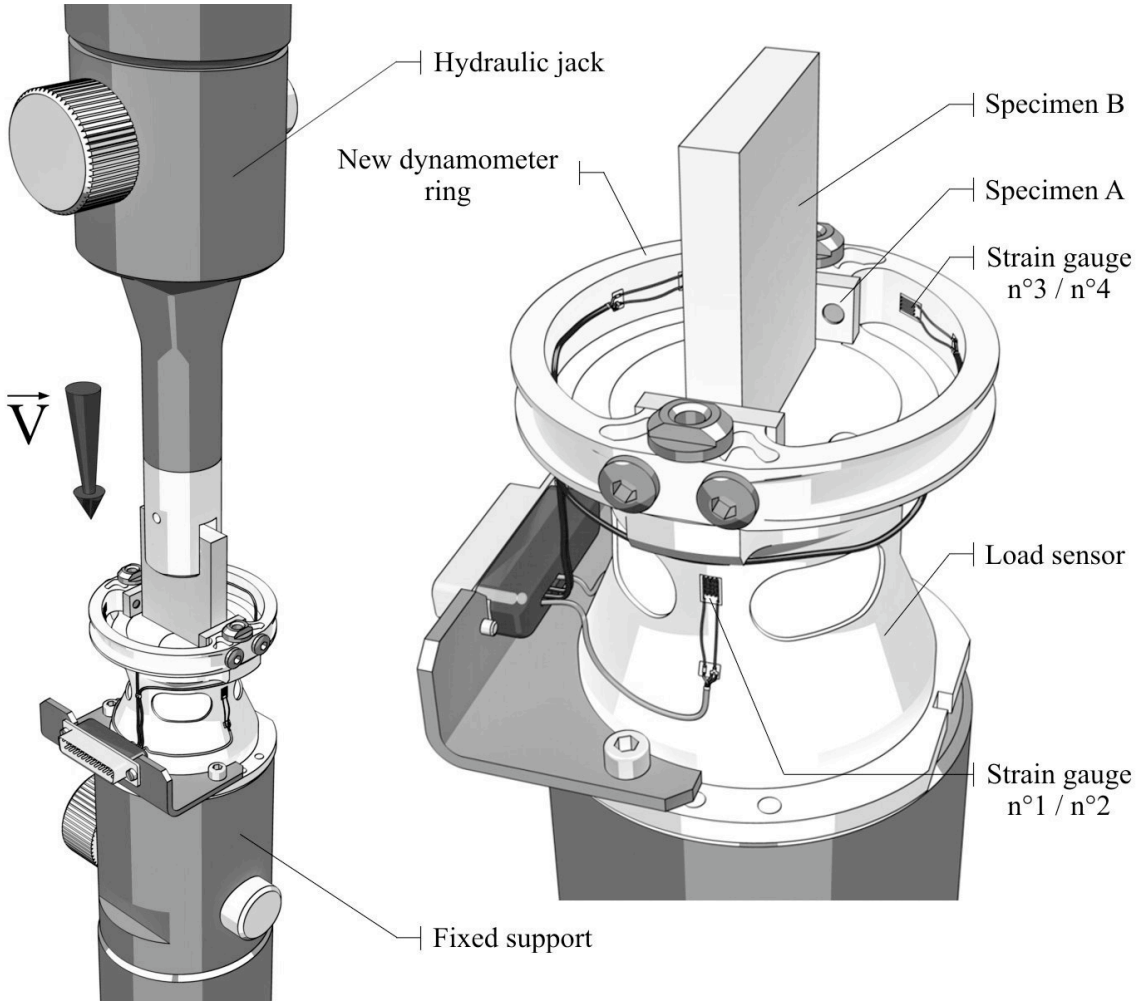

Figure 4.4: Views of modified friction device adapted on a hydraulic machine.

4.3.2 Static Calibrations of the Dynamometer Ring and the Load Sensor

The aim of these experimental calibrations is to determine the elastic response of the dynamometer ring and the load sensor under static loading and consequently the output voltage of the Wheatstone quarter bridges[2]. The results of this calibration are used to convert the current from both quasi-static and dynamic approaches. The role of the ring is to apply a quasi constant normal force F_N on the specimens during the test. This force is generated by its elastic deformation. The new design of the dynamometer ring is presented in Figures 4.4 and 4.5. Its mass has decreased by 20% and its stiffness increased by 48% with respect to the original shape of the dynamometer ring Philippon et al. [2004]. Before each test, two steady rectangular specimens of material A (dimensions $W_A \times L_A \times H_A$) are symmetrically fixed by screws on the inner parallel surfaces of the ring. During the friction test, a moving rectangular specimen of material B (dimensions $W_B \times L_B \times H_B$) is located between the two previous specimens A.

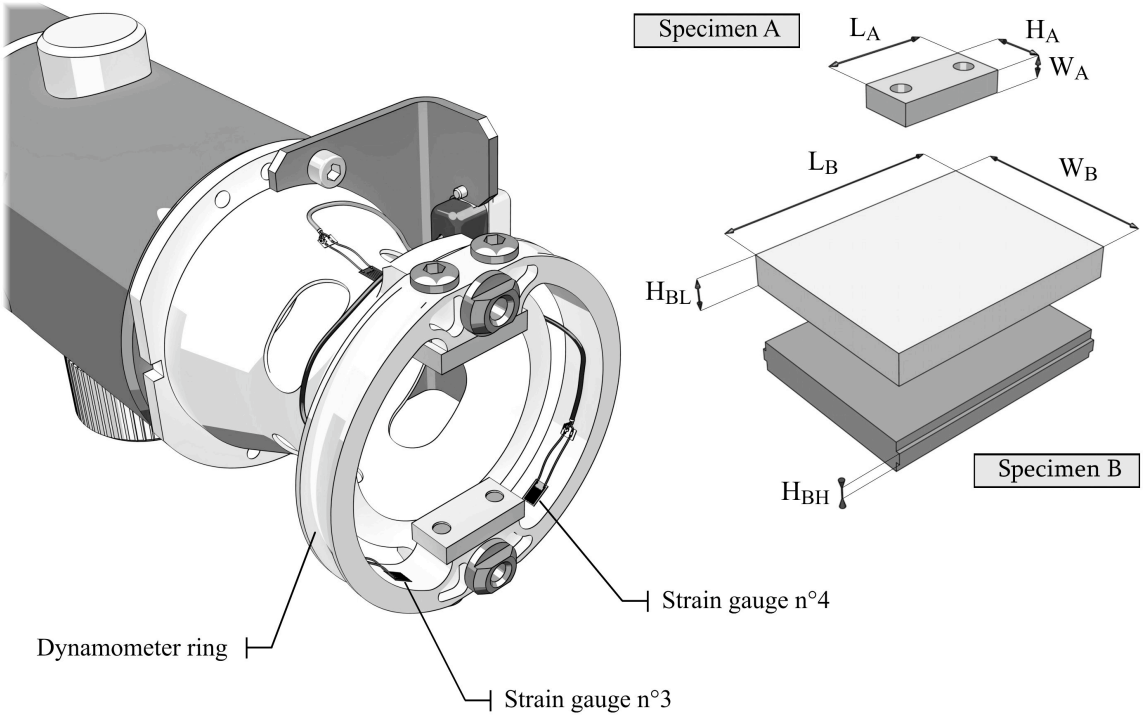

Figure 4.5: Dynamometer ring and dimensions of specimens A and B.

[2]A Wheatstone bridge is a measuring instrument invented by Samuel Hunter Christie in 1833 and improved and popularized by Sir Charles Wheatstone in 1843. It is used to measure an unknown electrical resistance by balancing two legs of a bridge circuit, one leg of which includes the unknown component. Its operation is similar to the original potentiometer except that in potentiometer circuits the meter used is a sensitive galvanometer

One of the major parameters of the experiment is the apparent normal force F_N applied on the sliding surface of the specimens during the test. In order to determine the values of W_B and W_A for a selected pressure, a static calibration of the dynamometer ring was carried out. The calibration was performed on a tensile testing machine in static conditions. An axial force T is applied and distance δ between the inner of parallel surfaces of the ring is measured by an extensometer. The static calibration chart is shown in Figure 4.7(a). The calibration procedure is partially shown in Figure 4.7(a). In addition, to ensure that the deformation remains in the elastic domain, numerical simulation were performed with a finite element code (ABAQUS). The results of the ring calibration are presented in Figure 4.7(a) and shows, firstly the variation of distance δ as a linear function of T and secondly, the good agreement between experimental data and numerical results. Furthermore, these numerical simulations allowed to check the maximum value of δ to guarantee an elastic behavior of this main part. Thus, two apparent normal pressures p for the tests were selected, and the dimensions of W_B, H_B, W_A and H_A were determined. The possibility to control the apparent normal force F_N with the widths W_A and W_B of both specimens and the ring stiffness lead to distinction between the low and high pressure levels ($8-9$ and $80MPa$), see Figure 4.5. During the previous experiments Philippon et al. [2004] and Sutter et al. [2004], it was assumed that apparent normal force F_N remained constant. Nevertheless, regarding to the variations of the specimen geometry such as the contact between the sliding surfaces of specimen B or changes of the surface roughness, due to the machining process, it is important to control the value of the apparent normal force F_N generated by the dynamometer ring during the test.

The calibration of the ring and load sensor was conducted with the use of the tensile testing machine, force extensometers and strain gauges. This particular setup, presented in Figure 4.7, uses the ability to generate the tensile and compressive force by the hydraulic jack and apply the specific load on both, ring as well as the load sensor. In the case of ring calibration, the jack applying tensile force begins to stretch the ring. Extensometers mounted on both sides of the setup (Figure 4.7(a)) measure the displacement generated by a particular force applied by the hydraulic jack. This relation is captured and presented in Figure 4.8(a). On the other hand the same force displacement relation of the load sensor is obtained by applying the compressive force by the jack on the load sensor itself (Figure 4.7(b)). The displacement of the central part of the load sensor captured by the mounted strain gauges, together with the particular force applied by the tensile testing machine finally gives the force-displacement relation for the load sensor. It is important to notice that despite the different values of current used in different channels the values of occurring force is the same. Both relations, for the dynamometer ring and load sensor, are presented in Figure 4.8.

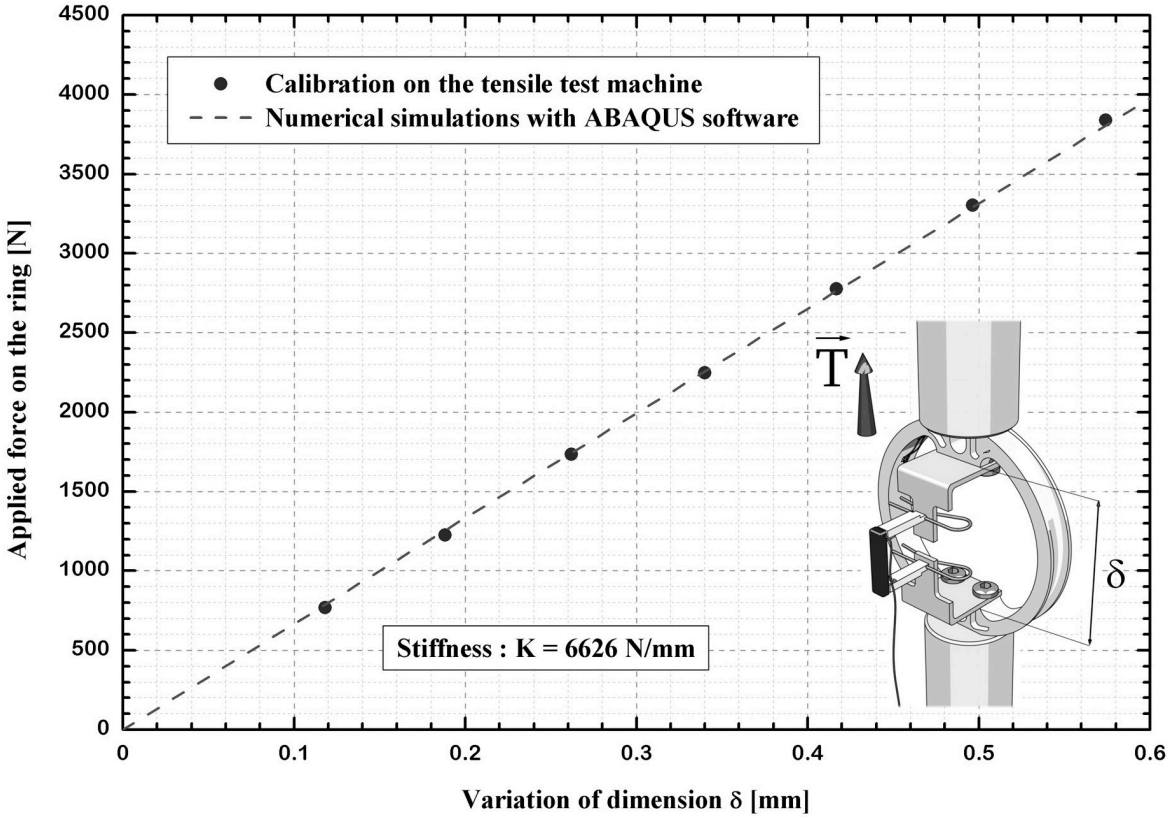

Figure 4.6: Static calibration of the dynamometer ring.

4.3.3 Placing the Strain Gauges and the Sensitivity of the Loading Surface

After calibrating the dynamometer ring it is possible to determine the normal force F_N. The final output of these experiments, however, requires one more value $F_T(t)$ to be determined in order to obtain the change of the friction coefficient according to the Friction Coulomb Law (Equation 4.1)

$$\mu(t) = \frac{F_T(t)}{F_N} \tag{4.1}$$

where $F_N(t)$ is the change of the frictional force during the time of the experiment. Obtaining the behavior of this time dependent value is strictly linked to measuring the displacement occurring on the frictional device during the experiment.

The evolution of the displacement occurring on the frictional device will be most accurate if the correct value of the displacement is recorded, i.e. the strain gauge will be located at a point of maximum displacement. The proper prediction of the region of this displacement is the combined effort of the experimental results and the numerical computations. The strain gauge measures the deformation where it is attached. Necessary connections are made for the Wheatstone quarter bridges. Hence, the numerical simulations allowed one to localize the area of the dynamometer ring where the stresses are the highest for an imposed displacement. Due to this simulation this section was

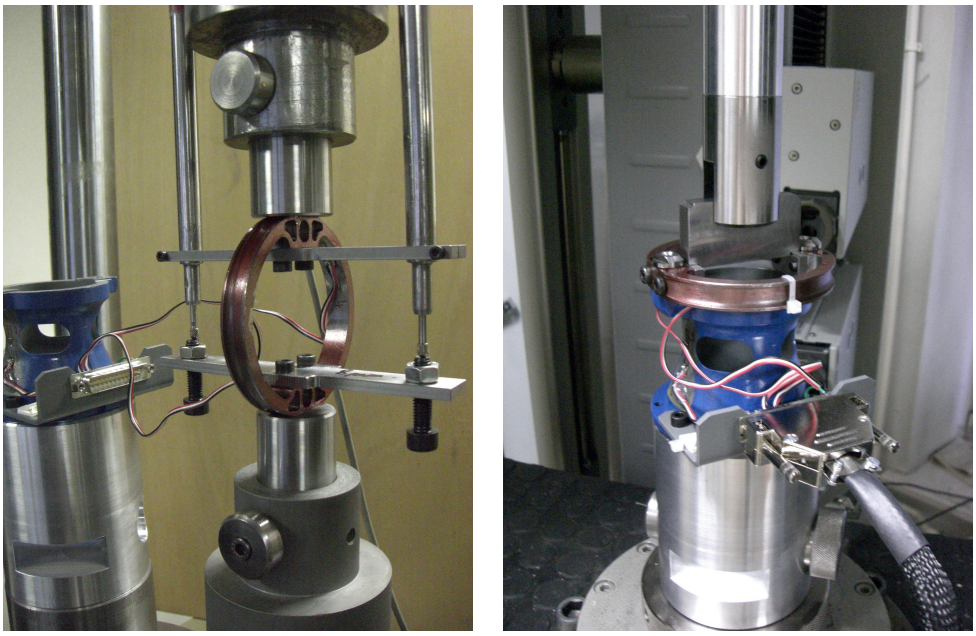

(a) (b)

Figure 4.7: Calibration of the ring (4.7(a)) and of the load sensor (4.7(b)).

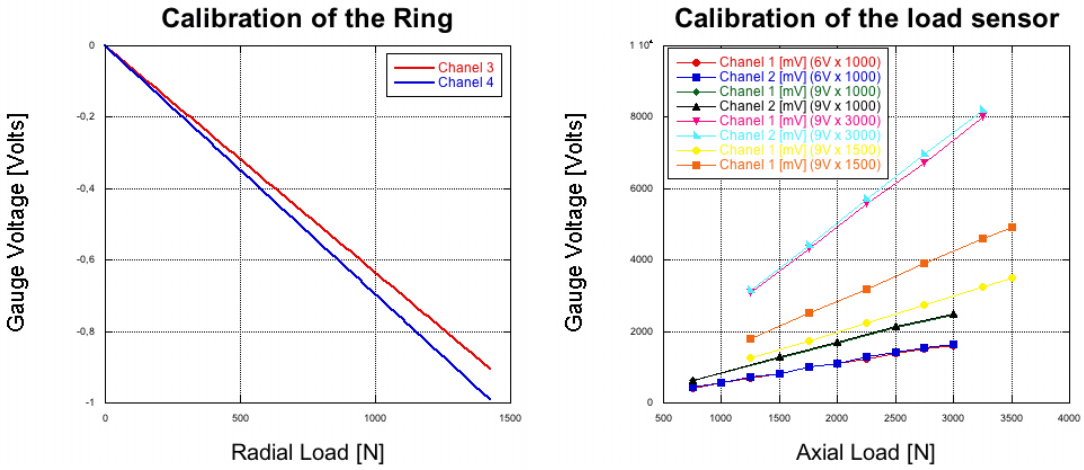

(a) (b)

Figure 4.8: Figure 4.8(a) presents the calibration of the ring and 4.8(b) presents the calibration of the load sensor for different channels with different values of used current.

selected to mount a strain gauge. To acquire a second measurement of the local deformation, another strain gauge was symmetrically glued. Each of them is connected to form a Wheatstone quarter-bridge configuration. Both strain gauge recordings are processed to provide the average value of apparent normal force F_N.

Frictional force F_T generated during the sliding process is obtained by means

of the load sensor. This part is also equipped with two strain gauges (n^o1 and n^o2) which are glued on the thin tube, see Figure 4.13. Its geometry has been improved by numerical simulations allowing to define precisely strain measurement for a loading range varying from 100 to 8000 Newtons. To meet this requirement, the sensor stiffness was deceased by introducing specific strain concentration zones identified by numerical studies using the ABAQUS FE code, see Figure 4.9.

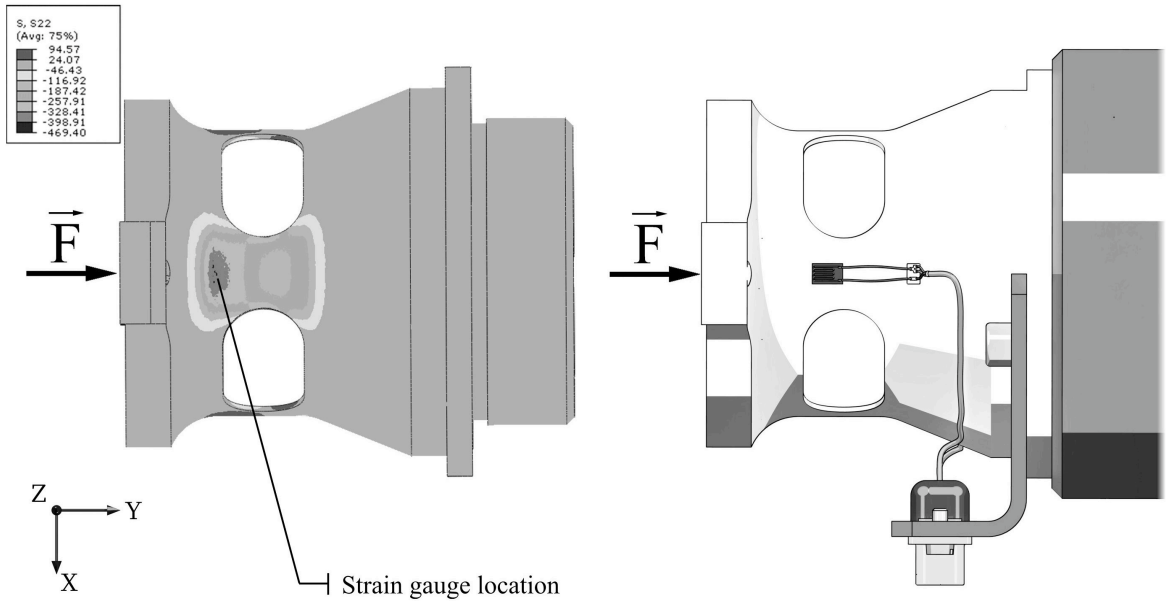

Figure 4.9: Strain gauge location on the load sensor.

The load sensor holds up the ring. The contact zone between these two component parts is restricted to two symmetrical narrow zones as seen in Figure 4.9. The determination of tangential or frictional force F_T is provided by processing of the two strain gauge recordings. Like the ring, each of them was connected to form a Wheatstone quarter-bridge configuration. Experimental data of load sensor calibration are presented in Figure 4.10. These ones were performed on static testing machine for different settings of the Wheatstone bridge. During the calibration process, the dynamometer ring and specimens A were in place on the load sensor so that it is as similar as possible to the real friction test, see Figure 4.10.

4.3.4 Cross-sensitivity

During the design of a dynamometer capable for measuring independently two or three components of an applied force, it is very important to pay additional attention to the value of the cross-sensitivity. This intrinsic property is measured generally by means of a static calibration where the load is applied on only one direction on the sensor. Following that, the output voltages provided by the different kinds of sensor (Wheatstone bridges, piezoelectric sensor) have to be converted into force values to estimate the coupling or the interferences between the different measured components. Ideally, it should be zero or as small as possible. In all cases, the cross-sensitivity value

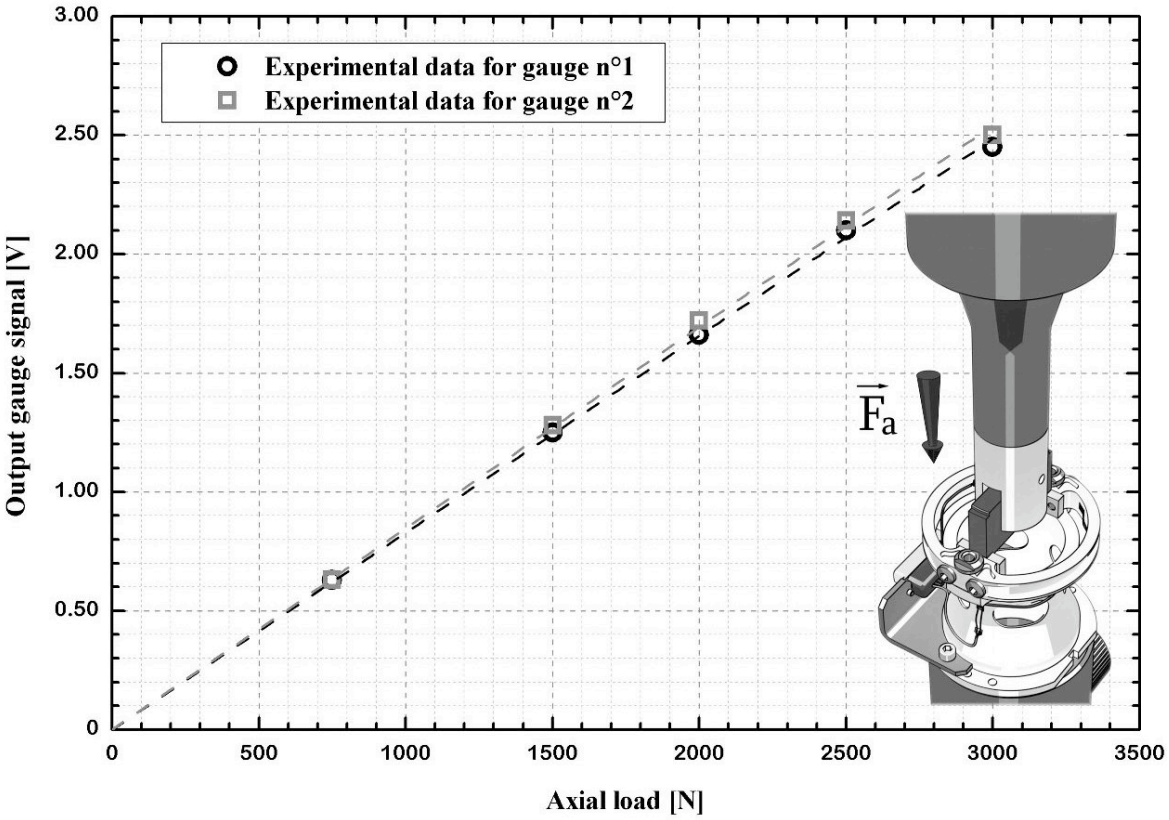

Figure 4.10: Experimental results of the load sensor calibration.

must be ascertained and taken into account in the experimental data processing.

In the literature, the cross-sensitivity value of a few dynamometers was sometimes investigated and reported. For instance, the aim of the combined-type tool dynamometer Kim and Kim [1997] was to measure the cutting and thrust forces for machining process. The provided data showed the output voltages of these components during a static calibration. Assuming that the strain gauge parameters were similar, the cross-sensitivity could reach 10%. Later only the cutting force value has been measured and analyzed for different parameters such as materials, velocity and depth of cut. On the other hand, for the original dynamometer devices made up of four hexagonal rings fixed rigidly between two plates Korkut [2003], Yaldiz and Unsacar [2006*a*,*b*], Yaldiz et al. [2006] designed for milling and turning processes investigation, the cross-sensitivity measured during a static calibration was smaller than 2% and often close to 1%. It allows the independent determination of the three force components Korkut [2003], Yaldiz and Unsacar [2006*a*,*b*] and of the torque component Yaldiz et al. [2006]. Figure 4.11 shows the average deformation ε_{yy} where the strain gauges n^o1 and n^o2 are located when a static load F_C is applied only on the side of gauge n^o1. The result of this numerical simulation shows the low coupling between the two sides of the dynamometer allowing to carry out two frictional force F_T measurements for one sliding test with the same experimental conditions. The cross-sensitivity of the load sensor is less than

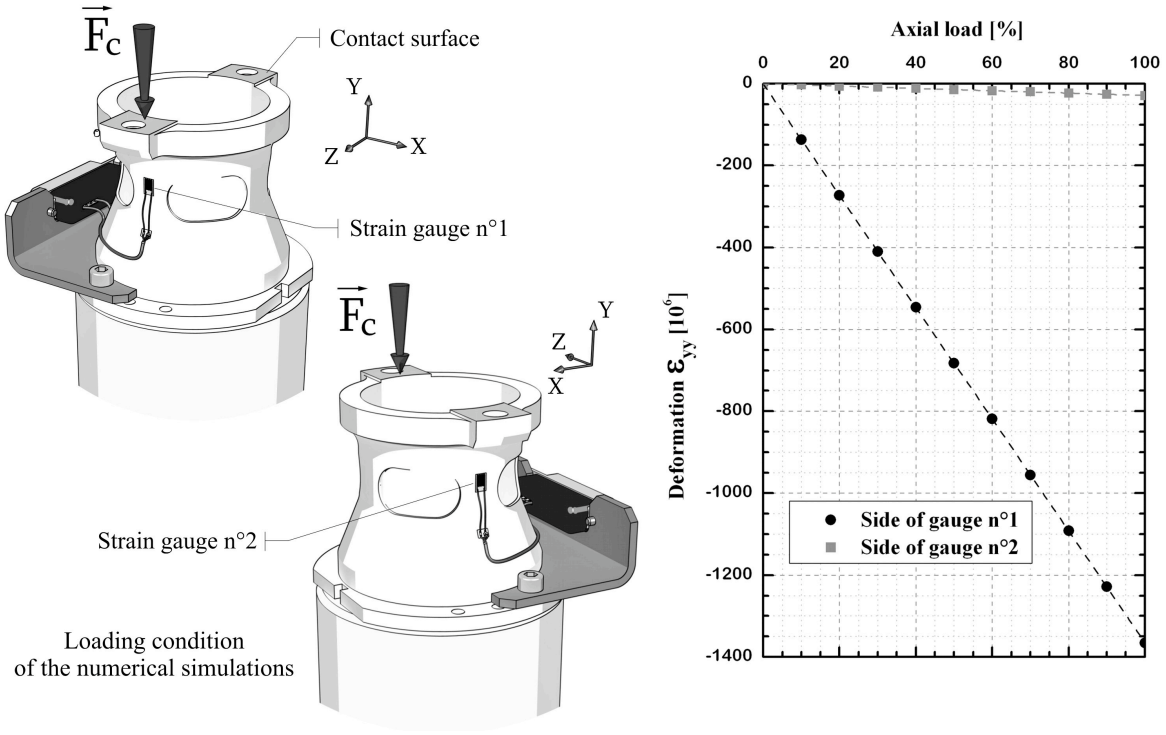

Figure 4.11: Cross sensitivity of the load sensor.

2.1%. Subsequently, the effects of cross-sensitivity can be neglected.

4.3.5 Data Acquisition Set up Description

The description of the data acquisition in this section is based on the quasi-static approach, however, the data acquisition for dynamic approach is created based on the very same rules and is briefly presented in Section 4.5. Each of the strain gauges located on the tribometer device is used with a Wheatstone quarter-bridge configuration connected to a signal conditioning amplifier system (Vishay 2200). The voltage variations of four strain gauges are recorded by a set of two digital oscilloscopes (Lecroy WaveSurfer 44 Xs and Lecroy WaveJet 344) as presented in Figure 4.12. Additionally, the load cell of the hydraulic testing machine allows obtaining the value of the total axial force F generated by the sliding process. The signals given by the strain gauges (n^o1 and n^o2 of load sensors) are proportional to the frictional force F_T. Note that in the theory, the total axial force F measured by the load cell should be equal to $2F_T$ due to the symmetric contact surfaces. The hydraulic jack displacement is also recorded during the friction test to control the evolution of sliding velocity V, see Figure 4.12. Further, the signal from the strain gauges via oscilloscopes is recorded on a PC and using the calibration techniques appropriately evaluated.

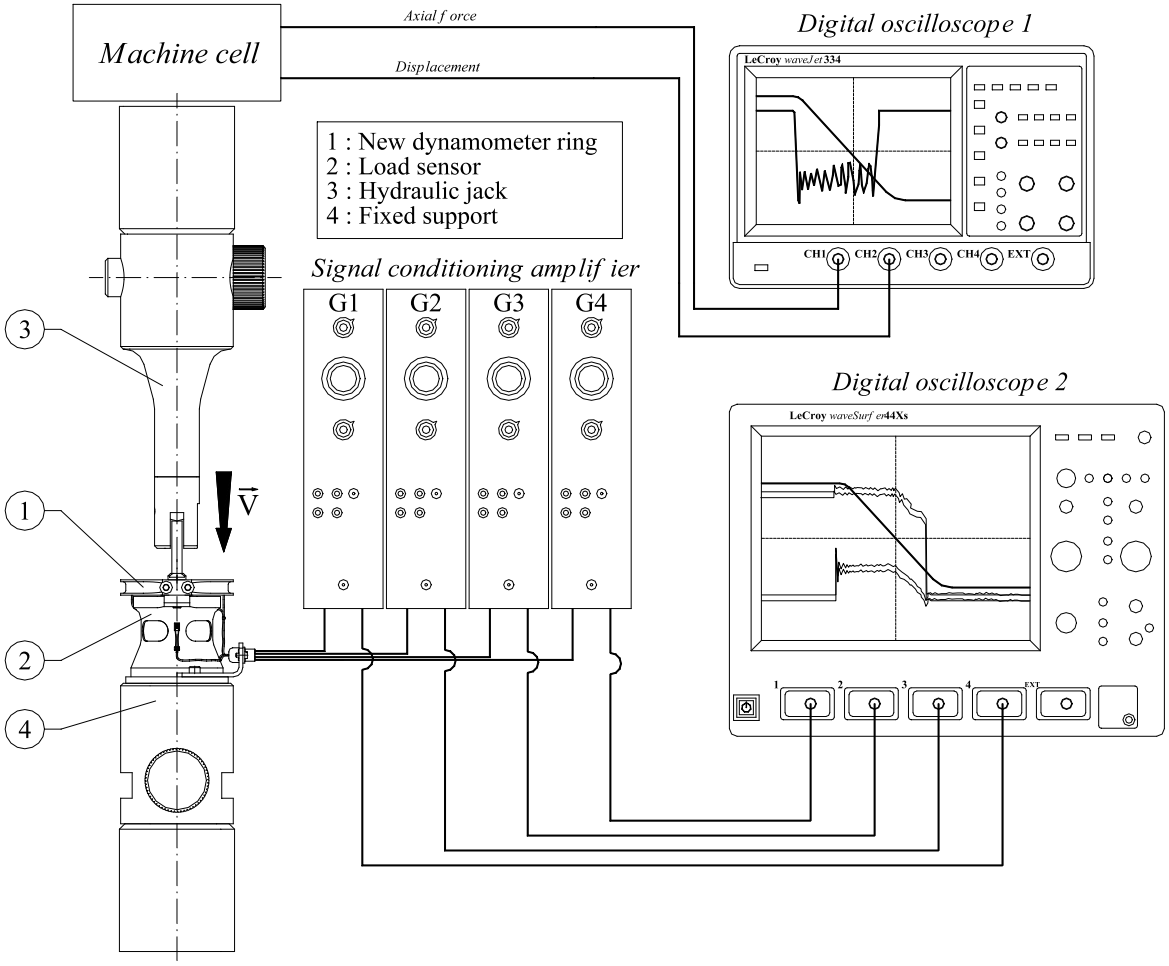

Figure 4.12: Data acquisition system of the set-up.

4.4 Quasi-Static Approach with Use of Hydraulic Jack

The main goal of further development of the frictional device initially proposed and presented by Philippon et al. [2004] is to increase the sliding velocity during the experiments performed on the gas gun. Experimental results with use of the initially proposed device, were successful for the range of velocity up to $60m/s$. Further increase of sliding velocity was causing instabilities in the measurements due to the generation of too high frequencies imposed by the impacting projectile and too small rigidity of the frictional device. These phenomena cause very big fluctuations and vibrations of the strain gages making it impossible for the oscilloscopes to properly register the occurring values.

The goal of this research is to determine the friction coefficient for a wide range of velocities. Using even the most recent and most sophisticated experimental techniques it is not yet possible to conduct experiments with such high velocities. Therefore, the presented friction model and the constitutive relation will be validated utilizing the highest velocities possible for the earlier mentioned experimental setup by Philippon et al. [2004]. Utilizing the observations of the current trends of the experimental results

and using the theoretical models for very high velocities and temperatures will allow one to extend the numerical simulation to include the desired velocities. However, to have the spectrum of the friction coefficients with respect to the complete range of velocities, including the velocities up to $5m/s$ one should also utilize the quasi static approach. For this case the hydraulic machine is used. This setup is presented in Figure 4.13.

It was already mentioned in the previous section that the experimental process consists of the quasi-static and dynamic approaches. However, for both cases the friction device has the exact same configuration. Two smaller specimens A (Steel 1080) and one larger specimen B (VascoMax 300), with their dimensions presented in Figure 4.5, are placed in the friction device as shown in Figure 4.13. Both specimens

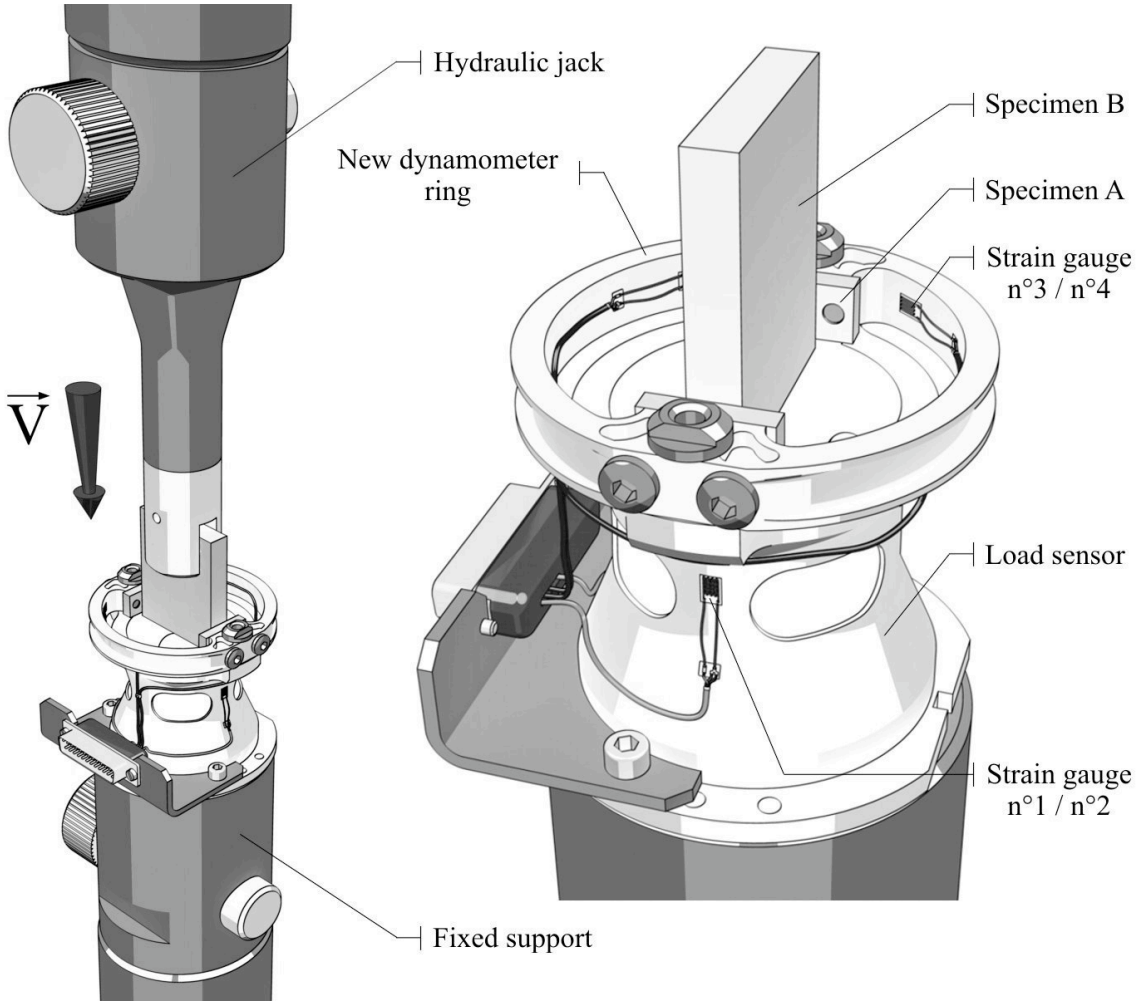

Figure 4.13: Views of modified friction device adapted on a hydraulic machine.

A are screwed to the dynamometer ring which is next screwed to the friction device. Due to calibration of the dynamometer ring (Section 4.3.2) and knowing the distance between both specimens A attached to the dynamometer ring and dimensions of the specimen B it is possible to determine the normal force F_N acting on the specimen B. This force is assumed to be constant within the entire experimental event and even

more it is monitored by two strain gauges mounted on the dynamometer ring. The strain gauges are also glued to the load sensor of the friction device in a particular place which resulted from the numerical simulation (Section 4.3.2).

The quasi static experimental process, with velocities up to $4m/s$ utilizes the hydraulic machine where setting the particular velocity is easy. It is assumed that the velocity is constant during the experiment unlike in the dynamic approach since the hydraulic jack applies constant pressure on specimen B, delivering constant velocity. The normal force from the dynamometer ring applied through both specimens A and acting on specimen B is constant during most of the experimental process. Knowing the length of the specimen B and the depth of the adaptation cut for the projectile it is easy to calculate the sliding distance along which the normal force is constant. Any possible force fluctuations are due to geometrical imperfections of the prepared specimens or unsymmetric impact of the hydraulic machine. The hydraulic device with the specifically profiled pseudo-projectile starts to approach the specimen B with a specific constant velocity (Figure 4.14(a)). At some point the pseudo-projectile reaches the specimen B (Figure 4.14(b)) and with the same constant velocity starts to push specimen B downwards (Figure 4.14(c)). This starts to generate the friction between both specimens A and B. The displacements occurring on the frictional device is registered by the strain gauges. This information is sent to the computer which converts these data to the frictional force resulting from this process (more information about registering the displacements by strain gauges and converting them to the frictional force with the use of the computer is presented in Section 4.6). The experiment is concluded and the pseudo-projectile is stopped after the specimen B looses contact with both specimens A (Figure 4.14(d)). The main and most important outcome of this experimental setup is the function of the frictional force with respect to the duration of the experiment. The main stages of the experimental event with use of the hydraulic machine is presented in Figure 4.14.

4.5 Dynamic Approach with Use of the Gas Gun

The dynamic experimental process is considered to start with the velocity in the range of $5m/s$. In this case with the help of the gas gun the experiment is being performed. The schematic setup of the dynamic experiment is presented in Figure 4.15. Figure 4.17(c) presents a photograph of the entire experimental setup.

The gas gun first introduced by Sutter et al. [2003] allows to perform successful experiments with velocities in the range from $10m/s$ to $100m/s$. The friction device has been adapted on this setup Philippon [2004]. However the experimental team at the University of Metz is still developing and upgrading their frictional device. By increasing the stiffness and at the same time decreasing the mass of the device, they were able to perform the successful tests with the velocity in the range of $100m/s$ which is a significant improvement to the previous results and one of the best performance in the world. The modified frictional device (in comparison to this presented by Philippon et al. [2004]) capable of measuring the friction during experiments even with the higher velocities is introduced and discussed in this section. It is important to note

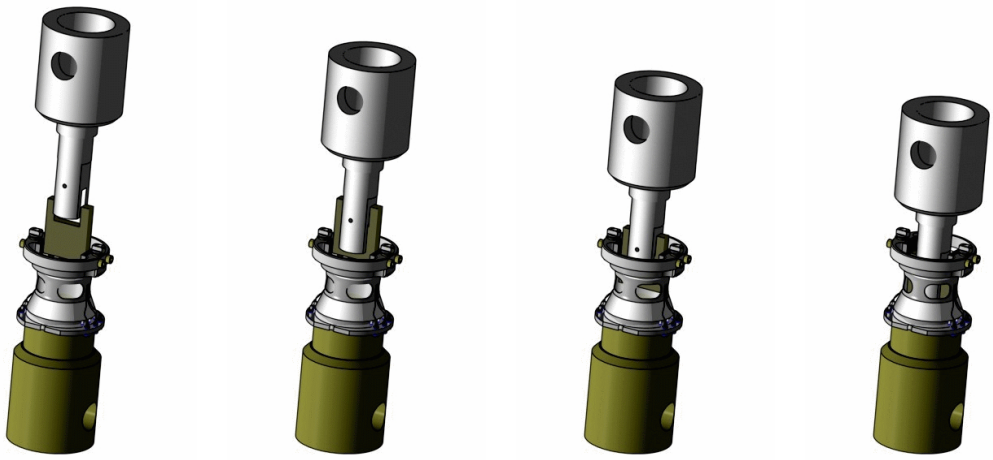

(a) (b) (c) (d)

Figure 4.14: 4.14(a) Initial setup of the friction experiment with the hydraulic machine. 4.14(b) Initial contact of the pseudo-projectile and specimen B. 4.14(c) Actual experiment: friction between specimens A and specimen B. 4.14(d) End of the experiment when the contact between specimens A and B is lost.

that despite the big differences with the relative velocity between the two specimens for quasi static and dynamic approaches the experimental device presented in Figure 4.3 is the same.

The tribometer device is adapted on a specific support made up of a long tube with an adaptor (adaptation bearing at the extremity of this tube) and two supports. This assembly has been fixed rigidly on a beam where Kolsky bar is usually mounted. The gas gun propels a projectile (striker) which enables to reach velocities varying from $25m/s$ to $100m/s$. Two photodiodes ($D1$ and $D2$) fixed at the gas gun exit allow the initial velocity measurement and the positions of the projectile at different instants. The entire setup of the experimental device for the dynamic approach with the use of the gas gun, including the Wheat-stone quarter-bridge configuration connected to a signal conditioning amplifier system and further recording the signal oscilloscopes is presented in Figure 4.16.

The projectile of a specific shape (Figure 4.17(a)) with a mass of $m_p = 254g$ (for comparison the impacted specimen B has a mass of $m_s = 182g$) is launched with the help of very high pressure produced by the gas gun (Figure 4.17(d)). It approaches the photodiodes and mounted experimental frictional device with the specimens that is already placed as is clearly visible on Figure 4.17(b). All stages of the experiment concentrated on the frictional device visualized in the order of appearance, such as launching the striker, passing the stream of light generated by the photodiodes, impacting the specimen, pushing the specimen B through and finally loss of contact between specimens A and B is schematically presented in Figures 4.18 and 4.19. The projectile is guided in the launch tube to avoid any rotation and to ensure a precision of about $0.015mm$ in the lateral position at the exit of the tube. It is not possible

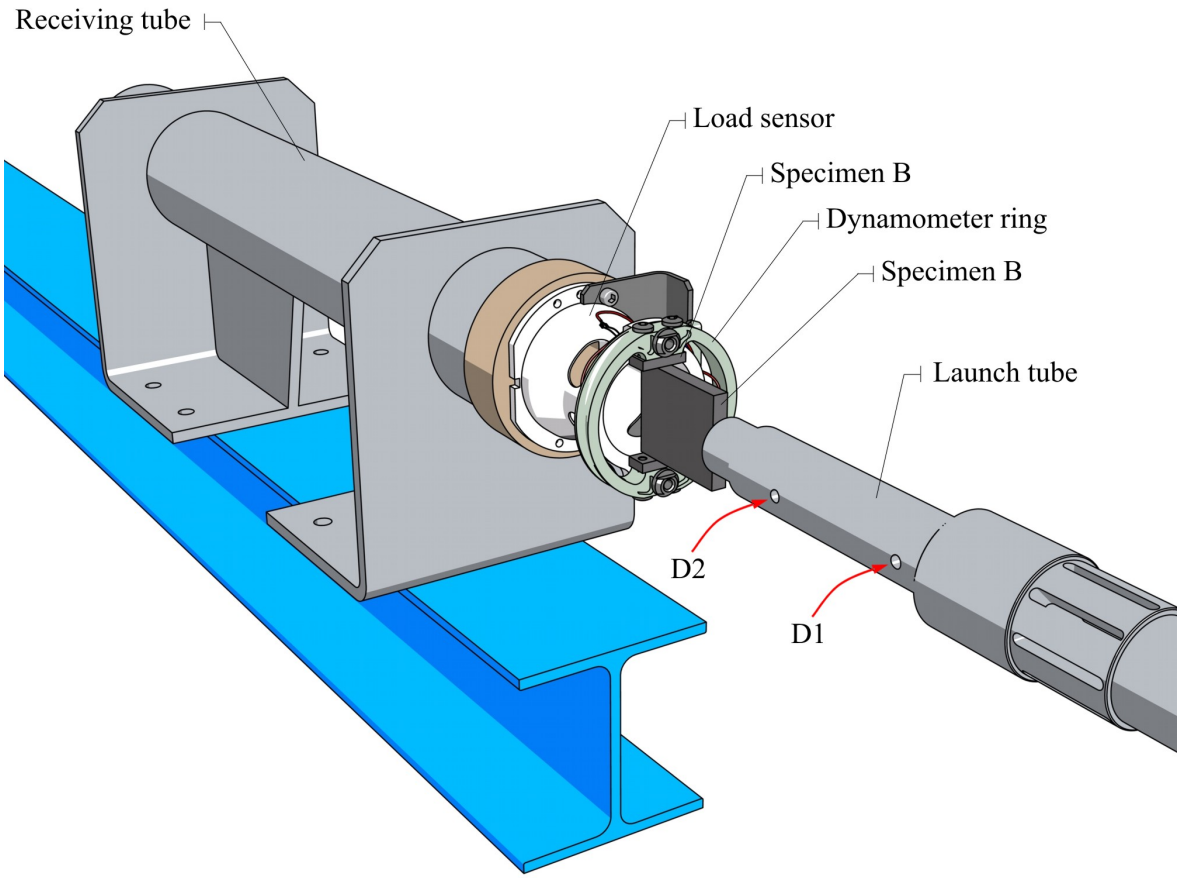

Figure 4.15: The schematic description of the experimental setup used for this research and initiated by Philippon et al. [2004].

to program the gas gun to deliver particular projectile velocity during the experiment, however, the estimated calibration bridging the generated pressure with the final velocity at the exit of the launch tube is presented in the following section. Therefore just before the end of the launching tube the two photodiodes (see Figure 4.17(b) on the right) are not only measuring the initial velocity but also the final, decreased velocity of the test. While the projectile is passing, the stream of light is disconnected in the following photodiodes. Knowing the distance between photodiodes ($80mm$) and the time interval between the light discontinuity it is easy to calculate both velocities. The shape and comparison of the size of the projectile with respect to impacted specimen B is presented in Figure 4.17(a).

It was tested and proved by Philippon et al. [2004] and Philippon [2004] that the losses of kinetic energy during the impact are barely affecting the velocity in case of the experiments performed on the hydraulic jack. In fact the decrease of the velocity during the impact is less than 4%, therefore it is assumed that the initial velocity of the specimen B is equal to the velocity measured by the load cell. In case of the dynamic experiments however, the velocity decrease of proceeding projectile is substantial and illustrates the amount of energy necessary to overcome friction forces. The detailed

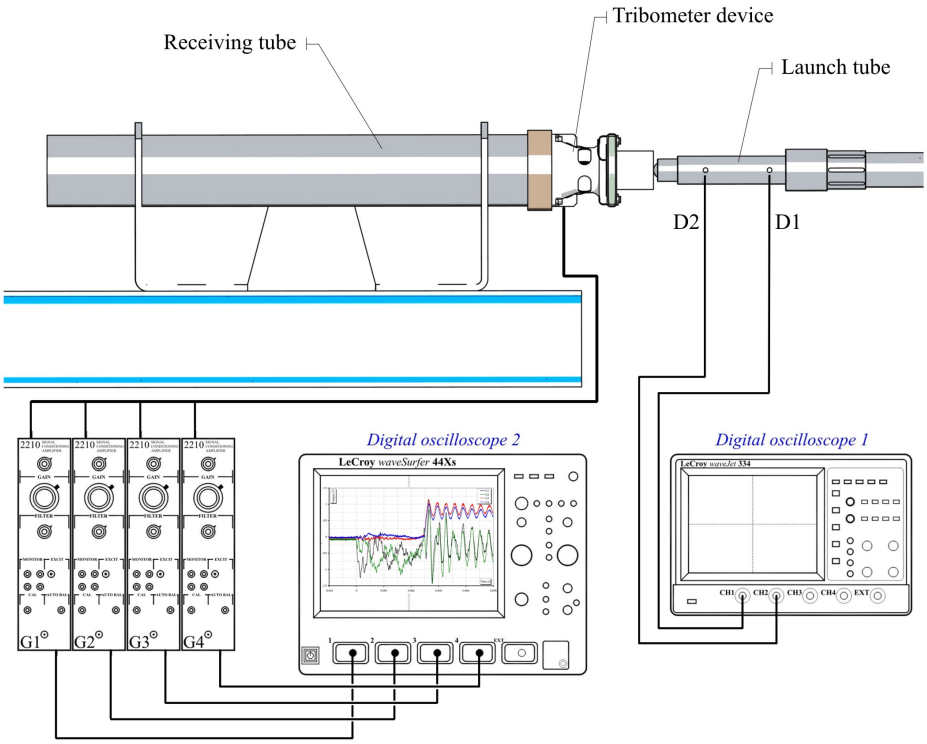

Figure 4.16: The schematic description of the entire experimental setup including the registering devices utilized for this research.

analysis of initial and final velocity of the projectile is considered in the following section. A dynamometer ring, which calibrates the compressive normal force F_N during the friction process, is mounted at the entry of the second tube (Figures 4.17(b)). A normal load of up to $4000N$ can be applied by a device which weighs only a few hundred grams. The measurements during the friction between specimens A and B in the case of the dynamic approach (Figure 4.19(c)) are recorded and registered in the computer in the same way as they were recored for the quasi-static approach. Due to the high speed of both, impacting projectile and specimen B it is necessary to engage the receiving tube which slows down both elements with a shock absorber which entirely stops the tested specimen B and the projectile, absorbing the entire kinetic energy. The final view at the friction device after conducting dynamic test is presented in Figure 4.19(d).

In case of both approaches i.e. quasi-static and dynamic, the outcome of the experiments is the same, namely the function of the frictional force with respect to the time of experiment. The strategy in obtaining the results is the same for both cases however the used equipment is different. The following sections will concentrate on presenting and analyzing the obtained results pointing out the most crucial and important aspects of the experimental procedure and introducing the pioneering experimental results never performed before.

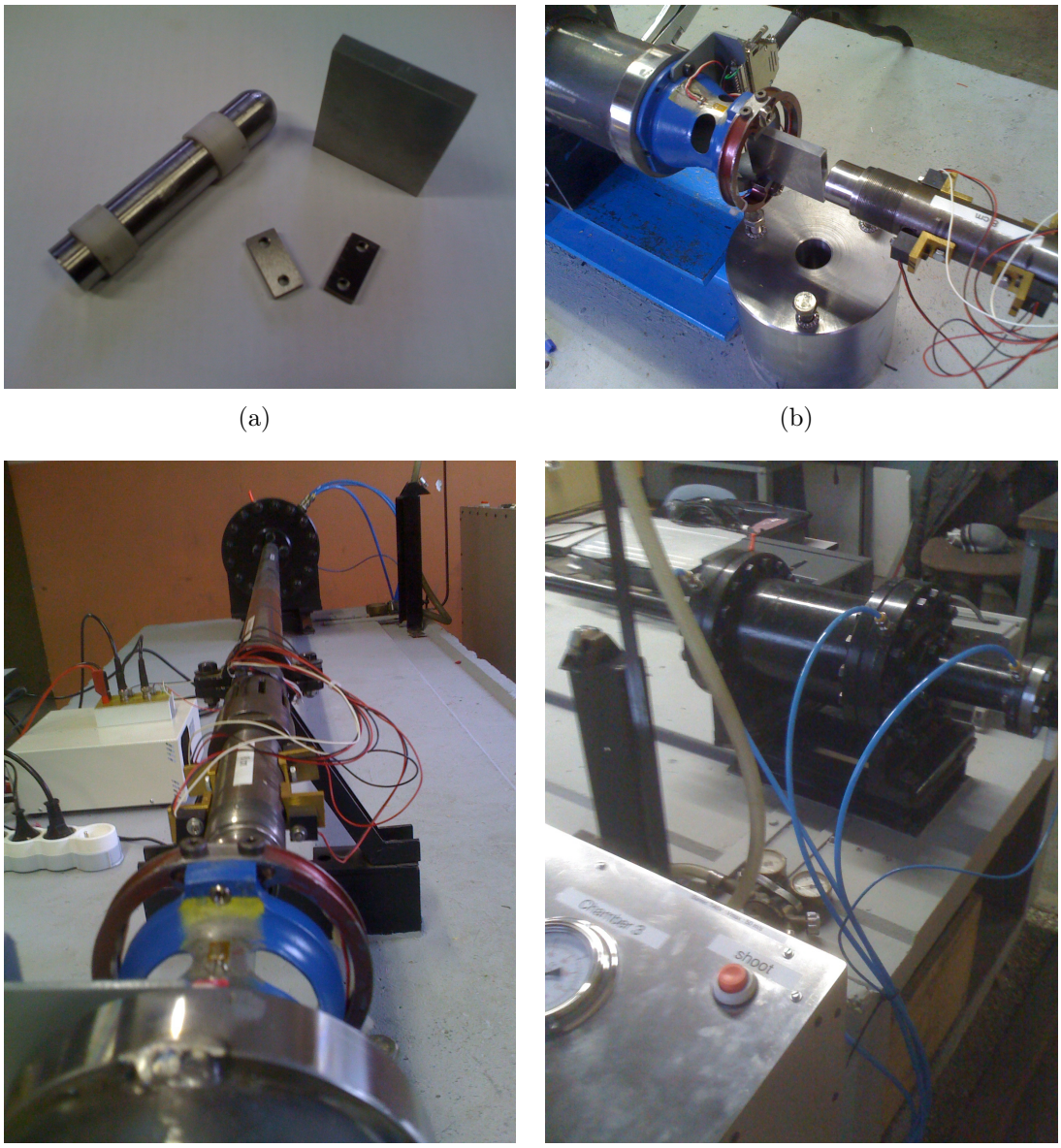

(a) (b)

(c) (d)

Figure 4.17: 4.17(a) shows the specimens and projectile used in the experiment. 4.17(b) presents the frictional device mounted on the receiving tube with the placed specimens and photodiodes on the right. 4.17(c) shows the entire experimental setup. 4.17(d) presents the gas gun with the part of the launching tube.

4.6 Final Description and Experiment Results

4.6.1 Quasi-static Approach with the Use of the Hydraulic Jack

All the tests were performed on a high speed hydraulic testing machine ZWICK Rel 1873 RAC, which can deliver a maximum tensile or compressive force up to $100kN$ with a maximum jack displacement of $150mm$ for a maximum velocity up to $5m/s$. In

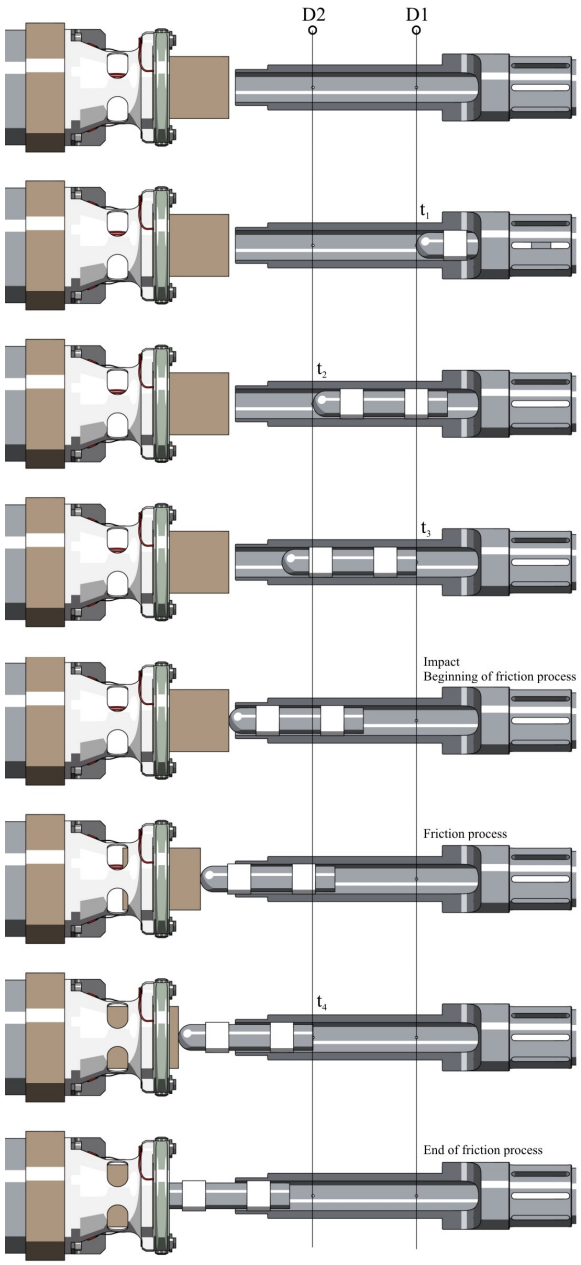

Figure 4.18: All stages of the projectile position during the dynamic sliding friction test.

this study, the tests were carried out for a range of sliding velocities V varying from 0.12 to $3.72 m/s$ and for a sliding displacement of $60 mm$. The whole device is held onto the fixed support of the machine (see Figure 4.13). The initial recordings presented in this section are obtained for the specimens A and B made of the same material (XC38 French standard steel) and for the main set of data obtained for Steel 1080 and VascoMax 300. Before each test, specimen B is placed between the two specimens A by the elastic deformation of the ring using a clamping tool. This elastic deformation

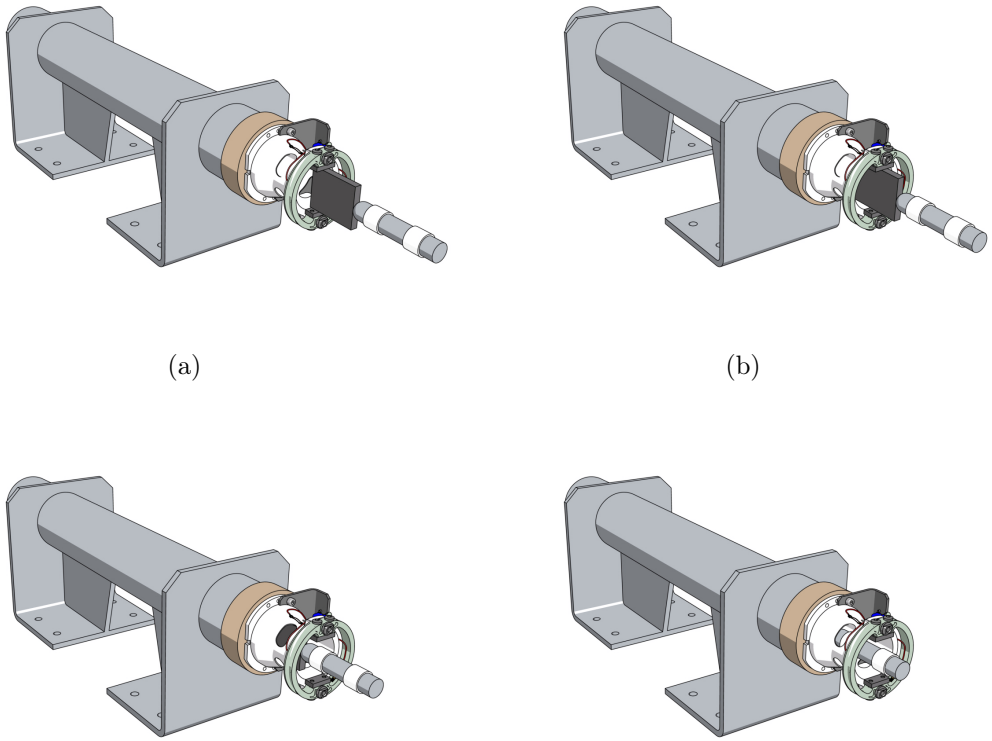

(a) (b)

(c) (d)

Figure 4.19: 4.19(a) presents the initial setup of the friction experiment with the gas gun just before the impact of the projectile. 4.19(b) shows the projectile impacting specimen B. 4.19(c) presents the experimental part: friction between specimens A and B with high relative velocity between them. 4.19(d) shows the end of the experimental process; end of the frictional contact between specimens A and B, and the destination of specimen B with the projectile in the receiving tube.

induces a gap between the ring and the specimen and allows the placement of specimen B. Two different thicknesses H_B are used to apply the two apparent normal pressures p on the sliding surface (see Figure 4.5). The first configuration corresponding to low value of the apparent normal pressure p is obtained with an increase of the dimension δ equal to $0.2mm$ and an apparent contact surface between the specimens with about $96mm^2$ ($H_A \times H_{BL}$). Slight variations of these geometrical parameters led to a low normal pressure p varying from 8 to $9MPa$. High apparent pressure p, in the range from 70 to $80MPa$, is obtained with an increase of δ equal to $0.6mm$ and a decrease of H_B (see dimension H_{BH} in Figure 4.5). Finally, the imposed experimental parameters are the apparent normal pressure p and the sliding velocity V, whereas the measured parameters are normal force F_N applied by the ring, two frictional forces F_T provided by the load sensor and total axial force F recorded by the load cell machine. Typical oscillograms obtained from the four strain gauge recordings are shown in Figures 4.20

and 4.21. These recordings are related to the sliding velocities $V = 0.865m/s$

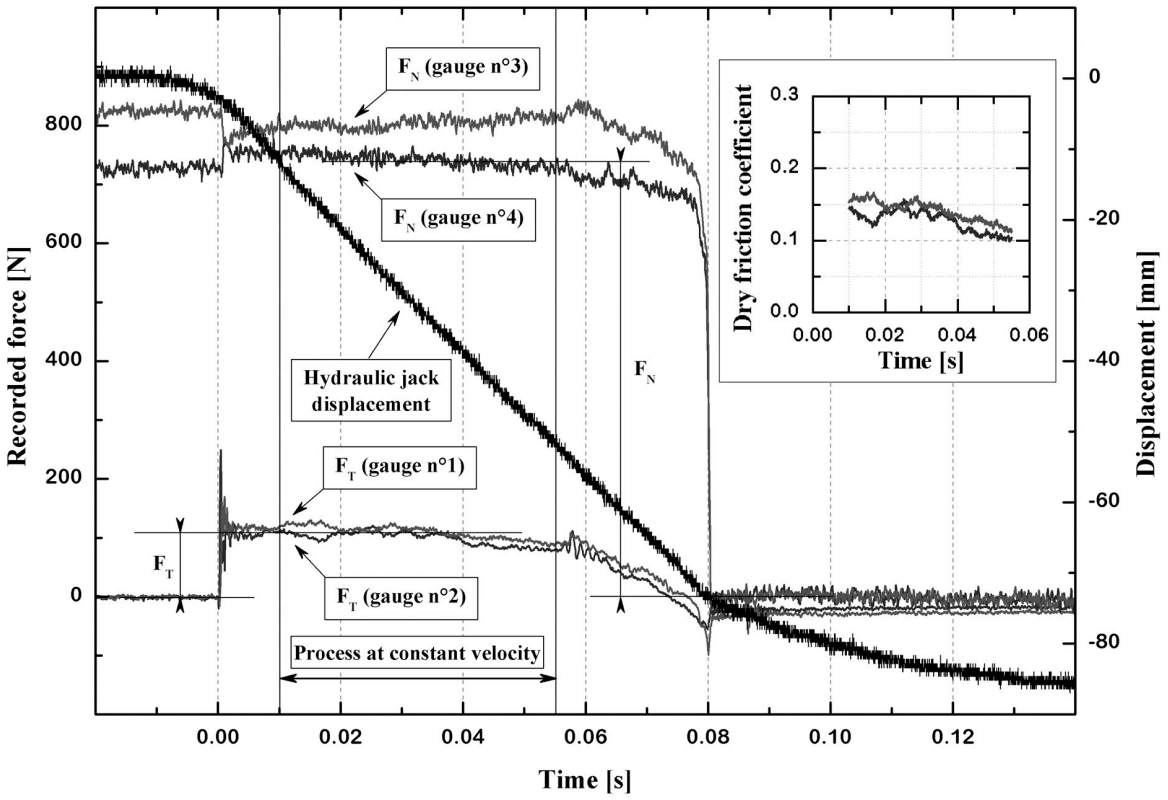

Figure 4.20: Normal and tangential forces evolution obtained from recorded strain gauge signals and hydraulic jack displacement for a low normal pressure $p = 7.99MPa$ and for a sliding velocity $V = 0.865m/s$ (test n^o3).

and $V = 1.57m/s$ for the apparent normal pressures $p = 7.99MPa$ (test L.P. n^o3) and $p = 76.4MPa$ (test H.P. n^o6) respectively. Only a partial phase of the sliding test is conducted at constant sliding velocity V. Indeed, it is not possible to reach immediately a constant speed of the jack with the hydraulic technology for this testing equipment. This is more accurate for the highest velocities V, however in that case it is impossible to avoid the decrease in the sliding velocity. This phenomenon is discussed in the next section concerning dynamic experimental results on a gas gun. During the phase of constant velocity, the recordings show quasi constant force levels as well as normal force F_N and frictional force F_T. They also show a peak at the beginning of the process, due to the impact between the moving jack and specimen B. Following this first peak, the quasi constant level is observed until the decrease of the tangential force F_T due to the progressive loss of contact between specimens A and B. Dry friction coefficient μ is calculated from the ratio between the frictional and apparent normal forces. The thumbnails show the evolution of coefficient μ during the process at constant sliding velocity V. The good sensitivity of this new device enables one to detect slight variations of μ, caused for instance due to geometrical imperfections Faure et al.

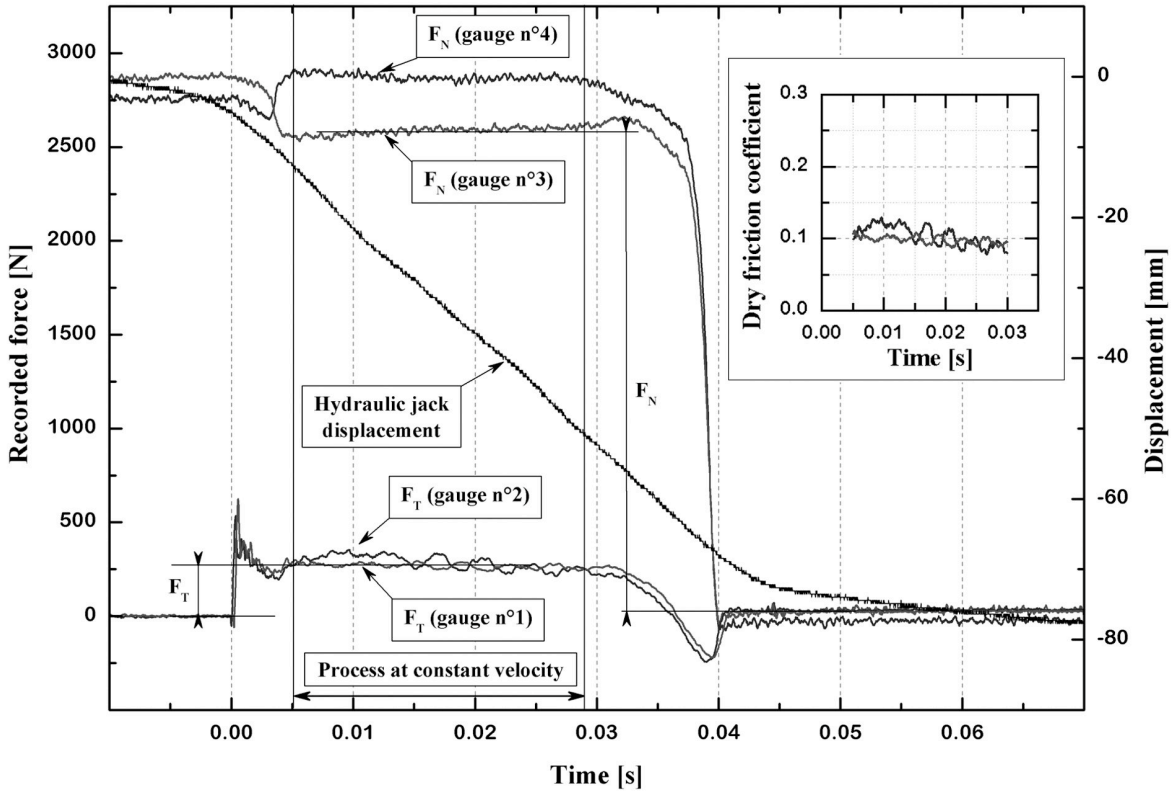

Figure 4.21: Normal and tangential forces evolution obtained from recorded strain gauges signals and hydraulic jack displacement for a high normal pressure $p = 76.4MPa$ and for a sliding velocity $V = 1.570m/s$ (test n^o6).

[2009*b*,*d*].

Figure 4.22 illustrates a recording of the hydraulic machine load cell, corresponding to a low pressure test performed at a sliding velocity $V = 1.56m/s$ (test L.P. n^o5). From the raw signal data, one can observe high magnitude and periodic oscillations generated by the dynamic behavior of the machine cell. The value of the main frequency is obtained by a Fast Fourier Transform (F.F.T.). A filter is then applied allowing one to determine easier the average value of the total sliding force F. Filtering is a process of selecting frequency components from a signal. A FFT filter performs filtering by using Fourier transforms to analyze the frequency components in the input signal. The filter used is a band block filter type, allowing only frequency components outside a specified range to pass and remove all frequencies within the chosen range, defined by the previous FFT analysis. Total force F is of the order of the sum of the frictional forces F_T. The low level of forces (a few hundreds newtons) in comparison to the load capacity of the cell ($100kN$) could explain this difference.

Nevertheless, one can ascertain from these small sliding velocities, that the roughness value of the contact surface affects, generally, the frictional force F_T as mentioned in the literature. A decrease in the dry friction coefficient for an increasing apparent

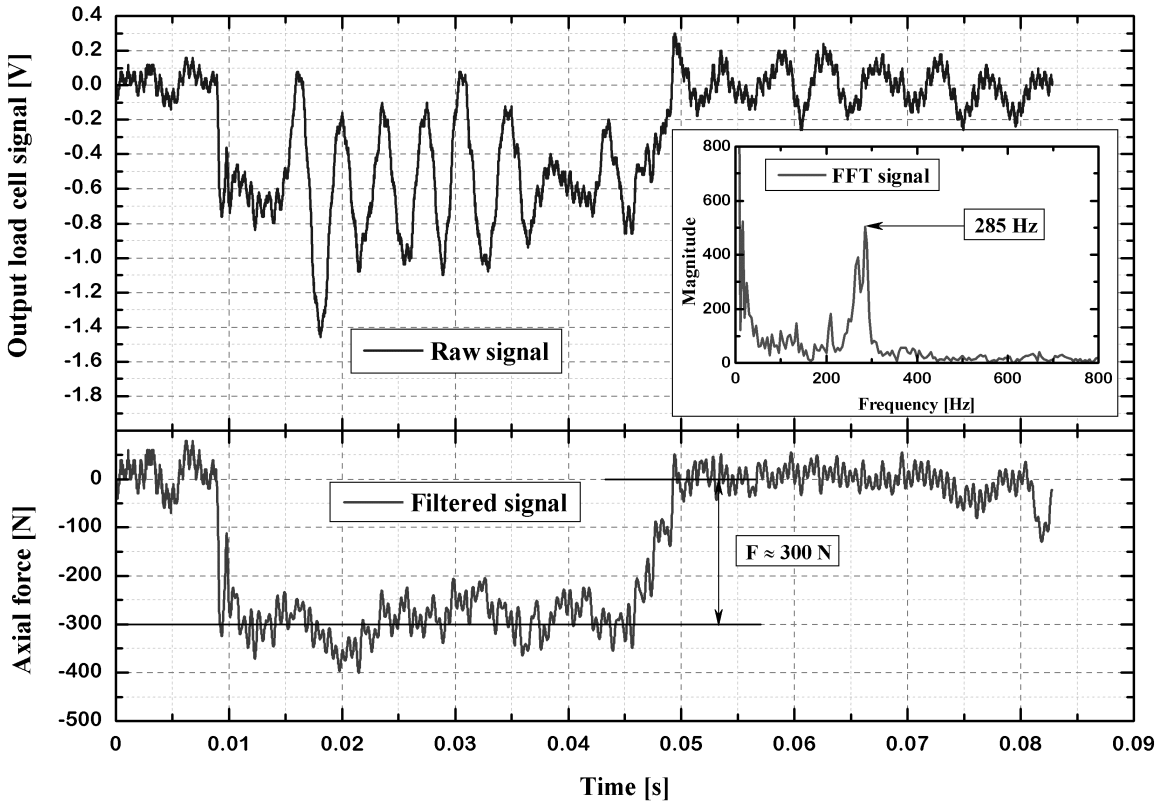

Figure 4.22: Machine cell signals recorded during test n^o5 - L.P ($V = 1.559m/s$, $p = 9.01m/s$).

normal pressure p can be noticed. The steel-on-steel dry friction coefficients measured are in good agreement with those obtained by Lim and Ashby [1987], Lim et al. [1989].

In order to gather all information, such as displacements and velocity, in order to obtain the frictional and normal forces occurring during the experiments, it is necessary to use the complete experimental setup. Four strain gauges glued on the load sensor and the dynamometer ring (4 channels are used) are connected to form four separate Wheastone quarter-bridges as already described in detail in Section 4.3. Two other channels of the Lecroy oscilloscopes are used for the displacement jack and the force cell measurement. The procedure of obtaining results and registering them on the computer is described in detail in Section 4.3.5, in particular Figure 4.12. The value of the current in the Wheatstone bridges recorded by means of the oscilloscopes is adjusted accounting for external conditions and possible external disturbances. It should be noted that the possible large oscillations may be caused not only by other experimental machines operating within close vicinity of the testing equipment used for this research but primarily due to the dynamic behavior of the hydraulic machine and low sensitivity of the load cell to measure small forces for this range of sliding velocities.

Two sets of experiments for static and quasi-static loads were performed in a very similar manner. The first approach consists of 9 attempts for the low pressure between tested specimens and 9 attempts for the high pressure configuration. The specimens

made of XC 38 French standard steel as previously described are investigated. The second set of tests consist of 9 attempts with different sliding velocities for the tribopair consisting of Steel 1080 and Steel VascoMax 300. In the second approach the normal pressure is constant. In the first scenario all experiments apart from one trial (due to acquisition problems of the load cell) for high normal pressure were successful and for the second scenario the first, second and seventh tests were not successful and therefore the outcomes of those will not be considered in this work. Considering the linear part of the displacement of the hydraulic jack measured in time as well as noticing the significant force changes indicating the loss of contact between tested specimens and showing the exact time of the particular experiment it is possible to determine the velocity during the experiment (Table 4.5). Outputs for Experiment 3 for the Steel 1080 and VascoMax pair are presented in Figure 4.23. One needs to note, that the negative values on Figure 4.23(b) do not have any specific physical meaning. It is simply due to the particular setting of the oscilloscopes before the experiment begins. The most important part of this graph is the jump reflecting the loss of contact between the specimens. From this sudden change it is possible to estimate the normal force occurring during the experiment and comparing it with the theoretical value which can be computed based on the calibration of the device. The large oscillations of the signal in Figures 4.23(c) and 4.23(d) are primarily due to the dynamic behavior of the hydraulic machine when tests are performed at high velocity ($V > 1.5m/s$) and also the noise caused by the continuous use of another experimental device within the close proximity of the testing setup. However, this disturbance did not affect the final results of the presented experiments. It was ensured that this is not repeated for the dynamic experimental approach where this kind of disturbance could entirely distort the results. The dynamic experiments on the gas gun device were conducted in a separate designated area that excluded the possibility of any external disturbances. All of the readings measured by Wheatstone bridges are in the units of voltage (Volts). Therefore in order to obtain the results presented in Figure 4.23 one has to convert them into the units of force using the calibration information presented in Section 4.3. In Table 4.1, the conversion ratio for both the load sensor and dynamometer ring are presented.

Table 4.1: Conversion ratios between units of current and units of force

Device type	**Channel #**	**Strain Gauge**	**Conversion Ratio**
Load Sensor	1	1	1 Volt = 603 Newtons
Load Sensor	5	2	1 Volt = 590 Newtons
Dynamometer Ring	3	3	1 Volt = 1575 Newtons
Dynamometer Ring	6	4	1 Volt = 1437 Newtons

After obtaining all the necessary data the friction coefficient can be calculated. Performing the conversion analysis followed by statistical averaging and smoothing techniques one obtains the resulting forces during the performed experiments. These relations in case of experiment 3 for Steel 1080 and VascoMax pair are presented in Figure 4.24. Tables 4.2, 4.3 and 4.4 summarize all information regarding the experimental results for contact with different material pairs. It is very important to note

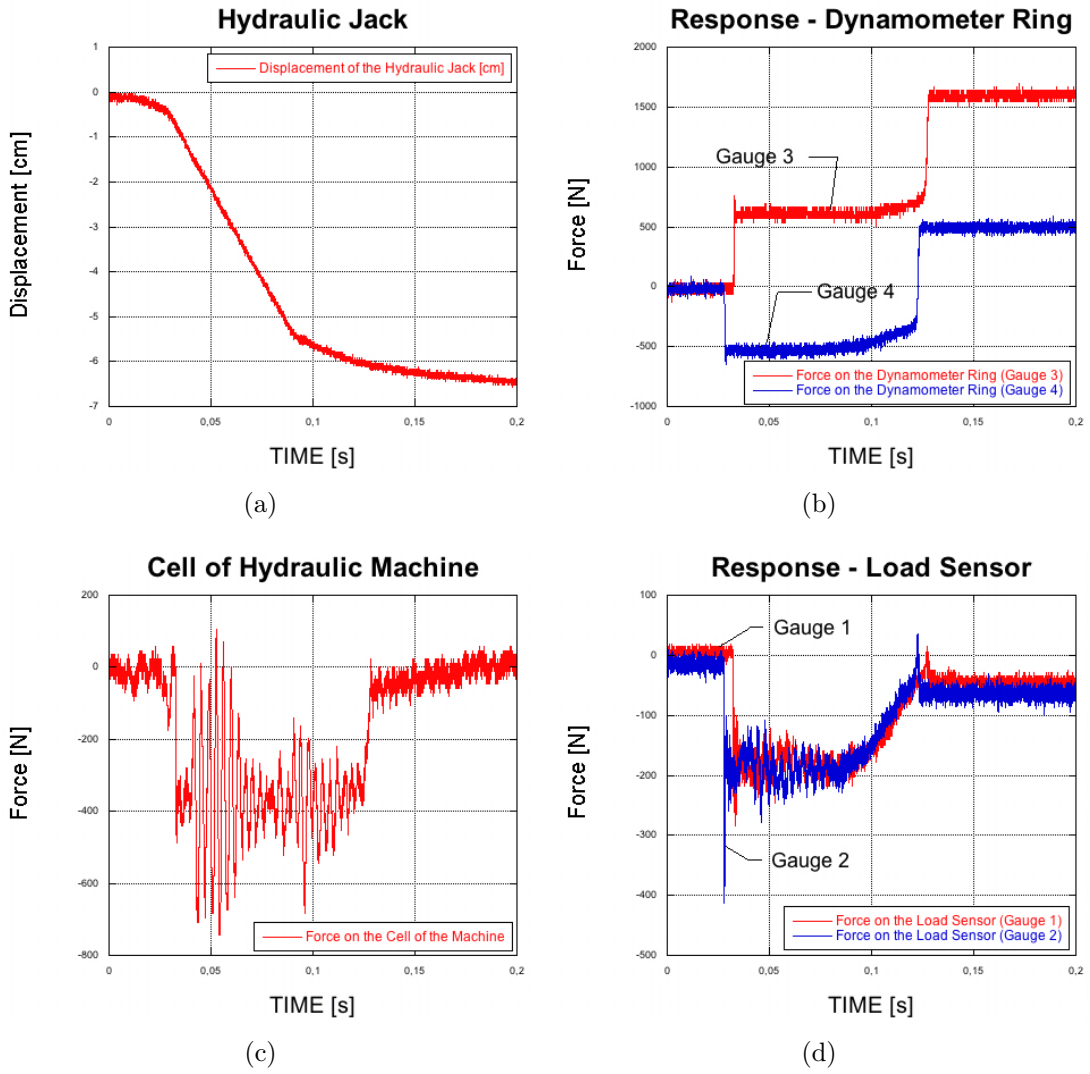

Figure 4.23: 4.23(a) presents the displacement of the hydraulic jack within the duration of the experiment, 4.23(b) presents the voltage read by the stain gauges mounted on the dynamometer ring, 4.23(c) shows the response of the cell of the hydraulic machine during experiment 3 and finally 4.23(d) shows the response of the load sensor in terms of voltage occurring on the mounted strain gauges. All presented results consider Experiment 3.

that the change of the width of specimen B values presented in Table 4.4 (top W_1 and bottom W_2) affects the change of the normal force. There is a very good correlation between the change of width and the change of the normal force during the particular experiments. The difference in the friction coefficients in Table 4.4 arises from the different measuring approaches; one is based on the cell of the hydraulic machine and the second one is based on the strain gauges mounted on the load sensor. Both values slightly differ, however, the overall trend is very similar for both cases and is presented in Figure 4.25.

Table 4.2: Experimental data for the low pressure sliding tests for the standard steel on standard steel pair.

Low Pressure Tests - L.P.; 7.81 MPa<p<9.01 MPa								
Test	Sliding Velocity V [m/s]	W_1 [mm]	Total axial force F [N]	Average frictional force F_T [N]	Average normal force F_N [N]	Apparent normal pressure p [MPa]	Dry friction coefficient μ Machine Cell	Load Sensor
1	0.122	48.220	270	94	835	8.70	0.16	0.11
2	0.123	48.200	350	115	770	8.02	0.23	0.15
3	0.865	48.210	270	116	767	7.99	0.18	0.15
4	0.872	48.210	260	95	750	7.81	0.17	0.16
5	1.559	48.200	300	137	865	9.01	0.17	0.16
6	1.575	48.190	200	70	750	7.81	0.13	0.09
7	2.661	48.190	220	110	780	8.13	0.14	0.14
8	2.370	48.200	230	85	850	8.85	0.14	0.10
9	3.723	48.200	290	70	800	8.33	0.18	0.09

Table 4.3: Experimental data for the high pressure sliding tests for the standard steel on standard steel pair.

High Pressure Tests - H.P.; 70.83 MPa<p<77.78 MPa								
Test	Sliding Velocity V [m/s]	W_1 [mm]	Total axial force F [N]	Average frictional force F_T [N]	Average normal force F_N [N]	Apparent normal pressure p [MPa]	Dry friction coefficient μ Machine Cell	Load Sensor
1	0.111	48.590	940	325	2770	76.94	0.17	0.12
2	0.110	48.600	840	320	2785	77.36	0.15	0.11
3	0.874	48.600	740	340	2762	76.72	0.13	0.12
4	0.874	48.600	500	180	2712	75.33	0.09	0.07
5	1.570	48.600	–	265	2775	77.08	–	0.10
6	1.570	48.600	700	285	2750	76.39	0.13	0.10
7	2.750	48.600	640	270	2800	77.78	0.11	0.10
8	2.720	48.580	560	290	2585	71.81	0.11	0.11
9	2.990	48.580	690	340	2550	70.83	0.14	0.13

Table 4.4: Experimental data of the low pressure sliding tests for Steel 1080 and VascoMax pair. W_1 and W_2 are the widths on the top and bottom of the specimens, respectively.

Steel 1080 and VascoMax pair for low pressure $p \approx 9MPa$								
Test	Sliding Velocity V [m/s]	W_1 [mm]	W_2 [N]	Machine Cell Force [N]	Load Sensor Force F_T [N]	Average normal force F_N [MPa]	Dry friction coefficient μ Machine Cell	Load Sensor
3	0.85	48.200	48.196	345	292	1025	0.33	0.28
4	1.63	48.192	48.188	262	252	1020	0.33	0.25
5	1.66	48.190	48.171	279	310	920	0.33	0.33
6	2.76	48.188	48.181	264	218	800	0.33	0.27
8	2.73	48.164	48.185	224	270	780	0.33	0.28
9	0.31	48.168	48.178	379	306	810	0.46	0.37

The obtained friction coefficients, presented in Figures 4.25(a) and 4.25(b), are in very good agreement with the theory presented in the literature Lim et al. [1989], Oden and Martins [1984] i.e. there is a significant decrease of the friction coefficient due to the sliding velocity increase and due to the roughness reduction. The main goal

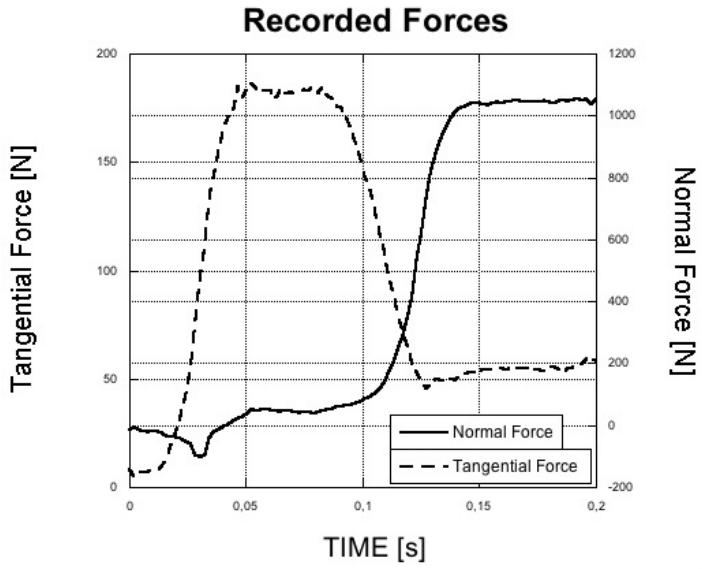

Figure 4.24: Normal and tangential forces occurring in Experiment 3 processed using the calibration analysis followed by the statistical smoothing techniques

of this work is to present and describe frictional relations between Steel 1080 and Steel VascoMax. The other steel-on-steel pair is presented as a reference in explaining the experimental setup and experimental process. For the quasi static approach with the lowest sliding velocity it was expected that the friction coefficient would be the highest due to the *stick-slip* criterion. Moreover another interesting property was observed. In most of the cases the value of the friction coefficient strongly affects the roughness decrease. In Table 4.5, the final comparison of the friction coefficient and roughness decrease is presented. It can be clearly seen that except for experiment number 6 all other experiments show the same trend- the lower the friction coefficient the lower the decrease of the roughness. This phenomenon indicates that the change in friction coefficient does not only depend on the sliding velocity or temperature but also is affected by the roughness of the sliding surface. Another interesting property shown in Figure 4.25 is the average dry friction coefficient calculated with the use of the data obtained from the load sensor and the cell on the hydraulic machine. Despite the slight difference of these coefficients for the low velocities the overall trend with the increase of the velocity brings them closer (Figure 4.25). The increased values of friction coefficient for machine cell are due to inertia effect distorting the accuracy of the measurements. Due to this inertia effect, it is accepted that more precise results are obtained by the load sensor and the results obtained by the machine cell are placed only for reference.

The test setup description and its new experimental improvements are novel contribution in this research area. Two pairs of materials have been tested for a sliding velocity varying from 0.2 to $4m/s$ and for two apparent normal pressures. The first experimental results reported in this work are used as pioneer results and will be completed in a second step with high impact velocity. The results are used to model the friction coefficient with the applied velocity as it was reported for example by Philippon et al. [2004]. The goal of this part is to demonstrate that using this device with the

complete procedure, the friction coefficient is measured and linked to roughness evaluation. The main goal in addition to the experiments is to propose a better friction coefficient modeling, coupling pressure, velocity, temperature and roughness evolution using internal variables.

The data obtained for the Steel 1080 on Steel VascoMax friction tests must be considered as the first experimental results obtained. The effects of the sliding velocity on the surface roughness changes and on the dry fiction coefficient have been clearly observed and hence should be underlined. The obtained results as well as the experimental setup is reliable as indicated by the updatability and accuracy of the results. Due to limited amount of tests the spread of the results may be high (Figure 4.25) however, with a bigger number of tests the single results would converge to these obtained with the mathematical averaging techniques.

Table 4.5: Comparison of average dry friction coefficient with the average roughness decrease based on the measurements before and after the set of all experiments for Steel 1080/VascoMax pair.

Exp #	μ	**Velocity**	**Roughness**: **Initial** $[nm]$	**Final** $[nm]$	**Decrease [%]**
3	0.28	0.85m/s	553.74	500.57	9.60
4	0.25	1.63m/s	450.46	417.33	7.35
5	0.33	1.66m/s	548.07	437.72	20.13
6	0.27	2.76m/s	576.25	485.64	15.72
8	0.28	2.73m/s	488.41	454.77	6.88
9	0.37	0.31m/s	680.73	405.38	40.04

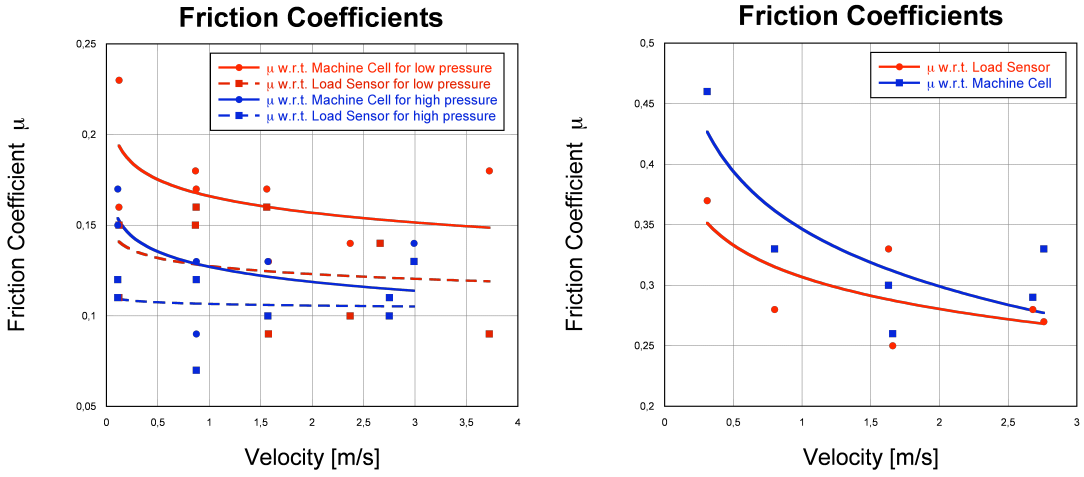

(a) (b)

Figure 4.25: Final results of the quasi-static experimental approach capturing the friction coefficients for different velocities for: 4.25(a) the Standard Steel pair and 4.25(b) Steel 1080/VascoMax pair.

4.6.2 Dynamic Approach with the Use of the Gas Gun

All the tests were performed on the modified Hopkinson Bar tube developed by the research team at ENIM, France, which can deliver a velocity between $10m/s$ and $100m/s$ depending on the length of the launching tube, pressure generated applied by the gas gun and the mass of the projectile. In this study, the tests were carried out for a range of sliding velocities V varying from 21.27 to $52.63m/s$ and for a sliding displacement of $60mm$, similarly to the quasi-static approach. The whole device is held onto the receiving tube, fixed rigidly on the I beam as presented in Figure 4.15. Unlike the quasi-static approach, the dynamic approach was not initiated with the set of trial experiments with the XC38 French standard steel specimens. In order to eliminate possibly many experimental imperfections such as misalignment, asymmetric impact, lack of rigid connection between the receiving tube and the base I beam, six trial experiments were conducted with the trial specimens. A bad alignment between both launch tube and receiving tube affects the strain gauge measurements. The impact may generate a flexural mode of the load sensor. However, the dynamic behavior of the main parts can be identified on the recordings during and after the test. The analysis of modal tests by use of impact hammer and accelerometers should confirm the observed frequency values.

The recordings presented in this section are obtained for specimens A and B and include the set of data obtained for the Steel 1080 and VascoMax 300. Before each test, similarly as for the quasi-static approach, specimen B is placed between two specimens A by elastic deformation of the ring using a clamping tool. This elastic deformation induces a gap between the ring and the specimen and allows the placement of specimen B. Thickness H_B regulates the amount of the apparent normal pressure p applied on the sliding surface (see Figure 4.5), consistent with the calibration results introduced in Section 4.3.2, particularly in Figure 4.7(a).

The dynamic configuration of the apparent normal pressure p is obtained with an increase of the dimension δ equal to $0.2mm$ and an apparent contact surface between the specimens with about $96mm^2$ ($H_A \times H_{BL}$). Slight variations of these geometrical parameters led to an applied normal pressure p varying from $9.11MPa$ to $12.5MPa$. Finally, the imposed experimental parameters are the apparent normal pressure p and the sliding velocity V, whereas the measured parameters are the normal force F_N applied by the ring and the two frictional forces F_T provided by the load sensor.

Before conducting the main set of experiments the calibration of the gas gun is performed. The main goal was to link the pressure generated by the gas gun with the projectiles velocity at the end of the launch tube. The projectile for this calibration was launched from the middle of the tube. The sliding velocity varies linearly according to the pressure in the gas gun (for this range of pressure). Table 4.6 represents the measurement of the initial velocity V_{init} (just before the impact). The use of t_1, t_2, t_3 and t_4 provides the position of the projectile during the sliding process, and consequently the exact friction distance. For some experiments, particularly with the higher velocity the projectile was launched from the very beginning of the launching tube and hence was able to obtain higher velocities. This is the reason why the maximum obtained velocities are higher than the ones presented in this table.

Table 4.6: Relation between generated pressure and final velocity for the projectile launched from the middle of the tube

Test #	**Pressure** $[Bar]$	$\mathbf{t_1}$-$\mathbf{t_2}$ $[ms]$	$\mathbf{t_3}$-$\mathbf{t_4}$ $[ms]$	$\mathbf{V}_{12}$ $[m/s]$	$\mathbf{V}_{34}$ $[m/s]$
1	1.00	4.68	4.60	17.07	17.39
2	1.50	3.80	3.80	21.05	21.05
3	2.00	3.12	3.16	25.64	25.31
4	2.50	2.88	2.88	27.77	27.77
5	3.00	2.56	2.56	31.25	31.25
6	3.50	2.38	2.38	33.61	33.61
7	4.00	2.18	2.22	36.69	36.03
8	5.00	1.94	1.98	41.23	40.40

The gas gun calibration spanning pressure with velocity is very useful, however, it is extremely important to notice that the initial sliding velocity of the specimen B is greater than the final sliding velocity. It was noted in all tests that it is impossible to avoid the decrease of sliding velocity. It is due to the fact that comparable masses of both, the projectile ($m_p = 254g$) and specimen B ($m_s = 182g$) are of the same order and hence the generated kinetic energy by the launched projectile is relatively too small with respect to the mass of the specimen B. The losses of total kinetic energy are considerable and hence so is the loss in velocity. As presented in Table 4.7 the velocity decrease during the sliding process oscillates between $30 - 40\%$. It is important to notice that tests $1 - 4$ were performed with the projectile launched from the middle of the tube according to the previously performed calibration and test $5 - 8$ with the projectile launched from the beginning of the tube, hence with the same pressure the obtained velocities are higher. Despite the decrease of sliding velocity it was noted that the normal force F_N is held quasi constant during the experimental process until the loss of contact between specimens A and B. Dry friction coefficient μ is calculated from the ratio between the frictional and apparent normal forces. The thumbnails show the evolution of coefficient μ during the process at constant sliding velocity V. The good sensitivity of this new device enables one to detect slight variations of μ, caused for instance by geometrical imperfections.

Table 4.7: The velocity decrease analysis. Tests $1 - 4$ were launched from the middle of the tube whereas tests $5 - 8$ were launched from the beginning of the tube.

Test #	**Pressure** $[Bar]$	$\mathbf{t_1}$-$\mathbf{t_2}$ $[ms]$	$\mathbf{t_3}$-$\mathbf{t_4}$ $[ms]$	$\mathbf{V}_{12}$ $[m/s]$	$\mathbf{V}_{34}$ $[m/s]$	$\mathbf{V}_{drop}$ $[\%]$
1	1.50	3.02	5.04	26.49	15.85	40.2
2	1.50	3.76	7.60	21.27	10.52	50.3
3	2.00	3.16	5.04	25.31	15.87	37.3
4	3.00	2.60	3.80	30.76	21.05	31.6
5	3.00	2.02	3.12	39.60	25.64	35.3
6	4.00	1.70	2.70	47.05	29.62	37.0
7	4.00	1.70	2.70	47.05	29.62	37.0
8	5.00	1.52	2.40	52.63	33.33	36.7

On the raw signal data, one can observe high magnitude and periodic oscillations generated by the dynamic behavior of the machine cell. The value of the main

frequency is obtained by a Fast Fourier Transform (F.F.T.). A filter is then applied allowing one easier determination of the average value of the total sliding force F. Filtering is a process of selecting frequency components from a signal. A FFT filter performs filtering by using Fourier transforms to analyze the frequency components in the input signal. The filter used is a band block filter type, allowing only frequency components outside a specified range to pass and remove all frequencies within the chosen range, defined by the previous FFT analysis. Total force F is of the order of the sum of the frictional forces F_T.

In order to gather all information to obtain frictional and normal forces occurring during the experiments, it is necessary to use the complete experimental setup as presented in Figure 4.16. Four strain gauges glued on the load sensor and the dynamometer ring are connected to form four separate Wheastone quarter-bridges as already described in details in the previous section. Two other channels of the Lecroy oscilloscope are connected to the photodiodes with capability of registering initial and final velocities. The value of the current in the Wheatstone bridges recorded by means of the oscilloscopes is adjusted accounting for external conditions and possible external disturbances. It should be noted that the possible large oscillations may be caused not only by other experimental machines operating within close vicinity of the testing equipment used for this research but primarily due to the dynamic behavior of the load sensor.

The set of dynamic experimental approach for the Steel 1080 and VascoMax 300 tribopair consists of 8 attempts with low pressure between the tested specimens. No high pressure configuration was taken into account since the desired pressure for this problem was estimated by the computer simulations, conducted with the DADS software, and oscillates around $10MPa$ (see Hale [2010]). As previously mentioned, this approach maintained the normal pressure at the quasi constant level. In this scenario all experiments apart from the second trial (due to acquisition problems) were successful and delivered interesting and pioneer results.

Considering the distance between the two photodiodes ($80mm$) and the time during which the tip and the tale of the projectile is passing disconnecting the stream of light generated by both photodiodes it is possible to calculate the initial and final velocity (Table 4.7). The significant change of normal force F_N indicates the loss of the contact between tested specimens. This phenomenon indicates the return of the dynamometer ring to its initial configuration. This part enables one to compute the applied normal force during the experiment. The physical outputs of all eight experiments, i.e. the converted values to the units of forces, are presented in Figures 4.26 and 4.27. Note, that the negative values on these figures do not have any specific physical meaning. It is simply due to the particular setting of the oscilloscopes before the experiment begins. The conversion analysis is possible due to the calibration information. The results of the conversion analysis for this particular setup are presented in Table 4.8.

The filtered signals presented on Figures 4.26 and 4.27 are further analyzed. Mathematical averaging and smoothing techniques are very helpful in establishing normal and tangential force. Using these values a friction coefficient may be evaluated. This value however, cannot be considered for a constant sliding velocity. The accurate

Table 4.8: Conversion ratios between units of current and units of force

Channel #	Strain Gauge	Bridge Excitation	Gain	Calibration
1	G1	9.00	1000	Volt = 603 Newtons
2	G2	9.00	1000	Volt = 590 Newtons
3	G3	2.00	1000	Volt = 1575 Newtons
4	G4	2.00	1000	Volt = 1437 Newtons

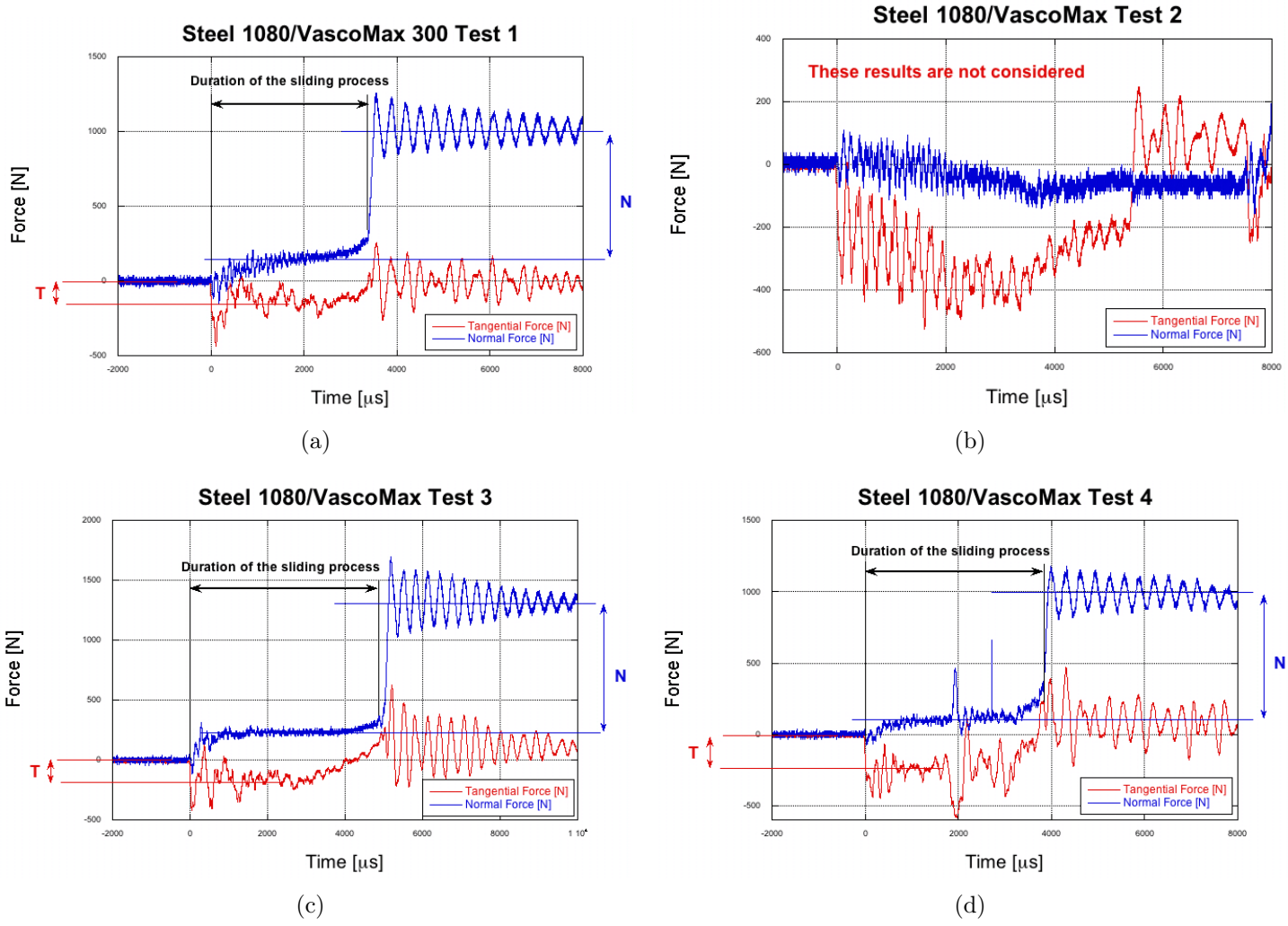

Figure 4.26: 4.26(a), 4.26(b), 4.26(c) and 4.26(d) present the experimental outputs recorded by oscilloscopes after launching the projectile from the middle of the tube (velocity calibration in Table 4.6). With the use of calibration information (Section 4.3.2) the values of the current were converted to the unit of force.

measurement of the position of the projectile could provide some information about the friction work and the energy consumption. The complete set of the results from this set of experiments is presented in Table 4.9 and the relation between initial impact velocity and calculated friction coefficient is presented in the Figure 4.28.

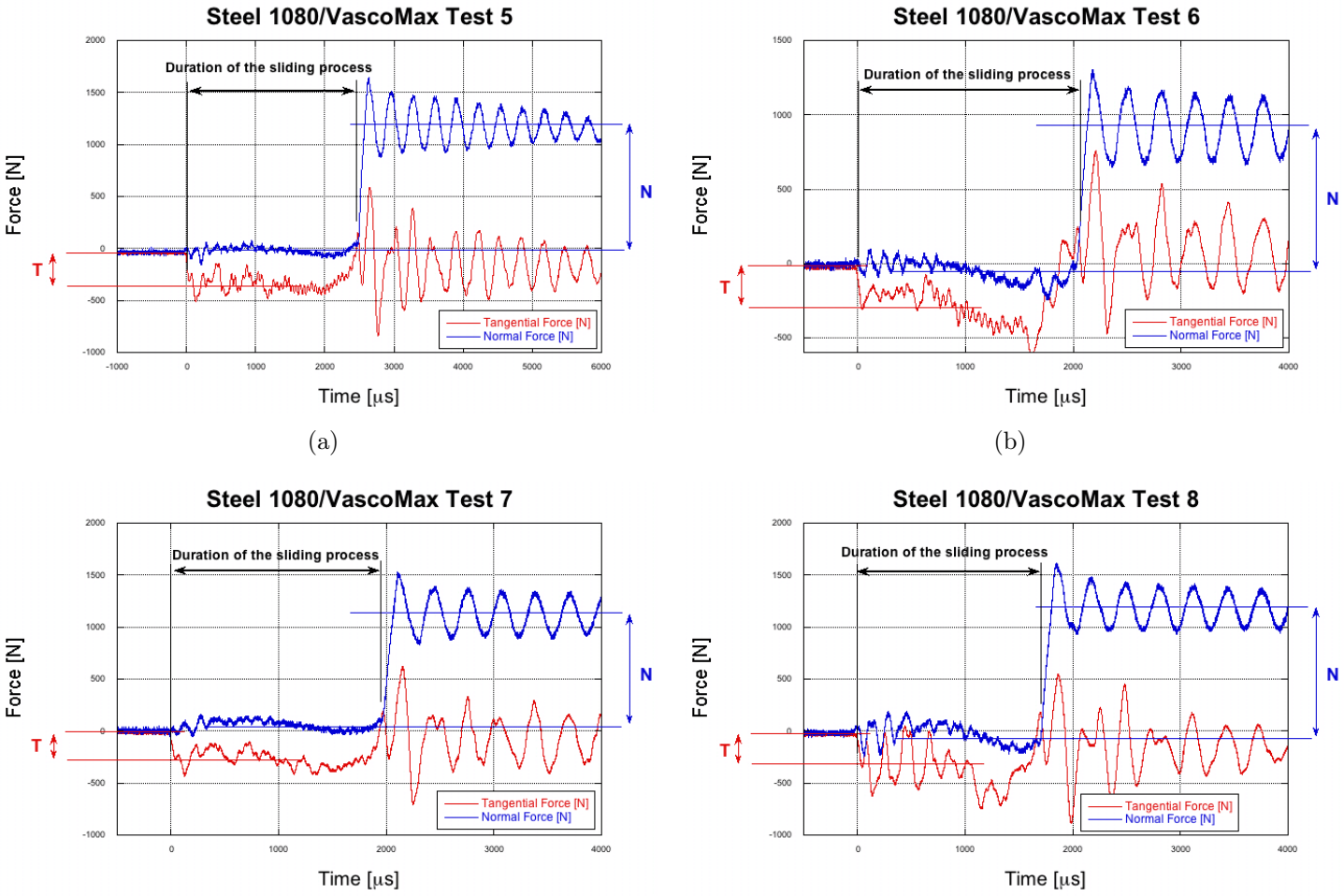

Figure 4.27: 4.27(a), 4.27(b), 4.27(c) and 4.27(d) present the experimental outputs recorded by oscilloscopes after launching the projectile from the beginning of the tube. With the use of calibration information (Section 4.3.2) the values of the current were converted to the unit of force.

Table 4.9: Experimental data for the low pressure elevated sliding velocity tests for the Steel 1080 on VascoMax 300 pair .

Test #	$\mathbf{V}_{12} = \mathbf{V}_{impact}$ $[m/s]$	$\mathbf{V}_{34}$ $[m/s]$	$\mathbf{V}_{drop}$ [%]	**Time duration of friction process** $[ms]$	$\mathbf{F}_N$ $[N]$	**normal pressure** $[MPa]$	$\mathbf{F}_T$ $[N]$	μ
1	26.49	15.85	40.2	3362	744	7.75	131	0.18
2	21.27	10.52	50.3	—	—	—	—	—
3	25.31	15.87	37.3	5000	688	7.17	212	0.31
4	30.76	21.05	31.6	3822	783	8.16	227	0.29
5	39.60	25.64	35.3	2487	1142	11.9	372	0.33
6	47.05	29.62	37.0	2020	958	10.0	263	0.27
7	47.05	29.62	37.0	1970	966	10.1	272	0.28
8	52.63	33.33	36.7	1703	1141	11.9	331	0.29

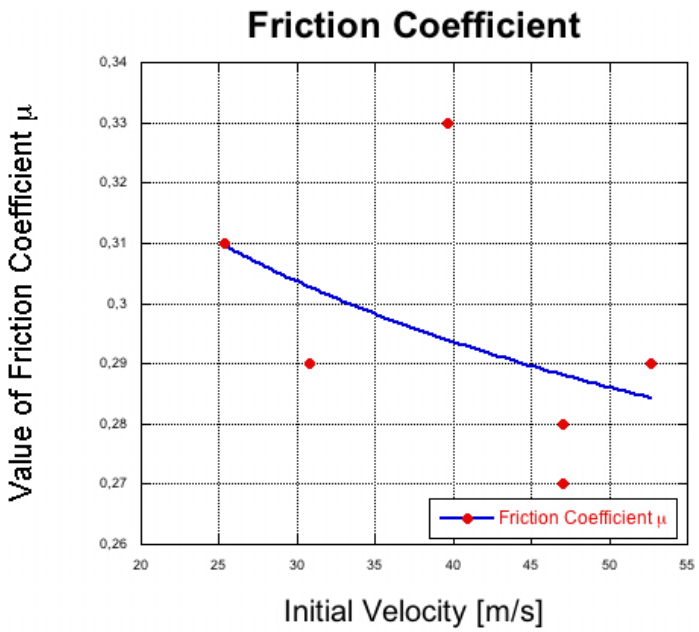

Figure 4.28: Final results of the dynamic experimental approach capturing the friction coefficients for different velocities for Steel 1080/VascoMax pair.

The obtained friction coefficients cannot be treated as the ones in the quasi-static approach, i.e. for the constant sliding velocity. It can be easily shown that the loss of kinetic energy due to the friction forces and sliding phenomenon is significant. For the velocity decrease in the range of 50% the kinetic energy decreases almost four times whereas for a velocity decrease of 30% the energy decreases two times. This is a very intuitive explanation presenting the amount of energy consumed only by friction. It can be noticed that the averaged values of the friction coefficient decrease and stays in good agreement with the literature, such as Lim et al. [1989], Oden and Martins [1984], but not as significantly as in case of quasi-static approach where the sliding velocity was kept constant during the entire process. The decrease of the friction coefficient as well as the roughness decrease would be more significant with the increase of sliding velocity if the loss of the kinetic energy would be low. It was clearly shown that for all the cases the value of the velocity strongly affects the roughness decrease. Moreover, the jumpy character of the friction coefficients is a result not only of purely statistical nature, i.e. insignificant amount of conducted tests, but also have its more physically based explanation in different velocity of shear band propagation due to existence of, so called, hot spots. This problem was elaborately presented and discussed in Glema et al. [2009].

In Table 4.10, the final comparison of the initial velocity, friction coefficient and roughness decrease is presented. It can be clearly seen that with the initial velocity increase the roughness decrease is larger. No other conclusions could be observed from such a limited number of tests. The percent wise drop of velocity oscillates between 30 and 40%. No particular relation between the drop of velocity, friction coefficient and roughness decrease was observed as is clearly visible in Table 4.10.

The loss of kinetic energy strongly affects obtained results. Despite the new

Table 4.10: The comparison of the average dry friction coefficient with the average roughness decrease and drop of velocity during the sliding process based on the measurements before and after the set of all dynamic experiments for Steel 1080/VascoMax pair.

$\mathbf{V}_{init}$ $[m/s]$	$\mathbf{V}_{final}$ $[m/s]$	$\mathbf{V}_{drop}$ [%]	**Roughness decrease** [%]	μ
26.49	15.85	40.2	10.39	0.18
21.27	10.52	50.3	11.45	—
25.31	15.87	37.3	3.99	0.31
30.76	21.05	31.6	10.97	0.29
39.60	25.64	35.3	8.19	0.33
47.05	29.62	37.0	12.83	0.27
47.05	29.62	37.0	15.93	0.28
52.63	33.33	36.7	20.55	0.29

frictional device measuring the dry friction coefficient with the use of linear sliding velocity which is the first device of its kind, there are still some imperfections and hurdles that require further attention. The device primarily introduced by Philippon et al. [2004] keeps on evolving. It is enhanced on the regular basis by the research team at ENIM, France, with the collaboration of the CSM (Computational Solid Mechanics) team at LSU. Both teams are slowly addressing the new ideas and possible innovative applications. The ultimate goal of this entire project is to design and manufacture the friction device capable of measuring the friction coefficient for constant linear sliding velocity reaching up to $300m/s$. Despite the fact that this device becomes more and more sophisticated it will still take plenty of joint effort for modifications and upgrades before the final goal will be achieved.

The experimental results obtained for the Steel 1080 on Steel VascoMax must be considered as the first experimental results, however the effects of the sliding velocity on the surface roughness changes was clearly observed and hence should be underlined. The obtained results as well as the experimental setup has tremendously evolved and is quite reliable at this time. Due to limited amount of tests the spread of the results may be high (Figure 4.28) however, with sufficient amount of tests the single results would converge to those obtained with the mathematical averaging techniques.

4.7 Conclusions Regarding Dry Friction Experiments

The motivation and evolution of this pioneering dry friction device is presented in this Chapter. The overview on the existing friction measuring techniques is given, clearly indicating the necessity for the development of the new frictional device capable of handling both linear sliding velocities and elevated normal pressure.

Further on, the detailed introduction to the frictional device is given. The device description, its design and application is presented. Problems such as static calibration

of both distinct parts supported by conducted numerical simulations is given and described in details. Further discussion, again supported by numerical analysis, validates the placing of the strain gauges and explains the problems of sensitivity of loading surface and cross-sensitivity. The entire experimental setup is then discussed explaining the mounting of the strain gauges located on the tribometer device, showing the configuration of the Wheatstone quarter-bridges, presenting the signal conditioning amplifier system and the digital oscilloscopes which all together create one uniform data acquisition system.

Following that the quasi-static and dynamic approaches are introduced. The frictional device is the same for both approaches and only the impacting devices are changing between hydraulic jack and a gas gun. The detailed description of both approaches is given describing both systems in detail.

The most important part of this chapter, the experimental results, is then given. In the quasi-static approach the obtained friction coefficients are in very good agreement with the theory presented in the literature. A significant decrease of the friction coefficient is demonstrated due to the sliding velocity increase and due to the roughness reduction. Moreover another interesting property is observed. In most of the cases the value of the friction coefficient strongly affects the roughness decrease. It can be clearly seen that except for one experiment all other experiments show the same tendency i.e. the lower the friction coefficient the lower the decrease in the roughness. This phenomenon indicates that the change in friction coefficient does not only depend on the sliding velocity or temperature but also is affected by the roughness of the sliding surface. The obtained results are very definitive and will be improved in the close future as the frictional device is further developed and enhanced.

Finally the results for the dynamic approach are presented and discussed. The determination of the technical details such as velocity measurement, friction and normal force calculation with the use of the calibration information and computing the final friction coefficient results in the complete experimental approach description. The filtered signals and smoothing mathematical techniques enables one to obtain precise values of normal and tangential forces. It is shown that the loss of kinetic energy due to friction forces and sliding phenomenon is significant. It is noticed that the values of the friction coefficient decrease and stay in good agreement with the existing literature, however, not as significant as in the case of the quasi-static approach where the sliding velocity was kept constant during the entire process. The decrease of the friction coefficient as well as the roughness decrease is more significant with the increase of the sliding velocity if the loss of the kinetic energy is low. It was clearly shown that for all the cases the increase of the velocity strongly affects the roughness decrease. No particular relation between the drop of the velocity, friction coefficient and roughness decrease is observed. The loss of kinetic energy strongly affects the obtained results. Despite this pioneering frictional device measuring the dry friction coefficient with the use of linear sliding velocity which is the first of its kind, still there are some imperfections and matters that require further attention.

Chapter 5

Theoretical Model

5.1 Introduction

There is an increasing need to improve the reliability and life of tribological components that are prone to severe contact stresses in engineering applications such as cutting tool for metals, gun tubes, engine exhaust valves, engine turbocharger components, rail gun environment, jet engine gear box splines and gears, and slippers on high-speed test track sleds. Severe contact stresses in such applications generate high temperatures and creates thermomechanical gouging and wear due to high velocity sliding between contacting materials. In order to better facilitate the design components and improve performance of these engineering applications, it is necessary to first understand the physical behavior of high speed environment that is made up of two major components in contact. This contact, at hypervelocity, can cause two important phenomena such as gauging and wear. These highly complex coupled problems require the solutions of three conservation equations such as mass, momentum, and energy, as well as the establishment of two relationships such as material constitutive model and equation of state.

A wide range of research is being performed at universities, national laboratories, and industry to identify materials, surface treatments, and to provide improved wear properties. However, most of this research is conducted under limited velocities and use the phenomenological models for the material evaluation (Andrews et al. [1997], Deters and Proksch [2005], Hardell and Prakash [2008], Hutchings [2006], Ireman [2005], Ireman et al. [2002, 2003], Ireman and Nguyen [2004], Kolmogorov [1996], Laursen [2002], Mishina [1998]). Several phenomenological models are used extensively in the simulation of large deformations of metals at high strain-rates and high temperatures. However, Banerjee [2007] showed, in his study on the evaluation of plastic flow stress of the phenomenological models, that the accuracies of those models vary significantly at high temperatures and under high-strain-rate conditions.

The field of research dealing with wear modeling is still very elusive yet there has been progress made in the understanding of many aspects of the wear mechanisms. The definition of the wear is stated in Hutchings [2006] as "the loss of material from a surface, transfer of material from one surface to another or movement of material within a single surface". This definition can be simplified as damage to a solid surface

generally involving progressive loss of material due to relative motion between that surface and a coating surface or substance. A close look at the activity leading to wear is at the dimensional level of $10nm$ where material structure can be seen as nanocrystalline. In addition this small scale phenomenon, local high spots (asperities), produce high stresses over short time scales in the order of micro seconds whereas strain rates are in the order of $10^4 - 10^7 s^{-1}$.

Another important aspect is the time dependent high temperature produced by the energy dissipation through the contact interaction. Due to both, high strain rates and temperature it is possible to observe in wear of metals the formation of adiabatic shear bands at the micro scale. This is clearly indicated by the roughness decrease presented in Chapter 3. Hardell and Prakash [2008] studied experimentally the friction and wear behaviors of the different tool steels sliding against Al Si-coated high-strength steel at elevated temperatures. They conducted two kinds of tests such as temperature ramp tests with continuously increasing temperature from 40 to 800^oC and constant temperature tests at 40^o, 400^o and 800^oC. Their results have shown that both the friction and wear of tool steel/Al-Si coated high-strength steel pairs are temperature dependent. Friction decreased with increasing temperature whereas wear of the steel tool increased with temperature. It is also clearly visible during the friction experiments and roughness measurements performed in this research. With the increase of velocity one can notice the increase of the temperature. It is clearly observable that with the increase of the velocity, and hence temperature, the friction coefficient decreases. The roughness increase is not that clearly noticeable with the velocity increase but it is due to the decrease of kinetic energy during the sliding process and hence decrease of sliding velocity. On the other hand, the Al–Si-coated high-strength steel showed significantly lower wear rates at 800^oC as compared to those at 40^o and 400^oC. Ko et al. [1997] presented the experimental research program aimed at studying wear problems based on concepts involving contact mechanics and fracture mechanics with the aid of the finite element techniques. They pointed out that under wet sliding conditions, wear debris trapped in the contact zone was more prone to be pulverized and compacted into a smooth and continuous third-body layer covering the wear scar. Another important conclusion of this study is that the coefficient of friction in the steady-state conditions is insensitive to the surface hardness and the initial surface finish, i.e. initial roughness. Ireman and co-workers Ireman [2005], Ireman et al. [2002, 2003], Ireman and Nguyen [2004] developed a continuum model that couples damage, wear and friction. The model was based on a continuum model including the gradient of the damage variable. The important feature of this model was to be within a thermodynamic framework, where it is assured that the principles of thermodynamics are satisfied. They shown qualitatively how the evolution of damage may influence the wear behavior and how damage may be initiated by the wear process.

Many of the features described here make it obvious that the highly complex nature of the wear problem cannot be solely treated by using macro scale phenomenological models. Therefore, a clear need exists for the development of a realistic and reliable physical based material model within the framework of multiscale modeling that can be utilized in severe contact stress applications. The major consideration is

to develop an experimental/theoretical model for the material constitutive behavior in order to better characterize and predict the internal failure surrounding the gouging and wear events. The verification and validation process of the proposed theory includes both: the verification of the proposed constitutive model required to ensure the developer, and especially the user, that the mechanics and numerical algorithms implemented are correct, and are consistent with the information in the documentation and calibration of the proposed model by specification of various material constant or constitutive parameters for each material (Section 6). In most cases values for these parameters are obtained by fitting the predicted material behavior to the laboratory data for various load paths and strain rates. The validation of the theory requires the comparisons with structural response experiments. These self obtained data are presented in Chapter 2. In this regard the proposed theory is implemented as user defined subroutine VUMAT in the explicit finite element code ABAQUS to analyze the structural response of the high speed sliding experiment between Steel 1080 and steel VascoMax 300. The description of these experiments performed in ENIM, France are presented in details in Chapter 4. The findings of this research effort will be invaluable in providing a multiscale material model and numerical procedure that will be used within a hydrocode to better facilitate the design components of the severe contact stress applications occurring in shoe/slipper configuration in HHSTT, New Mexico.

Severe contact stress problems generate high temperature and create thermomechanical gouging and wear due to high velocity sliding between contacting materials. In order to better facilitate the design components and improve performance of these engineering applications, it is necessary to better understand the physical behavior of high speed environment that is made up of two major components in contact (Voyiadjis, Lodygowski and Deliktas [2009]). Therefore, the major consideration is given to develop an experimental/theoretical model for the material constitutive behavior in order to better characterize and predict the internal failure surrounding the gouging and wear events.

In this research the investigation of the wear phenomenon is carried first, which later may be extended to incorporate gauging problems such as those occurring at HHSTT, New Mexico. The principle of virtual power is used by introducing the contributions from damage and its corresponding gradients as a measure of micro motion of damage within the bulk. In addition two internal state variables are introduced on the contact interface, one measuring the tangential slip and another measuring the wear. By using these internal state variables together with displacement and temperature, the constitutive model is formulated with state laws based on the free energies and the complimentary laws based on the dissipation potentials. The proposed theoretical model is implemented as user defined subroutine VUMAT in the explicit finite element code ABAQUS to analyze the structural response of the high speed sliding experiment between Steel and VascoMax steel as performed in ENIM, France (see Chapter 4). This model provides a potential feature for enabling one to relate the non-local continuum plasticity and damage of the bulk material to friction and wear at the contact interfaces. The findings of this research effort is invaluable in providing a multiscale material model and numerical procedure that will be used

within a hydrocode to better facilitate the design components of the severe contact stress applications.

5.2 Basic Constitutive Models for Impact Problems

Constitutive, or stress-strain laws, represent mathematical models that describe the macroscopic material behavior that results from the internal constitution of a material – description of how materials respond to various loadings. This is the most intensely researched field within solid mechanics because of its complexity and the importance of accurate constitutive models for practical engineering problems. To establish the constitutive relationship, the plasticity formulation takes the most important part since the behavior of most materials shows that most deformation occurs in the inelastic range even though the purely elastic deformation exists. The importance of constitutive laws has been enhanced significantly with the great increase in development and application of many modern computer-based technicques such as the finite element, finite difference, and boundary integral equation methods. In any engineering analysis, these constitutive laws play a crucial role providing reliability to the results obtained from the numerical prodedures. In this section the most commonly used constitutive formulations for dynamic and impact problems will be given along with the application examples.

Several constitutive relationships have been proposed for metallic materials under impact loading for use in computational mechanics that vary from being purely empirical to highly theoretical. The empirical models are based on available experimental observations, while the latter are based on the microscopic nature of the material. The multiaxial stress state of the material is usually expressed in terms of the equivalent (Huber von Mises) stress σ_{eq}, and many constitutive relations define this stress in terms of the accumulated plastic strain ε_{eq}, plastic strain rate $\dot{\varepsilon}_{eq}$ and temperature T as:

$$\sigma_{eq} = f(\varepsilon_{eq}, \dot{\varepsilon}_{eq}, T) \tag{5.1}$$

The form given in Eq. (5.1) can easily be adapted to most computer codes since it uses variables already available in most of the commercial codes. Numerous of constitutive relations of this type have been proposed by many researchers. Among them Perzyna [1963, 1966, 1971], Litonski [1977], Johnson and Cook [1983], Zerilli and Armstrong [1987], Rusinek and Klepaczko [2001].

Johnson and Cook [1983] proposed a phenomenological constitutive relation that has been widely used in impact analysis (Kay [2003], Cinnamon et al. [2006]) due to its simplicity in particular in practical engineering approaches. Recently it is the most common model provided by commercial finite element software. Being simple and straightforward it very often serves as a base for further development of more complicated relations accounting for more complex phenomena. Uncountable times it was used as a reference point while comparing the new numerical results created with use of modified or new constitutive relations (Zerilli and Armstrong [1987], Johnson and Holmquist [1988], Borvik et al. [2002] and many others). The expression proposed

back in Johnson and Cook [1983] is of a form:

$$\sigma_{eq} = (A + B(\varepsilon_{eq})^n)(1 + Cln\dot{\varepsilon}^*_{eq})(1 - T^{*m}) \tag{5.2}$$

however very often in the literature slightly modified version of this expression is available:

$$\sigma_{eq} = (A + B(\varepsilon_{eq})^n)(1 + \dot{\varepsilon}^*_{eq})^C(1 - T^{*m}) \tag{5.3}$$

where A, B, C, n and m are five material constants. The dimensionless strain rate is given by $\dot{\varepsilon}^*_{eq} = \frac{\dot{\varepsilon}_{eq}}{\dot{\varepsilon}_0}$, where $\dot{\varepsilon}_0$ is a user-defined reference strain rate. The homologous temperature T is defined by $T^{*m} = (T - T_r)(T_m - T_r)$, where the suffixes r and m indicate room and melting temperatures, respectively. The various phenomena such as strain hardening, strain-rate hardening and temperature softening are uncoupled in the constitutive relation, and the model is purely empirical. It should be noticed that Holmquist and Johnson (Holmquist and Johnson [1991]) also have proposed a modification of the strain-rate term in the original *Johnson-Cook* constitutive relation.

While the modified *Johnson-Cook* constitutive relation (Johnson and Cook [1983]) is purely empirical, the *Zerilli-Armstrong* constitutive relation (Zerilli and Armstrong [1987]) is based on dislocation theory. Each material structure type has a different constitutive behaviour based on dislocation mechanics for that particular structure. The formulation is based on the idea of thermally activated motion of dislocations, and three constitutive relations have been developed. Depending on the structure, the models have six to eight material constants: σ_a, A, B, n, α_0, α_1, β_0 and β_1. For BCC metals (body centered cubic metals, Figure 5.1 on the left), the dislocation motion is governed mainly by the interaction with the overall lattice potential. The thermally activated motion is not dependent on the strain, so the strain hardening becomes independent of strain rate and temperature:

$$\sigma_{eq} = \sigma_a + Bexp(-\beta T) + A\varepsilon^n_{eq} \tag{5.4}$$

where

$$\beta = \beta_0 - \beta_1 ln\dot{\varepsilon}_{eq} \tag{5.5}$$

For a FCC structure (face centered cubic metals, Figure 5.1 on the right), the thermally activated motion is produced by dislocation intersections which are leading to strain-rate and temperature dependent strain hardening

$$\sigma_{eq} = \sigma_a + A\varepsilon^n_{eq} exp(-\alpha T) \tag{5.6}$$

where

$$\alpha = \alpha_0 - \alpha_1 ln\dot{\varepsilon}_{eq} \tag{5.7}$$

In the original paper by Zerilli and Armstrong [1987] $n = \frac{1}{2}$. As HPC metals (hexagonal close-packed metals) have a stress-strain behavior falling somewhere in between BCC and FCC metals, the constitutive relation is described through a combination of the predominant interaction in the *bcc* structure and the predominant interaction in the FCC structure:

$$\sigma_{eq} = \sigma_a + Bexp(-\beta T) + A\varepsilon^n_{eq} exp(-\alpha T) \tag{5.8}$$

where α and β are described in Equations 5.7 and 5.5, respectively. This model is also applicable to steel alloys as well as HPC metals. By excluding some of the parameters one can either return to the original BCC model or the original FCC model. Since the *Zerilli-Armstrong* constitutive relation is theoretically based, it may seem reasonable to assume this relation to be a better choice than the *Johnson-Cook* (JC) ((Johnson and Cook [1983]) relation for this type of impact problems. However, *Zerilli-Armstrong* (ZA) (Zerilli and Armstrong [1987]) constitutive relation is of a more complex form and involves coupling between the different effects. Therefore this relation requires more experiments in order to determine the appropriate material constants.

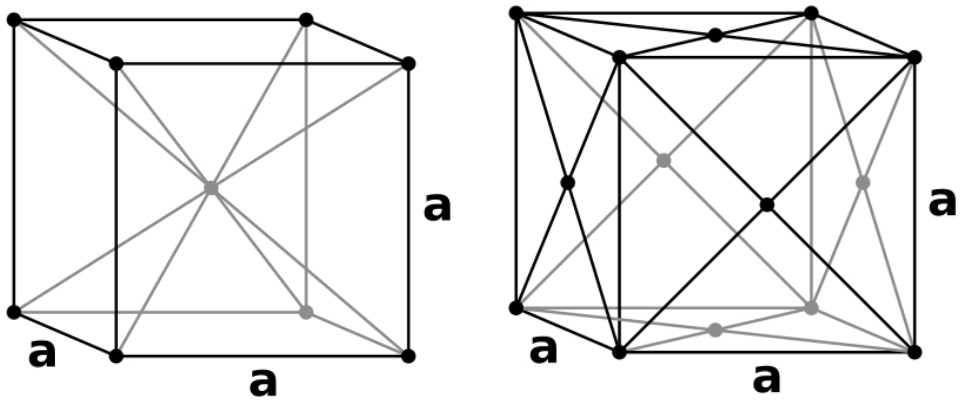

Figure 5.1: The *bcc* crystal structure on the left. The fcc crystal structure on the right

It is very important to notice that any kind of steel is an alloy, consist of more than one particular material however most of it's content is iron. For the simplicity in many researches steel is assumed to behave like a BCC metal. In order to address this problem it is necessary to introduce more advanced physically based theories as presented by Voyiadjis et al. [2003], Voyiadjis and Abed [2005], Voyiadjis et al. [2008] which also addresses some inconsistencies in the Zerilli-Armstrong model (Zerilli and Armstrong [1987]).

5.3 Different Approaches for Solving Impact Problems

More recently constitutive models that consider elastic-viscoplastic deformations at very high strain-rates have been proposed and employed to model high compression and high velocity impact phenomena. However many recent studies validate or base their assumptions on JC and ZA constitutive relations. In the work of Steinberg and Lund [1989] the new constitutive relation was developed which is capable to span wide range of strain rates $10^{-4}/s$ to $10^{6}/s$. This model is valid for the wide strain-rate range and accounts for pressure and temperature dependency of yield strength and shear modulus, work hardening, pressure dependent-melting as well as Bauschinger and strain-rate effect. The experimental validation is given and the successfully reproduced rate-dependent, shock-induced phenomena in tantalum are presented.

In the work of Nemat-Nasser and Isaacs [1997] it is shown that a combination of the long-range, plastic strain-dependent barrier and a short-range temperature- and strain rate dependent barrier provides a simple and effective description for the flow stress of tantalum and tantalum-tungsten alloys, over a broad range of strains, strain rates, and temperatures. These authors Introduced new constitutive models and validated the obtained results (experimental and numerical) with the use of JC and ZA models.

Meyers et al. [2002] used the ZA model in describing the response of metals at high-strain-rate deformation by incorporating dislocation dynamics, twining, grain-size, stacking fault, and solution hardening effects. They presented a mechanism for dislocation generation that provided a constitutive description of plastic deformation based on the theory of thermally activated processes.

A set of constitutive-microdamage equations are presented in the work of Eftis et al. [2003]. These relations can model shock compression, and the microdamage and fracture that can evolve following hypervelocity impact. The equations are appropriate for polycrystalline metals. For impact at a projectile velocity of 6.0km/s, numerical simulations are preformed that describe the impact of spherical soda-lime glass projectiles with aluminum 1100 rectangular target plates. Three ratios of the projectile diameter to the target thickness are chosen for the simulations, providing a wide range of damage features. The simulated impact damage is compared with experimental damage of corresponding test specimens, illustrating the capability of the model.

Voyiadjis and Abed [2005] and Abed and Voyiadjis [2005] in their works develop of microstructural physical based constitutive models in order to characterize the deformation behavior of body centered cubic (BCC) and face centered cubic (FCC) metals under different strain rates and temperatures. The concept of thermal activation energy as well as the dislocations interaction mechanisms is used in the derivation procedure taking into consideration the effect of the mobile dislocation density evolution on the flow stress of the deformed material. The derivation of the *Zerilli-Armstrong* (Zerilli and Armstrong [1987]) physical based model for both (BCC) and (FCC) metals is investigated and a number of modifications are incorporated such as the evolution of mobile dislocation density. The authors make a comparison between several experimental data obtained from the literature for tantalum (Ta), niobium (Nb), molybdenum, (Mo), vanadium (V) (BCC metals) and Oxygen Free High Conductivity ($OFHC$) Copper (Cu) (an FCC metal) for evaluating the proposed models. The observed improvements of the proposed models in particular for elevated temperatures are described and commented.

In the work of Rusinek et al. [2007] a very comprehensive research including both experimental and numerical analysis of the failure process of mild steel sheets subjected to normal impact by hemispherical projectiles is presented. The experiments have been performed using a direct impact technique based on Hopkinson tube (see Section 4.1) as a force measurement device. The test covered wide range of impact velocities accounting lubricated and dry friction conditions between specimen and projectile. The material behavior of impacted specimen was approximated by three different constitutive models in particular the JC relation. The authors obtained numerical results which showed good correlation with the experiments.

It is very important to mention that the classical rate-independent plasticity theory or local theory does not posses an intrinsic length-scale, which leads to numerical stability problems such as mesh dependency, in particular, for problems exhibiting strain localization phenomena. However, many regularization procedures were introduced in the literature to accommodate this problem for non-local plasticity, viscoplasticity and damage. Among them are viscoplastic models (Glema et al. [2000], Needleman [1988], Perzyna [1963], Wang et al. [1996]), thermal dissipation models (Le Monds and Needleman [1986]), non-local problems (Aifantis [1984], Bazant and Pijaudier-Cobot [1988], Voyiadjis and Dorgan [2001]) and gradient models (Aifantis [1992], Bassani [2001], De Borst and Sluys [1991], Fleck and Hutchinson [1997], Voyiadjis et al. [2003, 2001], Zbib and Aifantis [1992]).

5.4 Basic Framework for This Approach

5.4.1 Introduction

This section shows the basic concepts and framework for the theoretical model presented in the Section 5.6. The experimental data is retrieved from the various works of Hassan and his co-workers (Bari and Hassan [2001, 2002], Corona et al. [1996], Hassan et al. [1992], Hassan and Kyriakides [1992, 1994*a*,*b*]). First the derivation of the governing equations of the model are outlined. It was shown by Hassan and his co-workers that the important factor in multiaxial cyclic plasticity is the kinematic hardening formulation. The importance of incorporating a measure of that degree of *multiaxiality* is of a prime interest as well as the determination of the plastic strain increment.

Work-hardening behavior has been investigated first by Prager [1956], using a linear relation between the backstress and the plastic strain, and accounting for the drift of the yield surface along the plastic strain rate tensor. The theory presented in this approach is reasonably well for uniaxial tension and compression tests as well as capturing the stable cyclic loading. Yet, the perfect clousure of the backstress when dealing with non-symmetric stress-controlled tests does not alow such a model to account for ratchetting both in uniaxial and multiaxial tests. An improvement has been attempted by Mroz [1967, 1969], using multi-surface but keeping a linear relation between the backstress and the plastic strain for each part of the curve. Hence, the simulation of nonproportional cyclic stress-strain experiments has indeed been enhanced, but the model is still incapable of capturing any ratchetting rate.

At the same time, Armstrong and Frederick [1966] modified Prager's rule by adding a dynamic recovery part, since linear hardening was not efficient and not physically based. The model behaves particularly well in uniaxial tension or compression, but constantly overpredicts cyclic strain accumulation for cycli experiments with mean stress, slightly for uniaxial and dramatically for multiaxial, unless parameter C is determined from a multiaxial test.

Ziegler [1959] adopted a model stating that the direction of the yield surface drift is along the direction of the center of the current yield surface from the stress state. Phillips and Lee [1979] proposed a drift direction along the stress rate, after numerous experiments on some class of metals. These two models however, fail to predict biaxial

experiments, and moreover the Ziegler's model did not provide the ratchetting effect in the first cycle of the constant pressure axialy-strained vessel.

Chaboche et al. [1989] modified the Frederic-Armstrong model by using additive components that would take effect only for specific range of the plastic strain in order to be able to reproduce the backstress curve more accurately. This has been so far the most important improvement contributed to cyclic plasticity. Chaboche [1991] further modified his own model by modulating the last dynamic recovery that is shown to be the most important in ratchetting simulations. A threshold is incorporated that eliminates the dynamic recovery at high plastic strains. This rule is seen to be promising in simulating ratchetting experiments (Hassan and Kyriakides [1992, 1994*a*]).

Ohno and Wang [1993*a*,*b*] designed a model from the Frederic-Armstrong backstress using critical surfaces. The critical surface is supposed to provide the model with a memory effect, recording the path on a unit-radius-sphere. The model, along with the one presented by Chaboche, are one of the best know despite of their complexities. The Ohno model behaves well for uniaxial and small number of multiaxial cycles, but it then predicts rapid shakedown of the ratchetting when experiments show constant ratchetting rate after a first nonlinear part in early cycles. Voyiadjis and Sivakumar [1991*a*,*b*] and later Voyiadjis and Basuroychowdhury [1998] investigated two-surface formulation that combined Phillips and Lee [1979] and Tseng and Lee [1983], to account for experiments showing the direction of the drift of the yield surface to be in between the plastic strain rate and the stress rate. The uniaxial and multiaxial ratchetting is similar to the Frederick-Armstrong rule. However, their model gives more accurate orientation of the plastic strain rate direction.

The main problem in these models seems to be that none of them take into account the change in the shape of the yield surface. As has been shown by Bari and Hassan [2002], the direction of the plastic flow is most important in multiaxial experiments, hence all models try to compensate for this change in shape which they cannot take into account. However, Voyiadjis and his co-workers introduced several distortional yield models (Voyiadjis and Foroozesh [1990], Voyiadjis et al. [1995]). Intense research and deep investigation in this area led to the development of Frederic-Armstrong-Phillips-Chaboche model formulated and presented by Voyiadjis and Abu Al-Rub [2003]. The basic assumption on the Huber von Mises type plasticity, numerical algorithm is the base framework for both theoretical model presented in Section 5.6 and numerical simulation presented in Chapter 7.

5.4.2 Thermodynamically Consistent Constitutive Equations

In this section, the main concepts of elasticity and plasticity are outlined followed by the discussion and formulation on the kinematic and isotropic hardening models. Since the elasto-plastic response of anisotropic materials is considered here, the hardening in plasticity is introduced as a hidden independent internal state variables in the thermodynamic state potential. The Helmholtz free specific energy is considered as the thermodynamic state potential depending on both observable and internal state variable. The form of this potential in terms of the observable variable (T) and internal

state variables $(\boldsymbol{\varepsilon}^e, p, \boldsymbol{\alpha}^{(k)})$ can be given as:

$$\Psi = \hat{\Psi}(\varepsilon^e_{ij}, T, p, \alpha^k_{ij}) \tag{5.9}$$

where p and $\boldsymbol{\alpha}^{(k)}$ $(k = 1, 2, ..., M)$ variables characterize the isotropic and kinematic hardening flux variables in plasticity, respectively, and M being the number of desired kinematic hardening components. In Equation (5.9) T characterizes the temperature and $\boldsymbol{\varepsilon}^e$ is the elastic component of the strain tensor where for small strain problems an additive decomposition of the strain into an elastic and plastic part is assumed as:

$$\varepsilon_{ij} = \varepsilon^e_{ij} + \varepsilon^p_{ij} \tag{5.10}$$

where the superscripts e and p designate the elastic and plastic components, respectively. It is assumed for the elastic and plastic processes to be independent. The rate of the isotropic hardening variable of plasticity, $\dot{p}$, is defined as the effective plastic strain rate and expressed as:

$$\dot{p} = \sqrt{\frac{2}{3}\dot{\varepsilon}^p_{ij}\dot{\varepsilon}^p_{ij}} \tag{5.11}$$

The time derivative of the Equation (5.9) with respect to its internal state variables is given by:

$$\dot{\Psi} = \frac{\partial \Psi}{\partial \varepsilon^e_{ij}}\dot{\varepsilon}^e_{ij} + \frac{\partial \Psi}{\partial T}\dot{T} + \frac{\partial \Psi}{\partial p}\dot{p} + \sum_{k=1}^{M}\frac{\partial \Psi}{\partial \alpha^{(k)}_{ij}}\dot{\alpha}^{(k)}_{ij} \tag{5.12}$$

Form the second law of thermodynamics the Clausius-Duhem inequality is expressed as follows:

$$\sigma_{ij}\dot{\varepsilon_{ij}} - \rho(\dot{\Psi} + s\dot{T}) - q_i\frac{T_{,i}}{T} \geqslant 0 \tag{5.13}$$

where $\boldsymbol{\sigma}$ is the Cauchy stress tensor, ρ is the material density, q_i is the heat flux vector, $T_{,i}$ is the temperature gradient, s is the specific entropy per unit mass, and $\dot{\varepsilon}$ is the total strain rate. Substituting Equation (5.14) into Equation (5.13) yields the following expression:

$$\left(\sigma_{ij} - \rho\frac{\partial \Psi}{\partial \varepsilon^e_{ij}}\right)\dot{\varepsilon^e_{ij}} + \sigma_{ij}\dot{\varepsilon}^p_{ij} - \rho\left(\frac{\partial \Psi}{\partial T} + s\right)\dot{T} - \rho\frac{\partial \Psi}{\partial p}\dot{p} - \sum_{k=1}^{M}\rho\frac{\partial \Psi}{\partial \alpha^{(k)}_{ij}}\dot{\alpha^{(}_{ij}k) - q_i\frac{T_{,i}}{T} \geqslant 0 \tag{5.14}$$

from which the following thermodynamic state laws are obtained:

$$\sigma_{ij} = \rho\frac{\partial \Psi}{\partial \varepsilon^e_{ij}}; \quad s = -\frac{\partial \Psi}{\partial T}; \quad R = \rho\frac{\partial \Psi}{\partial p}; \quad X^{(k)}_{ij} = \rho\frac{\partial \Psi}{\partial \alpha^{(k)}_{ij}} \quad (k = 1, 2, ..., M) \tag{5.15}$$

Equation (5.15) describes the relation between the internal state variables and their associated thermodynamic conjugate forces, where $\boldsymbol{\sigma}$, s, R, and $\mathbf{X}^k$ $(k = 1, 2, ..., M)$ are the conjugate forces corresponding to the internal state variables $\boldsymbol{\varepsilon}^e$, T, p, and $\boldsymbol{\alpha}^{(k)}$, respectively.

Through this formulation a thermodynamic consistent model suitable for plasticity of ductile materials is obtained. The internal state variables are selected independently of one another. Moreover, one can assume decoupling between elastic and

hardening with the specific energy being decomposed into elastic and plastic parts as follows:

$$\Psi = \hat{\Psi} e(\varepsilon_{ij}^{e}) + \hat{\Psi}^{p}(p, \alpha_{ij}^{k}, T) \tag{5.16}$$

Hence, the Helmholtz free energy Ψ can be expressed in an analytical form of each of its internal state variables as follows:

$$\rho\Psi = \frac{1}{2}(\varepsilon_{ij} - \varepsilon_{ij}^{p}) E_{ijkl} (\varepsilon_{ij} - \varepsilon_{ij}^{p}) + \frac{1}{3} \sum_{k=1}^{M} C^{(k)} \alpha_{ij}^{(k)} \alpha_{ij}^{(k)} + Q(p + \frac{1}{b} e^{-bp}) \tag{5.17}$$

where $\mathbf{E}$ is the fourth-order elastic stiffness tensor and C, Q and b are material dependent constants.

The thermodynamic state laws can be obtained from the thermodynamic potential, Equation (5.17), by making use of Equation (5.15) as shown below:

$$\sigma_{ij} = E_{ijkl}(\varepsilon_{ij} - \varepsilon_{ij}^{p}) \tag{5.18}$$

$$X_{ij}^{(k)} = \frac{2}{3} C^{k} \alpha_{ij}^{(k)} \tag{5.19}$$

$$R = Q(1 - e^{-bp}) \tag{5.20}$$

where $\mathbf{X}^{(k)}$ $(k = 1, 2, ..., M)$ are the variables that describe the movement of the yield surface corresponding to the kinematic hardening, and R is the variable that describes the change in the size of the yield surface corresponding to the isotropic hardening.

It is further assumed that the kinematic hardening conjugate force $\mathbf{X}$, consists of M components proposed by Chaboche and Rousselier [1983], where each component is made to evolve independently, such that:

$$X_{ij} = \sum_{k=1}^{M} X_{ij}^{(k)} \tag{5.21}$$

It follows from Equation (5.19) that $\mathbf{X}$ can be rewritten as:

$$X_{ij} = \frac{2}{3} \sum_{k=1}^{M} C^{(k)} \alpha_{ij}^{(k)} \tag{5.22}$$

The Chaboche model has gained popularity and has been implemented into several commercial finite element codes in recent years. This model shows an excellent correlation with the experimental results for monotonic and cyclic loadings (Lemaitre and Chaboche [1990]).

In order to describe the evolution equation of the internal state variables, one needs to define first the plastic dissipation energy, Π, as a sum of the product of the associated variables with the corresponding flux variables in such a way that it can be given by substituting the thermodynamic state laws, Equation (5.15), back into the Clausius-Duhem inequality, Equation (5.14):

$$\Pi = \sigma_{ij} \dot{\varepsilon}_{ij}^{p} - \sum_{k=1}^{M} X_{ij}^{(k)} \dot{\alpha}_{ij}^{(k)} - R\dot{p} \geqslant 0 \tag{5.23}$$

Using the Legendre-Fenchel transformation of the plastic dissipation potential F, one can obtain the complementary laws in the form of the flux variables as function of the dual variables as follows:

$$F = F(\sigma_{ij}, X_{ij}^{(k)}, R; \varepsilon_{ij}^{e}, \alpha_{ij}^{(k)}, p) \geqslant 0 \tag{5.24}$$

In this work the evolution equation of the internal state variables are obtained through the use of the generalized normality rule of thermodynamics. In this regard the evolution laws for the plastic strain rate $\dot{\boldsymbol{\varepsilon}}^{p}$, the rate of the kinematic hardening flux $\dot{\boldsymbol{\alpha}}^{k}$ $(k = 1, 2, ..., M)$, and the rate of the isotropic hardening flux $\dot{p}$, can be obtained by utilizing the calculus of the function of several variables with the Lagrange multiplier $\dot{\lambda}$, in order to construct the objective function Ω in the following form:

$$\Omega = \Pi - \dot{\lambda} F \tag{5.25}$$

In order to obtain $\dot{\varepsilon}^{p}$, $\dot{\alpha}^{(k)}$, $\dot{p}$, the following conditions are used to maximize the objective function Ω, respectively:

$$\frac{\partial \Omega}{\partial \sigma_{ij}} = 0, \quad \frac{\partial \Omega}{\partial X_{ij}^{(k)}} = 0, \quad (k = 1, 2, ..., M), \quad and \quad \frac{\partial \Omega}{\partial R} = 0 \tag{5.26}$$

By Substituting Equation (5.25) into the above relations, the corresponding evolution laws, $\dot{\boldsymbol{\varepsilon}}^{p}$, $\dot{\boldsymbol{\alpha}}^{(k)}$, $\dot{p}$ are obtained, respectively, as follows:

$$\dot{\varepsilon}^{p} = \dot{\lambda} \frac{\partial F}{\partial \sigma_{ij}} \quad \dot{\alpha}_{ij}^{(k)} = -\dot{\lambda} \frac{\partial F}{\partial X_{ij}^{(k)}} \quad (k = 1, 2, ..., M) \quad \dot{p} = -\dot{\lambda} \frac{\partial F}{\partial R} \tag{5.27}$$

where $\dot{\lambda}$ is the multiplier of time-independent plasticity which will be determined later.

The next important step is the selection of the appropriate form of the dissipation potential F, in order to establish the desired constitutive equations that describe the mechanical behavior of the material.

5.4.3 Plastic Dissipation Potential and Evolution Equation

Nonlinear evolution equations for plastic hardening flow rules are required in order to obtain good correlation with the experimental results. In order to obtain a nonlinear kinematic hardening rule, the plastic potential function F, is chosen to be different than the yield function f. This is achieved by a proper selection of the analytical form of the potential that is defined in Equation (5.24). In order to be consistent and satisfy the generalized normality rule of thermodynamics, the following form of the plastic potential function F, is defined here as follows:

$$F = f + \frac{3}{4} \sum_{k=1}^{M} \frac{\gamma^{(k)}}{C^{(k)}} X_{ij}^{(k)} X_{ij}^{(k)} - \frac{3}{2} \frac{\dot{\sigma}_{ij}}{\dot{p}} \sum_{k=1}^{M} \frac{\beta^{(k)}}{C^{(k)}} X_{ij}^{(k)} \tag{5.28}$$

where γ and β are constants used to adjust the units of the equation. f is a yield function of the Huber von Mises type defined as follows:

$$f \equiv \sqrt{\frac{3}{2}(\tau_{ij} - X_{ij})(\tau_{ij} - X_{ij})} - (\sigma_{yp} + R) \leqslant 0 \tag{5.29}$$

where τ_{ij} is the deviatoric part of the Cauchy stress tensor $\boldsymbol{\sigma}$, $\tau_{ij} = \sigma_{ij} - \frac{1}{3}\delta_{ij}\sigma_{kk}$, X_{ij} is the backstress tensor or the kinematic hardening conjugate force, α_{ij} is the initial yield stress of the material under uniaxial tension and R is the variable defining the change in the size of the yield surface corresponding to isotropic hardening. The evolution equation of $\mathbf{X}$ and R are derived below.

The model presented here, introduced by Voyiadjis and Abu Al-Rub [2003], is based on several theories developed over the years. The second term on the right hand side of Equation (5.28) is included in order to retain the Armstrong and Frederick [1966] nonlinear kinematic hardening rule. The inclusion of the third term is motivated by the experimental observations of Phillips et al. [1974] and Phillips and Weng [1975] that show that the motion of the center of the yield surface in the stress space is directed between the gradient to the surface at the stress point and the stress rate direction at that point.

Introducing Equation (5.28) (plastic potential function) into Equation (5.27) (evolution laws) the following expressions are obtained:

$$\dot{\varepsilon}^p_{ij} = \dot{\lambda}\frac{\partial f}{\partial \tau_{ij}} = -\dot{\lambda}\frac{\partial f}{\partial X_{ij}} \tag{5.30}$$

$$\dot{p} = \dot{\lambda} \tag{5.31}$$

$$\dot{\alpha}^{(k)}_{ij} = -\dot{\lambda}\left(\frac{\partial f}{\partial X^{(k)}_{ij}} + \frac{3}{2}\frac{\gamma^{(k)}}{C^{(k)}}X^{(k)}_{ij} - \frac{3}{2}\frac{\dot{\sigma}_{ij}}{\dot{p}}\frac{\beta^{(k)}}{C^{(k)}}\right) \tag{5.32}$$

Now substituting Equations (5.29) and (5.31) into Equation (5.30) give the following expression for the evolution of the plastic strain tensor $\dot{\boldsymbol{\varepsilon}}^p$:

$$\dot{\varepsilon}^p_{ij} = \frac{3}{2}\left(\frac{\tau_{ij} - X_{ij}}{\sigma_{yp} + R}\right)\dot{p} \tag{5.33}$$

Utilizing the Equation (5.28) and (5.29) the following relation is also found:

$$\dot{\varepsilon}^p_{ij} = -\dot{\lambda}\frac{\partial f}{\partial X^{(k)}_{ij}} \tag{5.34}$$

Hence, substituting Equation (5.31) and (5.35) into Equation (5.32) yields the following expression for the evolution of the k-th term of the kinematic hardening flux variable, such that:

$$\dot{\alpha}^{(k)}_{ij} = \dot{\varepsilon}^p_{ij} - \frac{3\gamma^{(k)}}{2C^{(k)}}X^{(k)}_{ij}\dot{p} + \frac{3\beta^{(k)}}{2C^{(k)}}\dot{\sigma}_{ij} \quad (k = 1, 2, ..., M) \tag{5.35}$$

Further, taking the time derivative of the conjugate forces of Equations (5.18), (5.19), (5.20) and (5.22) yields the following relations:

$$\dot{\sigma}_{ij} = E_{ijkl}(\dot{\varepsilon}_{ij} - \dot{\varepsilon}^p_{ij}) \tag{5.36}$$

$$\dot{X}^{(k)}_{ij} = \frac{2}{3}C^k\dot{\alpha}^{(k)}_{ij} \quad (k = 1, 2, ..., M) \tag{5.37}$$

$$\dot{R} = bQ\dot{p}e^{-bp} \tag{5.38}$$

$$\dot{X}_{ij} = \frac{2}{3}\sum_{k=1}^{M} C^{(k)}\dot{\alpha}^{(k)}_{ij} \tag{5.39}$$

By substituting Equation (5.35) into Equation (5.37), the following evolution equation for the backstress tensor is obtained, such that:

$$\dot{X}_{ij}^{(k)} = \frac{2}{3} C^{(k)} \dot{\varepsilon}_{ij}^{p} - \gamma^{(k)} X_{ij}^{(k)} \dot{p} + \beta^{(k)} \dot{\sigma}_{ij} \tag{5.40}$$

$C^{(k)}$, $\gamma^{(k)}$ and $\beta^{(k)}$ are material constants to be calibrated from available experimental data.

Substitution of Equation (5.35) into Equation (5.39) results in a general expression for the evolution equation for the kinematic hardening rule, such that:

$$\dot{X}_{ij}^{(k)} = \left(\frac{2}{3} C^{(k)} \dot{\varepsilon}_{ij}^{p} + \beta^{(k)} \dot{\sigma}_{ij} \right) - \gamma^{(k)} X_{ij}^{(k)} \dot{p} \tag{5.41}$$

where

$$C = \sum_{k=1}^{M} C^{(k)}, \quad \gamma X_{ij} = \sum_{k=1}^{M} \gamma^{(k)} X_{ij}^{(k)}, \quad \beta = \sum_{k=1}^{M} \beta^{(k)}, \quad \dot{X}_{ij} = \sum_{k=1}^{M} \dot{X}_{ij}^{(k)} \tag{5.42}$$

The backstress is then used in conjunction with the bounding surface concept as proposed by Krieg [1975], Dafalias and Popov [1975, 1976] and modified by Voyiadjis and Basuroychowdhury [1998].

The derived kinematic hardening model (Equation (5.41)) shows that a new term is generated in the evolution equation of the backstress of the model by Armstrong and Frederick [1966]. If $\gamma = \beta = 0$, one retrieves the classical linear kinematic hardening rule (Prager [1956]). If $C = \gamma = 0$, this implies that the movement of the yield surface is along the direction of the stress rate as suggested by Phillips and Weng [1975]. If $C \neq 0$, $\beta \neq 0$, and $\gamma \neq 0$, one obtains the Voyiadjis-Kattan kinematic hardening rule (Voyiadjis and Kattan [1991, 1990]), which shows the motion of the center of the yield surface in the stress space is directed between the gradient to the surface at the stress point and the stress rate direction at that point. This confirms well to the experimental observations by Phillips and his co-workers (Phillips and Lee [1979], Phillips et al. [1974], Phillips and Weng [1975]). If $\gamma \neq 0$ a nonlinearity is introduced which imposes the introduction of the plastic potential as a modification of the yield function. This allows proper modeling of the cyclic behavior of many metals. Hence, the γ term determines the rate at which the saturation of the backstress decreases with increasing plastic strain. In addition, if $C \neq 0$, $\gamma \neq 0$, $\beta = 0$, one obtains the additive decomposition of the backstress into M-components of the Fredrick and Armstrong hardening type as proposed by Chaboche and Rousselier [1981, 1983]. Motivated by all of those models, the derived kinematic hardening rule is referred to as **FAPC** (Fredrick and Armstrong-Phillips-Chaboche) rule (Voyiadjis and Abu Al-Rub [2003]). All the corresponding kinematic hardening flow rules may be obtained as special cases of the current derived FAPC rule. In order to derive the evolution of the isotropic hardening function, a relation between R and p can be obtained from Equation (5.20), such that:

$$p = -\frac{1}{b} ln \left(1 - \frac{R}{Q} \right) \tag{5.43}$$

which upon substituting it into Equation 5.38 yields the following expression for $\dot{R}$, such that:

$$\dot{R} = b[Q - R]\dot{p} \tag{5.44}$$

This expression is similar to the evolution equation proposed by Chaboche [1991], Chaboche et al. [1989], where it is further proposed that the asymptotic value Q of the isotropic hardening is no longer constant but depends on the memory of deformation (q). In this work the form suggested by Chaboche [1991] is used, as follows:

$$Q = Q_M + (Q_0 - Q_M)e^{-2\mu q} \tag{5.45}$$

where Q_M, Q_0, and μ are material constants. The variable q stores one-half of the plastic strain amplitude in each cycle $\|\Delta\varepsilon^p/2\|$, which in turn depends on the total strain amplitude to which the material is subjected in cyclic loading.

5.4.4 The Elasto-Plastic Tangent Stiffness

The plastic flow requires that the representative point of the stress state does not leave the yield surface, which is termed the consistency condition in plasticity. In order to find the plastic multiplier, $\dot{\lambda}$, the consistency condition ($\dot{f} = 0$) is used, such that:

$$\dot{f} \equiv \frac{\partial f}{\partial \tau_{ij}}\dot{\tau_{ij}} + \sum_{k=1}^{M} \frac{\partial f}{\partial X_{ij}^{(k)}}\dot{X}_{ij}^{(k)} + \frac{\partial f}{\partial R}\dot{R} = 0 \tag{5.46}$$

However from the yield function in Equation (5.29), it is shown that $\partial f/\partial \boldsymbol{X}^{(k)} = \partial f/\partial \boldsymbol{X}$. Using this result along with Equation (5.21), the consistency condition can be written as follows:

$$\dot{f} \equiv \frac{\partial f}{\partial \tau_{ij}}\dot{\tau_{ij}} + \frac{\partial f}{\partial X_{ij}}\dot{X}_{ij}^{(k)} + \frac{\partial f}{\partial R}\dot{R} = 0 \tag{5.47}$$

Furthermore, the consistency condition maybe expressed as follows by using $\partial f/\partial \sigma = -\partial f/\partial \boldsymbol{X}$:

$$\frac{\partial f}{\partial \sigma_{ij}}(\dot{\sigma}_{ij} - \dot{X}_{ij}) - \dot{R} = 0 \tag{5.48}$$

Substitution of the evolution equations presented in Equations (5.36), (5.41), and (5.44) into Equation (5.48) gives the plastic multiplier, $\dot{\lambda}$, as follows:

$$\dot{\lambda} = \left\langle \frac{(1-\beta)}{H}\frac{\partial f}{\partial \sigma_{ij}}E_{ijkl}\dot{\varepsilon}_{kl} \right\rangle \tag{5.49}$$

where $\langle x \rangle$ denotes the MacAuley bracket defined as $\langle x \rangle = (x + |x|)/2$, which designates the positive part of x, and H is given by

$$H = C + \frac{\partial f}{\partial \sigma_{ij}}E_{ijkl}\frac{\partial f}{\partial \sigma_{kl}}(1-\beta) - \gamma X_{ij}\frac{\partial f}{\partial \sigma_{ij}} + b(Q - R) \tag{5.50}$$

The elasto-plastic tangent stiffness, $\boldsymbol{D}$, is defined by the rate relation, Equation 5.36, such that:

$$\dot{\sigma_{ij}} = D_{ijkl}\dot{\varepsilon}_{kl} \tag{5.51}$$

or

$$\dot{\sigma_{ij}} = E_{ijkl}(\dot{\varepsilon}_{ij} - \dot{\varepsilon}^p_{ij}) = E_{ijkl}\left(\dot{\varepsilon}_{kl} - \dot{\lambda}\frac{\partial f}{\partial \sigma_{kl}}\right) \tag{5.52}$$

with the following condition

$$D_{ijkl} = \begin{cases} E_{ijkl} & \text{if } f < 0 \text{ or } \dot{f} < 0 \ (\dot{\lambda} = 0,\ \dot{\lambda}f = 0) \\ E_{ijkl} - \frac{1-\beta}{H} - E_{ijrs}\frac{\partial f}{\partial \sigma_{rs}}E_{klmn}\frac{\partial f}{\partial \sigma_{mn}} & \text{if } f = 0 \text{ or } \dot{f} = 0 \ (\dot{\lambda} > 0,\ \dot{\lambda}f = 0) \end{cases} \tag{5.53}$$

The role of the viscoplastic or gradient term regularization in setting the character of the governing differential equations as well as introducing a length scale is of a great importance. The dynamic inelastic behavior cannot be characterized using the classical inelasticity theory as it does not incorporate material length scales and consequently it cannot predict mesh-insensitivities. However, the developed elasto-viscoinelasticity theory can be used for this purpose. Rate dependency (viscosity) allows the spatial difference operator in the governing equations to retain its ellipticity and the initial value problem (the Cauchy problem) is well-posed. This is very important particularly in the softening zone, where governing equation would become parabolic. The use of more advanced theory of viscoinelasticity gives the possibility to obtain mesh-insensitive results. Since the rate-independent inelastic response is obtained as a limit case when the relaxation time is equal to zero; hence, the theory of viscoinelasticity offers the localization limiter (or regularization procedure) for the solution of dynamic initial-boundary value problems under different type of loadings. Due to that one can use the theory of viscoinelasticity to predict mesh objective results in dynamic related problems.

Theoretically, for rate-independent solids localization is associated with loss of ellipticity of the equations governing incremental equilibrium. Furthermore, finite-element solutions exhibit inherent mesh dependence, and the minimum width of the band of localized deformation is given by the mesh spacing. This is clearly an undesirable state of affairs and stems from the character of the continuum equations. This drawback in the classical inelasticity arises from the fact that they do not posses any information about the size of the localization zone and, therefore, a length scale has to be incorporated. Therefore in Section (5.6) the theoretical model is by far more enhanced and the regularization process is taken care of by introducing the proper length scale as well as additional gradient terms. Due to this the governing equation does not only remains elliptical but also the solution is mesh independent.

5.5 Numerical Algorithm

In this section the numerical algorithm based on radial return method and backward Euler integration is presented. The radial return algorithm is now extensively used in Finite Element Codes (see Simo and Hughes [1998], Belytschko et al. [2000]).

5.5.1 Discretization of the Constitutive Equation

Using the backward Euler method to discretize the constitutive equations between the time steps n and $n+1$, Equation (5.29) becomes:

$$f^{(n+1)} \equiv \sqrt{\frac{3}{2}(\tau_{ij}^{(n+1)} - X_{ij}^{(n+1)})(\tau_{ij}^{(n+1)} - X_{ij}^{(n+1)})} - (\sigma_y + R^{(n+1)}) \leqslant 0 \tag{5.54}$$

and the evolution of the different state variables are obtained after discretization of Equations (5.11), (5.21), (5.30), (5.40), (5.44) such that:

$$X_{ij}^{(n+1)} = \sum_{k=1}^{M} (X_{ij}^{k})^{(n+1)} \tag{5.55}$$

$$(X_{ij}^{(k)})^{(n+1)} = (X_{ij}^{(k)})^{n} + \Delta X_{ij}^{(k)} \tag{5.56}$$

$$\Delta X_{ij}^{(k)} = \frac{2}{3} C^{(k)} \Delta \varepsilon_{ij}^{p} - \gamma^{k} X_{ij}^{(k)} \Delta p + \beta^{k} \Delta \sigma_{ij} \tag{5.57}$$

$$\Delta R = b(Q - R^{(n+1)}) \Delta p \tag{5.58}$$

$$\Delta \varepsilon_{ij}^{p} = \Delta \lambda N_{ij}^{(n+1)} \tag{5.59}$$

$$N_{ij}^{(n+1)} = \sqrt{\frac{3}{2}} \frac{\tau_{ij}^{(n+1)} - X_{ij}^{(n+1)}}{\|\tau_{kl}^{(n+1)} - X_{kl}^{(n+1)}\|} \tag{5.60}$$

$$\Delta \sigma_{ij} = E_{ijkl} \Delta \varepsilon_{kl}^{e} \tag{5.61}$$

$$\varepsilon_{ij}^{(n+1)} = \varepsilon_{ij}^{e,(n+1)} + \varepsilon_{ij}^{p,(n+1)} \tag{5.62}$$

It can be easily proved that for the Huber von Mises plasticity and yield criterion the increment of the plastic multiplier is equal to the increment of the equivalent plastic strain $\Delta\lambda = \Delta p$. If the internal variables at time $t = n$ are known and the increments in time and strain are given, then $\sigma_{ij}^{(n+1)}$ can be determined. ABAQUS deals with the numerical solver, however, the user with the help of the user subroutine (VUMAT) defines the constitutive relations capable of calculating the time and strain increments necessary for ABAQUS to obtain stress increment $\Delta\sigma_{ij}$, and finally stress in the next time step $\sigma_{ij}^{(n+1)}$ is calculated.

5.5.2 Return Mapping Algorithm

Let us consider that both, σ_{ij}^{n} and $\Delta\varepsilon_{ij}$ are given. One now proceeds to obtain the corresponding $\Delta\sigma$ that lies on the stress strain curve and satisfies the yield condition. However, the relation $\Delta\sigma_{ij} = E_{ijkl}\Delta\varepsilon_{kl}$ is valid only in the elastic domain. Hence stress-strain curve needs to be built while moving along it towards ε_{ij}^{final}. Therefore the algorithm is mainly divided into two different parts: the elastic predictor and the plastic corrector in order to remain on the yield surface.

5.5.2.1 Elastic Predictor

The elastic predictor is obtained by assuming the strain increment $\Delta\varepsilon_{ij}$ is totally elastic, therefore Equation (5.61) holds and one can write:

$$\sigma_{ij}^{tr} = \sigma_{ij}^{n} + E_{ijkl}\Delta\varepsilon_{kl} \tag{5.63}$$

For this trial stress state, the yield function is given by:

$$f^{(tr)} \equiv \sqrt{\frac{3}{2}(\tau_{ij}^{(tr)} - X_{ij}^{(n)})(\tau_{ij}^{(tr)} - X_{ij}^{(n)})} - (\sigma_y + R^{(n)}) \tag{5.64}$$

At this point three possible scenarios arise, which are briefly explained:

- The previous stress state is elastic, and remains elastic after the strain increment is applied, since $f^{tr} \leqslant 0$. This means that the stress state is still elastic at step $(n+1)$ or that the stress lies exactly on the yield surface. In this case no further calculations are needed which follows $\sigma_{ij}^{tr} = \sigma_{ij}^{(n+1)}$.
- The previous stress state is elastic, however, after the strain is applied, one obtains $f^{tr} > 0$, which means that the material is undergoing its first plastic deformation during this step. In order to smooth the transition from elastic to plastic domain, a special algorithm is developed that will be addressed later. However, one needs to return to the yield surface at this point, and $\sigma_{ij}^{tr} \neq \sigma_{ij}^{(n+1)}$.
- The previous stress state is plastic, and so is the next one, in which case $f^{tr} > 0$ and $\sigma_{ij}^{tr} \neq \sigma_{ij}^{(n+1)}$.

5.5.2.2 Plastic Corrector

Returning to the yield surface is the purpose of the radial return algorithm. This part of the algorithm is called the plastic corrector, because it will be shown later that the plastic strain is the key to the returning exactly on the yield surface. If $f^{(n+1)} > 0$, then σ_{ij}^{tr} cannot be accepted as the stress state at $n+1$, $\sigma_{ij}^{(n+1)}$, due to yielding. One needs to find a different expression for $\sigma_{ij}^{(n+1)}$ beginning with the Hook's law (Equations (5.61) and (5.62)), such that:

$$\begin{aligned}
\sigma_{ij}^{(n+1)} &= E_{ijkl}(\varepsilon_{kl}^{(n+1)} - \varepsilon_{kl}^{p,(n+1)}) \\
&= E_{ijkl}(\varepsilon_{kl}^{(n)} + \Delta\varepsilon_{ij} - \varepsilon_{kl}^{p,(n)} - \Delta\varepsilon_{ij}^{p}) \\
&= E_{ijkl}(\underbrace{\varepsilon_{kl}^{(n)} - \varepsilon_{kl}^{p,(n)}}_{\varepsilon_{kl}^{e,(n)}} + \Delta\varepsilon_{kl} - \Delta\varepsilon_{kl}^{p}) \\
&= E_{ijkl}(\varepsilon_{kl}^{e,(n)} + \Delta\varepsilon_{kl}) - E_{ijkl}\Delta\varepsilon_{kl}^{p} \\
&= \sigma_{ij}^{tr} - E_{ijkl}\Delta\varepsilon_{kl}^{p}
\end{aligned} \tag{5.65}$$

Therefore, one observes that in order to return to the yield surface and find $\sigma_{ij}^{(n+1)}$, the tensor $\Delta\varepsilon_{ij}^{p}$ is needed. Obtaining this tensor is the next step in the return mapping algorithm.

5.5.2.3 Calculation of $\Delta\sigma$

Exact formulation. Recalling Equation (5.61) one has to calculate $\Delta\lambda$ and $N_{ij}^{(n+1)}$. The term $\Delta\lambda$ is determined using a discretized consistency condition as stated earlier, and $N_{ij}^{(n+1)}$ is determined through a slight approximation. The Radial Return algorithm assumes that

$$N_{ij}^{(n+1)} = N_{ij}^{tr} \tag{5.66}$$

which is graphically demonstrated on the Figure 5.2. Most of the time $X^{tr} \neq X^{n+1}$ and τ^{tr}, X^{tr} and X^{n+1} are aligned nonetheless.

Hence, one needs to formulate the continuum consistency condition presented

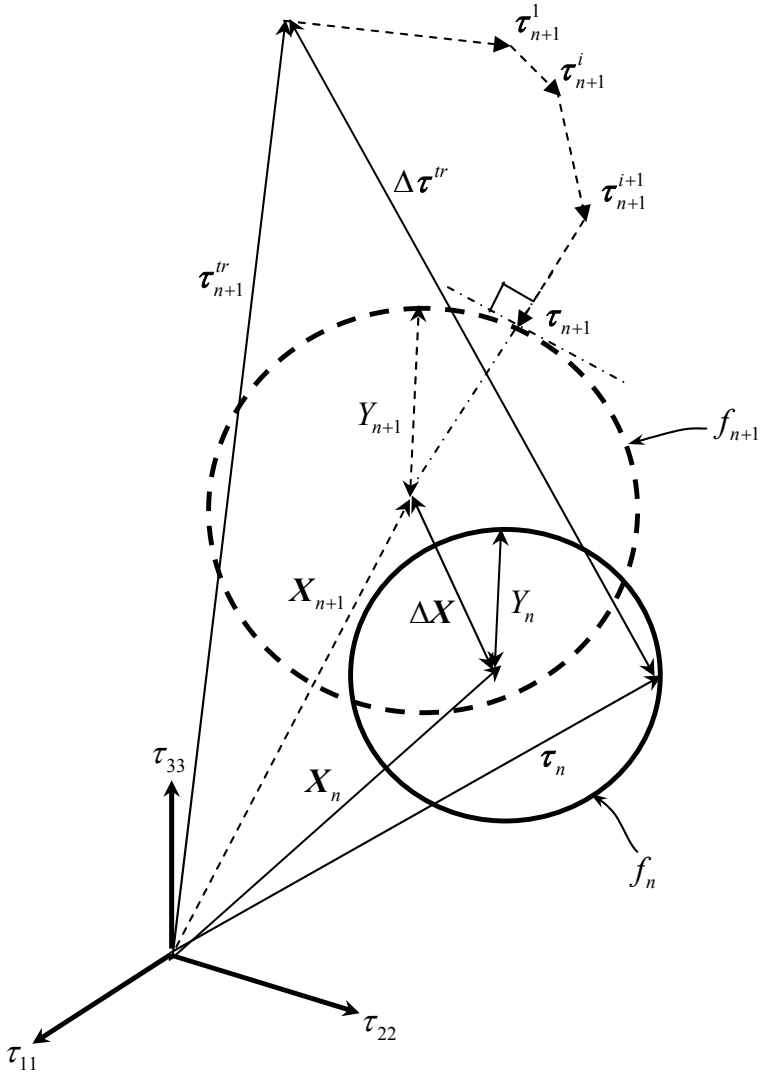

Figure 5.2: General idea and concept of the representation of the Elastic predictor and viscoplastic corrector algorithm.

in Equation (5.46). One can easily show that

$$\frac{\partial f}{\partial \sigma_{ij}} = \frac{\partial f}{\partial \tau_{ij}} = N_{ij} = -\frac{\partial f}{\partial X_{ij}} \ , \ \frac{\partial f}{\partial R} = 1 \tag{5.67}$$

Therefore, Equation (5.46) becomes

$$\dot{f} = N_{ij}(\dot{\sigma}_{ij} - \dot{X}_{ij}) - \dot{R} = 0 \tag{5.68}$$

Now, substituting Equations (5.40) and (5.44) into Equation (5.68), one obtains:

$$\dot{f} = 0 = N_{ij}\left(\dot{\sigma}_{ij} - \sum_{k=1}^{M}\left[\frac{2}{3}C^{(k)}\dot{\varepsilon}^{p}_{ij} - \gamma^{(k)}X^{(k)}_{ij}\dot{p} + \beta^{(k)}\dot{\sigma}_{ij}\right]\right) - b(Q-R)\dot{p} \tag{5.69}$$

In the same time, multiplying Equation (5.18) by N_{ij} enables one to write the following relation:

$$N_{ij}E_{ijkl}(\dot{\varepsilon}_{kl} - \dot{\varepsilon}^{p}_{kl}) = N_{ij}\sum_{k=1}^{M}\left[\frac{2}{3}C^{(k)}\dot{\varepsilon}^{p}_{ij} - \gamma^{(k)}X^{(k)}_{ij}\dot{p} + \beta^{(k)}\dot{\sigma}_{ij}\right] - b(Q-R)\dot{p} \tag{5.70}$$

Using the incremental form of the stresses in the elastic domain represented by Equation (5.30) is used along with Equation (5.31) together with the equilibrium between the increment of plastic multiplier $\dot{\lambda}$ and equivalent plastic strain $\dot{p}$ to obtain the expression for λ given as:

$$\dot{\lambda} = \frac{1}{H}\left(1 - \sum_{k=1}^{M}\beta^{(k)}\right)N^{tr}_{ij}E_{ijkl}\dot{\varepsilon}_{kl} \tag{5.71}$$

where H is the plastic modulus given by following relation:

$$\begin{aligned} H = &\left(1 - \sum_{k=1}^{M}\beta^{(k)}\right)N^{tr}_{ij}E_{ijkl}N^{tr}_{kl} + \frac{2}{3}\left(\sum_{k=1}^{M}C^{(k)}\right)N^{tr}_{ij}N^{tr}_{ij} \\ &- \left(\sum_{k=1}^{M}\gamma^{(k)}X^{(k)}_{ij}\right)N^{tr}_{ij}\sqrt{\frac{2}{3}N^{tr}_{ij}N^{tr}_{ij}} + b(Q-R)\sqrt{\frac{2}{3}N^{tr}_{ij}N^{tr}_{ij}} \end{aligned} \tag{5.72}$$

In the above expression for H, every state variable is taken at step n except N_{ij} which, as already discussed, is taken at the end of the elastic predictor step according to the radial return assumption. Having solved for $\dot{\lambda}$, one can now update every state variable at step $n+1$, but before that, one needs to express the increments of the state variables with respect to $\Delta\lambda$ and N_{ij}. For the sake of completeness, the final form of the discussed variables is expressed below:

$$\Delta\sigma_{ij} = E_{ijkl}\Delta\varepsilon^{e}_{kl} \tag{5.73}$$

$$\begin{aligned} \Delta X^{(k)}_{ij} = &\frac{\beta^{(k)}}{1+\gamma^{(k)}\Delta\lambda}E_{ijkl}\Delta\varepsilon_{kl} \\ &+ \frac{\beta^{(k)}}{1+\gamma^{(k)}\Delta\lambda}\left(\frac{2}{3}C^{(k)}N^{tr}_{ij} - \gamma^{(k)}X^{(k)}_{ij} - \beta^{(k)}E_{ijkl}N^{tr}_{kl}\right) \end{aligned} \tag{5.74}$$

$$\Delta R = \frac{b}{1+b\Delta\lambda}(Q - R^{n})\Delta\lambda \tag{5.75}$$

Solving a nonlinear scalar equation. As seen from Equation (5.65), one can readily obtain $\sigma_{ij}^{(n+1)}$ if $\Delta\varepsilon_{ij}^{p}$ is known. If one assumes isotropic elasticity, along with the various assumptions presented before, then the problem can be reduced to solving a nonlinear scalar equation.

Using the following notation for the deviatoric parts as follows:

$$\tau_{ij} = I_{ijkl}^{dev}\sigma_{kl} \tag{5.76}$$

one can rewrite Equation (5.65) in the deviatoric space in the following way, keeping in mind the assumption for the incompressible materials ($\frac{\partial f}{\partial \sigma_{ij}} = \frac{\partial f}{\partial \tau_{ij}}$):

$$\begin{aligned}
\tau_{ij}^{(n+1)} &= I_{ijkl}^{dev}(\sigma_{kl}^{tr} - E_{klmn}\Delta\varepsilon_{mn}^{p}) \\
&= I_{ijkl}^{dev}\sigma_{kl}^{tr} - I_{ijkl}^{dev}E_{klmn}\Delta\lambda N_{mn}^{(n+1)} \\
&= \tau_{ij}^{tr} - 2G\Delta\lambda I_{ijkl}^{dev}N_{kl}^{(n+1)} \\
&= \tau_{ij}^{tr} - 2G\Delta\lambda N_{ij}^{(n+1)}
\end{aligned} \tag{5.77}$$

where G is the shear modulus. Combining Equation (5.78) with Equation (5.55) yields:

$$\tau_{ij}^{(n+1)} - X_{ij}^{(n+1)} = \tau_{ij}^{tr} - 2G\Delta\lambda N_{ij}^{(n+1)} - \sum_{k=1}^{M}(X_{ij}^{(k)})^{(n+1)} \tag{5.78}$$

Using the Equation (5.74) and Equation (5.75) one can express $X_{ij}^{(n+1)}$ and $R^{(n+1)}$ only with respect to $\Delta\lambda$ and $N_{ij}^{(n+1)}$:

$$\begin{aligned}
{}^{(n+1)}X_{ij}^{(k)} &= A_{n+1}^{(k)}({}^{(n)}X_{ij}^{(k)} + \left(\frac{2}{3}C^{(k)} + 2G\beta^{(k)} + 2G\beta^{(k)}\right)\Delta\lambda N_{ij}^{(n+1)} \\
&\quad - \beta^{(k)}E_{ijkl}\Delta\varepsilon_{kl}
\end{aligned} \tag{5.79}$$

$$R^{(n+1)} = B_{n+1}(R^{(n)} + bQ\Delta\lambda) \tag{5.80}$$

where

$$A_{(n+1)}^{(k)} = \frac{1}{1+\gamma^{(k)}\Delta\lambda}, \quad B_{n+1} = \frac{1}{1+b\Delta\lambda} \tag{5.81}$$

Substituting Equation (5.79) into Equation (5.78), one finds the following expression:

$$\begin{aligned}
\tau_{ij}^{(n+1)} - X_{ij}^{(n+1)} = \tau_{ij}^{tr} &- \sum_{k=1}^{M} A_{n+1}^{(k)\,n}X_{ij}^{(k)} - \Bigg[2G\left(1 + \sum_{k=1}^{M}A_{n+1}^{M}A_{n+1}^{(k)}\beta^{(k)}\right) \\
&+ \frac{2}{3}\sum_{k=1}^{M}A_{n+1}^{(k)}C^{(k)}\Bigg]\Delta\lambda N_{ij}^{(n+1)} \\
&+ \left(\sum_{k=1}^{M}A_{n+1}^{(k)}\beta^{(k)}\right)E_{ijkl}\Delta\varepsilon_{kl}
\end{aligned} \tag{5.82}$$

Recalling Equation (5.60) it is easy to show that:

$$\tau_{ij} - X_{ij} = \sqrt{\frac{2}{3}}\|\tau_{kl} - X_{kl}\|N_{ij} \tag{5.83}$$

and substituting it into Equation (5.82), one obtains:

$$\begin{aligned}\sqrt{\frac{2}{3}}\left\|\tau_{kl}^{(n+1)} - X_{kl}^{(n+1)}\right\|N_{ij}^{(n+1)} = \sqrt{\frac{2}{3}}\left\|\tau_{kl}^{tr} - \sum_{k=1}^{M} A_{n+1}^{(k)\,n} X_{kl}^{(k)}\right\|N_{ij}^{tr} \\ - \left[2G\left(1 + \sum_{k=1}^{M} A_{n+1}^{(k)}\beta^{(k)}\right) + \frac{2}{3}\sum_{k=1}^{M} A_{n+1}^{(k)}C^{(k)}\right]\Delta\lambda N_{ij}^{(n+1)} \\ + \left(\sum_{k=1}^{M} A_{n+1}^{(k)}\beta^{(k)}\right)E_{ijkl}\Delta\varepsilon_{kl}\end{aligned} \tag{5.84}$$

Taking the tensor product of above the equation with $N^{(n+1)}$, and recalling the backward Euler hypothesis of $N_{ij}^{(n+1)} = N_{ij}^{tr}$ as well as well known result from the Huber von Mises plasticity $N_{ij}N_{ij} = \frac{3}{2}$, one obtains:

$$\begin{aligned}\sqrt{\frac{2}{3}}\left\|\tau_{kl}^{(n+1)} - X_{kl}^{(n+1)}\right\| = \sqrt{\frac{3}{2}}\left\|\tau_{ij}^{tr} - \sum_{k=1}^{M} A_{n+1}^{(k)\,n} X_{ij}^{(k)}\right\| \\ - \left[3G\left(1 + \sum_{k=1}^{M} A_{n+1}^{(k)}\beta^{(k)}\right) + \sum_{k=1}^{M} A_{n+1}^{(k)}C^{(k)}\right]\Delta\lambda \\ + \frac{3}{2}\left(\sum_{k=1}^{M} A_{n+1}^{(k)}\beta^{(k)}\right)N_{ij}^{tr}E_{ijkl}\Delta\varepsilon_{kl}\end{aligned} \tag{5.85}$$

The left hand side of Equation (5.85) is identified with the Huber von Mises yield function in Equation (5.29), and hence one can write:

$$Y^{tr} - \left[3G\left(1 + \sum_{k=1}^{M} A_{n+1}^{(k)}\beta^{(k)}\right) + \sum_{k=1}^{M} A_{n+1}^{(k)}C^{(k)}\right]\Delta\lambda + \frac{3}{2}\left(\sum_{k=1}^{M} A_{n+1}^{(k)}\beta^{(k)}\right)N_{ij}^{tr}E_{ijkl}\Delta\varepsilon_{kl} = \sigma_{yp} + R^{n+1} \tag{5.86}$$

where $Y^{tr} = \sqrt{\frac{3}{2}}\left\|\tau_{ij}^{tr} - \sum_{k=1}^{M} A_{n+1}^{(k)\,n} X_{ij}^{(k)}\right\|$. Equation (5.86) represents the algorithmic consistency condition for the considered internal state variables.

In order to solve the above nonlinear equation, one turns it into a scalar quantity

equal to zero in the following form:

$$\begin{aligned} W(\Delta\lambda) = Y^{tr} &- \left[3G\left(1+\sum_{k=1}^{M} A_{n+1}^{(k)}\beta^{(k)}\right) + \sum_{k=1}^{M} A_{n+1}^{(k)} C^{(k)}\right]\Delta\lambda \\ &+ \frac{3}{2}\left(\sum_{k=1}^{M} A_{n+1}^{(k)}\beta^{(k)}\right) N_{ij}^{tr} E_{ijkl}\Delta\varepsilon_{kl} \\ &- \left[\sigma_{yp} + B_{n+1}(R^n + bQ\Delta\lambda)\right] \\ &\equiv 0 \end{aligned} \tag{5.87}$$

Both $A_{n+1}^{(k)}$ and B_{n+1} are functions of $\Delta\lambda$. It can be shown that the nonlinear Equation (5.87) is a convex function of $\Delta\lambda$. Therefore, a Newton-Raphson method can be applied to solve it. The procedure to find the correct $\Delta\lambda$ that will yield $W = 0$ within the tolerance is based on the relation

$$\Delta\lambda_{i+1} = \Delta\lambda_i - \frac{W(\Delta\lambda_i)}{W'(\Delta\lambda_i)} \tag{5.88}$$

where W' is the gradient of W with respect to $\Delta\lambda_i$.

5.5.3 Smoothing of the Elastic-plastic Transition

The first initial plastic strain, if it appears during the loading, then it may be in between two iterations. Therefore, for each iteration before plasticity occurs, it is necessary to compute the highest elastic strain. If σ_{n+1}^c denotes the stress state at the point where the assumed stress path comes into contact with the initial yield surface, then one can writes:

$$\sigma_{n+1}^c = \sigma_n + \beta\Delta\sigma^{tr}; \quad 0 \leqslant \beta \leqslant 1 \tag{5.89}$$

where $\Delta\sigma_{ij}^{tr} = E_{ijkl}\Delta\varepsilon_{kl}$ is the trial stress and $\beta\sigma^{tr}$ is the amount of the stress needed to go from the previous stress state to the initial yielding surface. In this, $\beta\varepsilon$ is the portion of strain increment at which the plastic behavior is first encountered. Using the yield function to solve for β, $f(\sigma_{n+1}^c, X_n, R_n) = 0$, leads to a quadratic expression that can be approximated by a simple linear interpolation in f (Nayak and Zienkiewicz [1972]):

$$\beta = -\frac{f_0}{f_1 - f_0} \tag{5.90}$$

where $f_0 = f(\sigma_n, X_n, R_n) < 0$ and $f_1 = f(\sigma_{n+1}^{tr}, X_n, R_n) > 0$.

However, the nonlinearity of the current function f gives a small difference for β and a corrected value can be found using the following formula:

$$\beta = -\frac{f_0}{f_1 - f_0} - \frac{f_2}{N_{n+1}^{tr} : \Delta\sigma_{n+1}^{tr}} \tag{5.91}$$

where $f_2 = f(\sigma^c_{n+1}, X_n, R_n) \neq 0$.

The portion of the strain increment for elastoplastic deformation is given by $(1-\beta)\Delta\varepsilon_{ij}$ and is used as the new strain increment to compute the 'plastic stress'. Thus, the remaining part of the trial stress increment is given by $(1-\beta)E_{ijkl}\Delta\varepsilon_{kl}$.

5.6 Theoretical Model Statement

The theoretical model presented in this section is considered within a thermodynamic framework, where it is assured that the principles of thermodynamics are satisfied. Therefore, the virtual power relations are first defined and the principle of the virtual power along with the variational formulation are used to developed governing differential equations and their boundary conditions of the proposed theory. The principle of virtual power used by Voyiadjis and Deliktas [2009*a*,*b*] is different than those used previously by Voyiadjis and co-workers (Abu Al-Rub and Voyiadjis [2004, 2006], Abu Al-Rub et al. [2007], Dorgan and Voyiadjis [2003, 2006], Voyiadjis and Abu Al-Rub [2007], Voyiadjis and Almasri [2008], Voyiadjis and Abu Al-Rub [2005], Voyiadjis et al. [2003], Voyiadjis and Deliktas [2000*a*,*b*]), Gudmundson and co-workers (Fredriksson and Gudmundson [2005, 2007], Gudmundson [2004], Nygards and Gudmundson [2004], Tjernlund et al. [2006]), Willis and coworkers (Aifantis and Willis [2006, 2005], Fleck and Willis [2009*a*,*b*]) and, Gurtin and coworkers (Anand et al. [2005], Bittencourt et al. [2003], Cermelli et al. [2004], Gurtin [2000, 2004], Gurtin and Anand [2009], Gurtin and Needleman [2005]) where the principal of virtual power is modified by adding the contributions from damage and its corresponding gradients as a measure of micro motion of damage within the bulk. In addition two internal state variables are introduced on the contact interface, one measuring the tangential slip and another measuring the wear. By using these internal state variables together with displacements and temperature, the constitutive model is formulated with state laws based on the free energies and the complimentary laws based on the dissipation potentials. This model provides a potential feature for enabling one to relate the nonlocal continuum plasticity and damage of the bulk material to friction and wear at the contact interfaces.

One now defines a region $V \subset \Re^d$ $(d = 2, 3)$ with a piecewise smooth boundary Ω that occupies a continuously deformable body (Figure 5.3).

The boundary Ω is divided into three disjoint parts; Ω_t is the part of the boundary where the tractions are prescribed whereas the displacements are prescribed at the boundary Ω_u, and the unilateral contact interface is defined by the boundary Ω_c. The contact interfaces surface energy is considered as material boundary following the concept of Voyiadjis and Deliktas [2009*c*] and enhanced by the pioneering work of Fremond and Nedjar [1996] and its corresponding modification by Ireman et al. [2003].

The modified form of the internal virtual power is expressed in terms of the plastic strain, plastic strain gradient, damage and its gradients contribute to work per unit volume. Since contact interface plays an important role for the plastic deformation at the micron scale therefore it is further assumed that if internal work develops in the region occupied by the damaged elastic plastic continuum, an additional contribution

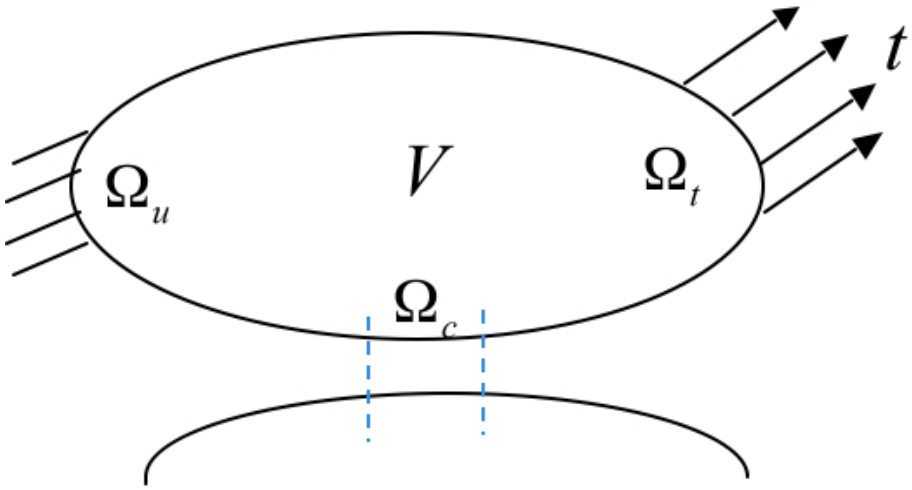

Figure 5.3: A deformable body with unilateral contact

to the internal virtual work should be considered. This new formulation does not only provide the internal interface energies but also introduces two additional internal state variables for the contact surfaces.

One of these new state variables measures friction and the other measures the wear. By using these internal state variables together with displacement and temperature, the constitutive model is formulated as usual by state laws utilizing free energies and complimentary laws based on the dissipation potentials. In the light of the above discussion the structure of the internal virtual power, P_{int} is, therefore, expressed in terms of energy contribution of volume and interface as follows

$$\begin{aligned} P_{int} &= \int_V (\sigma_{ij}\dot{\varepsilon}^e_{ij} + X_{ij}\dot{\varepsilon}^p_{ij} + S_{ijk}\dot{\varepsilon}^p_{ij,k} + Y_{ij}\dot{\phi}_{ij} + \Gamma_{ijk}\dot{\phi}_{ij,k})dV \\ &+ \int_{\Omega_c} \Re^c_{ij}\dot{\varepsilon}^{cp}_{ij}d\Omega_c + \int_{\Omega_c} \aleph^c_{ij}\dot{\phi}^c_{ij}d\Omega_c + \int_{\Omega_c} Q^c\dot{\varphi}^c d\Omega_c + \int_{\Omega_c} q^c_i v^t_i d\Omega_c \end{aligned} \tag{5.92}$$

The superscripts are used to describe c for contact, n for normal and t for traction. σ_{ij} is the Cauchy stress and p_i is the contact traction vector. The tensor X_{ij} is the driving stress work conjugate to the plastic strain, $\dot{\varepsilon}^p_{ij}$, and S_{ijk} is the micro-stress work conjugate to the plastic strain gradient, $\dot{\varepsilon}^p_{ij,k}$. The tensors Y_{ij} and Γ_{ijk} are the damage related internal forces work conjugate to ϕ_{ij} and $\phi_{ij,k}$, respectively. $\Re_{ij}$ and $\aleph_{ij}$ are internal forces conjugate to $\dot{\varepsilon}^{cp}_{ij}$ and $\dot{\phi}^c_{ij}$, respectively. Furthermore, q_i and Q^c are the contact forces associated to the friction slip, v^t_i and the wear φ^c. The external virtual power is expressed as

$$P_{ext} = \int_{\Omega_t} t_i v_i d\Omega_t + \int_{\Omega_t} m^t_{ij}\dot{\varepsilon}^p_{ij}d\Omega_t + \int_{\Omega_t} \eta_{ij} m^t_{ij}\dot{\phi}_{ij}d\Omega_t \tag{5.93}$$

t_i is the surface traction vector. m^t_{ij} and η^t_{ij} are the micro-traction tensors work conjugate $\dot{\varepsilon}^p_{ij}$ and $\dot{\phi}_{ij}$ respectively. The non local differential equation of the flow rule

and its relevant nonstandard boundary condition are derived by using the principle of virtual power $P_{ext} - P_{int} = 0$ and imposing integration by parts, the divergence theorem, and keeping in mind that $\sigma_{ij}\dot{\varepsilon}^p_{ij} = \tau_{ij}\dot{\varepsilon}^p_{ij}$ and $\dot{\varepsilon}^e_{ij} = \dot{\varepsilon}_{ij} - \dot{\varepsilon}^p_{ij}$ one can obtain the following relation

$$\begin{aligned}
&\int_{\Omega_t}(t_i - \sigma_{ij}n_j)v_i d\Omega_t + \int_{\Omega_t}(-p_i - \sigma_{ij}n_j)v_i d\Omega_t + \\
&\int_V(\sigma_{ij,j})v_i dV + \int_V(\tau_{ij} - X_{ij} + S_{ijk,k}\dot{\varepsilon}^p_{ij}dV + \int_V(\Gamma_{ijk,k} - Y_{ij})\dot{\psi}_{ij}dV + \\
&\int_{\Omega_t}(-\Re_{ik} - S_{ijk}n_k)\dot{\varepsilon}^{pI}_{ij}d\Omega_I + \int_{\Omega_t}(-\aleph_{ij} - \Gamma_{ijk}n_k)\dot{\phi}^I_{ij}d\Omega_I + \\
&\int_{\Omega_c}Q^c\dot{\varphi}d\Omega_c + \int_{\Omega_c}q_i v^t_i d\Omega_c + \int_{\Omega_t}(m_{ik} - S_{ijk}n_k)\dot{\varepsilon}^{pc}_{ij}d\Omega_c + \\
&\int_{\Omega_t}(\eta_{ij} - \Gamma_{ijk}n_k)\dot{\phi}_{ij}d\Omega_t = 0
\end{aligned} \tag{5.94}$$

From Equation (5.94) one can obtain the new balance laws associated to plasticity, damage, friction, and wear as follows

$$\left.\begin{array}{c}\sigma_{ij,j} = 0 \\ \tau_{ij} = X_{ij} + S_{ijk,k} \\ \Gamma_{ijk,k} - Y_{ij} = 0\end{array}\right\} \text{ in } V \tag{5.95}$$

Standard and non standard boundary conditions on the boundaries, Ω_t and Ω_c are obtained respectively:

$$\left.\begin{array}{c}t_i = \sigma_{ij}n_j \\ m_{ij} - S_{ijk}n_k = 0 \\ \eta_{ij} - \Gamma_{ijk}n_k = 0\end{array}\right\} \text{ on } \Omega_t \tag{5.96}$$

$$\left.\begin{array}{c}\Re_{ik} + S_{ijk}n_k = 0 \\ \aleph_{ij} + \Gamma_{ijk}n_k = 0 \\ \\ -p_i = \sigma_{ij}n_j \\ Q^c = 0 \\ q_i = 0\end{array}\right\} \text{ on } \Omega_c \tag{5.97}$$

Consequently forces Q^c and q_i are simply equal to zero. These boundary conditions at the contact interface create a coupling between damage and wear. In addition to balance laws one needs constitutive assumptions that couple internal forces to the state variables. A general framework for the thermodynamical forces and state variables are obtained by using free energies and the dissipation potential in the style of the standard material. Such approach is consistent with satisfying the second law of thermodynamics

which states that the rate change of total free energy must be less than the external power i.e. $\dot{\Upsilon} \leqslant P_{ext}$, where the total free energy can be defined as

$$\Upsilon = \int_V \rho\psi_v dV + \int_{\Omega_c} \psi_c d\Omega_c \tag{5.98}$$

where ρ is the mass density, $\psi_v = \psi_v(\varepsilon^e, \varepsilon^p, \phi, \nabla\varepsilon^p, \nabla\phi)$ is the free energy in volume, V, and $\psi_c = \psi_c(u, v, \varphi, \varepsilon^p, \phi)$ is the free energy on the contact surface Ω_c. Thermodynamical Clausius-Duhem inequalities for both the bulk and the contact interface are given as follows

$$\begin{aligned} \Phi_v = \sigma : \dot{\varepsilon}^e + X : \dot{\varepsilon}^p + Y : \dot{\phi} + S : \nabla\dot{\varepsilon}^p + \Gamma : \nabla\dot{\phi} - \rho\dot{\psi}_v \geqslant 0 \\ \Phi_c = p : \dot{u} + \Re\dot{\varepsilon}^p + \aleph\dot{\phi} + q_t\dot{v} + Q\dot{\varphi}_c \geqslant 0 \end{aligned} \tag{5.99}$$

By taking the time derivatives of the Helmholtz free energy and substituting them into Equation (5.99) one can obtain the definitions for the thermodynamical forces as

$$\begin{aligned} X_{ij} = \rho\frac{\partial\psi_v}{\partial\varepsilon^p_{ij}}, \quad S_{ijk} = \rho\frac{\partial\psi_v}{\partial\varepsilon^p_{ij,k}}, \quad Y_{ij} = \rho\frac{\partial\psi_v}{\partial\phi_{ij}}, \quad \Gamma_{ikj} = \rho\frac{\partial\psi_v}{\partial\phi_{ij,k}}, \\ \aleph_{ij} = \rho\frac{\partial\psi_c}{\partial\phi^c_{ij}}, \quad \Re_{ij} = \rho\frac{\partial\psi_c}{\partial\varepsilon^{cp}_{ij}}, \quad q_i = \rho\frac{\partial\psi_c}{\partial v_i}, \quad Q = \rho\frac{\partial\psi_c}{\partial\varphi} \end{aligned} \tag{5.100}$$

and the dissipation inequalities are given by

$$\begin{aligned} X_{ij}\dot{\varepsilon}^p_{ij} + S_{ijk}\dot{\varepsilon}^p_{ij,k} + Y_{ij}\dot{\phi}_{ij} + \Gamma_{ijk} \geqslant 0 \\ \Re\dot{\varepsilon}^{cp}_{ij} + \aleph_{ij}\dot{\phi}^c_{ij} + Q\dot{\varepsilon} + q_i\dot{v}_i \geqslant 0 \end{aligned} \tag{5.101}$$

The dissipation inequalities given by Equation (5.101) are also defined as the rate of conservation of work into heat. In classical plasticity it is usual to specify some evolution equation for the plastic strain and then to define the rate of dissipation or rate of plastic work as inner product of stress with rate of plastic strain (Hill [1948]). Alternatively as suggested by Ziegler [1983] and later by Ziegler and Wehrli [1987] a possibly maximum rate of the dissipation is first postulated and then the evolution equation of the state variables are derived from the rate of dissipation function. This line of thought was followed by Rajagopal and Srinivasa [2004] in a somewhat modified way. To the contrary of Ziegler's work where he first postulated certain orthogonally conditions that implies a criterion of maximum rate of dissipation under certain circumstances, however, Rajagopal and Srinivasa [2004] started directly by assuming a physically plausible maximum rate of dissipation condition and then showed later that certain normality and convexity conditions are necessary and sufficient for the assumed dissipation. As it is clearly seen from the above discussion and from Equations (5.100) and (5.101) for the complete modeling of the inelastic behavior of the material the constitutive equations must be specified for the stress response as well as for the evolution of the internal state variables. The evolution of the state variables can be obtained from the maximum principles of rate of dissipation where it is assumed that for any given values of flux variable, the values of the dissipations are uniquely defined and

correspond to the maximum principles by assuming the existence of dissipation potentials for both bulk material and interface (Coleman and Gurtin [1967], Coleman and Noll [1963]). The corresponding maximum principles for bulk material and interface can be written as follows: the number of unknown internal state variables of the model can be determined by solving the constraint minimization problem of the energy dissipation by using the Lagrange multiplier method and assuming the existence of the constraint surfaces for plasticity and damage respectively (Voyiadjis, Deliktas, Faghihi and Lodygowski [2009]) such that

$$\begin{gathered}\dot{\varepsilon}^p_{ij} = \dot{\lambda}^p \frac{\partial f^p}{\partial X_{ij}}, \quad \dot{\varepsilon}^p_{ij,k} = \dot{\lambda}^p \frac{\partial f^p}{\partial S_{ijk}}, \quad \dot{\phi}_{ij} = \dot{\lambda}^d \frac{\partial g}{\partial Y_{ij}}, \quad \dot{\phi}_{ij,k} = \dot{\lambda}^d \frac{\partial g}{\partial \Gamma_{ijk}}, \\ \dot{\varepsilon}^{cp}_{ij} = \dot{\lambda}^{cp} \frac{\partial f^{cp}}{\partial \Re_{ij}}, \quad \dot{\phi}^c_{ij} = \dot{\lambda}^{cp} \frac{\partial g^c}{\partial \aleph_{ij}}, \\ \dot{\varphi} = \dot{\lambda}^c \frac{\partial f^c}{\partial Q}, \quad \dot{v}_i = \dot{\lambda}^c \frac{\partial f^c}{\partial q_i}, \\ \dot{\lambda}^p f^p = 0, \quad \dot{\lambda}^{cp} f^{cp} = 0, \quad \dot{\lambda}^d g = 0, \quad \dot{\lambda}^{cd} g^c = 0, \quad \dot{\lambda}^c f^c = 0\end{gathered} \tag{5.102}$$

Equations (5.102) provide enough equations for the unique solution for the described inelastic material behavior with the unknowns, $(\dot{\varepsilon}^p_{ij}, \dot{\varepsilon}^p_{ij,k}, \dot{\phi}_{ij}.\dot{\phi}_{ij,k}, \dot{\varepsilon}^{cp}_{ij}, \dot{\phi}^c_{ij}, \dot{\varphi}, \dot{v}_i, \dot{\lambda}^p, \dot{\lambda}^{cp}, \dot{\lambda}^d, \dot{\lambda}^{cd}, \dot{\lambda}^c)$. From Equations (5.100) and (5.102) it is clear that the thermodynamically consistent formulation will be complete once the thermodynamically admissible functional forms are described for the following scalar thermodynamic potentials, $(\Psi_v, \psi^c, f^p, f^{cp}, g, g^c$ and $f^c)$.

5.6.1 Defnitions of the Thermodynamically Admissible Potentials

Free Energies

In this section specific forms of the free energies and the dissipation potentials are proposed in order to develop a model for strain gradient plasticity theory. The choice of the form of the thermodynamic potentials is very important since it constitutes the bases in deriving the constitutive equations. The complexity of any model is directly determined by the form of the thermodynamic potentials and by the number of conjugate pair of variables. In this work, however, one postulates the following general definition of energy:

Functional form of the free energy for the grain core material

$$\Psi_v = \frac{1}{2}\varepsilon^e_{ij} E(\phi)_{ijkl} \varepsilon^e_{ij} + \frac{1}{2} a_1 \varepsilon^p_{ij} \varepsilon^p_{ij} + \frac{1}{2} a_2 \varepsilon^p_{ij,k} \varepsilon^p_{ij,k} + \frac{1}{2} a_3 \phi_{ij} \phi_{ij} + \frac{1}{2} a_4 \phi_{ij,k} \phi_{ij,k} \tag{5.103}$$

where a_i are the material related constants. The contact interface energy coupling damage with wear is given as

$$\Psi_c = \frac{1}{2}\beta_p \varepsilon^{cp}_{ij} \varepsilon^{cp}_{ij} + \alpha_p \frac{1}{2} ||\varepsilon^{cp}_{ij}|| + k\varphi \frac{1}{2} ||\delta_{ij} - \phi^c_{ij}|| + \psi^c_C(u_n, \varphi) + \psi^c_D(u_t, v) \tag{5.104}$$

where β_p characterizes the interfacial hardening of the material due to plasticity while α_p describes the interfacial yield strength and, k is the wear coefficient. These interfacial material parameters can be determined via dislocation transfer phenomena where their physical justification are made from observations obtained by nanoindentation tests with the boundary layer at the contact region as well as from the roughness measurements introduced in Chapter 3. The expressions for the free energies ψ_C^c and ψ_D^c are given as follows

$$\begin{aligned}
\psi_C^c(u_n,\varphi)\begin{cases} I_C(u_n,\theta) & \begin{cases} 0 & u_n-\varphi\leqslant 0 \\ \infty & u_n-\varphi>0 \end{cases} \\ \text{or} & \frac{1}{2}\epsilon_N\langle\varphi\rangle^2 \end{cases} \\
\psi_D^c(u_t,v)\begin{cases} I_D(u_t,v) & \begin{cases} 0 & u_t-v=0 \\ \infty & u_t-v\neq 0 \end{cases} \\ \text{or} & \frac{1}{2}||\mathbf{I}-\phi||\kappa||\mathbf{v}|| \end{cases}
\end{aligned} \tag{5.105}$$

where κ represents how slip influences the dislocation density on the contact surface. Equation (5.96) admits two alternative forms; the first one where the stiffness associated with contact interface is infinite. In this case the indicator functions such as I_C and I_D are used to define the interface condition. The second case is where a finite compliance of the interface is considered. From Equations (5.103)-(5.105) one can retrieve the definitions of the energetic part of the thermodynamic forces in the bulk as follows

$$\begin{aligned}
X_{ij} &= \rho\frac{\partial\Psi_V}{\partial\varepsilon_{ij}^p} = a_1\varepsilon_{ij}^p \\
S_{ijk} &= \rho\frac{\partial\Psi_V}{\partial\varepsilon_{ij,k}^p} = a_2\varepsilon_{ij,k}^p \\
Y_{ij} &= \rho\frac{\partial\Psi_V}{\partial\phi_{ij}} = \frac{1}{2}\varepsilon_{ij}^e E(\phi)_{ijkl}\varepsilon_{ij}^e + a_3\phi_{ij} \\
\Gamma_{ijk} &= \rho\frac{\partial\Psi_V}{\partial\phi_{ij,k}} = a_4\phi_{ij,k}
\end{aligned} \tag{5.106}$$

while for the interfaces

$$\begin{aligned}
\Re_{ij} &= \rho\frac{\partial\Psi^c}{\partial\varepsilon_{ij}^{cp}} = \beta_p\varepsilon_{ij}^{cp} - \alpha_p\frac{\varepsilon_{ij}^{cp}}{||\varepsilon_{ij}^{cp}||} \\
\aleph_{ij} &= \rho\frac{\partial\Psi^c}{\partial\phi_{ij}^c} = -k\varphi\frac{\phi_{ij}^c}{||\delta_{ij}-\phi_{ij}^c||}
\end{aligned} \tag{5.107}$$

For the contact surface the normal stress can be obtained by taking the partial derivatives of the first term in Equation (5.105). This leads to the classical Kuhn-Tucker conditions for the interface such as

$$Q\geqslant 0;\quad \varphi\leqslant 0;\quad Q\varphi=0 \tag{5.108}$$

which describes the case where no stored energy due to normal stresses is considered. However, if one considers to use alternatively the derivative of the quadratic form given

by the second term of Equation (5.105) the normal traction force can be obtained as

$$Q = \frac{\partial \psi^c}{\partial \varphi} = \epsilon_N \langle \varphi \rangle \tag{5.109}$$

and the interface friction force can be obtained by taking the partial derivatives of Equation (5.104)

$$q_i = \frac{\partial \psi^c}{\partial v_i} = \kappa ||\mathbf{I} - \phi|| \frac{\mathbf{v}}{||\mathbf{v}||} \tag{5.110}$$

The condition for the interface contacting surface, S^c_{rs} is defined as fully dissipative. Therefore, the dual form of the dissipation potential for the contact surface is defined as

$$\Phi^c = ||\boldsymbol{\xi}|| + kQp_n \leqslant \mu p_n + kp_n \left(1 - \frac{1}{2}(1-\varphi)^2\right) \tag{5.111}$$

where $\boldsymbol{\xi} = \mathbf{p_t} - \mathbf{q}$, the term μ is the well known coefficient of friction and k is the wear coefficient. The mathematical aspects of the thermodynamic consideration of the theory for such form of the free and dissipation potential, dissipation inequalities, minimization problem and existence of the uniqueness of the solutions are discussed in detail in recent studies of Voyiadjis, Deliktas, Lodygowski, Palazotto, Philippon, Rusinek, Faure and Chevrier [2009*b*]. Here, the governing equations for the coupled viscoplastic damage behavior are defined by the following constitutive relations:

$$\begin{gathered}
\dot{\sigma}_{ij} = E_{ijkl}(\phi)\dot{\varepsilon}^e_{kl} - A_{ijkl}\dot{\phi}_{kl} - \beta_{ij}\dot{T} \\
\tau_{ij} = X_{ij} + S_{ijk,k} \\
f^p = (X_{ij}X_{ij} + l^2 S_{ijk}S_{ijk})^{1/2} - \sigma_f(\dot{E}^p) \leqslant 0 \\
\dot{\lambda}^p \geqslant 0 \quad \dot{\lambda}^p f^p \geqslant 0 \quad \dot{\lambda}^p \dot{f}^p = 0 \\
g = (Y_{ij}Y_{ij} + l^2 \Gamma_{ijk}\Gamma_{ijk})^{1/2} - \sigma(\dot{\kappa}) \leqslant 0 \\
\Gamma_{ijk,k} - Y_{ij} = 0 \\
\dot{\lambda}^d \geqslant 0 \quad \dot{\lambda}^d g \geqslant 0 \quad \dot{\lambda}^d \dot{g} = 0
\end{gathered} \tag{5.112}$$

and for the contact interface

$$\begin{gathered}
\Re_{ik} + S_{ijk} n_k = 0 \\
f^c = (\Re_{ij}\Re_{ij})^{1/2} - \sigma_f(\dot{\varepsilon}^p) \leqslant 0 \\
\dot{\lambda}^{cp} \geqslant 0 \quad \dot{\lambda}^{cp} f^c \geqslant 0 \quad \dot{\lambda}^{cp}\dot{f}^c = 0 \\
\aleph_{ij} + \Gamma_{ijk} n_k = 0 \\
g^c = (\aleph_{ij}\aleph_{ij})^{1/2} - \sigma(\dot{\phi}) \leqslant 0 \\
\dot{\lambda}^{cd} \geqslant 0 \quad \dot{\lambda}^{cd} g^c \geqslant 0 \quad \dot{\lambda}^{cd}\dot{g}^c = 0
\end{gathered} \tag{5.113}$$

where $\dot{E}^p$ is the effective nonlocal flow rate such that $\dot{E}^p = \sqrt{\dot{\varepsilon}^p_{ij}\dot{\varepsilon}^p_{ij} + l_p^2 \dot{\varepsilon}^p_{ij,k}\dot{\varepsilon}^p_{ij,k}}$. The nonlocal effective damage flow rate is defined by $\dot{\kappa} = \sqrt{\dot{\phi}^p_{ij}\dot{\phi}^p_{ij} + l_d^2 \dot{\phi}^p_{ij,k}\dot{\phi}^p_{ij,k}}$. In this constitutive model two characteristic material length scales are introduced. They are the plastic length scale, l_p and the damage length scale, l_d respectively. Length scales may be obtained experimentally as demonstrated by Voyiadjis and co-workers (Almasri and Voyiadjis [2010], Voyiadjis, Almasri and Park [2010], Voyiadjis and Peters [2010]). The term α is the thermal expansion coefficient, $\dot{T}$ is the rate of absolute temperature, $\mathbf{I}$ is the second order identity tensor, and $\mathbf{A}$ is the fourth order tensor defined as

$$A_{ijkl} = \left[- \frac{\partial E_{ijmn}}{\partial M^{-1}_{abuv}} \varepsilon^e_{mn} + \frac{\partial \beta_{ij}}{\partial M^{-1}_{abuv}} (T - T_r) \right] \frac{\partial M^{-1}_{abuv}}{\partial \phi_{kl}} \tag{5.114}$$

The fourth order damage tensor $\mathbf{M}$ is function of the second order damage tensor, $\boldsymbol{\phi}$. Its explicit form can be found in the works of Voyiadjis and co-workers (Voyiadjis and Abu Al-Rub [2003], Voyiadjis and Park [1997], Abu Al-Rub and Voyiadjis [2005], Dorgan and Voyiadjis [2003, 2006], Kattan and Voyiadjis [1993]). The functional form of the flow rule of plasticity is given as follows

$$\sigma(\dot{E}^p) = \sigma_y + R(\dot{E}^p)\left[1 + (c_p(T - T_r)\dot{E}^p)^{1/m}\right] \tag{5.115}$$

where σ_y is the initial yield strength, and c_p is the specific heat. The evolution equations for isotropic and hardening laws are given as follows

$$\dot{R} = \mu \dot{E}^p q e^{-\mu E^p} \tag{5.116}$$

$$\dot{\mathbf{X}} = \frac{2}{3} C \dot{\boldsymbol{\varepsilon}}^p - \gamma \mathbf{X} \dot{E}^p + \beta \dot{\boldsymbol{\sigma}} \tag{5.117}$$

and Voyiadjis and Abu Al-Rub [2003] defined q as

$$q = q_m + (q_m + q_0)e^{-2\mu q} \tag{5.118}$$

and m, q_m, q_0, μ, C, γ and β are the material constants to be calibrated from available experimental data. Similarly, one can define the flow rules of damages as follows

$$\sigma(\dot{\kappa}) = Y_0 + K(\dot{\kappa})\left[1 + (c_p(T - T_r)\dot{\kappa})^{1/m}\right] \tag{5.119}$$

where Y_0 is initial damage threshold, $\left(\dot{\kappa} = \sqrt{\dot{\tilde{\boldsymbol{\phi}}} : \dot{\tilde{\boldsymbol{\phi}}}}\right)$, and the nonlocal damage tensor isdefined as $\tilde{\boldsymbol{\phi}} = \boldsymbol{\phi} + \frac{1}{2}\boldsymbol{\ell^2 \nabla^2 \phi}$. The evolution of damage anisotropic hardening equation is given by Voyiadjis and Deliktas [2000*a*] as follows

$$K(\kappa) = \lambda\zeta\left(\frac{\kappa}{\lambda}\right)^{\xi}\delta_{ij}\tilde{\phi}_{ij} + \delta_{ij}\lambda Y_0^2 \tag{5.120}$$

where λ is the Lame constant. Equation (5.120) was based on the work first defined by Voyiadjis and Park [1997]. The exponent, ζ represents the damage hardening parameter, and ξ denotes the damage growth rate. The influences of these parameters on the response of the material was studied by Voyiadjis and Deliktas [1997]. It is clearly seen that the presented gradient approach involving the combination of plasticity and damage phenomena dictates the necessity of more than one length parameter in the gradient description. However, the full utility of the proposed gradient-type theory hinges on ones ability to determine the constitutive lengthscale parameters that tend to be expressed in terms of macroscopic measurable material parameters. Tsagrakis et al. [2003] conducted similar work, where they tend to express the plasticity isotropic hardening length parameter as $\ell = \sqrt{2b/\mu}$ where μ is the shear modulus and the material parameters b must be calibrated from micromechanical tests where size effects and plastic and damage heterogeneity are encountered. Examples of such tests are micro- and/or nano-indentation tests (Stelmashenko et al. [1993]), micro-bending tests (Stolken and Evans [1998]), and microtorsion tests (Fleck et al. [1994]).

In a recent work by Voyiadjis et al. [2003] and Voyiadjis and Abu Al-Rub [2007], a micromechanical model that nonlinearly couples statistically stored dislocations (SSDs) and geometrically necessary dislocations (GNDs) is used to derive an analytical form for the length-scale parameter ℓ in terms of measurable microstructural physical parameters. It was shown that ℓ is proportional to the mean free-path distance between dislocations. Voyiadjis et al. [2003], and Voyiadjis and Abu Al-Rub [2007] also presented a method for identifying ℓ from micro- and nano-indentation experiments. That work, therefore, provides an initial effort for identification of the current material intrinsic length parameters from micro or nano experiments. Voyiadjis and co-workers (Almasri and Voyiadjis [2010], Voyiadjis, Almasri and Park [2010], Voyiadjis and Peters [2010]) demonstrated experimentally the determination of such length scales.

Chapter 6

Calibration of the Proposed Model

6.1 Introduction

One of the most challenging tasks of building an accurate model that represents well the behavior if a material is to define the material constants. In effect, such material constants obviously vary from model to model and it would be more accurate to refer to it as material parameters. It may even very depending on what phenomenon one is trying to capture. A major goal of the solid mechanics behavior modeling would be indeed to define a model describing properly any behavior of a material (such as uniaxial, multiaxial, nonlinear) with just one set of parameters, determined from a set of experiments. As a matter of fact, it has been argued in the past that models calibrated only through the uniaxial tests cannot represent more complicated behavior (Bari and Hassan [2002]) hence in this approach the validation of the obtained material constants was conducted based on uniaxial and cyclic loading tests described in detail in Chapter 2. Adjusting the material constants for bigger variety of experimental tests (not only uniaxial one) makes the obtained parameters more universal and significantly increases the possibility of avoiding the errors regarding more advanced numerical examples.

Identification of the material constants associated with any proposed material model is one of the most challenging issues for researchers in order to obtain better representation of their material models. The identification procedure for the material constants involved in the described backstress evolution equation is based on available experimental results. In this case, the experimental results were obtained as a part of this research and are presented in detail in Chapter 2. If limited test data are available, C, γ, β, can be based on the stress-strain data obtained from the uniaxial tension or compression experiments, or both combined- cyclic loading experiments. This approach is usually adequate when the simulation involves only a few cycles of loading. The details of the procedure to determine the material constants are outlined below. Although it may be lengthy, it is important to describe such procedures in order to better understand these constitutive models.

6.2 Theoretical Approach

Within this section, the procedure to determine some of the material parameters for this model will be outlined, using the uniaxial tension test conducted in the laboratories of LSU, and described in Chapter 2. In this section the theoretical approach for the rough material constants estimation is presented. However, this procedure further requires some small practical adjustments necessary to precisely mimic the experimental curves presented in the previous chapter.

Integration of the backstress evolution law, Equation (5.41), over a half cycle of the stress-strain data can be performed by assuming that for each data point $(\sigma_i, \varepsilon_i^p)$ a value of X is obtained such that:

$$X = \sigma - (\sigma_{yp} + R) \tag{6.1}$$

Using the Equation (6.1) the stress rate can be expressed as follows:

$$\dot{\sigma} = \dot{X} + \dot{R} \tag{6.2}$$

For the uniaxial tension or compression loading and more generally, in proportional loading, if the plastic strain increment in the direction of loading is $\dot{\varepsilon}^p$, $\dot{\varepsilon}_{11}^p = \dot{\varepsilon}^p$ and since the plastic straining is assumed to be incompressible (Poisson ratio is effectively $\nu = 0.5$), then the effective plastic strain rate, $\dot{p}$, becomes:

$$\dot{p} = \sqrt{\frac{2}{3}\dot{\varepsilon}_{ij}^p \dot{\varepsilon}_{ij}^p} = \dot{\varepsilon}^p \tag{6.3}$$

With use of the above equations, namely Equation (6.3) and (6.3), Equation (5.41) can be rewritten as follows:

$$dX = \frac{2}{3} C d\varepsilon^p + \beta dX + \beta dR - \gamma X d\varepsilon^p \tag{6.4}$$

It is seen that the term containing $\dot{\sigma}$ is not used here. This is because the β parameters will be used as a way to refine the behavior of this model later on. In the first step, one needs only to determine C and γ. Using the expression for $\dot{X}$, one can integrate Equation (6.4) into the following close form expression:

$$X = \frac{2C}{3\gamma} + \left(X_0 - \frac{2C}{3\gamma} \right) exp\left(\frac{-\gamma}{1-\beta} (\varepsilon^p - \varepsilon_0^p) \right) \tag{6.5}$$

and the state (ε_0^p, X_0) results from the previous flow. Using a finite set of points in the uniaxial backstress-plastic strain curve one can approximate the curve in the form of Equation (6.5). One now calculates C, γ, and β so that the curve passes through the data such that the sum of squares of the vertical differences between the curve and the various data points is minimized (i.e. by using the least-squares error approach). Equation (6.5) is not directly amenable to a least-squares error fit because the equation is not that of a straight line. However, the equation can be re-arranged in the following form:

$$ln\left(\frac{2C/3\gamma - X_0}{2C/3\gamma - X} \right) = \frac{\gamma}{1-\beta} exp(\varepsilon^p - \varepsilon_0^p) \tag{6.6}$$

With known values of $\frac{2C}{3\gamma}$ the least-squares error fit can be used to fit Equation (6.6). Close to the saturation point of the stress, $\mathbf{X}$, the hardening (kinematic and isotropic) increment tends to zero. Thus, by substituting $d\mathbf{X} = 0$ into Equation (6.4), $\mathbf{X}$ is reduced to:

$$X_s = \frac{2C}{3\gamma} \tag{6.7}$$

hence, Equation (6.6) can be written as:

$$ln\left(\frac{X_s - X_0}{X_s - X}\right) = \frac{\gamma}{1-\beta} exp(\varepsilon^p - \varepsilon_0^p) \tag{6.8}$$

Note that Equation (6.8) is of the form:

$$y = ax \quad \text{with} \quad y = ln\frac{X_s - X_0}{X_s - X}, \quad a = \frac{\gamma}{1-\beta}, \quad \text{and} \quad x = e^{(\varepsilon^p - \varepsilon_0^p)} \tag{6.9}$$

which is the equation of a straight line. That is, one performs a linearizing transformation. Thus, one can now apply a least-squares fit of the transformed variables in the forgoing form. It may be remarked that here it is not necessary to use a process of updating the variables ε_0^p and X_0. The state (ε_0^p, X_0) results from the previous flow, with the flow always expressed by the same evolutionary equation.

The value of a for a least-squares fit is given by:

$$a = \frac{n\sum(xy) - (\sum x)(\sum y)}{n\sum(x) - (\sum x)^2} \tag{6.10}$$

where n is the number of data points and

$$\sum x = \sum_{i=1}^{n} x_i, \quad \sum(x^2) = \sum_{i=1}^{n}(x_i)^2, \quad \text{and} \quad \left(\sum x\right)^2 = \left(\sum_{i=1}^{n} x_i\right)^2 \tag{6.11}$$

One now obtains C and γ from Equations (6.7) and (6.9), as follows:

$$C = \frac{3}{2} X_s a(1-\beta) \quad \text{and} \quad \gamma = a(1-\beta) \tag{6.12}$$

However, one has not yet determined the value of β corresponding to a least-squares error fit. Actually, one has obtained only a least-squares fit of C and γ for a specified value of β. To determine β, one needs to minimize the squares of the errors:

$$e^2 = \sum_{i=1}^{n} [\bar{X} - X]^2 \tag{6.13}$$

where $\bar{X}$ is the backstress value from the actual data at the n data points, and X is the backstress value from Equation (6.5). One does not perform this minimization by finding where the derivative of the error squared is zero. Instead, one searchs for a value of β for which the error is smallest. That is, β is increased in increments from

its possible smallest value to the first data point until the error, which first decreases, begins to increase. One, then, successively halves the increment size and searches the region around the minimum until the value of β is found to a desired level of accuracy. It is clear from Equation (5.53) that $\beta = \sum_{k=1}^{M} \beta^{(k)} = 1$; otherwise the elastic-plastic tangent modulus will be greater than the initial elastic modulus, which is not true. This constraint minimizes the computational cost in finding the converged value of $\beta^{(k)}$.

6.3 Practical Adjustments

After obtaining the material parameters using the method outlined in Section 6.2, one often has to slightly modify or change the calculated values in order to obtain a reasonable fit. The methodology described above gives a very good initial constants estimate which, however, needs to be further compared with the numerical approach. It is emphasized here that there can be a non-negligible difference between what Equation (6.5) represents and what the finite element software computes, since the finite element method is by nature an approximation of the real solution. Hence, a set of material constants has to be checked using the finite element software itself, in this case ABAQUS (ABAQUS [2009]) with the self defined and self implemented subroutine VUMAT, before the model is validated. Reproducing a uniaxial monotonic and cyclic loading condition and comparing with the experimental results used to calibrate the model is necessary in this case.

In the end one must not forget that, no matter how close one is to the experiments in one type of tests, the model might behave in a totally different way for another stress-strain path. A good set of constants is therefore not a set that matches perfectly such loading path, but one that matches satisfactorily as many paths as one can compare with. Hence in this research, the comparison includes not only uniaxial monotonic loading tests but the cyclic loading for the static and dynamic conditions as well.

6.4 Constant Determination for Steel 1080 and VascoMax

Verification of the proposed constitutive model requires that the modeling and numerical algorithms implemented are correct. In this section one point material model is used to calibrate the developed constitutive model by specifying various material constants, or constitutive parameters, for each material. Values for these parameters are obtained by using the initial theoretical analysis presented in Section 6.2 and further corrections by fitting the predicted material behavior to the laboratory data for various load paths presented in the previous section. Some of the already established material constants are obtained from the literature (Yun and Palazotto [2007]). The values of the material constants for Steel 1080 and Steel VascoMax are presented in Table 6.1. Finite element simulations are performed by implementing the proposed

viscoplastic constitutive model in the commercial finite element code ABAQUS 6.8.3 (ABAQUS [2009]). The material model is implemented computationally as a user defined subroutine (VUMAT) for the dynamic analysis in the FEA code (ABAQUS). User subroutines provide an extremely powerful and flexible tool for the analysis. The equations of motion are solved with the help of a finite element package (ABAQUS), and the constitutive law by a solver for ordinary differential equations. The relevant constitutive information is passed to ABAQUS by a subroutine VUMAT which has to be supplied by the user. Starting from an equilibrium state at time, ABAQUS performs an (incremental) loading as well as with the time increment Δt, and an initial guess $\Delta\varepsilon$, for the strain increment. The user subroutine VUMAT has to supply ABAQUS with a new Cauchy stress. Tensor $\sigma + \Delta\sigma$ is updated according to the constitutive law as well as with the derivative of stress with respect to the strain increment.

Table 6.1: Material constants for Steel 1080 and VascoMax for the presented constitutive model based on the approach by Voyiadjis et al. [2003]

Material Constant	**Symbol**	**Steel 1080**	**Steel VascoMax**
Yong's Modulus	E	$203GPa$	$180GPa$
Poisson Ratio	ν	0.3	0.3
Density	ρ	$7800kg/m^3$	$8000kg/m^3$
The Initial Yield Strength	σ_{yp}	$440MPa$	$1.25GPa$
Isotropic Hardening Modulus	r	12	1
Kinematic Hardening Rule	C	$12 \cdot 10^9$	$2 \cdot 10^9$
	γ	40	6
	β	0.1	0.316
Isotropic Hardening Rule	q_M	$300 \cdot 10^6$	$170 \cdot 10^6$
	q_0	$10 \cdot 10^6$	$7 \cdot 10^6$
	μ	10	10
Melting Temperature	T_{melt}	$1670K^0$	$1685K^0$
Reference Temperature	T_{ref}	$295K^0$	$295K^0$
Thermal Softening Exponent	T_{soft}	0.5	0.5
Rate Sensitivity Exponent	m	1	1
Relaxation time/Viscosity	T_{relax}	0.005	0.005
Specific Heat	C_p	$460J/kg \cdot K$	$452J/kg \cdot K$

In this example, a uniaxial tension specimen is loaded with prescribed velocities and with different meshes in order to verify the appropriate material parameters for this numerical simulation. The results are compared to the experimentally obtained curves from Chapter 2. In this regard a simple rectangular geometry is used for the uniaxial tension problem subjected to low and high velocities (Figure 6.1).

Due to the symmetry, only a quarter of the problem is considered and solved with the mesh of one axisymetric element and boundary conditions (see Figure 6.1). The material parameters used in the simulation are listed in Table 6.1. In this simulation the effect of strain rate on the stress-strain curve is also investigated.

The main goal of this approach is to determine the material constants and sim-

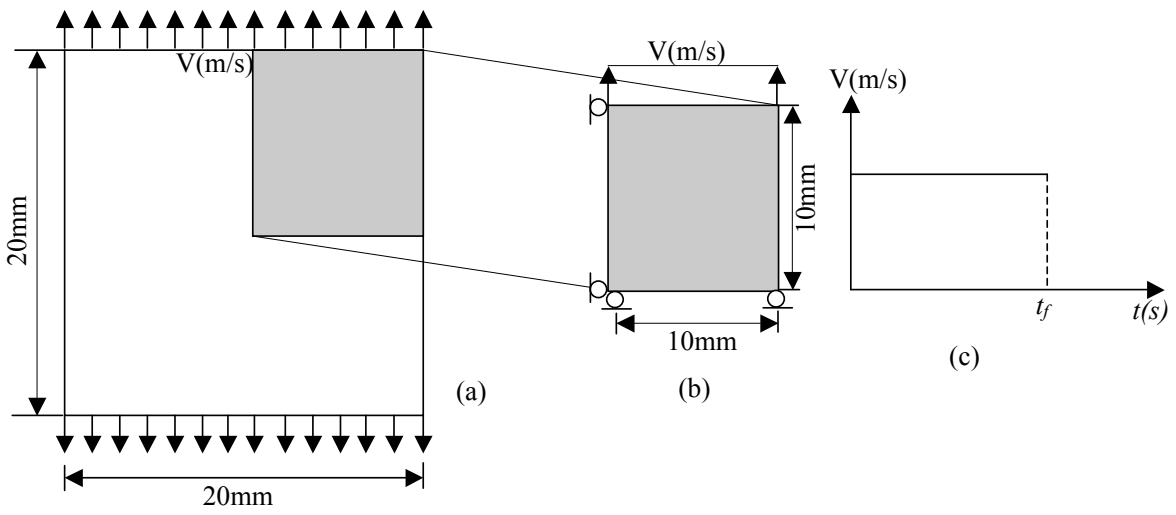

Figure 6.1: Problem description for a simple uniaxial tension specimen.

ulate the strain rate and all conditions exactly as they occur in the experiments. In the following Section 6.5 the obtained results of the strain-stress relationship according to the constitutive model introduced in the previous sections are presented. The implemented theory is extremely adequate in characterizing the behavior of the material used in this research.

6.5 Numerical Approach vs the Experiments

In this section the comparison of the experimental uniaxial loading of a steel 1080 specimen with the computational simulation using the model by Voyiadjis, Deliktas, Lodygowski and Park [2010] (solid line), based on the model Voyiadjis and Abu Al-Rub [2003] is presented in Figure 6.2(a). Significant improvement and precision in simulating the experimental approach is due to the gradient approach (Voyiadjis, Deliktas, Lodygowski, Palazotto, Philippon, Rusinek, Faure and Chevrier [2009*b*]) and elaborated conditions for the yield surface. Figure 6.2(b) represents the same type of experiment; however, in this case the tested material is Steel VascoMax. Again the comparison of experiment, with the computational model is very successful.

Figures 6.3(a) and 6.3(b) compare the model and experimental results for the cyclic loading for both Steel 1080 and Steel VascoMax, respectively. Similar to the uniaxial case, the theory with incorporated gradient theory simulates well the experimental results for the cyclic loading. The comparison of the computational stress-strain relationships show very good accuracy of the calibrated constitutive model with the conducted experiments. There is relatively very small difference between the experimental and computational results. This way, the calibrated constitutive model is validated by the comparison to the experimental approach and can be used for more sophisticated applications concerning friction and wear, as shown in the next chapter.

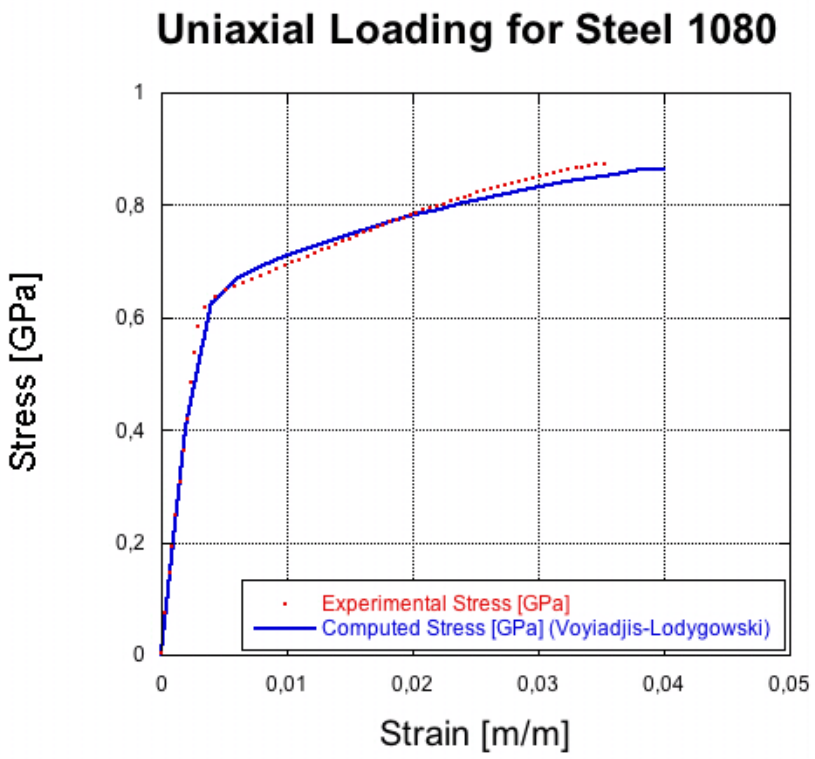

(a)

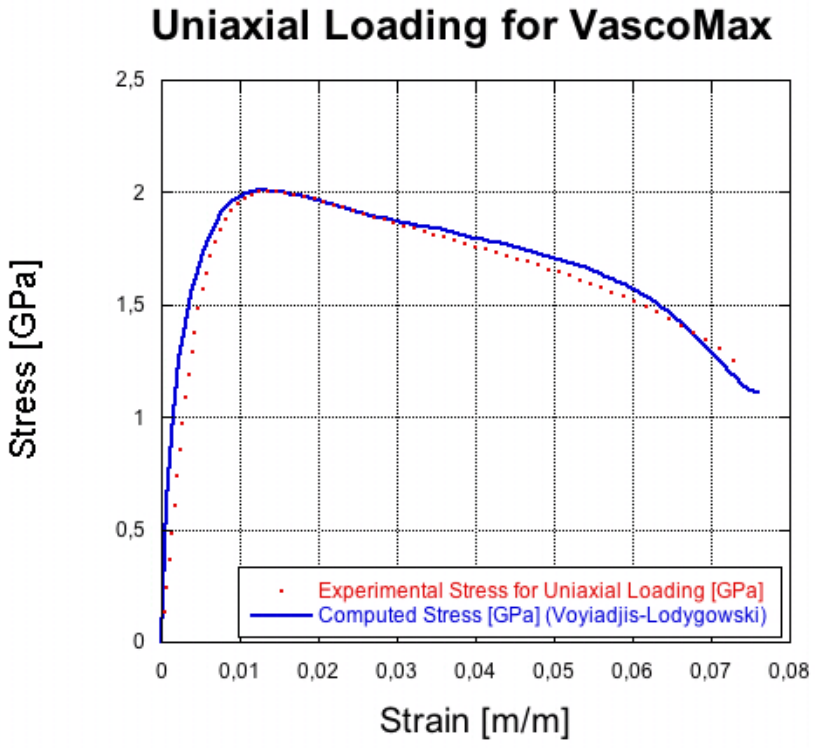

(b)

Figure 6.2: Comparison of experimental and computational results for the uniaxial loading: 6.2(a) Steel 1080 and 6.2(b) VascoMax using the proposed constitutive model.

.

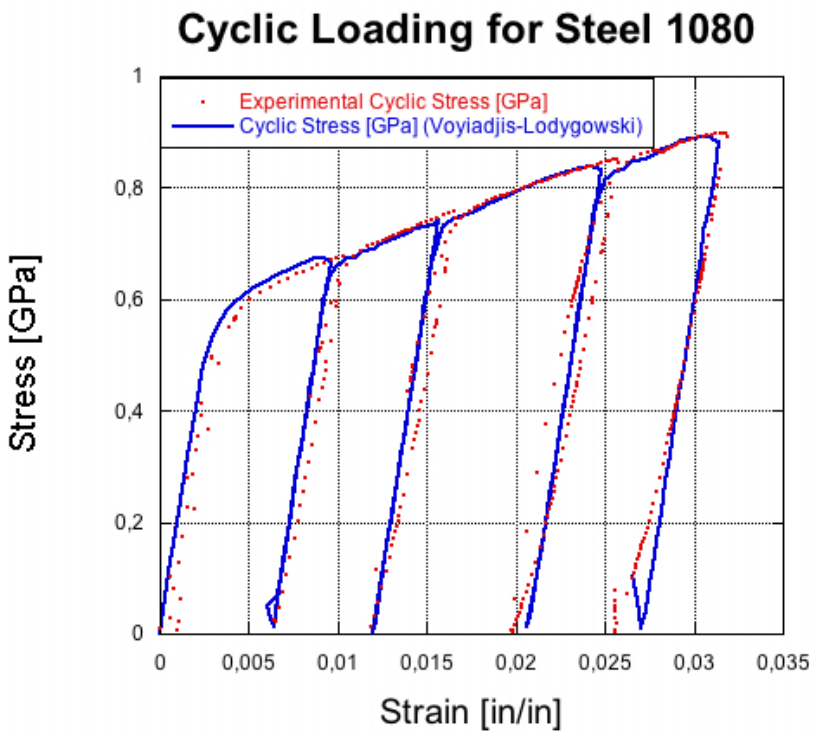

(a)

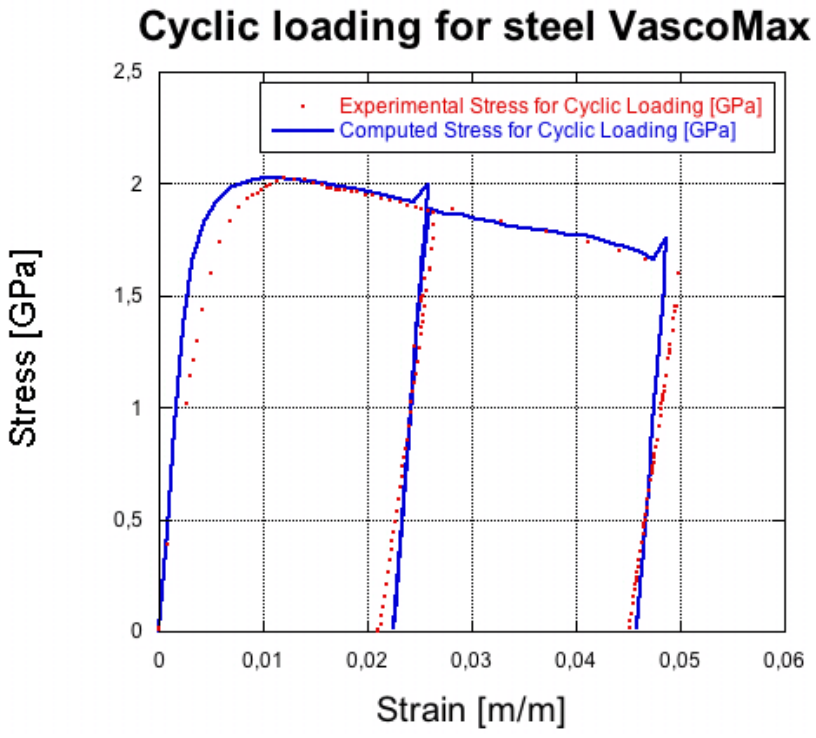

(b)

Figure 6.3: Comparison of experimental and computational results for the cyclic loading: 6.3(a) Steel 1080 and 6.3(b) VascoMax using the proposed constitutive model. .

Chapter 7

Numerical Applications

7.1 Introduction

In this Chapter the application of the developed gradient theory presented in Chapter 5 utilizing the calibration of the constitutive model with necessary obtained material constants from Chapter 6 is presented. The example chosen for this work is not accidental and is strongly related to the tribology research field.

The experimental work on the study of friction between metallic surfaces was conducted in collaboration with the National Engineering School of Metz (ENIM), France. A modified Hopkinson's bar, developed by Philippon et al. [2004], simulates high velocity contact between two surfaces. The experimental device, presented again in Figure 7.1, described and characterized in detail in Chapter 4, is capable of conducting and investigating the dry friction between two different materials for large span of velocities V and applied normal pressures p. For the sake of this research material A and material B are made of Steel 1080 and Steel VascoMax, respectively, and are mainly made up of two distinct parts. A dynamometer ring allows applying a known apparent normal force F_N on the contact surfaces between specimens A and B and monitoring it during the experimental process with use of strain gauges. A thin tube, on which another set of two strain gauges is glued, measure the tangential force due to friction. The ring is mounted on the thin tube (load sensor) and rigidly fixed by two screws. Specimen B is placed between two specimens A fixed symmetrically in the inner surfaces of the dynamometer ring. The value of the apparent normal force F_N exerted by this ring is calibrated by the thickness of specimen A and the width of specimen B as already described in Section 4.3.2.

In this experiment, a high speed projectile is fired inside the tube of a gas gun towards the specimen B mounted between specimens A. During the impact it is assumed that projectile passes the entire kinetic energy on specimen B and hence the impact velocity becomes the initial velocity of the specimen B sliding between specimens A (Philippon et al. [2003]). During this sliding process the variation of contact and normal forces are recorded with the use of the set of oscilloscopes. The contact force exerted on the dynamometer (in Figure 7.1), can be predicted by measuring the change in length of the friction device using strain gauges. Moreover, the latter (along with the sliding surface) are processed using SEM to characterize the topography of the

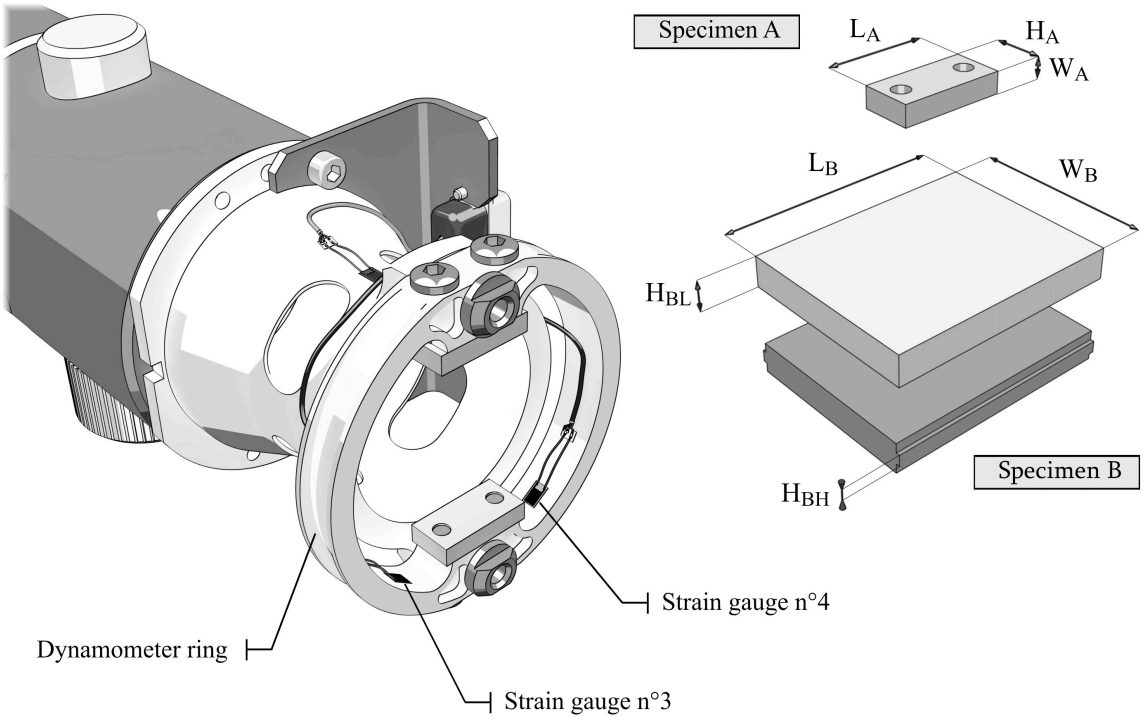

Figure 7.1: A brief recall of the experimental approach presented in detail in Chapter 4.

before and after surfaces (Chapter 3) and consequently the size of contacting asperities.

In this experiment, roughness measured through the SEM is characterized by the software package (Vision32) provided by Veeco Meteorology Group. The characterization of the sled shoe and the track surface indicates the roughness of $4 - 8\mu m$ and it is postulated that damage phenomena are generated from dislocation generation at between crystallographically misoriented single crystals (at the microscale). However, the roughness of the prepared and machined specimens is significantly smaller $(0.4 - 0.8\mu m)$. In order to further characterize the sliding interfaces, the experimental study as previously described is conducted (see Figure 7.1) and again the measurement procedure in the same manner is performed.

7.2 Procedure Description

The simulations and validation of previously described experiments are performed with the finite element commercial software ABAQUS according to the proposed theory, coded as a VUMAT subroutine. The simulations performed here are the closest and as accurate as the experiments discussed in Chapter 4. The set of simulations is performed for the constant value of normal force, and hence normal pressure, but for a large range of sliding velocities. The simulations capture the development of surface temperature,

plastic deformation as well as the frictional forces. The different mesh sizes are also considered to show the lack of the mesh dependency due to the gradient formulation adopted in this work according to the proposed theory. Two sets of simulations are carried out for sliding velocities between $0m/s - 4m/s$ and $10m/s - 100m/s$, mimicking the two sets of experimental results.

The registration of the frictional force is done by defining the group of nodes on each specimen A and summing the occurring reaction forces afterward to obtain the final tangential force. The friction coefficient results presented in Chapter 4 are of a significant importance to the ABAQUS data input. The change of the friction coefficient is grasped in an exponential decay function providing the friction coefficient input $\mu(V)$ for different velocities.

In this approach one concentrates on comparing the recorded computational temperature and its evolution. The temperature is treated as the major variable in the analysis of the high velocity contact problem. Moreover, further development of the experimental device will shortly enable capturing the flash temperatures. When such measurements are available, it will be of a significant importance to compare them with the implemented theory.

7.3 Abaqus Input

The 3D geometry created in the environment of ABAQUS CAE is closely mimicking the setup of specimens A and B in the conducted friction experiments. The graphical representation of this model is presented in Figure 7.2. Based on the nomenclature presented in Figure 7.1 the following dimensions for the numerical model were defined:

- For specimen A representing steel 1080: $L_A = 28mm$, $H_A = 12mm$ and $W_A = 5mm$.
- For specimen B representing steel VascoMax: $L_B = 80mm$, $W_B = 49mm$ and $H_{BL} = 10mm$.

The analysis was performed in Abaqus Explicit, widely used for all sort of dynamic approaches, as a temperature-displacement analysis. The material constants were defined according to information presented in Chapter 6 and in accord with the theory presented before. The material model was implemented as a VUMAT subroutine which deals with the material response and stress-strain relationship. At the same time, when VUMAT governs material response Abaqus performs numerical analysis according to the coded of unrevealed numerical algorithm. Hence, it is not possible to interfere with Abaqus computations treating it as sort of 'black box' and the only modification can be made by the user in the field of material response.

7.3.1 Loading Steps

The analysis is divided into three loading steps which take place one after the other. The first step, called *initial step* defines the external temperature condition,

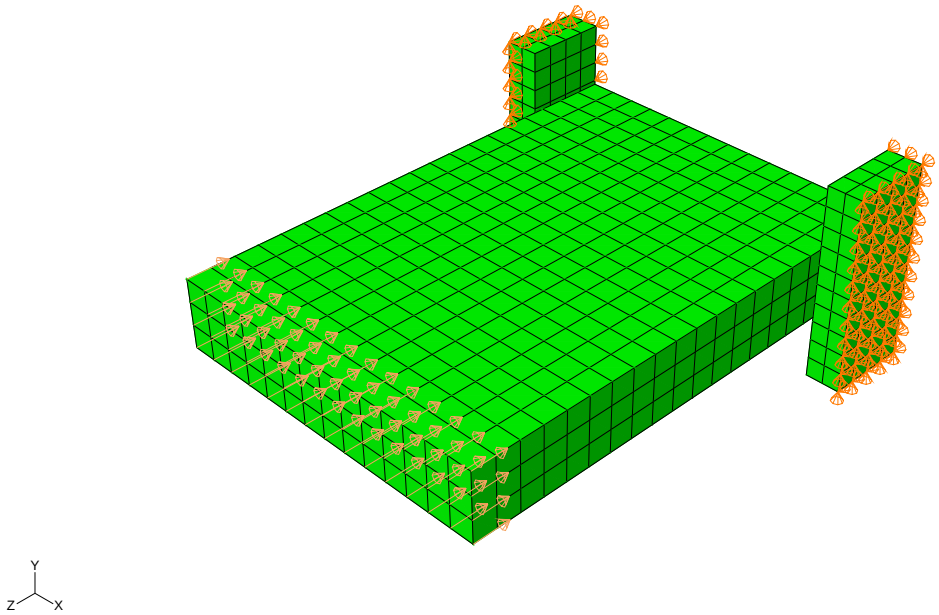

Figure 7.2: The geometry of specimens described in Chapter 4 used for the numerical simulations.

$T_{init} = 293K$. This step is not time related, hence time is not defined here. The second step, called *loading step* defines displacement boundary conditions, loading boundary conditions, and interactions between the materials sliding against each other. All these characteristics are described in the following subsections. The time duration can be defined here and is set to be $0.001sec$, as the loading and all boundary condition are applied instantly. The last, third step, with the use of information provided in the previous steps already starts the calculations. All characteristics given in the first two steps apply here and give the necessary information to carry out the computations of the initial value problem. The velocity boundary conditions are specified and based on them, the time duration of the simulation is computed. The optimal duration of the simulation ends right before the loss of contact between sliding specimen B and the held specimen A.

7.3.2 Boundary Condition

Displacement and loading boundary conditions regarding two smaller specimens A are defined in the second analysis step and the velocity boundary conditions are applied in the last, sliding step. All boundary conditions are defined in the reference coordinate system visible in the left bottom corner in Figure 7.2. The boundary conditions in the second step are applied as follows: rotations about all directions as well as the displacement in y and z direction of the two outside large surfaces of both specimens A (as marked in Figure 7.2) that are fixed. At the same time along the last free, not fixed direction x the normal pressure is applied. For all conducted here analysis the pressure is equal to $9MPa$, equally divided and applied on the outside surface of

the specimen A creating the squeezing effect of the inside specimen B. Determination of this value was conducted by the collaborating research team from Air Force Institute of Technology, Ohio (Hale [2010]) and also applied in the experimental approach described in Chapter 4. Two back surfaces of specimens A have fixed displacement in z direction in order to capture the reaction force necessary to calculate the friction coefficient.

The third step introduces the velocity boundary condition applied to the front surface of specimen B in the negative z direction. This boundary condition is applied instantly and forces the sliding process of specimen B between both specimens A, applying the normal pressure at the same time. The rest of the boundary conditions defined in the previous step are also valid in this last numerical step.

7.3.3 Interactions

The last information necessary to conduct this 3-dimensional analysis is the definition of the interactions occurring on the contact interface between two sliding surfaces of specimens A and B. It is defined as surface to surface contact. The contact is defined using the kinematic contact method and applying the finite sliding criterion. All theoretical background regarding these definitions can be found in ABAQUS [2009]. These properties are defined in the loading step and is propagated to the final sliding step.

7.4 Obtained Results

The procedure is conducted in the following manner. The set of surface nodes on the inner part of specimen A is created. It is important to note that not all inner nodes are in contact with specimen B and not all of them experience the temperature changes. However, it is the most precise way to determine the global temperature change of the inner part of specimens A. The temperature is recorded for each node on the previously mentioned surface and finally the average temperature is calculated. The exact same procedure is conducted for specimen B. In this case however, the entire surface $L_B \times H_{BL}$ gets in contact during the duration of the simulation. These results are presented in Figures 7.3(a) and 7.3(b).

As clearly visible in Figure 7.3(a), the increase of sliding velocity causes the increase of the average temperature. This increase is in a good agreement with the theoretical approach presented by Bowden and Hughes [1939] and Bowden and Persson [1960]. Despite the fact that the overall increase is substantial, it is not linear with respect to the velocity increase unlike the increase of maximum temperature occurring on specimen A (Figure 7.4(a)). It can be clearly seen that the particular increase of velocity for higher range of velocities does not give the same increase of temperature (i.e. almost quadrupling the velocity does not result in quadrupling the temperature).

Despite the fact that the overall temperature increase is substantial, it is not linear with respect to the velocity. It must be noted that unlike the increase of maximum temperature occurring on specimen A occurring to be almost linear, the increase of

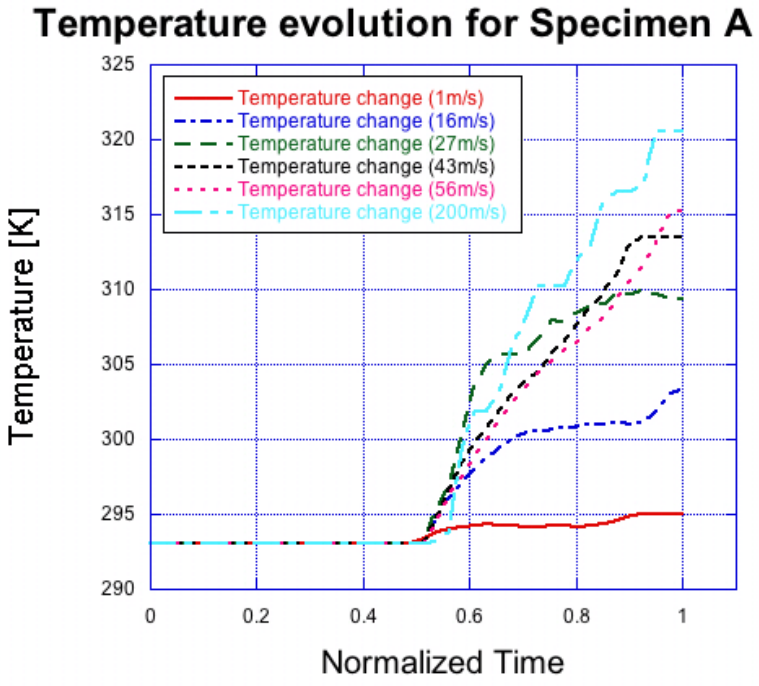

(a)

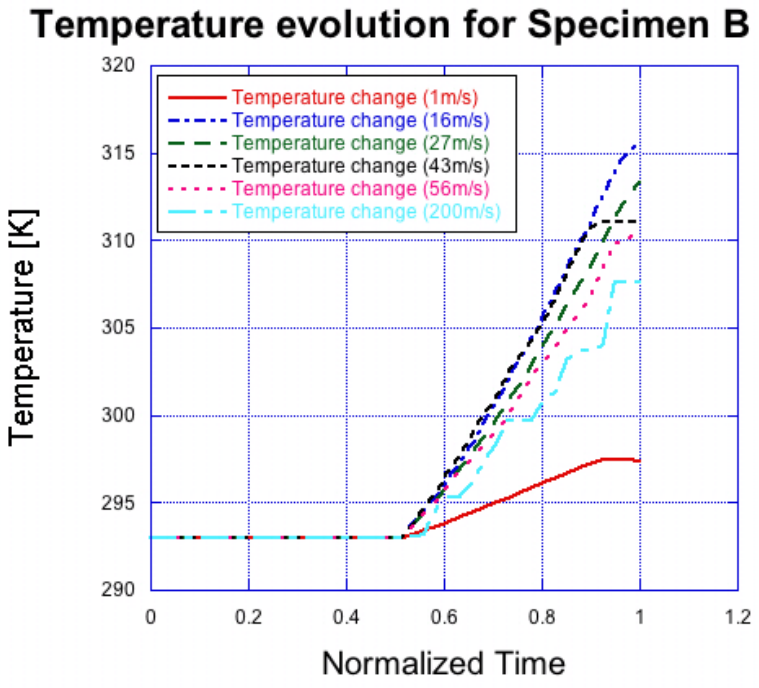

(b)

Figure 7.3: 7.3(a) Temperature evolution as an average from the entire inner surface of specimen A. 7.3(b) Temperature evolution of the contact surface $L_B \times H_{BL}$ of specimen B (see Figure 7.2). .

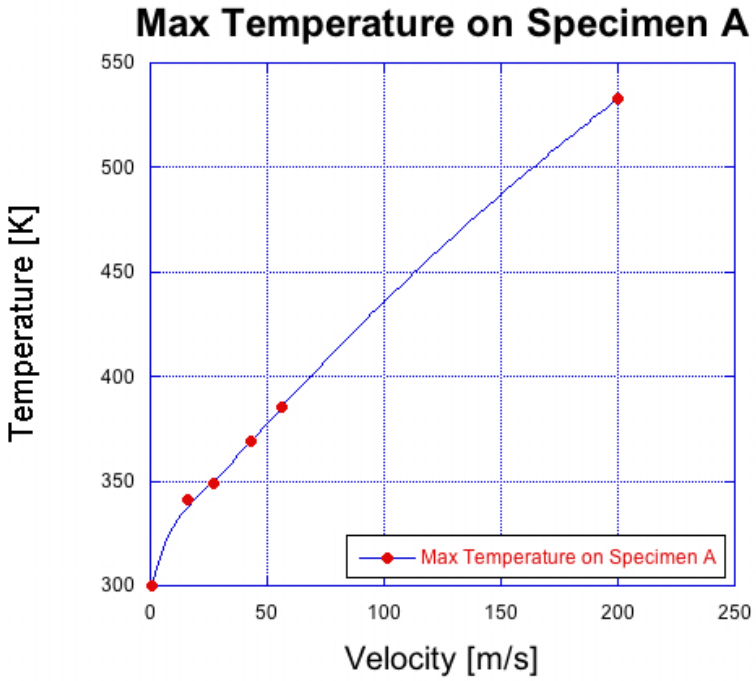

(a)

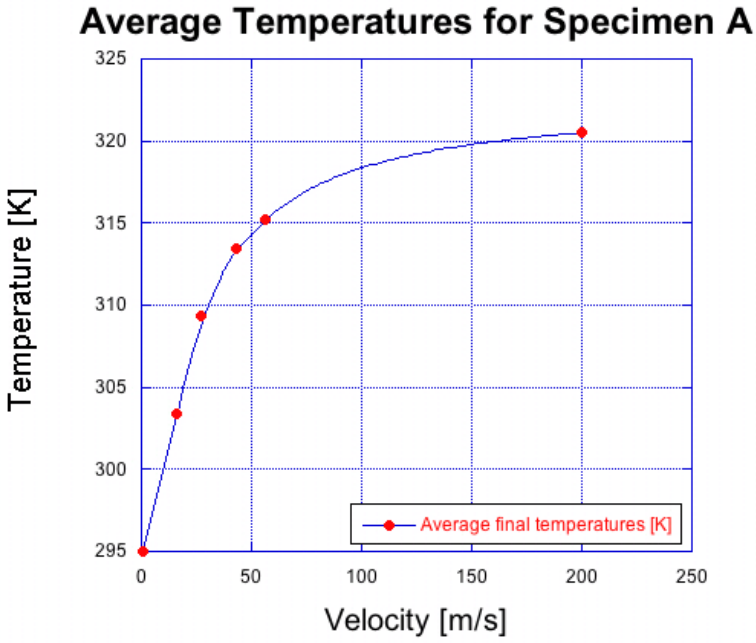

(b)

Figure 7.4: 7.4(a) Maximum temperatures occurring during the sliding process on the inside surface of specimen A for particular velocity. 7.4(b) Average final temperatures of the inside part of specimen A.

the average temperature with respect to velocity is logarithmic and converging to some critical temperature. It can be clearly seen that the increase of velocity, particularly

for higher values, does not give the same increase of temperature. This phenomenon is captured in Figure 7.3(b) and stays in a good correlation with the theories and experimental results presented in a vast variety of sources such as Oden and Martins [1984], Lim et al. [1989], Philippon et al. [2003] and others. It is theoretically clear and also confirmed by formulations presented earlier that due to dry friction the generated heat will logarithmically increase reaching some particular level.

In case of specimen B, however, due to large increase of sliding velocity and the fact that the entire sliding surface is not constantly in contact during the sliding process the temperature does not increase with the increase of the sliding velocity. It is assumed in the theoretical formulations as well as in the computational approach that 90% of the entire plastic energy is converted into heat. With the increase of the sliding velocity and the strain rate the generated shear bands do not manage to widen. Hence, the generated plastic energy decreases in comparison with the plastic energy generated for the lower sliding velocities resulting in smaller temperature increases. Moreover this fact invokes a very good heat resistance of high strength steel VascoMax and provides valuable information for the usage of steel VascoMax, in particular, the application to the shoe construction in the Holloman High Speed Test Track, New Mexico.

Chapter 8

Final Remarks and Conclusions

8.1 Basic Conclusions

Severe contact stress problems are theoretically modeled through coupling continuum damage with strain gradient plasticity. This is achieved by introducing the contributions of damage and its corresponding gradients in the virtual power relations as measures of micro motion of damage within the bulk. By using these internal state variables together with displacement and temperature, the constitutive model is formulated with state laws based on the free energies and the complimentary laws based on the dissipation potentials. The temperature is taken into consideration as the major variable in the analysis of the high velocity contact problem.

The proposed theoretical model is partially implemented as user defined subroutine VUMAT in the explicit finite element code ABAQUS to analyze the structural response of the ultra high speed sliding experiment between Steel and VascoMax steel at Ecole de'Nationale Institut der Mechanic, at Metz France. Results of these analyses conclude the following points:

- The proposed theory is verified successfully in the simulation of the material response with respect to hardening and softening behaviors under uniaxial and cyclic loading cases. The reliable and robust simulation capability of the model shows that the theory is extremely adequate in characterizing the behavior of steel 1080 and Steel VascoMax, respectively. Accurate material model parameters that are needed for the simulation of the experimental work in the study of friction between metallic surfaces is conducted by the author in collaboration with the National Engineering School of Metz (ENIM), France.

- The simulations of the above experimental set up are performed with the finite element commercial software ABAQUS according to the proposed theory and coded as a VUMAT subroutine. The set of simulations is performed for different values of normal force and sliding velocity capturing the development of surface temperatures, plastic deformations as well as the frictional forces. Different mesh sizes are also considered to show the lack of mesh dependency due to the non-local gradient formulation adopted in this work according to the proposed theory.

The simulations are carried out for a set of sliding velocities between 10m/s and 200m/s.

- The increase of sliding velocity causes the increase of the average temperature. This increase is in good agreement with the theoretical approach presented by Bowden and Hughes [1939], and Bowden and Persson [1960]. Despite the fact that the overall increase is substantial, it is not linear with respect to the velocity unlike the increase of maximum temperature occurring on the specimen. It can be concluded that the particular increase of velocity for higher range of velocities does not give the same increase of temperature (i.e. almost quadrupling the velocity does not result in quadrupling the temperature).

This model provides a potential feature for enabling one to relate the non-local continuum plasticity and damage of the bulk material to friction and wear at the contact interfaces. The findings of this research effort is invaluable in providing a material model and numerical procedure that will be used within a hydrocode to better facilitate the design components of severe contact stress applications.

8.2 Chapters Summary

Chapter 1 gives the insight on friction and wear problem and introduces the main motivation of pursuing the research in this tribology field. The main part of this Chapter is devoted to the description of Holloman High Speed Test Track which is considered to be the longest and most advanced test track facility in the world. Moreover, the attention is directed at the physical phenomena occurring on the interface between track and slipper.

Next, in Chapter 2, the material characterization is considered. The sophisticated materials, such as steel VascoMax, used often for the army application, have very limited amount of data published in widely available literature and publications. Therefore, utilizing the material samples obtained from Dr Anthony Palazotto, from the Air Force Institute of Technology, both kind of steels are experimentally tested in the uniaxial monotonic and cyclic loading tests. These data are of a crucial importance in further validation of the theoretical model. Hence, the tests are performed in the LSU laboratories and the results are compared with Yun and Palazotto [2007], the only available and comparable source. After the successful validation of the obtained results one moves to another experimental approach.

Measuring the initial and final roughness before and after the friction experiments, respectively, and hence the wear of the material samples, is the main topic of Chapter 3. Due to the fact, that during the friction experiments wear occurs, with the use of advanced scanning devices with incorporated abilities to give statistical information regarding the scanned surface. Three sets of experiments, which are described in details, are performed in order to obtain the roughness change and hence the occurring wear. The results presented for polished experiments are of the most significant importance. It is shown, that the decrease of roughness is strictly connected to the sliding velocity during the experiments. Moreover, with the increase of sliding velocity

the increase of wear is very noticeable. The most important conclusion arriving from this Chapter shows the presence of wear during the sliding process and links this wear with the sliding velocity.

Chapter 4 contains the most important and most sophisticated experimental approach measuring the friction force during the sliding process. This Chapter reveals the complexity of the experimental setup and its development, and explains all necessary aspects that needs to be considered in order to fully prepare and utilize the friction device for the experiment. The most important outcome of this Chapter are the quasi-static and dynamic friction test results, considered for the friction coefficient μ. This coefficient is further considered as a function of sliding velocity. These extremely valuable measurements are of a crucial importance for the numerical simulations and provide the friction coefficient data necessary to perform them. This Chapter concludes the experimental part and further consideration proceeds to the theory, simulations and applications.

Chapter 5 consists of two major part. The first one is devoted to the detailed description of the FAPC model (proposed by Voyiadjis and Abu Al-Rub [2003]) which is the starting point not only to further development of the theoretical approach but also the starting point for the numerical approach and implementation. The constitutive relations are given along with the precise description of the numerical approach, necessary to understand the numerical algorithm, including problems such as discretization of the constitutive equations, radial return mapping and smoothing the elaso-plastic transition. In the second part of this Chapter the theory developed and already presented in Voyiadjis, Deliktas, Lodygowski and Park [2010] is stated. The new approach of the non-local modeling of heterogeneous media to assess high velocity frictional contact using coupled viscoplasticity damage model is clearly stated and explained in details. The novel concept of introducing two additional variables responsible for friction and wear along with the gradient formulation for plastic and damage terms makes this model by far more superior for problems accounting for friction. The parts concerning the gradient terms of plasticity are implemented and provide the mesh independent results. The damage, wear and friction approach of the theoretical aspect however, is left as a work to be developed in the future. The experiments described in Chapters 3 and 4 are of crucial importance in obtaining wear and frictional material constants embedded in the presented theory.

Chapter 6 presents the method of obtaining the material constants for the presented constitutive model. Parametric studies are very complex and difficult on its own and there is plenty of research conducted in this area. In this chapter with the use of the least square method the estimation of some of the material constants is possible, particularly those connected to the hardening laws. It should be noted, that some of the material constants are obtained from the steel tables and other sources. Second part of this Chapter presents the practical adjustments to mimic the curves from Chapter 2 in a more accurate way. Finally the obtained material constants and application of constitutive model in the simple monotonic and cyclic uniaxial tension is presented. The positive verification of the proposed theory gives the confidence and allows to move to more complicated examples as presented in Chapter 7.

Chapter 7, provides the numerical examples validating the presented theory. The

numerical simulation is used to mimic the friction experiments from Chapter 4. The numerical model shows exactly the same setup as the experiment. The obtained results are in an accord with the theory presented in the literature. Moreover, the gradient approach provides mesh independent results. The results are commented in detail, the proper figures are presented and the comparison to existing theories is made.

8.3 Future Perspectives

As already stated the experimental approach is a continuous process with constant enhancements of the frictional device. In the close future the development of newer device is going to be accomplished and it is expected to conduct the friction experiments for velocities up to $200m/s - 300m/s$. Moreover, the development of a particular surface thermometer, capable of measuring the flash temperature, is about to be accomplished and adopted on the frictional device. With this enhancement it will be possible to compare the temperature, the independent variable, occurring during the experimental results as well as the numerical approach.

The theoretical part is consistent and well developed, however, it needs to be fully incorporated in the numerical algorithm. With the use of the friction and roughness experimental results it is possible to calibrate the constant responsible for wear and friction and compare the results with the existing simulations. It should be perfectly clear that this enhancement will provide more precise computations, more elaborated analysis and above all, the results will mimic the physical behavior at a superior level.

Bibliography

ABAQUS [2009], *ABAQUS (2009) Users Manual*, version 6.8.3 edn, Providence, RI.

Abed, F. H. and Voyiadjis, G. Z. [2005], 'A consistent modified zerilli-armstrong flow stress model for bcc and fcc metals for elevated temperatures', *Acta Mechanica* **175**, 1–18.

Abu Al-Rub, R. K. and Voyiadjis, G. [2004], 'Analytical and experimental determination of the material intrinsic length scale of strain gradient plasticity theory from micro- and nano-indentation experiments', *International Journal of Plasticity* **20**(6), 1139–1182.

Abu Al-Rub, R. K. and Voyiadjis, G. Z. [2006], 'A finite strain plastic-damage model for high velocity impact using combined viscosity and gradient localization limiters: Part i – theoretical formulation', *International Journal of Damage Mechanics* **15**, 293–334.

Abu Al-Rub, R. and Voyiadjis, G. [2005], 'A direct finite element implementation of the gradient-dependent theory', *International Journal for Numerical Methods in Engineering* **63**(4), 603–629.

Abu Al-Rub, R., Voyiadjis, G. and Bammann, D. [2007], 'A thermodynamic based higher-order gradient theory for size dependent plasticity', *International Journal of Solids and Structures* **44**(9), 2888–2923.

Aifantis, E. C. [1984], 'On the microstructural origin of certain inelastic models', *Journal of Engineering Materials and Technology* **106**, 326–330.

Aifantis, E. C. [1992], 'On the role of gradient in the localization of deformaiton and fracture', *International Journal of Engineering Science* **30**, 1279–1299.

Aifantis, K. and Willis, J. [2006], 'Scale effects induced by strain gradient plasticity and interfacial resistance in periodic and randomly heterogeneous media.', *Mechanics of Materials* **38**(702-716).

Aifantis, K. and Willis, J.R., . [2005], 'The role of interface in enhancing the yield strength of composite and polycrystal', *Journal of the Mechanics and Physics of Solids* **53**, 1047–1070.

Almasri, A. and Voyiadjis, G. [2010], 'Nanoindentation in fcc metals: Experimental study', *Acta Mechanica* **12**, 1–10.

Anand, L., Gurtin, M., Lele, S. and Gething, C. [2005], 'A one-dimensional theory of strain-gradient plasticity: Formulation, analysis, numerical results', *Journal of the Mechanics and Physics of Solids* **53**(8), 1789–1826.

Andrews, K., Shillor, M. and Wright, S. [1997], 'A dynamic thermoviscoelastic contact problem with friction and wear', *International Journal of Engineering Science* **35**(14), 1291–1309.

Archard, J. F. [1953], 'Contact and rubbing of flat surfaces', *International Journal of Physics* **24**(8), 981–988.

Armstrong, P. and Frederick, C. [1966], A mathematical representation of the multiaxial bauschinger effect, Cegb report rd/b/n/731, Berkeley Laboratories, R&D Department, CA.

ASM [1997], *Friction and Wear Testing*, ISBN 0871706172, ASTM.

Banerjee, B. [2007], An evaluation of plastic flow stress models for the simulation of high-temperature and high-strain-rate deformation of metals. Report.

Bari, S. and Hassan, B. [2001], 'Kinematic hardening rules in upcoupled modeling for multiaxial ratchetting simulation', *International Journal of Plasticity* **17**, 885–905.

Bari, S. and Hassan, B. [2002], 'An advantement on the on cyclic plasticity modeling for multiaxial ratchetting simulation', *International Journal of Plasticity* **18**, 873–894.

Bassani, J. L. [2001], 'Incompatibility and a simple gradient theory of plasticity', *Journal of Mechanics and Physics of Solids* **49**, 1983–1996.

Bazant, Z. P. and Pijaudier-Cobot, G. [1988], 'Nonlocal continuum damage, localization instability and convergence', *Journal of Applied Mechanics* **55**, 287–293.

Belytschko, T., Liu, W. and Moran, B. [2000], *Nonlinear Finite Elements For Continua And Structures Nonlinear Finite Elements For Continua And Structures*, John Wiley & Sons Ltd.

Bittencourt, E., Needleman, A., Gurtin, M. and Van der Giessen, E. [2003], 'A comparison of nonlocal continuum and discrete dislocation plasticity predictions', *Journal of the Mechanics and Physics of Solids* **51**, 281–310.

Borvik, T., Langseth, M., Hopperstad, O. and Malo, K. [2002], 'Perforation of 12mm thick steel plates by 20mm diameter projectiles with flat, hemispherical and conical noses, part 1- experimental study', *International Journal of Impact Engineering* **27**, 19–35.

Bowden, F. P. and Freitag, E. [1958], 'The friction of solids at very high speeds i. metal on metal; ii. metal on diamond', *Proceedings of the royal society of London, series A: Mathematical and physical sciences* **248**, 350–367.

Bowden, F. P. and Hughes, T. P. [1939], 'The friction of clean metals and the influence of absorbed gasses. the temperature coefficient of friction', *The Scholarly Journal Archive* **A172**, 263–279.
URL: *http://www.jstor.org/*

Bowden, F. P. and Persson, P. A. [1960], 'Deformation heating and metling of solids in high speed friction', *Proceedings of Royal Society of London A* **260**, 433–458.

Bowden, F. P. and Tabor, D. [1950], 'Friction and lubrication of solids', *Clarendon Press, Oxford* **1**.

Castro, L., Viéville, P. and Lipinski, P. [2006], 'Correction of dynamic effects on force measurements made with piezoelectric dynamometers', *International Journal of Machine Tools and Manufacture* **46**, 1707–1715.

Cermelli, P., Fried, E. and Gurtin, M. [2004], 'Sharp-interface nematic-isotropic phase transitions without flow', *Archive for Rational Mechanics and Analysis* **174**(2), 151–178.

Chaboche, J. [1991], 'On some modifications of kinematic hardening to improve the description of ratchetting effects', *International Journal of Plasticity* **7**, 661–678.

Chaboche, J., Nauailhas, D., Paulmier, P. and Policella, H. [1989], 'Problems of describing ratchetting on cycli plasticity and viscoplasticity', *Recherche Aerospatiale* **1**, 64–79.

Chaboche, J. and Rousselier, G. [1981], On the plastic and viscoplastic constitutive equations based on the internal variables concept, *in* T. ONERA, ed., 'International Seminar on Inelastic Analysis and Life Prediction in High Temperature Environment', Vol. 3, Paris.

Chaboche, J. and Rousselier, G. [1983], 'On the plastic and viscoplastic constitutive equations. part i: rules deceloped with internal variables concept. part ii: application of internal variable concept to 316 stainless steel', *Journal of Pressure Vessel Technology* **ASME 105**, 153–164.

Cinnamon, J. C., Palazotto, A. N. and Kennan, Z. [2006], 'Material characterization and development of a constitutive relationship for hypervelocity impact of 1080 steel and vascomax 300', *International Journal of Impact Engineering* **33**, 180–189.

Clifton, J. and Klopp, R. [1985], 'Pressure-shear plate impact testing', *Metals Handbook 8, Mechanical Testing* pp. 230–239.

Coleman, B. and Gurtin, M. [1967], 'Thermodynamics with internal state variables', *Journal of Chemical Physics* **47**, 597–613.

Coleman, B. and Noll, W. [1963], 'The thermodynamics of elastic materials with heat conduction and viscosity', *Archive for Rational Mechanics and Analysis* **13**(167-178).

Corona, E., Hassan, B. and Kyriakides, S. [1996], 'On the performance of kinematic hardening rules in predicting the a class of biaxial ratchetting histories', *International Journal of Plasticity* **12**, 117–145.

Couetard, Y. [2000], Caractérisation et étalonnage des dynamométres à six composantes pour torseur associé à un système de forces, PhD thesis, Université de Bordeaux, Bordeaux, France.

Dafalias, Y. and Popov, T. [1975], 'A model of nonlinearly hardening materials for complex loading', *Acta Mechanica* **21**, 173–192.

Dafalias, Y. and Popov, T. [1976], 'Plastic internal variables formulism in cyclic plasticity', *Journal of Applied Mechanics, ASME* **43**, 645–651.

De Borst, R. and Sluys, L. J. [1991], 'Localization in a cosserate continuum under static and dynamic loading condition', *Computer Methods in Applied Mechanics and Engineering* **90**, 805–827.

Degroot, M. [1980], *Probability and Statistics*, Addison-Wesley.

Deters, L. and Proksch, M. [2005], 'Friction and wear testing of rail and wheel material', *Wear* **258**, 981–991.

Dorgan, R. and Voyiadjis, G. [2003], 'Nonlocal dislocation based plasticity incorporating gradients of hardening', *Mechanics of Materials* **35**(8), 721–732.

Dorgan, R. and Voyiadjis, G. [2006], 'A mixed finite element implementation of a gradient-enhanced coupled damage-plasticity model', *International Journal of Damage Mechanics* **15**(3), 201–235.

Eftis, J., Carrasco, C. and Osegueda, R. [2003], 'A constitutive-microdamage model to simulate hypervelocity projectile-target impact, material damage and fracture', *International Journal of Plasticity* **19**, 1321–1354.

Espinosa, H., Patanella, A. and Fischer, M. [2000*a*], 'Dynamic friction measurements at sliding velocities representative of high-speed machining processes', *Journal of Tribology* **122**, 834–848.

Espinosa, H., Patanella, A. and Fischer, M. [2000*b*], 'A novel dynamic friction experiment using a modified kolsky bar apparatus', *Experimental Mechanics* **40**(2), 138–153.

Faure, L., Philippon, S., Lodygowski, A., Voyiadjis, G., Rusinek, A., Chevrier, P. and Dossou, E. [2009*a*], Design of a dynamometer capable of capturing the dry friction force in dynamic conditions, *in* A. Rusinek and P. Chevrier, eds, 'International Workshop in Memory of J.J.R. Klepaczko', Paul Verlaine University, Metz, France, pp. 189–197.

Faure, L., Philippon, S., Lodygowski, A., Voyiadjis, G., Rusinek, A., Chevrier, P. and Dossou, E. [2009*b*], Design of a dynamometer capable of capturing the dry friction force in dynamic conditions, *in* A. Rusinek, ed., 'International Workshop in Memory of J.J.R. Klepaczko', Metz, France.

Faure, L., Philippon, S., Lodygowski, A., Voyiadjis, G., Rusinek, A., Chevrier, P. and Dossou, E. [2009*c*], Evolution of an original device allowing the determination of the dry fricion coefficient in dynamic conditions, *in* 'Theoretical and experimental approaches for the dynamic industrial processes', Carlos III University in Madrid, p. 31.

Faure, L., Philippon, S., Lodygowski, A., Voyiadjis, G. Z., Rusinek, A., Chevrier, P. and Dossou, E. [2009*d*], Evolution of an original device allowing the determination of the dry fricion coefficient in dynamic conditions, *in* 'Theoretical and experimental approaches for the dynamic industrial processes', Carlos III University in Madrid, Madrid, p. 31.

Fleck, N. A. and Hutchinson, J. W. [1997], 'Strain gradient plasticity', *Advanced Applied Mechanics* **33**, 295–361.

Fleck, N., Muller, G., Ashby, M. and Hutchinson, J. [1994], 'Strain gradient plasticity - theory and experiment', *Acta Metallurgica et Materialia* **42**(2), 475–487.

Fleck, N. and Willis, J. [2009*a*], 'A mathematical basis for strain gradient plasticity theory- part i: Scalar plastic multiplier', *Journal of the Mechanics and Physics of Solids* **57**(1), 161–177.

Fleck, N. and Willis, J. [2009*b*], 'A mathematical basis for strain gradient plasticity theory- part ii: Tensorial plastic multiplier', *Journal of the Mechanics and Physics of Solids* **57**(7), 1045–1057.

Fredriksson, P. and Gudmundson, P. [2005], 'Size-dependent yield strength and surface energies of thin films', *Materials Science and Engineering a-Structural Materials Properties Microstructure and Processing* **400**, 448–450.

Fredriksson, P. and Gudmundson, P. [2007], 'Competition between interface and bulk dominated plastic deformation in strain gradient plasticity', *Modelling and Simulation in Materials Science and Engineering* **15**(1), 61–69.

Fremond, M. and Nedjar, B. [1996], 'Damage, gradient of damage and principle of virtual power', *International Journal of Solids and Structures* **33**(8), 1103.

Glema, A., Lodygowski, T. and Perzyna, P. [2000], 'Interaction of deformation waves and localization phenomena in inelastic solids', *Computer Methods in Applied Mechanics and Engineering* **183**, 123–140.

Glema, A., Lodygowski, T., Sumelka, W. and Perzyna, P. [2009], 'The numerical analysis of the intrinsic anisotropic microdamage evolution in elasto-viscoplastic solids', *International Journal of Damage Mechanics* **18**, 205–231.

Gudmundson, P. [2004], 'A unified treatment of strain gradient plasticity', *Journal of the Mechanics and Physics of Solids* **52**(6), 1379–1406.

Gurtin, M. [2000], 'On the plasticity of single crystals: free energy, microforces, plastic-strain gradients', *Journal of the Mechanics and Physics of Solids* **48**(5), 989–1036.

Gurtin, M. [2004], 'A gradient theory of small-deformation isotropic plasticity that accounts for the burgers vector and for dissipation due to plastic spin', *Journal of the Mechanics and Physics of Solids* **52**(11), 2545–2568.

Gurtin, M. and Anand, L. [2009], 'Thermodynamics applied to gradient theories involving the accumulated plastic strain:the theories of aifantis and fleck and hutchinson and their generalization', *Journal of the Mechanics and Physics of Solids* **57**, 405–421.

Gurtin, M. and Needleman, A. [2005], 'Boundary conditions in small-deformation, single-crystal plasticity that account for the burgers vector', *Journal of the Mechanics and Physics of Solids* **53**(1), 1–31.

Hale, C. S. [2010], Consideration of Wear Rates at High Velocity, PhD thesis, Air Force Institute of Tchnology, Wright-Patterson Air Force Base, Ohio.

Hardell, J. and Prakash, B. [2008], 'High-temperature friction and wear behaviour of different tool steels during sliding against al-si-coated high-strength steel', *Tribology International* **41**, 663–671.

Hartley, K. A., Duffy, J. and Hawley, R. H. [1985], 'The torsional kolsky (split-hopkinson) bar, mechanical testing', *Metal Handbook 8* **9**, 218–230.

Hassan, B., Corona, E. and Kyriakides, S. [1992], 'Ratchetting in cyclic plasticity, part ii: multiaxial behavior', *International Journal of Plasticity* **8**, 117–146.

Hassan, B. and Kyriakides, S. [1992], 'Ratchetting in cyclic plasticity, part i: uniaxial behavior', *International Journal of Plasticity* **8**, 91–116.

Hassan, B. and Kyriakides, S. [1994*a*], 'Ratchetting of cyclically hardening and softening materials: I. uniaxial bahavior', *International Journal of Plasticity* **10**, 149–184.

Hassan, B. and Kyriakides, S. [1994*b*], 'Ratchetting of cyclically hardening and softening materials: Ii. multiaxial bahavior', *International Journal of Plasticity* **10**, 185–212.

Hill, R. [1948], 'A theory of the yielding and plastic flow of anisotropic metals', *Proc Roy Soc London* **Ser A 193**, 281–297.

Holmquist, T. and Johnson, G. R. [1991], 'Determination of constants and comparison of results for various constitutive models', *Journal of Applied Physics* **1**, 853–860.

Hutchings, I. [2006], *The challenge of wear in wear-mechanisms, material and practice*, Jhon Willey and Sons Ltd (editor G.W. Stochowiak).

Ireman, P. [2005], 'Algorithms for gradient damage models based on a semi-smooth newton method', *Computer Methods in Applied Mechanics and Engineering* **194**, 727–741.

Ireman, P., Klarbring, A. and Stroemberg, N. [2002], 'Finite element algorithms for thermoelastic wear problems', *European Journal of Mechanics and Solids* **21**(423–440).

Ireman, P., Klarbring, A. and Stromberg, B. [2003], 'A model of damage coupled to wear', *International Journal of Solids and Structures* **40**, 2957–2974.

Ireman, P. and Nguyen, Q. [2004], 'Using the gradients of temperature and internal parameters in continuum thermodynamics.', *C. R. Mecanique* **332**, 249–255.

Johnson, G. R. and Cook, W. H. [1983], 'A constitutive model and data for metals subjected to large strains, high strain rates and high temperatures.', *7th International Symposium on Ballistics* **1**, 541.

Johnson, G. R. and Holmquist, T. [1988], 'Evaluation of cylinder-impact tests data for constitutive model constants', *Journal of Applied Physics* **64**(8), 3901–3910.

Johnson, K. L. [1995], 'Contact mechanics and the wear of metals', *Wear* **190**, 162–170.

Kattan, P. I. and Voyiadjis, G. [1993], 'Micromechanical modeling of damage in uniaxially loaded unidirectional fiber-reinforced composite laminae', *International Journal of Solids and Structures* **30**(1), 19–36.

Kay, G. [2003], Failure modeling of titanium 6al-4v and aluminum 2024-t3 with the johnson-cook material model, Final report, U.S. Department of Transportation, Federal Aviation Administration of Aviation Research, Washington, DC 20591.

Kennan, Z. [2005], Determination of the constitutive equations for 1080 steel and vascomax 300., Master's thesis, Air Force Institute of Tchnology, Wright-Patterson Air Force Base, Ohio.

Kim, J. and Kim, D. [1997], 'Development of a combined-type tool dynamometer with a piezo-film accelerometer for an ultra-precision lathe', *Journal of Material Processing Technology* **71**, 360–366.

Ko, P., Knowles, G. and Taponat, M. [1997], 'Friction characteristics and the wear process of metal pairs in sliding contacts with applications to modelling wear of power plant component', *Wear* **213**, 148–158.

Kolmogorov, V. [1996], 'Friction and wear model for a heavily loaded sliding pair, part i. metal damage and fracture model.', *Wear* **194**, 71–79.

Korkut, I. [2003], 'A dynamometer design and its construction for milling operation', *Material and Design* **24**, 631–637.

Krieg, R. [1975], 'A practical two surface plasticity theory', *Journal of Applied Mechanics, ASME* **42**, 641–646.

Laursen, T. [2002], *Computational contact and impact mechanics: fundementals of modeling interfacial phenomena*, Springer-Verlag, Heidelberg.

Le Monds, J. and Needleman, A. [1986], 'An analysis of shear band development incorporating heat conduction', *Mechanics of Materials* **5**, 363.

Lemaitre, J. and Chaboche, J. L. [1990], *Mechanics of Solid Materials*, Cambridge University Press, London.

Lim, S. C. and Ashby, M. F. [1987], 'Wear- mechanism maps', *Acta Metallurgica* **35**(1), 1–24.

Lim, S. C., Ashby, M. F. and Brunton, J. H. [1989], 'The effects of sliding conditions on the dry friction of metals', *Acta Mechanica* **37**(3), 767–772.

Litonski, J. [1977], 'Plastic flow of a tube under adiabatic torsion', *Bulletin of Polish Academy of Science* **25**, 7–14.

Martins, J., Oden, J. T. and Simoes, M. F. [1990], 'Rcent advances in engineering science- a study of static and kinetic friction', *International Journal of Engineering Science* **28**(1), 29–92.

Meyers, M., D.J., B., Vohringer, O., Kad, B., Xue, Q. and Fu, H. [2002], 'Constitutive description of dynamic deformation: physically-based mechanisms', *Material Science Engineering* **A322**, 194–216.

Michalowski, R. and Mroz, Z. [1978], 'Assiciated and non-associated sliding rules in contact friction', *Archives of Machanics* **30**, 259–276.

Mishina, H. [1998], 'Surface deformation and formation of original element of wear panicles in sliding friction.', *Wear* **215**, 10–17.

Montgomery, R. S. [1976], 'Friction and wear at high sliding velocity', *Wear* **36**, 275–298.

Mroz, Z. [1967], 'On the description of anisotropic work-hardening', *Journal of Mechanics and Physics of Solids* **15**, 163–175.

Mroz, Z. [1969], 'An attempt to describe the behavior of metal under cyclic loads using a more general work-hardening model', *Acta Mechanica* **7**(199-212).

Nayak, G. and Zienkiewicz, O. [1972], 'Convenient forms of stress invariants for plasticity', *Journal of the Structural Division* **98**(ST4), 949–954.

Needleman, A. [1988], 'Marerial rate dependent and mesh sensitivity in localization problems', *Computer Methods in Applied Mechanics and Engineering* **67**, 68–85.

Nemat-Nasser, S. and Isaacs, J. B. [1997], 'Direct measurement of isothermal flow stress of metals at elevated temperatures and high strain rates with application to ta and ta-w alloys', *Acta Materialia* **45**(3), 907–919.

Nygards, M. and Gudmundson, P. [2004], 'Numerical investigation of the effect of non-local plasticity on surface roughening in metals', *European Journal of Mechanics a-Solids* **23**(5), 753–762.

Oden, J. T. and Martins, J., eds [1984], *Models and Computational Methods for Dynamic Friction Phenomena*, Fenomech III, Stuttgart, Germany.

Ogawa, K. [1997], 'Impact friction test method by applying stress wave', *Experimantal Mechanics* **37**(4), 398–402.

Ohno, N. and Wang, J. [1993*a*], 'Kinematic hardening rules with critical state of dynamic recovery, part i: formulation and basic features for ratchetting bahavior', *International Journal of Plasticity* **9**, 375–390.

Ohno, N. and Wang, J. [1993*b*], 'Kinematic hardening rules with critical state of dynamic recovery, part ii: application to experiments of ratchetting bahavior', *International Journal of Plasticity* **9**, 391–403.

Palasantzas, G. [2004], 'Influence of self-affine roughness on the adhesive friction coefficient of a rubber body sliding on a solid substrate', *International Journal of Physics* **565**, 191–195.

Palazotto, A. N. [2007], Hypervelocity wear prediction. Presentation.

Persson, N. J. [1998], *Sliding Friction*, 1434-4904, Springer-Verlag.

Perzyna, P. [1963], 'The constitutive equations for rate-sensitive materials', *Quarterly of Applied Mathematics* **20**, 321–332.

Perzyna, P. [1966], 'Fundamental problems visco-plasticity', *Kuerti, H. (Ed), Advances in Applied Mechanics, Academic Press* **9**, 232–377.

Perzyna, P. [1971], 'Thermodynaic theory of viscoplastcity', *Advances in Applied Mechanics* **11**, 313–354.

Philippon, S. [2004], Etude Experimentale du Frottement Sec a Grandes Vitesses de Glissement, PhD thesis, University of Metz.

Philippon, S., Sutter, G., Dedourge, A. and Molinari, A. [2003], 'Etude experimentale du frottement', *International Journal of Mechanical Production Systems Engineering, High Speed Machining* pp. 57–60.

Philippon, S., Sutter, G. and Molinari, A. [2004], 'An experimental study of friction at high sliding velocities', *Wear* **257**, 777–784.

Phillips, A. and Lee, C. [1979], 'Yield surface and loading surfaces: experiments and recommendations', *International Journal of Solids and Structures* **15**, 715–729.

Phillips, A., Tang, J. and Ricciuti, M. [1974], 'Some new observations on yield surfaces', *Acta Mechanica* **20**, 23–39.

Phillips, A. and Weng, G. [1975], 'An analytical study of an experimentally verified hardening law', *Journal of Applied Mechanics, ASME* **42**, 375–378.

Pierce, J. L., Burton, C. A. and Brockman, R. A. [2008], Surface profile measurements from hhstt slipper and rail samples: Preliminary data, Technical report, University of Dayton.

Prager, W. [1956], 'A new method of analyzing stresses and strains in work-hardening plastic solids', *Journal of Applied Mechanics* **23**, 493–496.

Prakash, V. [1995], 'A pressure-shear plate impact experiment for investigating transient friction', *Experimantal Mechanics* **35**(4), 329–336.

Rajagopal, K. and Srinivasa, A. [2004], 'On the thermomechanics of materials that have multiple natural configurations. part i: viscoelasticity and classical plasticity', *Zeitschrift fuer angewandte Mathematik und Physik* **55**, 861–893.

Rajagopalan, S. and Prakash, V. [1999], 'A modified torsional kolesky bar for investigating dynamic friction', *Experimantal Mechanics* **39**(4), 295–303.

Rusinek, A. and Klepaczko, J. R. [2001], 'Shear testing of sheet steel at wide range of strain rates and a constitutive relation with strain-rate and temperature dependence of the flow stressss', *International Journal of Plasticity* **17**, 87–115.

Rusinek, A., Rodriguez-Martinez, J. A., Zaera, R., Klepaczko, J. R., Sauvelet, C. and Arias, A. [2007], Experimental and numerical analysis of failure process of mild steel sheets subjected to perpendicular impact by hemispherical projectiles. University of Paul Verlaine in Metz.

Simo, J. C. and Hughes, T. J. R. [1998], *Computational inelasticity*, Interdisciplinary Applied Mathematics, Springer, New York.

Steinberg, D. and Lund, C. [1989], 'A constitutive model for strain rates from 10^4 to $10^6/s$', *Journal of Applied Physics* **65**(4), 1528–1533.

Stelmashenko, N., Walls, M., Brown, L. and Milman, Y. [1993], 'Microindentation on w and mo oriented single crystals: An stm study', *Acta Metallurgica et Materialia* **41**(2855-2865).

Stolken, J. and Evans, A. [1998], 'A microbend test method for measuring the plasticity length-scale', *Acta Mater* **46**, 5109–5115.

Stupkiewicz, S. [2007], *Micromechanics of Contact and Interphase Layers*, ISSN 1613-7736, Springer.

Stupkiewicz, S. and Mroz, Z. [2003], 'Phenomenological model of real contact area evolution with account for bulk plastic deformation in metal forming', *International Journal of Plasticity* **19**, 323–344.

Sutter, G., Faure, L., Molinari, A., Ranc, N. and Pina, V. [2003], 'An experimental technique for the measurement of temperature fields for the orthogonal cutting in high speed machining', *International Journal of Machine Tools and Manufacture* **43**, 671–678.

Sutter, G., Philippon, S. and Garcin, F. [2006], 'Dynamic analysis of the interaction between an abradable material and a titanium alloy', *Wear* **261**, 686–692.

Sutter, G., Philippon, S. and Molinari, A. [2004], An experimental investigation of dry friction for a large range of sliding velocities, Technical report, 15th DYMAT Technical Meeting, Metz, France.

Tjernlund, J., Gamstedt, E. and Gudmundson, P. [2006], 'Length-scale effects on damage development in tensile loading of glass-sphere filled epoxy', *International Journal of Solids and Structures* **43**(24), 7337–7357.

Tounsi, N. and Otho, A. [2000*a*], 'Dynamic cutting force measuring', *International Journal of Machine Tools and Manufacture* **40**, 1157–1170.

Tounsi, N. and Otho, A. [2000*b*], 'Identification of machine-tool-workpiece system dynamics', *International Journal of Machine Tools and Manufacture* **40**, 1367–1384.

Tsagrakis, I., Konstantinidis, A. and Aifantis, E. [2003], 'Strain gradient and wavelet interpretation of size effects in yield and strength', *Mechanics of Materials* **35**(733-745).

Tseng, N. and Lee, G. [1983], 'Simple plasticity model for two-surface cyclic plasticity model for finite strains', *American Society of Civil Engineers* **109**(3), 795–810.

Voyiadjis, G. and Abu Al-Rub, R. [2003], 'Thermodynamic based model for the evolution equation of the backstress in cyclic plasticity', *International Journal of Plasticity* **19**(12), 2121–2147.

Voyiadjis, G. and Abu Al-Rub, R. K. [2007], 'Nonlocal gradient-dependent thermodynamics for modeling scale-dependent plasticity', *International Journal for Multiscale Computational Engineering* **5**(3-4), 295–323.

Voyiadjis, G. and Almasri, A. [2008], 'A physically based constitutive model for fee metals with applications to dynamic hardness', *Mechanics of Materials* **40**(6), 549–563.

Voyiadjis, G., Almasri, A. and Park, T. [2010], Experimental nanoindentation of bcc metals, 8 manuscript pages, Mechanics Research Communications.

Voyiadjis, G. and Basuroychowdhury, I. [1998], 'A plasticity model for multiaxial cyclic loading and ratchetting', *Acta Mechanica* **126**(19-35).

Voyiadjis, G. and Deliktas, B. [1997], 'Damage in mmcs using the gmc: theoretical formulation', *Composites Part B-Engineering* **28**(5-6), 597–611.

Voyiadjis, G. and Deliktas, B. [2009*a*], 'Formulation of strain gradient plasticity with interface energy in a consistent thermodynamic framework', *International Journal of Plasticity* **25**(10), 1997–2024.

Voyiadjis, G. and Deliktas, B. [2009*b*], 'Mechanics of strain gradient plasticity with particular reference to to decomposition of the state variables into energetic and dissipative components', *International Journal of Engineering Science* **47**(11-12), 1405–1423.

Voyiadjis, G. and Deliktas, B. [2009*c*], Modeling strengthening and softening in inelastic nanocrytalline materials with reference to the triple junction and grain boundaries using strain gradient plasticity. Journal of the Mechanics and Physics of Solids (unpublished).

Voyiadjis, G., Deliktas, B., Faghihi, D. and Lodygowski, A. [2009], Friction coefficient evaluation using physically based viscoplasticity model at the contact region during high velocity sliding. Submitted to Acta Mechanica, 26 manuscript pages.

Voyiadjis, G., Deliktas, B., Lodygowski, A., Palazotto, A., Philippon, S., Rusinek, A., Faure, L. and Chevrier, P. [2009*a*], High rate and frictional effects in wear of metals using strain gradient plasticity, *in* A. Rusinek and P. Chevrier, eds, 'International Workshop in Memory of J.J.R. Klepaczko', Paul Verlaine University, Metz, France, pp. 267–275.

Voyiadjis, G., Deliktas, B., Lodygowski, A. and Park, T. [2010], Non-local modeling of heterogeneous media to assess high velocity frictional contact using coupled viscoplasticity damage model. 31 manuscript pages.

Voyiadjis, G. and Foroozesh, M. [1990], 'Anisotropic distortional yield model', *Journal of Applied Mechanics* **57**, 537–547.

Voyiadjis, G. and Kattan, P. I. [1991], 'Phenomenological evolution equations for the backstress and spin tensors', *Acta Mechanica* **88**, 91–111.

Voyiadjis, G., Lodygowski, A. and Deliktas, B. [2009], Non-local coupling of friction and damage in high velocity wear, Technical report, Airforce Institut of Technology, Wright-Patterson Air Force Base, Ohio.

Voyiadjis, G. and Peters, R. [2010], Size effects in nano-indentation an experimental and analytical study. 23 manuscript pages.

Voyiadjis, G. and Sivakumar, S. [1991*a*], 'A robust kinematic hardening rule with ratchetting effects. part i: application to nonproportional loading cases', *Acta Mechanica* **107**, 117–136.

Voyiadjis, G. and Sivakumar, S. [1991*b*], 'A robust kinematic hardening rule with ratchetting effects. part i: theoretical formulation', *Acta Mechanica* **90**, 105–123.

Voyiadjis, G., Thiagarajan, G. and Patrakis, E. [1995], 'Constitutive modeling for granular media using anisotropic distortional yield model', *Acta Mechanica* **110**, 151–171.

Voyiadjis, G. Z. and Abed, F. H. [2005], 'Microstructural based models for bcc and fcc metals with temperature and strain rate dependency', *Mechanics of Materials* **37**, 355–378.

Voyiadjis, G. Z. and Abu Al-Rub, R. K. [2005], 'Gradient plasticity theory with a variable length scale parameter', *International Journal of Solids and Structures* **42**, 3998–4029.

Voyiadjis, G. Z., Abu Al-Rub, R. K. and Palazotto, A. N. [2003], 'Non-local coupling of viscoplasticity and anisotropic viscodamage for impact problems using gradient theory', *Archives of Machanics* **55**(1), 39–89.

Voyiadjis, G. Z., Abu Al-Rub, R. K. and Palazotto, A. N. [2008], 'Constitutive modeling and simulation of perforation of targets by projectiles', *Journal of the American Institute for Aeronautics and Astronautics* **46**(2), 304–316.

Voyiadjis, G. Z. and Deliktas, B. [2000*a*], 'A coupled anisotropic damage model for the inelastic response of composite materials', *Computer Methods in Applied Mechanics and Engineering* **183**, 159–199.

Voyiadjis, G. Z. and Deliktas, B. [2000*b*], 'Multi-scale analysis of multiple damage mechanics coupled with inelastic behavior of composite materials', *Mechanics Research Communications* **2.3**(27), 295–300.

Voyiadjis, G. Z., Deliktas, B. and Aifantis, E. C. [2001], 'Multiscale analysis of multiple damage mechanics coupled with inelastic behaviour of composite materials', *Journal of Engineering Mechanics* **2.7**(127), 636–645.

Voyiadjis, G. Z., Deliktas, B., Lodygowski, A., Palazotto, A. N., Philippon, S., Rusinek, A., Faure, L. and Chevrier, P. [2009*b*], 'High rate and frictional effects in wear of metals using strain gradient plasticity', *Proceedings of the International Workshop in Memory of J.R.R. Klepaczko* .

Voyiadjis, G. Z. and Dorgan, R. J. [2001], 'Gradient formulation in coupled damage-plasticity', *Archives of Machanics* **4-5**(53), 565–597.

Voyiadjis, G. Z. and Kattan, P. I. [1990], 'A coupled theory of damage mechanics and finite strain elasto-plasticity. i: Damage and elastic deformations', *International Journal of Engineering Science* **28**(6), 505–524.

Voyiadjis, G. Z. and Park, T. [1997], 'Local and iterfacial damage analysis of metal matrix composites using finite element method', *Engineering Fracture Mechanics* **56**(4), 483–511.

Wang, W. M., Sluys, L. J. and De Borst, R. [1996], 'Interaction between material length scale and imperfection size for localization phenomena in viscoplastic media', *European Journal of Mechanics-A/Solids* **2.3**(15), 447–464.

Yaldiz, S. and Unsacar, F. [2006*a*], 'Design, development and testing of a turning dynamometer for cutting force measurement', *Materials and Design* **27**, 839–846.

Yaldiz, S. and Unsacar, F. [2006*b*], 'A dynamometer design for measurement the cutting forces on turning', *Measurement* **39**, 80–89.

Yaldiz, S., Unsacar, F. and Saglam, H. [2006], 'Design, development and testing of a four-component milling dynamometer for the measurement of cutting force and torque', *Mechanical Systems and Signal Processing* **21**, 1499–1511.

Yun, S. and Palazotto, A. N. [2007], 'Damage mechanics incorporating two back stress kinematic hardening constitutive models', *Engineering Fracture Mechanics* **74**, 2844–2863.

Zbib, H. M. and Aifantis, E. C. [1992], 'On the gradient-dependent theory of plasticity and shear banding', *Acta Mechanica* **9**, 209–225.

Zerilli, F. and Armstrong, R. [1987], 'Dislocation-mechanics-based constitutive relations for material dynamics calculations', *Journal of Applied Physics* **61**(5), 1816–1825.

Ziegler, H. [1959], 'A modification of prager's hardening rule', *Applied Mathematics* **7**, 55–65.

Ziegler, H. [1983], *An Introduction to Thermomechanics*, 2 edn, North-Holland Series in Applied Mathematics and Mechanics, North-Holland, Amsterdam.

Ziegler, H. and Wehrli, C. [1987], 'On a principle of maximal rate of entropy production', *Journal of Non-Equilibrium Thermodynamics* **12**(3), 229–243.

Zineb, M. B., Philippon, S., Chevrier, P. and Lipinski, P. [2008], 'Détermination expérimentale de l'effort d'interaction aux grandes vitesses: application aux matériaux abradables', *Revue de Mécanique Appliquée et Théorique* **1**(10), 749–757.

Zsidai, L., Samyn, P., Vercammen, K., Van Acker, K., Kozma, M., Kalácska, G. and De Baets, P. [2004], 'Friction and thermal effects of engineering plastics sliding against steel and dln-coated counterfaces', *Tribology Letters* **17**(2), 269–288.

Vita

Adam Lodygowski was born in Poland in July 1981. He grew up in Poznan, his hometown, finished his primary music school and completed his high school education following which, he entered the Poznan University of Technology. After three years of his joint undergraduate and master's program, he left for the University of Hanover, Germany, where for another two years he continued his education. He returned to Poland in 2005 and defended his master thesis, which was written under the guidance of Professors Glema and Nackenhorst. Another year he spent working at Poznan University of Technology and intensely training for the Poland National Team in Rowing. In 2006 he left Poznan and began his doctoral studies at Louisiana State University in the United States under the supervision of Boyd Professor George Z. Voyiadjis. Two years later he joined also the Department of Mathematics to pursue the master's degree in mathematics with concentration in finance, in addition to the current program he was enrolled. After nearly four years from joining the LSU he completed the research and presented his dissertation. Mr. Lodygowski has been involved in wide spectrum of different research topics skilfully spanning the self conducted experimental studies with the theoretical and numerical approach. During his stay at LSU he independently taught three different classes and was a TA for additional five. He has nearly 10 publications published in several prestigious journals and conference proceedings in the field of tribology, structural engineering and engineering mechanics. He is also a co-author of the report submitted to the Air Force Institute of Technology. He will receive the degree of Doctor of Philosophy in civil engineering and Master of Science in Mathematics in May 2010. His future plans involve developing his teaching skills in the Department of Civil and Environmental Engineering at Poznan University of Technology, Poland, as well as working in the private sector utilizing mathematical skills acquired during his stay at LSU.